LIST OF CONTENTS

LISTS OF FIGURES

LIST OF TABLES

ABSTRACT

Ageing of outdoor insulation under low leakage currents are concerns for safety and reliability in transmission line operations. Overhead line elements such as insulators and ADSS (All Dielectric, Self-Supporting) cables are subject to electric fields, resultant leakage currents, and resulting surface discharges such as coronas and dry-band arcs. Under certain conditions, the normally benign long-term low current ageing effect may transform to more severe ageing forms, having a detrimental impact on the insulation materials and creating high rates of unexpected failures.

In this thesis, a series of experimental studies are reported which have created low current discharges under variable electrical and environmental conditions. The electrical properties of resulting arcs are investigated and their impact on the insulation materials is analyzed. Based on the test results, new modelling approaches have been developed for the simulation of dry-band arcing activity. The respective 'Double Sinusoidal Model' and 'PSCAD simulation' are able to simulate the voltage and current traces of low current arcs, while the 'Triple Cylinder Model' is used to analyze the heat flow around the arcing region. Based on both experiment and simulation, the phenomenon of 'dry-band arc compression' is reproduced. Research confirms previous suggestions that such a compression process may lead to more aggressive damage on insulation surfaces, and could possibly accelerate the long-term ageing effect into a short-term hazard. As a result, this thesis supports the argument that processes controlling insulation lifetime may not be continual and gradual, but are determined by extreme events such as the occurrence of dry-band arc compression.

DECLARATION

That no portion of the work referred to in the thesis has been submitted in support of an application for another degree or qualification of this or any other university or other institute of learning.

COPYRIGHT STATEMENT

The following four notes on copyright and the ownership of intellectual property rights must be included as written below:

I. The author of this thesis (including any appendices and/or schedules to this thesis) owns certain copyright or related rights in it (the "Copyright") and s/he has given The University of Manchester certain rights to use such Copyright, including for administrative purposes.

II. Copies of this thesis, either in full or in extracts and whether in hard or electronic copy, may be made **only** in accordance with the Copyright, Designs and Patents Act 1988 (as amended) and regulations issued under it or, where appropriate, in accordance with licensing agreements which the University has from time to time. This page must form part of any copies made.

III. The ownership of certain Copyright, patents, designs, trade marks and other intellectual property (the "Intellectual Property") and any reproductions of copyright works in the thesis, for example graphs and tables ("Reproductions"), which may be described in this thesis, may not be owned by the author and may be owned by third parties. Such Intellectual Property and Reproductions cannot and must not be made available for use without the prior written permission of the owner(s) of the relevant Intellectual Property and/or Reproductions.

IV. Further information on the conditions under which disclosure, publication and commercialisation of this thesis, the Copyright and any Intellectual Property and/or Reproductions described in it may take place is available in the University IP Policy (see http://www.campus.manchester.ac.uk/medialibrary/policies/intellectual-property.pdf), in any relevant Thesis restriction declarations deposited in the University Library, The University Library's regulations (see http://www.manchester.ac.uk/library/aboutus/regulations) and in The University's policy on presentation of Theses.

ACKNOWLEDGEMENTS

I would like to give my sincere appreciation to Prof. Simon Rowland, who was my PHD supervisor from 2007 to 2010 (also my MSc supervisor from 2006 to 2007), for his remarkable guidance and kindly help. With his academic effort and financial support, I managed to publish two journal papers (another two are being written for submission), five conference papers, and attended several electrical insulation conferences held in United Kingdom, Canada, South Africa and United States. From his inspiration, I decided to continue working in the Electrical Power Sector as a Power System Engineer in National Grid UK.

I wish to thank National Grid, who is the sponsor of my PhD project, for their financial and technical support in this work for three years, and the permission to publish academic papers.

I would like to express my sincere appreciation to Miss. Xiaolei Liu, who is my fiancée, for her positive attitude to encourage me continuously to pursue the PhD degree in this University. We met and fell in love during our MSc study and now she has been working in Lloyds Banking Group in London for two years. Thanks indeed for her understanding to allow me spend most of time doing research in Manchester, and apologize for insufficient accompany with her during this period.

Finally, my sincere gratitude is given to my beloved parents for motivating me to study in Manchester, for their encouragement and financial support. Although there are 5,000 miles from China to UK, our hearts are always closed to each others.

LIST OF ABBREVIATIONS

AC	Alternative current
ACF	Autocorrelation function
ADSS	All dielectric, self-supporting
A/D	Analog-to-digital
EPR	Ethylene propylene rubber
FFT	Fast Fourier transforms
I-t	Current against time
PDMS	Polydimethylsiloxane
PE	Polyethylene
PET	Polyethylene terephthalate
RMS	Root mean square
RTVSR	Room-temperature vulcanized silicone rubber
UV	Ultra-violet
V-I	Voltage against current
V-t	Voltage against time
XLPE	Cross-linked polyethylene

CHAPTER 1

INTRODUCTION

Ageing of outdoor insulation under low leakage currents are long-term effects in power systems. On overhead transmission lines, elements such as insulators, conductors and communication cables may suffer from this form of ageing. Under some circumstances, low current discharges such as corona, dry-band arcing or even flashover may develop on insulation surfaces, leading to erosion or damage thereby reducing the quality and reliability of insulation materials. This may eventually lead to mechanical failures of insulators and conductors, and dielectric failures of overhead line insulation. There is evidence to suggest high rates of transmission line faults.

1.1 TRANSMISSION LINE ELEMENTS

1.1.1 INSULATORS

The first high voltage insulator utilized in a power transmission line was invented in 1882. Development resulted in rapid growth over the 19th and 20th centuries [1]. The history of composite insulators dates back to the 1940s, when organic materials were applied in indoor insulator manufacture [2]. For the last thirty years, composite insulators have been increasingly used in modern power transmission systems, achieving excellent supporting and dielectric functions [1].

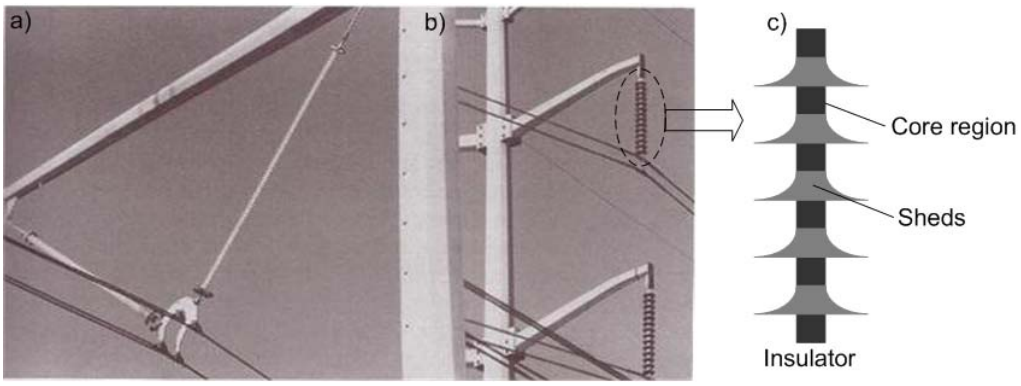

a) 500kV line using composite insulators, b) a 230kV line using cap and pin porcelain insulators [1], and c) Main structure of a composite insulator

Figure 1-1: Images of insulators on overhead transmission lines

Insulators have two main functions, which are mechanical support and dielectric insulation respectively. The mechanical function is to hold the conductors, sustain their weight stress on suspension towers (Figure 1-1), or their tension stress on tension towers. Dielectric supports must provide an electrical barrier between the metallic tower and transmission conductors in order to avoid flashover [3].

1.1.2 ADSS CABLE

All-dielectric, self-supporting (ADSS) cables have been proven as a standard method to install the optical fibres onto high voltage transmission lines, for the purposes of high-bandwidth network control and communication [4].

Figure 1-2 a) shows the construction of a typical twin circuit tower (UK) and the location of an ADSS cable, suspended independently of the phase conductors. The relative position of the ADSS cable between the six phase conductors may vary significantly between a tension tower and a suspension tower, because these two kinds of towers have different cable clamping locations. On a tension tower, the ADSS cable is installed between the bottom two conductors. On a suspension tower the ADSS is clamped roughly midway between the bottom four

conductors. In addition, because of the different mechanical properties of the conductors and the ADSS cable, they are strung with very different sags. This sag difference along with the clamping positions leads to changes in the relative position of an ADSS cable relative to the phase conductors between two such towers as illustrated in Figure 1-2 b).

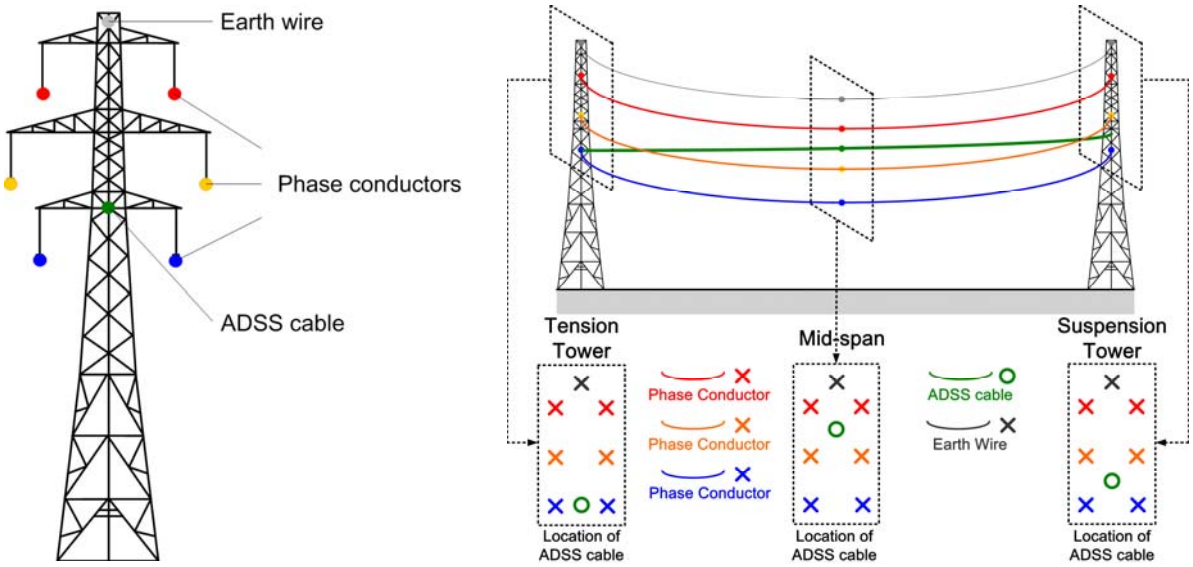

a) ADSS cable location on a suspension tower

b) ADSS cable location in an overhead line span

Figure 1-2: The location of ADSS cable on overhead transmission lines

1.2 Low Current Discharges

1.2.1 Electric Fields on Transmission Lines

On the overhead transmission line systems, an electrical field is created by the distributed capacitance and leakage currents between the phase conductors, the earth wire, the tower, insulators (and ADSS cable if applicable). Figure 1-3 gives an example of calculated electric field distribution around a tower. The voltage gradient varies with locations around the tower, with 100% of phase voltage appearance at the conductors and less than 1% of voltage near the tower and earth wire.

In addition, the electric field distribution changes across the whole span length between towers. Therefore, a voltage gradient is generated along the insulators or ADSS cable which drives low leakage currents on the subject insulation surfaces.

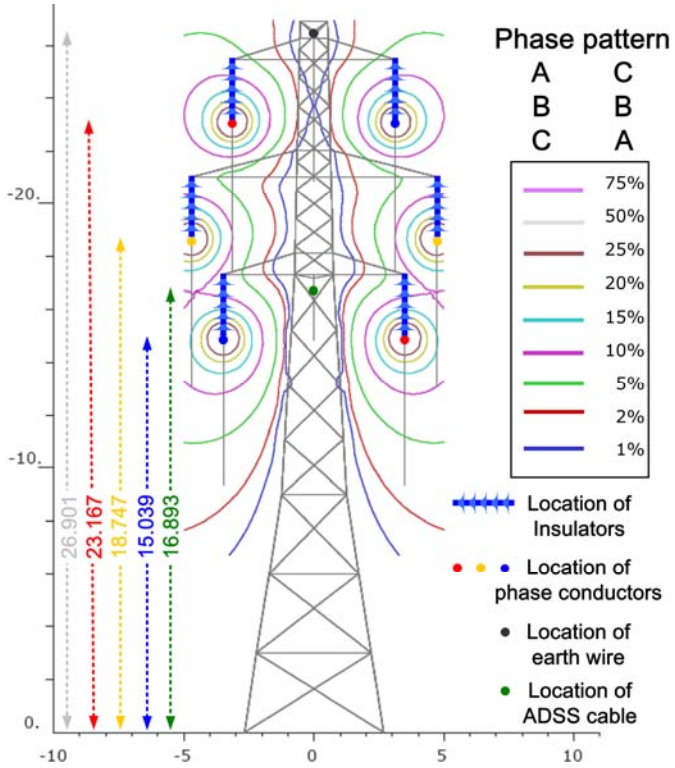

Figure 1-3: An example of electric field distribution around a typical L7 suspension tower on a 132 kV transmission line

1.2.2 Low Current Discharges on Insulators

As discussed previously, because the voltage gradients are distributed differently on insulators, leakage currents may flow on the insulator surface. As a result, dry-band arcing activity may occur on the insulator surface. The process is illustrated in Figure 1-4 (a part of this figure is from [3]).

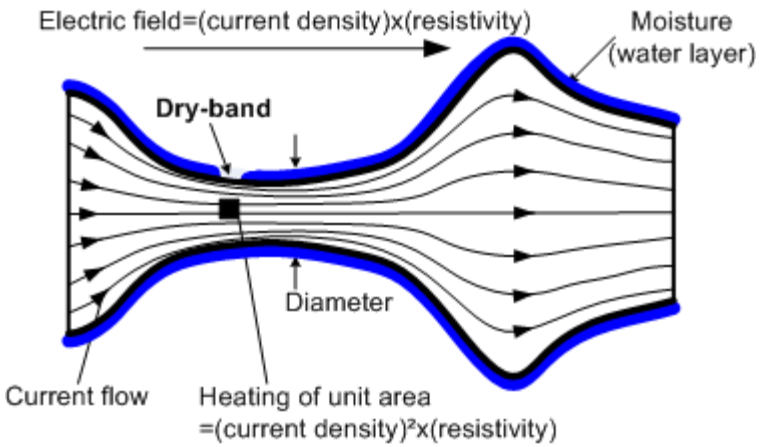

Figure 1-4: Surface joule heating on an arbitrary hydrophilic insulator shape which is polluted and wetted [3]

Moisture (a water layer) can be deposited on the insulator surface due to wet weather such as fog and rain, facilitated by any reduction of insulator surface hydrophobicity [3]. The Joule-heating from the leakage current causes the water layer to evaporate. The corresponding heating density calculation indicates that the area with the maximum current density is readily dried out. This first dry-out area may be located around the insulator core because the current density is relatively high there. As the water film is evaporated and becomes thinner, the surface resistivity also increases, accelerating the drying process. Higher resistivity leads to electric field increases. Following this effect, if the ionization field level is met, a discharge occurs. This form of discharge is a low current corona phenomenon. If the drying process creates a well defined dry-band area with a gap separating two extensive water layers, an arc may be established in the dry-band area and this is called a 'dry-band arc' [5].

1.2.3 Low Current Discharges on ADSS Cables

As shown in Figure 1-5, the electric field generated voltage gradients will be spread along the ADSS cable suspended between towers. This voltage gradient can be as much as tens of kilovolts dropped within

several metres along the cable [6]. If the surface of the cable becomes wet and conductive, the gradient is able to induce milliamp sized currents along its length. As the towers earth the cable via metallic clamps, the voltage reduces to zero at both ends of cable. The shape of current is however variable with different locations along the cable, and may turn to zero somewhere on the span. This characteristic is not reflected in this figure for simplification purpose.

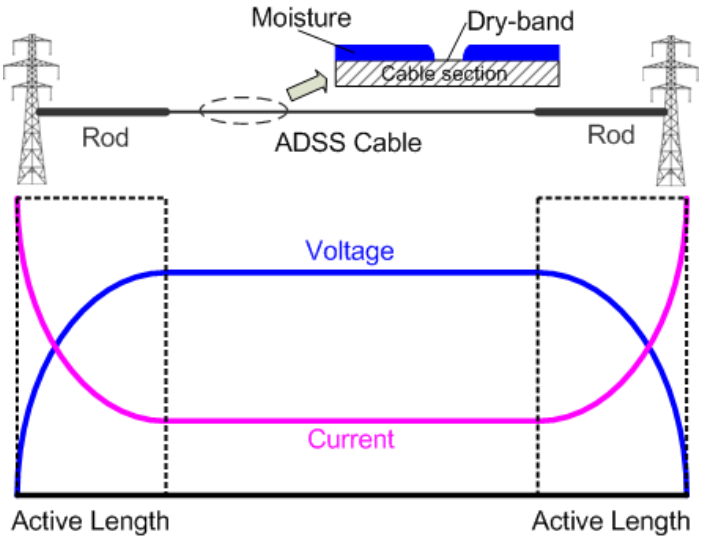

Figure 1-5: Schematic showing the relationship between the induced voltage, current and dry-band area on ADSS cable [6]

This current can give rise to heating on the cable. Following this heating effect, a dry-band will consequently occur on the surface if the cable is covered with moisture. The dry-band will possess higher impedance than other wet parts of the cable surface. This high impedance characteristic leads to a large voltage drop across the short section of dry-band. Eventually the dry-band arc may be formed [6].

1.3 OBJECTIVES

The objective of this thesis is to investigate ageing as a result of low surface currents for outdoor insulation on overhead transmission lines. The electrical discharges associated with the dry-band arcing phenomenon are the emphasis of this research. The detailed objectives are to:

1) Understand the impact of low current ageing on transmission line elements such as insulators and ADSS cables.

2) Understand low current dry-band arcing phenomenon on outdoor insulation surfaces.

3) Theoretically describe the cause of dry-band arc compression; analyze the reasons and situations for arcing compression happening.

4) Develop a series of experiments investigating low current arcs on insulation surfaces for different environmental and electrical conditions; experimentally study the rare but severe ageing forms of dry-band arc compression.

5) Develop mathematical models for the simulation of dry-band arcing and arc compression situations created in experimental work; further to model the heat flow inside the arc and from arc to its surroundings, especially on material surfaces.

6) Summarize the extreme ageing situations of low current arcing compression and their impact on outdoor insulation materials, based on both experimental and simulation work.

CHAPTER 2

BACKGROUND

2.1 COMPOSITE INSULATORS

Figure 2-1 demonstrates the typical structure of a composite insulator [7]. The fibreglass core is made of axially aligned glass fibres bonded together with organic resin. This design is able to achieve a reliable mechanical support for the suspension of transmission conductors [5]. However, this kind of fibreglass core without surface protection can not survive outdoor, high voltage applications. The moisture contamination and leakage current may lead to surface tracking, resulting in the fracture failure of the fibreglass composite core [8]. In order to prevent insulator core failure, sheds made from composite materials such as silicone rubber or ethylene propylene rubber (EPR) are moulded on to the fibreglass core for mainly two protection purposes. Firstly, these sheds can protect the insulator core from penetration of water, contamination and arcing plasma, dramatically reducing the possibility of the fibreglass core being damaged over its long-term service. Also, the dielectric materials of sheds can provide excellent electrical insulation between the insulators' upper and lower end fittings by increasing the 'creepage distance' and resistivity against surface current [3].

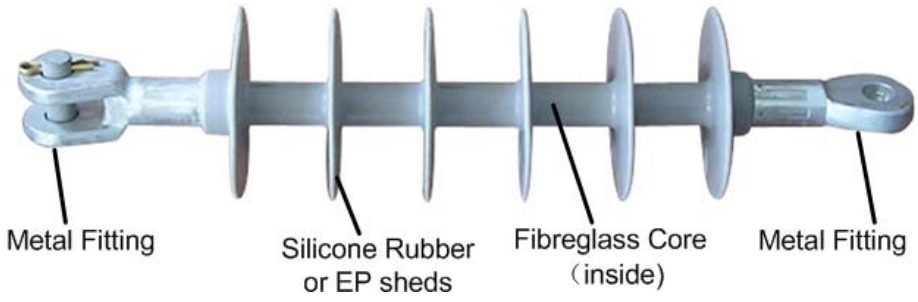

Figure 2-1: General arrangement of a composite insulator [7]

The main advantage of composite insulators is their excellent electrical insulation resulting from the surface dielectric. This strength is controlled by surface moisture and deposits [3]. Due to the low surface energy of some composite materials such as silicone rubber [9], composite insulators provide high hydrophobicity performance. Furthermore, some insulator coating materials such as silicone rubber demonstrate the ability to recover hydrophobicity after ageing [10]. As a result of these inherent abilities to repel water, composite insulators have a strong surface dielectric strength even when wet, so that they can be utilized in heavily contaminated areas [11], or higher voltage level power transmission systems [12].

Other advantages are: low weight, reduced damage possibility from vandalism such as gunshot, reduced levels of maintenance such as insulator washing [13], short construction periods and good contamination performance [14].

2.2 ADSS CABLE

Typically, an ADSS cable includes optical fibres embedded in loose tubes, a strength member and a sheath as their main parts. The structure of such a cable is shown in Figure 2-2 a) [15]. The cable investigated in this thesis is a ribbon-in-slot design manufactured by STC and is no longer made [16], and this cable structure is shown in Figure 2-2 b).

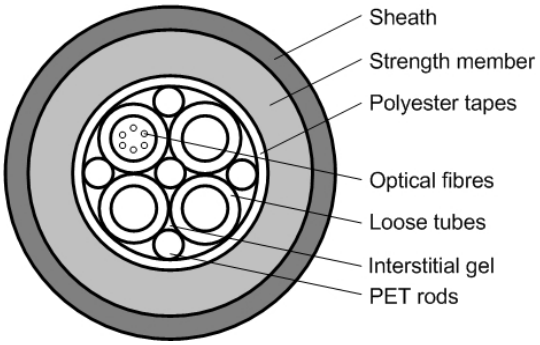

a) Typical modern structure of ADSS cable cross-section [15]

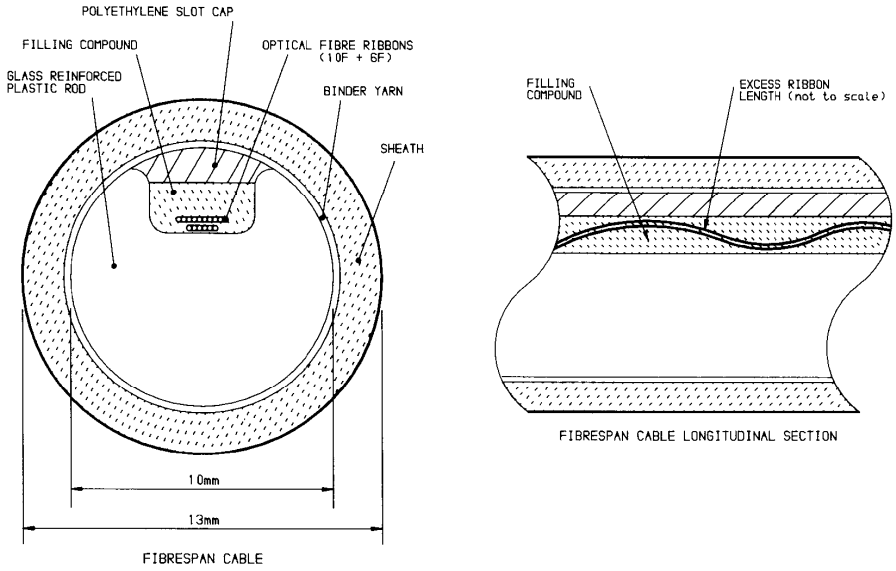

b) Structure of specified ADSS cable examined in this thesis [16]

Figure 2-2: Schematic of the structure of ADSS cables

The main functions of each part of the ADSS cable are described as follows: Optical fibres are used as the medium for communication. The advantage of optical fibres is their inherent immunity to electromagnetic

interference. Loose tubes or slotted cores are used to house and protect optical fibres. Loose tubes are stranded in order to provide the cable 'excess fibre length' to avoid optical fibres themselves being strained. In a slotted core this excess length is provided by the undulation of the ribbons. Typically modern ADSS cables utilize aramid yarns as strength members. Finally a sheath is used to protect cable elements from the environment. As long as moisture does not penetrate the cable the internal structure does not affect the electrical performance of the cable sheath. If the sheath is punctured and moisture penetrates the core, discharges can occur within the cable leading to thermal and ageing issues. Water blocking of a core is thus an essential design requirement [4, 17, 18].

2.3 SURFACE AGEING MECHANISMS

The insulation surfaces can be influenced by their outdoor service surroundings, as a result of environmental elements such as UV radiation, contamination and ultimately electrical discharges such as corona and dry-band arcing.

Solar UV radiation with wavelengths from 290 to 350 nm are incident on insulator surfaces. The associated photon energy (about 398 kJ/mole) is greater than the bond strength of molecules of some polymeric materials utilized for composite insulators. As the result, the composite surface can be degraded by UV from sunlight; furthermore, this degradation can be accelerated with the presence of moisture [3].

Generally, contamination deposition is retained more readily on aged composite insulators compared to porcelain insulators under the same environment [19]. The contamination distribution on a composite insulator has been found to be non-uniform, higher on both ends, but lower in the middle of an insulator string [20]. The contamination performance may depend on the profile as well as shape variation of shed design, and also the natural cleaning effects of rainfall and wind [3]. Some shed designs using separately moulded weather sheds may have weak points around their radial joints when exposed to contaminated environments [21]. Soluble contamination can increase the wetting process over the insulator surface, which may be considered as a contribution to the loss of hydrophobicity of insulator surface [3].

Low current electrical discharges such as corona or dry-band arcs can also lead to chemical reactions on polymers. An investigation of room-temperature vulcanized silicone rubber (RTVSR) under dry-band arcing was conducted and the reasons for hydrophobicity loss of this material is revealed in [22]: The basic polymer of RTVSR is polydimethylsiloxane

(PDMS). The molecular structure of PDMS is shown in Figure 2-3 a). The heat from dry-band arcing probably causes scission of -CH_3 groups from Si shown in Figure 2-3 b), the scission of the polymer backbone shown in Figure 2-3 c), as well as interchange of this backbone shown in Figure 2-3 d). The dots associated with •O, •Si and •CH_3 represent the free radicals that scission and the interchange reaction create. In the presence of moisture (H_2O), a hydrolysis reaction may occur as described in Figure 2-3 e) and Figure 2-3 f). The hydrolysis is followed by oxidation of hydrocarbon groups and crosslinking of siloxane bond in Figure 2-3 g). The increased oxygen and OH level are responsible for creating high hydrogen bonding forces between RTVSR and water (moisture) resulting in the rapid loss of hydrophobicity. The cross-linking results in embrittlement of the polymer.

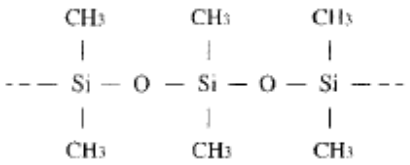

a) Molecular structure of PDMS

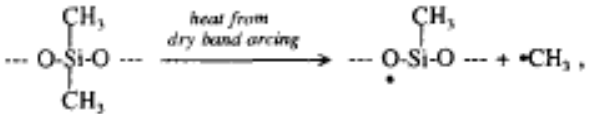

b) Scission of –CH_3 groups from Si

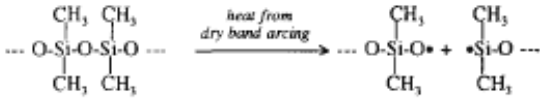

c) Scission of polymer backbone

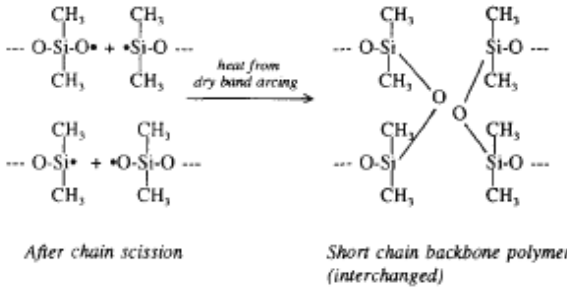

d) Interchange of backbone

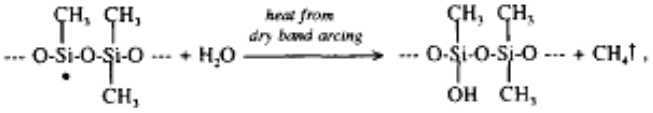

e) Hydrolysis of siloxane bonds

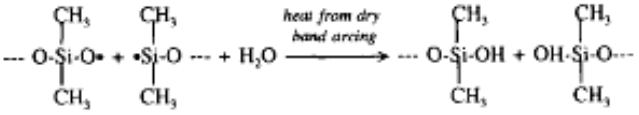

f) Hydrolysis of hydrocarbon groups

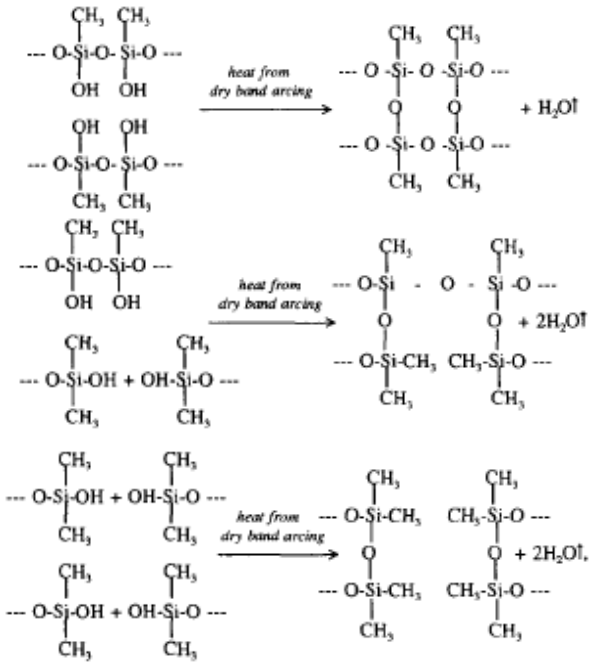

g) Oxidation of hydrocarbon groups and crosslinking of siloxane bond

Figure 2-3: Chemical reactions in RTVSR covered composite insulator surface by dry-band arc discharges [22]

2.4 PHYSICS OF LOW CURRENT DISCHARGES

2.4.1 CORONA

Corona is a kind of electrical discharge which can be present on composite insulators. There are two kinds of corona summarized below:

Corona on insulator hardware is generally a concern for composite insulators with the line voltage higher than 69 kV. This corona particularly occurs from the metallic insulator attachment hardware (normally the bottom hardware close to the line-end) in air or on an insulator surface. Evidence of corona cutting on the line-end shed of an 115 kV composite insulator is shown in Figure 2-4 [3].

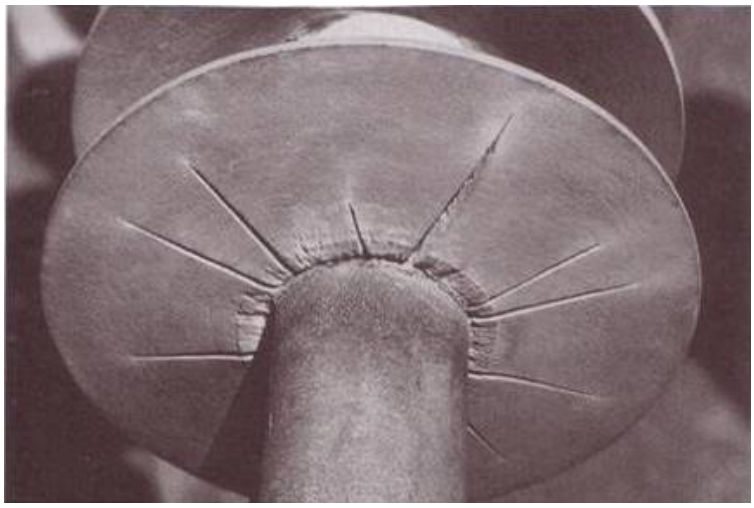

Figure 2-4: An evidence of corona cutting damage on composite insulator [3]

2.4.1.1 CORONA FROM METALS

The reason for corona ignition is that the voltage gradient distributed on insulator exceeds a threshold. The initial electric field for corona formation on a clean smooth surface in standard air density (760mm Hg and 25°C) is 21.2 kV/cm [3]. The 'average' inception voltage gradient for corona on a real object is determined by surface condition such as

roughness and contamination, as well as atmospheric effects such as humidity and air density δ which can be calculated as [5]:

$$\delta = \frac{b}{101.3}\frac{293}{T} \text{ kV/cm} \qquad 2\text{-}1$$

Where: b is air pressure (kPa) and T (K) is air temperature.

As a reference the standard atmospheric humidity is taken as 11 gm^{-3}, with absolute humidity varying between 1 gm^{-3} and 30 gm^{-3} [5].

Tests of aged insulators show that the 'surface factor' for corona discharge has been reduced to 0.7, which represents the corona inception potential gradient is reduced to 14.8kV/cm, 70% of its 'ideal' value [3].

The line voltage and radius of curvature of insulator hardware are fundamental in determining the magnitude and distribution of macroscopic voltage gradient are also domination factors for corona presence [3].

2.4.1.2 CORONA FROM WATER DROPS

Water drops on insulators can also result in corona when the magnitude of the surface electric field goes above a threshold value [23]. Windmar [24] has defined that the electric field required for water drop corona inception lies between 5-7 kV/cm for single or multiple droplets aligned in the same direction. Phillips's [25] experiment demonstrates that the threshold value is dependent on the surface material and the volume of water drop. He showed that the larger size of water drop, the higher threshold electric field is required, with 8.6 kV/cm corresponding to a 50 µl water drop and 9.6 kV/mm corresponding to a 125 µl volume. There are mainly two reasons why water drops can generate corona discharge

in electric fields: electric field enhancement [23] and water drop deformation [26]. Electric field studies around a hemispherical water drop on an insulating surface shows that the electric field is intensified in the region of the water drop contacting the insulating material (Figure 2-5) [23], which may increase the electric field in this region to, or above, the threshold value of corona. The water drop deformation is seen under AC voltage in Figure 2-6, which may contribute to corona generation from the tips of deformed water drops, where the curvature is relatively sharp [26]. Corona from water drops can also transform into dry-band arcs if the leakage current reaches a critical value around 1mA, this transition is detectable by partial discharge methods [27].

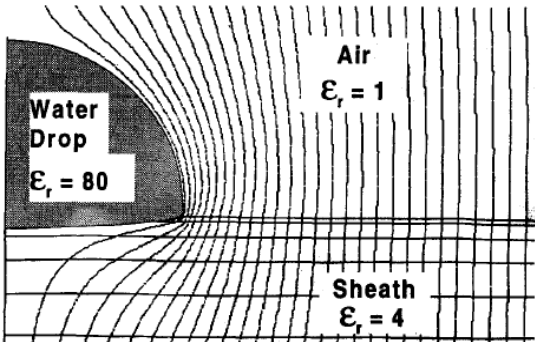

Figure 2-5: Equipotentials surrounding a hemispherical water drop on a polymer with a uniform E-field applied prior to the introduction the water drop [23]

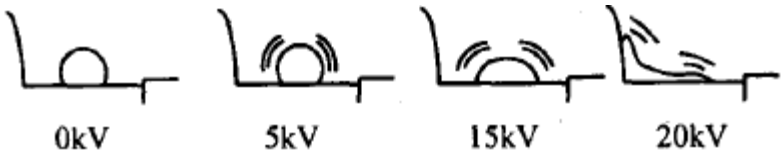

Figure 2-6: Behaviour of a water droplet under AC voltage [26]

Although the damage from corona discharge is a long-term performance issue, with an estimated time of 7.3 to 9.5 years leading to crack formation in a material [28], it is still a significant hazard for the service of composite insulators. Corona on insulator surfaces may lead to discoloration, erosion and even penetration of insulator housing materials [29], and finally damage the fibreglass rod by production of

acids from corona discharge leading to rapid mechanical failure through stress corrosion [3].

2.4.2 DRY-BAND ARCS

For dry-band arc ignition, electric field and power density over the insulator surface are given by

$$E = j\rho \quad 2\text{-}2$$

$$P = j^2\rho \quad 2\text{-}3$$

Where: E is the electric field, P is the power density, j is the surface current density and ρ is the surface resistivity.

The Joule heating from the leakage current causes the water film to evaporate. Its corresponding power density calculation indicates that the area with the maximum current density (j) will have the greatest power density and so will be dried first. For the insulator surface, this first dry-out area may be located around the insulator core because j is relatively high there. For the ADSS cable, this first dry-out area is most likely to be on the cable section near towers as the current is the greatest there as shown in Figure 1-5 [18]. As the water film is evaporated and becomes thinner, the surface resistivity (ρ) also increases accelerating the drying process. Following the resistivity rise, the electric field (E) in the electrolyte at this point ultimately increases. The electric field in the air just above this point has the approximately same value. As soon as the ionisation level in this air is met, a discharge occurs [5].

The threshold value of electric field for dry-band arc ionisation will be similar to that of the threshold for water corona ionisation, 5-7 kV/cm [24]. Huang's [30] electric field calculation along the dry-band before the arcing initiation demonstrates that the electric field is very large only

at the edge of the metal electrode / the water layer. Thus the breakdown initiation must occur there. The electric field is only responsible for arc initiation; it is the arc energy (represent by current) which determines the stability of an arc across a certain length of dry-band. Rowland's experiment [31] suggests that stable arcs are likely to occur if arcing currents above 2 mA are available. This is the subject of further study in this thesis.

2.4.3 FLASHOVER

Flashover can be considered as a development of dry-band arcing. Under certain conditions such as low surface resistivity due to contamination or ageing, or a momentary voltage surge because of lighting or switching impulses, a dry-band arc may propagate over the surface far enough to bridge the gap between the insulator sheds, or even over the whole insulator. The result is called a 'power arc' [3].

Hampton's criterion describes a model for dry-band arc extension [32]. In this criterion, the arc which is struck across a dry-band between two water films can extend its length over the wet surface if the voltage gradient in the arc, $(dV/dx)_{arc}$, is less than that on the neighbouring surface, $(dV/dx)_{surface}$, which is summarized in Table 2-1.

Table 2-1: Hampton's criterion for dry-band arc extension [32]

Judgement	Hampton's criterion	Dry-band arc extension
$(dV/dx)_{arc} < (dV/dx)_{surface}$	Met	Yes
$(dV/dx)_{arc} > (dV/dx)_{surface}$	Not met	No

In Rowland's experiment [17], Hampton's criterion is used to indicate the dry-band arc extension on ADSS cable surface. The judgement is based on the comparison of resistivity of an arc (R_{arc}) and the resistivity of the cable (R_{cable}). If R_{cable} is greater than R_{arc}, Hampton's criterion is

met, which means the dry-band arc can extend. Table 2-2 shows the test results for arc extension judgement.

Table 2-2: Hampton's criterion as a judgment tool for dry-band arc extension on ADSS cable surface [17]

Situation	Series impedance	$I_{\max}$ (mA)	$(dV/dx)_{arc}$ (kV/cm)	R_{arc} (kΩ/cm)	R_{cable} (kΩ/cm)	Hampton's Criterion
Test	0	100	0.4	4	6	Met
Test	2.5 MΩ	10	1.5	150	6	Not met
Service	complex	2	2.0	1000	10	Not met

Two comments are made regarding to Table 2-2. The first concerns R_{arc}: Due to the change of arcing voltage and current, R_{arc} is not truly constant. Research in this thesis indicates that for every current level, the lowest arc resistivity appears when the arcing current is at its peak [33]. This lowest arc resistivity is selected to be used in Hampton's criterion, because the most likely situation for arc extension is when the arcing current reaches maximum, which corresponds to the lowest arc resistivity.

The second comment is the effect of any current-limiting impedance on arcing extension. Rowland's first test in Table 2-2 gives rise to 100 mA arc current (peak) without the limitation of series impedance, Hampton's criterion is met for this case which means the dry-band arc can extend over adjacent water moisture. The other two tests limit the current to less than 10 mA, confining the arc to its dry-band area (Hampton's criterion not met), and so can not lead to dry-band arc extension and flashover.

Based on the second comment, the possibility of dry-band arc extension on a contaminated insulator is traditionally modelled in Figure 2-7 [3].

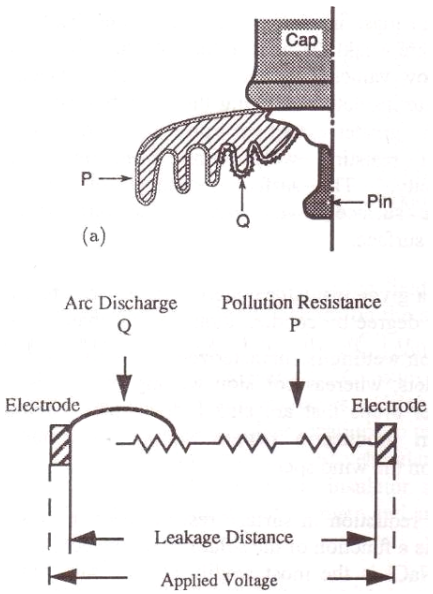

Figure 2-7: Schematic of dry-band arcing on a contaminated (polluted) insulator [3]

The pollution resistance (P) is considered as the current limiting impedance, which confines the arc discharge (Q) in the dry-band area. However, under a surface resistance threshold, caused by high levels of contamination, the dry-band arc may extend over the moisture to bridge the gap between insulator terminals leading to a flashover. In this case Hampton's criterion [32] is met.

2.5 ARCING DAMAGES ON INSULATORS AND ADSS CABLES

The arc damage to insulator surfaces are generally considered to be from 'power arcs'. An insulator test was conducted creating the arc current levels of 200 A - 1400 A (RMS) for 11 kV and 33 kV insulators [34]. High current discharges with $2x10^5$ A were used in a pulse repetition test in [35]. Another experimental research project created damaged non-ceramic insulator end fittings by power arcs with energy of 20 kA^2/sec – 25 kA^2/sec [36]. For iced insulators, flashover threshold currents of 120 mA to 180 mA were determined for leakage current and flashover performance [37]. Polluted conditions such as wet and contaminant conditions from rain or fog can accelerate the arc ageing mechanism on outdoor insulators [38, 39]. Because of the weaker chemical bonds that organic materials have compared with ceramics, composite insulators are more easily degraded by dry-band arcs [3]. This means thermal effect from arcs can change the chemical components of composite insulator materials; reducing the hydropobicity, resulting in a reduction of their withstand voltage [40]. Surface erosion can lead to roughening or even penetration of the weather sheds leading to failure of the fibreglass core of insulators [14]. However, under the low current arcing conditions on the insulator surfaces with leakage currents less than 10 mA, the ageing of the insulator surfaces was generally considered as non-harmful and normally not reported. This thesis will conduct further research on the low current ageing to the composite insulator materials by some extreme events which may damage the insulation materials much quicker than normal situations.

In outdoor service conditions, dry-band arcing activity can be developed on the ADSS cable surfaces [41-43]. The corresponding damage from dry-band arcs were reported for the transmission line levels of 110 kV 161 kV and 400 kV respectively [42, 44]. Corona effects also make

contributions to cable surface damage mostly occurring near the metallic cable clamping point [45]. A series of experiments have been conducted to artificially create dry-band arcs on the cable surfaces, and severe damage or failures from arcing phenomenon were observed [31, 46-48]. An extreme situation of dry-band arc compression was proposed, and it was suggested that this arc-length compression may bring more damage on ADSS cable sheath [17], and also on insulator material surfaces [49]. The author who reported initial measurement of surface hydrophobicity change on an ADSS cable in an MSc dissertation [50]. Evidence of UV ageing and electrical ageing was found on the cable sheath, and conclusion was made that the leakage current magnitude may have connection with the degree of cable surface degradation. This work has been further developed here in the following chapter of the thesis.

2.6 PREVIOUS EXPERIMENTS ON LOW CURRENT DISCHARGES

2.6.1 TESTS ARRANGEMENT

There have been many experiments conducted to create low current discharges under different conditions. The four typical test arrangements are as follows:

2.6.1.1 TESTING WITH INCLINED SAMPLES WITH CONTAMINANT FLOW

As shown in Figure 2-8, an inclined flat sample surface is used together with continuous wet contamination flow, to create dry-band arcs. This test follows the standard of ASTM D2303 [51]. By analyzing the surface temperature distribution using thermal camera, the dry-band and associated hot areas can be located typically on the bottom electrode, where the contamination accumulates. This test provides the basis for the Section 5.2 of '*Testing with Inclined Samples*' in this thesis, with the theory that the dry-band can move down on an inclined surface by mobile surface moistures.

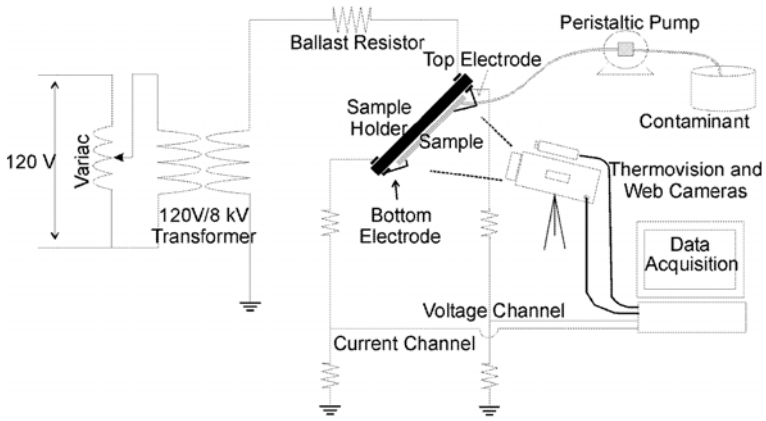

Figure 2-8: Test arrangement for measurement of voltage, current and temperature distribution on inclined sample surface [52]

2.6.1.2 DISCHARGES BETWEEN WATER DROPS

As shown in Figure 2-9, an arc is ignited between two water drops (A and B) with copper electrodes inserted into the respective drops [53]. This test drives the ideas for the Section 5.3 of '*Tests between Water Drops*' in this thesis, as such arrangement could provide the direct contact between arc and water droplets, removing the impact of metallic electrodes. This test also illustrates the deformation of drops under the electric fields, which might change the drops' dynamic physical separation (arc length) during the test.

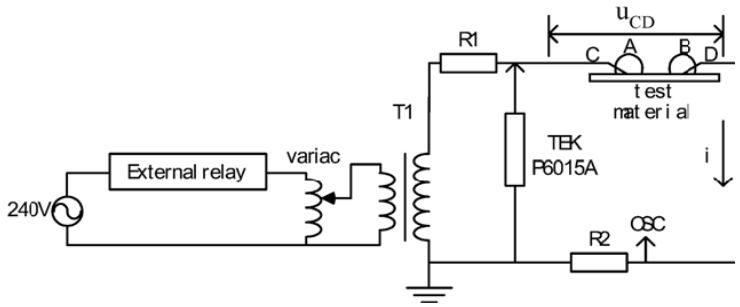

Figure 2-9: Test arrangement for measurement of electrical discharges between water drops [53]

2.6.1.3 NON-SHEDDED INSULATOR CORE IN A SALT-FOG CHAMBER

As shown in Figure 2-10, a salt-fog chamber with nozzles (according to IEC 507 standard [54]) was used to create wet conditions for dry-band arcing. The distribution of fog is controlled by the number of nozzles operating [55]. This test provides the basis for the part 5.1, '*Testing in a Fog Environment*' with a fog wetting method for dry-band arc formation and growth. A simplified insulator core shaped sample was also used in this test.

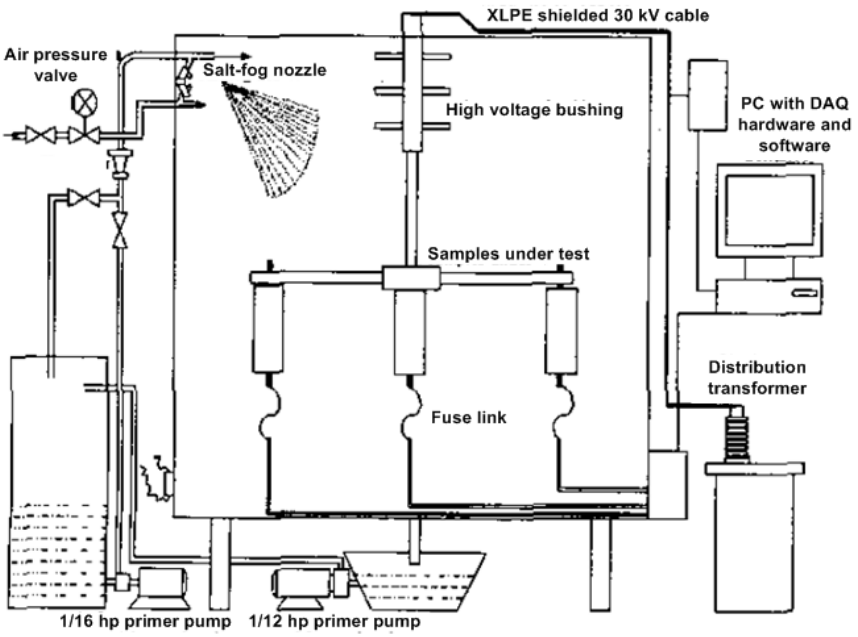

Figure 2-10: Test arrangement in salt-fog chamber with insulator core [55]

2.6.1.4 DRY-BAND ARCS UNDER WATER-SPRAY ON A ROD

Figure 2-11 shows another experimental method to create low current dry-band arcs on a rod by the deposition of sprayed moisture [48]. This test inspired the part of test arrangement in thesis part 5.4 of '*Tests with Artificial Wind and Rain*', to create wet rain conditions by using indoor spray systems to allow dry-band arc formation.

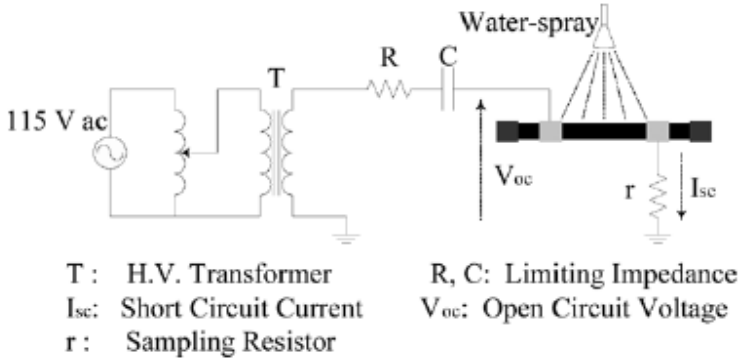

Figure 2-11: Test arrangement of dry-band arcing under the spray system on the ADSS cable [48]

2.6.2 RESULTS ANALYSIS

2.6.2.1 LEAKAGE CURRENT

The leakage current of discharges were either recorded by oscilloscope [53], A/D convertor [56] or a Labview system [48] during the testing period. A method named 'Fast Fourier transforms (FFT)' has been used to calculate the different components of the leakage current, which were named as fundamental, 3^{rd} and 5^{th} harmonic components. Research found that the low frequency components of leakage current can be used to study the ageing of insulation materials as arcing always appears with distortion in leakage currents [55]. In this thesis, the author has not used 3^{rd} harmonic analysis, but the leakage currents acquired from his experimental work contain 3^{rd} harmonics.

A time series modelling method named autocorrelation function (ACF) has been used to analyze the trend of data, which was leakage current in this case, over a period of 4000 minutes defined as 'early ageing period' during a salt-fog test of silicone rubber insulators. It is reported that the autocorrelation function of the third harmonic component of leakage current is the most suitable for indicating the ignition of dry-band arcing [57]

The leakage current flowing on the composite insulator surface could be separated into conductive current and dry-band arc current by using the methods of distortion factor and differential technique. Both methods were successfully used to identify the dry-band arc current component as tools for arc ignition detection [58].

2.6.2.2 ARC VOLTAGE

An investigation into arc voltage features corresponding to dry-band arcing growth has identified four stages as a) unstable discharging (sparking), b) short-term dry band arcing, c) more unstable discharging and final stable dry-band arcs. The arcing voltage characteristics for these stages are demonstrated in Figure 2-12. It is clearly shown the arc voltage performed distinguish characteristics from unstable discharges to stable arcs [48]. This is also a point of interest in this thesis, and further experimental analysis and modelling work will be conducted to investigate this phenomenon in sections 5.4 and 6.3.

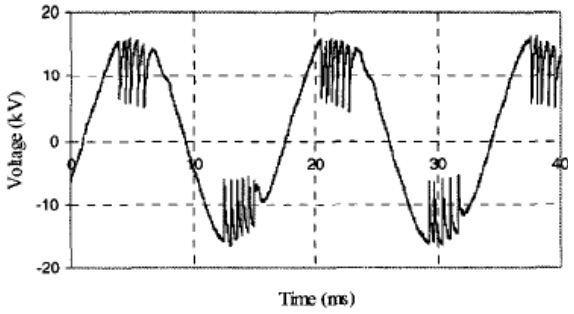

a) Typical voltage signal of unstable discharge (sparking)

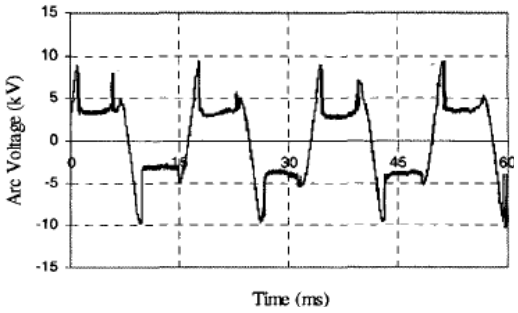

b) Typical voltage signal of dry-band arc

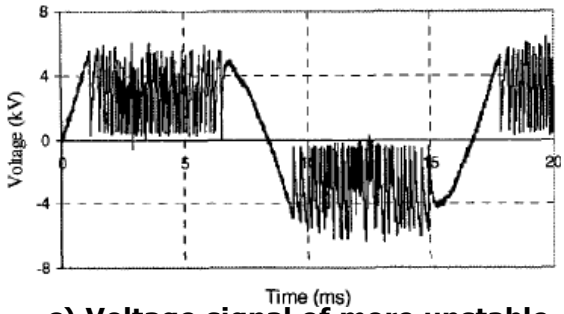

c) Voltage signal of more unstable discharge (serious sparking)

Figure 2-12: Test arrangement of dry-band arcing under the spray system on the ADSS cable [48]

2.6.2.3 ARC RESISTANCE

Pervious research has investigated instantaneous arc resistance (Figure 2-13 b) which was obtained by calculating the ratio of instantaneous arc voltage to arc current (Figure 2-13 a) [48]. In this thesis, the same

calculation method will be used for obtaining the instantaneous arc resistance in parts 5.1.5.2 and 5.2.5.6, with further arc resistance modelling in parts 6.1.2.3, 6.2.2.2 and 6.3.2.

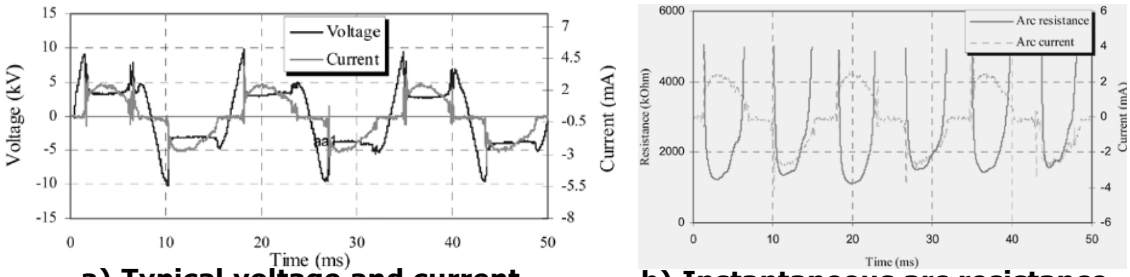

a) Typical voltage and current signals of dry band arcing

b) Instantaneous arc resistance

Figure 2-13: Arc resistance analysis from voltage and current signals [48]

2.6.2.4 ARC LENGTH

The relationship between the full arc length and open-circuit voltage was investigated and shown in Figure 2-14. It is found that the arc length increases with the rise of open-circuit voltage. The similar trend was found between full arc length and short-circuit current in Figure 2-14 b). A conclusion was made that current increase has more impact on the change of arc length than voltage increase [59]. Similar to this work, the respective arc length changes with voltage and current under the different experimental conditions will be further analyzed in the Chapter 5 of '*Experimental Part*' in this thesis.

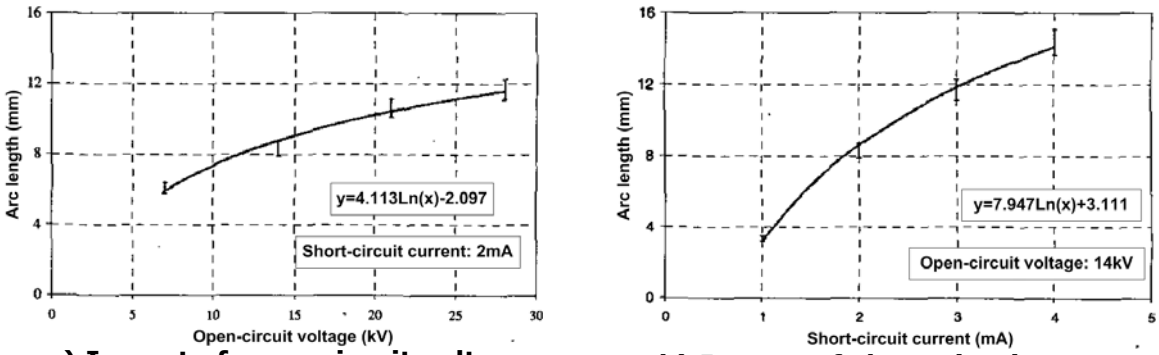

a) Impact of open-circuit voltage on arc length

b) Impact of short-circuit current on arc length

Figure 2-14: The relationship between arc length and arc current [59]

2.6.2.5 ARC POWER

Based on the measurement profiles of arcing current and arcing voltage, instantaneous arc power was obtained by multiplying them together, the results are shown in Figure 2-15 [48]. In this thesis, the same method will be used for instantaneous arc power calculation for different arcing conditions with an example in parts 5.2.5.7, and the further arc energy analysis in parts 5.2.5.8, 5.3.5.4, 5.4.5.1 and 5.4.5.2 respectively.

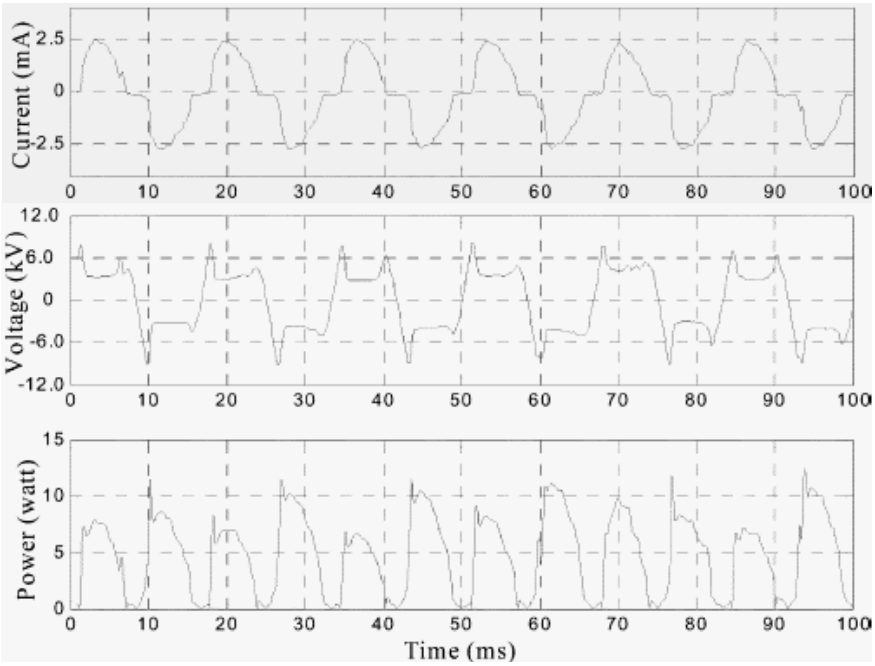

Figure 2-15: Instant arc power calculation based on arc voltage and arc current [48]

2.7 PREVIOUS SIMULATION OF ELECTRICAL DISCHARGES

2.7.1 ELECTRICAL MODELLING OF ARCS

A numerical simulation method for the modelling of dry-band arcs on ADSS cable surface was conducted in [60]. In this work, the simulation was based on an equivalent electric circuit as shown in Figure 2-16. This circuit was derived from an experimental test on a surface polluted ADSS cable. By observing the electrical properties of dry-band arcing, three periods were identified as: the period before arc channel breakdown, the period from breakdown to the time when arcing current / voltage reduces to zero, and the dielectric recovery period. A series of differential equations with 'state variables' was proposed based on the electric circuit corresponding to the three different periods, and all equations were solved by using Runge-Kutta method. An example of a simulation outcome is shown in Figure 2-17. This simulation work stimulated an idea for one of the modelling approaches in this thesis, as the '*PSCAD Simulation*' in parts 6.1.2, 6.2.2 and 6.3 was conducted following a similar idea. The identification of three different arcing periods in this literature work is also an important concept for the establishment of '*Double Sinusoidal Model*' in section 6.1.1 in the thesis.

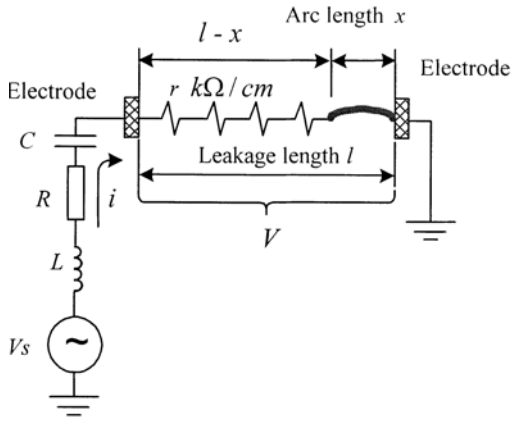

Figure 2-16: Equivalent circuit of experiment setup [60]

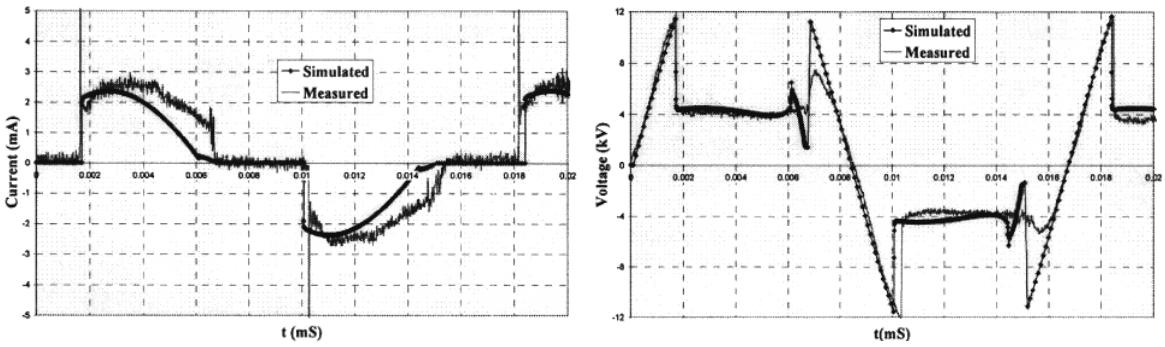

Figure 2-17: Simulation of voltage and current waves comparing with experimental results (breakdown voltage 12 kV, arc length 1.45 cm) [60]

A modelling of long arc in free air was studied in [61, 62]. By observing the measured voltage and current curves of arcing, an arc model, in terms of voltage and current, was presented as two equations, and an EMTP program was constructed based on the proposed model. The simulated voltage and current characteristics of the arcs together with instantaneous arcing resistance are shown in Figure 2-18 [61]. Although this work was focused on long, high current arcs, the work provided the idea for the '*Double Sinusoidal Model*', that the modelling equations can be driven based on the wave shapes of experimental results from thesis Chapter 5. The 'sign' function used in this work is also a tool to link together the three separate models in different arcing periods proposed in part 6.1.1 to create the entire '*Double Sinusoidal Model*'.

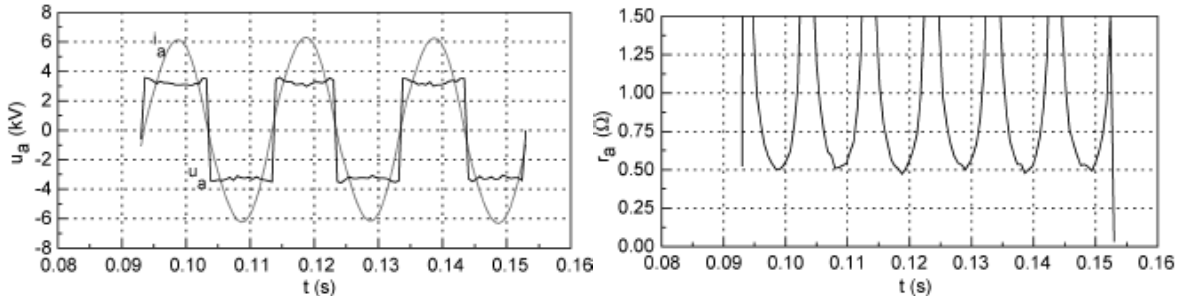

a) Current and voltage curves **b) Instantaneous arc resistance**

Figure 2-18: Simulation of current and voltage curves of arcs with instantaneous arc resistance [61]

2.7.2 THERMAL MODELLING OF ARCS

A thermal model for short arcs between high current contacts was built in [63]. In this research, a 'two section-thermal model' and 'three section-thermal model' were proposed as illustrated in Figure 2-19, in order to calculate the power flow through the arc to the two metallic contacts. The equations based on the models were developed [63]. This model was designed to analyze the high current (approximately 500 A), low voltage (approximately 20 V), short distance (0-0.006 m) and metal contact arcs in switchgear. In this thesis, this model will be further developed to analyze the low current (less than 10 mA) water electrode dry-band arcs. The original model was concentrated on the heat transfer from arcs to electrodes as the metal contacts of switchgear were the most concern when the switching arc was present. For the modelling of low current arcs in this thesis, the thermal flow from dry-band arcs to the material surface is of the most importance which needs to be further investigated. Therefore, the developed modelling details based on the original literature model will be discussed elsewhere in Part 6.4 of '*Modelling of Thermal Dynamics of Arcs*' in this thesis.

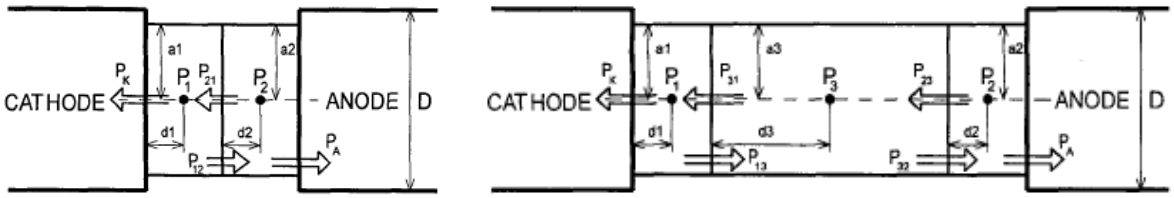

a) Two-solid thermal model **b) Three-solid thermal model**

Figure 2-19: Two-solid thermal model and three-solid thermal model for high current short distance arcs [63]

2.8 SUMMARY

A background review has been conducted in this chapter. The transmission line elements such as composite insulators and ADSS cable, which play a role (or part of a role) as outdoor insulation, have been surveyed. Their typical design structures together with the associated issues of low current ageing on their surface insulation materials have been reported. The potential damage from arcing activities on both insulators and cable surfaces has been reviewed. In addition, the possible chemical ageing mechanisms of silicone rubber surfaces has been studied.

The physics of low current discharges, such as corona, dry-band arcs and their progression to flashover, have been reviewed. The ignition conditions for corona on both metallic fittings and water droplet edges have been surveyed. Based on the literature, it is found that the electric field strength plays a vital role in the corona ignition, and the geometry of metallic surfaces and mobility of water surfaces could have a major impact on the electric field distribution for corona appearance. The evidence of resultant damage on the composite insulation materials have been demonstrated. The threshold electrical conditions for dry-band arcing formation on the insulation materials have been identified; electric field is also an important factor for dry-band arc ignition. The physical process of interaction between electric field, leakage current and dry surface resistivity for arc formation has been investigated. It is identified that the stability of sustained dry-band arc burning depends on the arc energy represented by the arc current level. Further, the criterions for dry-band arc extinction or further progress to flashover on insulator geometry and ADSS cable surface have been literature reviewed.

Previous experimental work on dry-band arcs on inclined sample surfaces, discharges between water droplets, electrical tests in salt-fog chambers and dry-band arcs under spray systems on a rod have been reviewed, as the literature support for the section 5 of this Thesis. Previous simulation work on arc modelling, both for electrical characteristics modelling and physical thermal modelling, have been surveyed, as the literature support for the section 6 of this Thesis.

CHAPTER 3

EVIDENCE OF LONG TERM LOW CURRENT AGEING

3.1 INTRODUCTION

An ADSS cable has been taken out of service after 15 years of service on a 132 kV transmission line between Ratcliffe-on-Soar Power Station and Nottingham. The cable is a ribbon-in-slot design with PE sheath manufactured by STC. This cable had experienced long term surface ageing in its service environment. Therefore, the opportunity was taken to study the cable sheath and investigate the evidence of low current ageing by using electric field calculations and contact angle measurements. This was a unique opportunity to study the impact of very low currents over an extended period in a benign natural environment. This is an extension of work from the author's MSc dissertation [50], and new results of contact angle measurements corresponding with further leakage current calculations will be reported in this thesis. This work is now published in [64, 65].

3.2 ELECTRIC FIELD CALCULATION

3.2.1 MODELLING APPROACH

Electrical field calculations around the ADSS cable on the transmission line system were carried out. Modelling design parameters were based on a span of line identified as DM30-DM31 with 314 m length and 6.66 m sag between Ratcliffe Power Station and Nottingham. L7 towers were utilized as both tension towers and suspension towers. The phase pattern of conductors was chosen following the on-site arrangement of

ABC CBA. The sag of ADSS cable was chosen as a typical value of 1.57 m, which is 0.5 percent of the span length.

The modelling of electric fields with the specified transmission line parameters above was built in the commercial package CDEGS and in particular the sub package HIFREQ, with assistance by Dr. Konstantinos Kopsidas. The results are displayed as follows.

3.2.2 MODELLING RESULTS

As discussed previously in part 1.1.2, the relative position of ADSS cable between the 6 phase conductors may vary along the line span. Therefore, the electric field distribution around cable can be different along the cable length. Figure 3-1 a), b) and c) demonstrate the space voltage potentials of electrical fields for the region near the tension tower, mid-span and the suspension tower respectively. In the case of the tension tower, the ADSS cable is located within the blue contour where the induced voltage is less than 1% of single phase transmission voltage, while for the mid-span, the ADSS cable is located between the red and blue area with an induced voltage 1%-2% of transmission phase voltage. Around the suspension tower, the ADSS cable is located again in the blue area with induced voltage less than 1% of transmission phase voltage. The simulated voltages on cable surface for these three locations are summarized in Table 3-1.

Table 3-1: Modelling parameter I_a for different levels of stable dry-band arcs

	Tension Tower	Mid-span	Suspension Tower
Induced Voltage	0.23 kV	3.94 kV	0.22 kV

From Table 3-1, the ADSS cable is considered to be installed in a suitable location where the induced voltage is no more than 2% of transmission voltage along its span length. At such low voltages

together with cable surface insulation resistance associated with a rural environment, no ageing associated with discharges would be expected [42].

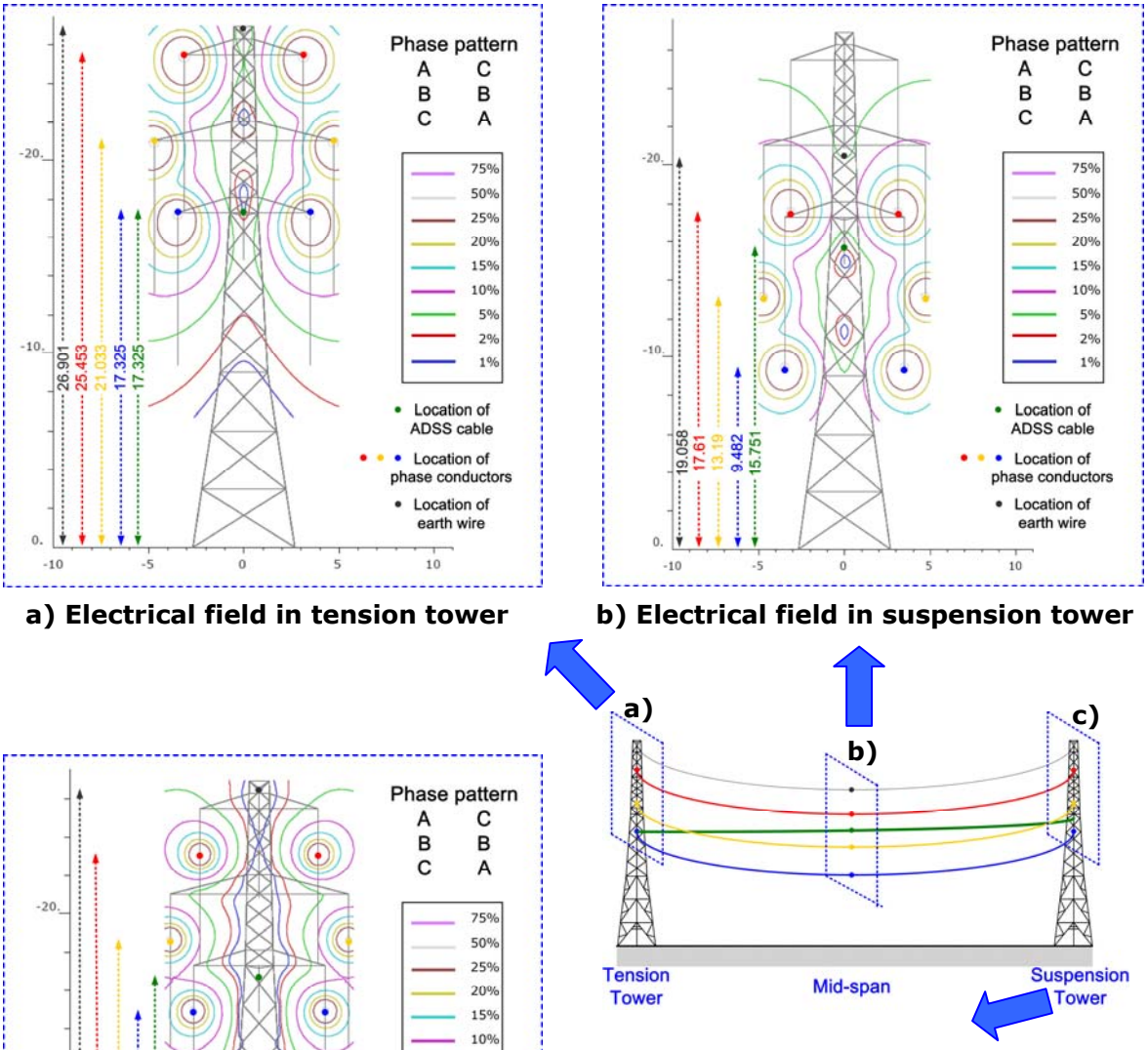

a) Electrical field in tension tower

b) Electrical field in suspension tower

c) Electrical field in mid-span

Figure 3-1: The parameters of L7 tower for electric field calculation (132kV)

The electric field leads to a voltage gradient along the ADSS cable, and ultimately drives a leakage current flowing on the cable surface. Figure 3-2 shows the calculated leakage currents along the span between two specific towers DM30-DM31 with different levels of cable surface resistance. The current has relatively high values at the towers and in the midway of two half spans, but returns to zero near the span centre. Besides, this current is asymmetric from the span midpoint due to the different cable arrangement technology between tension and suspension towers as discussed previously. For all the three cable resistivity cases considered, the maximum available leakage currents are lower than 0.15 mA for the entire span length, which are normally considered insufficient for the formation of dry-band arcs [42].

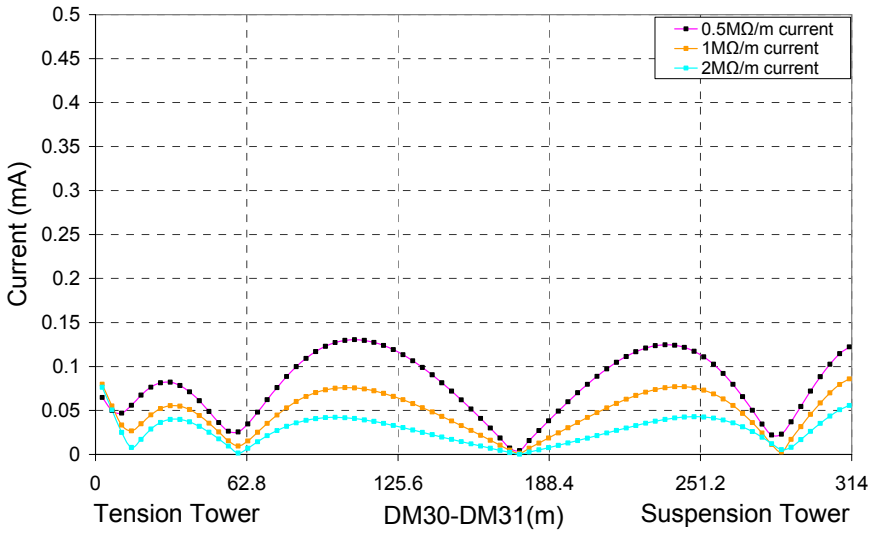

Figure 3-2: Current magnitudes along the DM27-DM28 ADSS cable span [65]

3.3 Visual Observation from Recovered Cable

Visual examination was conducted on the cable surface with the observation of glossy finish lost comparing with its virgin conditions. However, the cable sheath was still in good condition with no evidence of electrical discharge damage at any location. Therefore, the only possible ageing sources would be expected as UV radiation and low

surface leakage current. Figure 3-3 shows two image examples of cable segments.

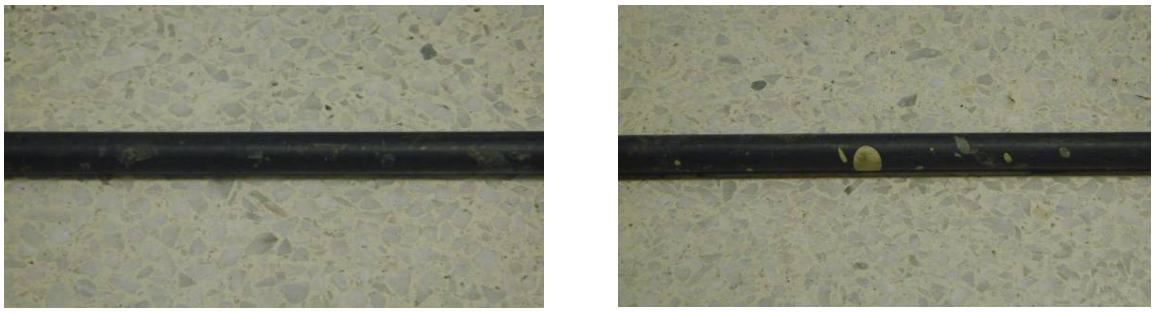

a) cable shows no major surface damage **b) cable deposits with some paint**

Figure 3-3: Example of visual inspected cable segments

3.4 CONTACT ANGLE MEASUREMENT

Contact angle measurement is a method to inspect the material surface conditions. Generally two states are defined: hydrophilic and hydrophobic. Water on hydrophilic surfaces of materials will give a relative lower contact angle, while water on hydrophobic material surfaces will perform a relative higher contact angle [65].

The contact angle measurement here was conducted by dripping a volume of 40 µl droplet onto the cable surface. A high definition image was taken and imported in software (Vistametrix) to calculate the relative contact angle. The measurement was carried out on the whole cable span of DM30-DM31. The first measurement was conducted twice for each cable location, and average value for the same location was evaluated. As a result, 106 points of data were obtained and further reduced to 40 points by combining the data from neighboring locations of the same region. The second measurement was carried out on a 5 meters' unused cable which had been exposed to natural sunlight in a drum yard for 15 years. The third measurement was conducted on artificially aged cable which was severely damaged by dry-band arcing in salt-fog chamber. This later cable was not manufactured at the same

time as the other two samples but had the same standard polyethylene sheath. The results from first, second and third measurements are summarized in Figure 3-4.

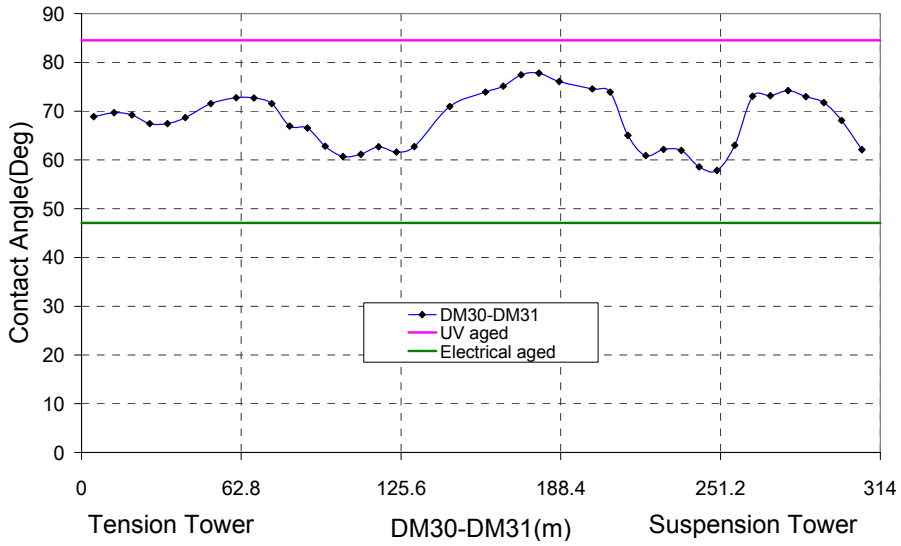

Figure 3-4: Contact angle results from a) whole cable span DM30-DM31, b) only UV aged cable, and c) only discharge aged cable [65]

According to Figure 3-4, the average values from the only UV aged cable and electrically aged cable are respectively upper and lower bounds throughout the whole test results. The span of DM30-DM31, which was aged both by UV radiation and variable low current, reflects the different contact angles along its span length. These results show that the UV-only ageing leads to the minimum cable surface degradation, while the discharge ageing makes the worst surface damage to the cable. The service-aged cable span (DM30-DM31) received more degradation than only UV aged cable, but less damage than the cable with relatively short-term high current. The average contact angle for the virgin cable without any forms of ageing was measured as 98.4°, which holds the highest value as expected.

3.5 Correlation of Contact Angle and Current within a Span

The measured contact angle and simulated leakage current within the span DM30-DM31 are displayed together in Figure 3-5. The result shows that the leakage current magnitude has strong correlation with the contact angle within the span. Generally the current peaks are corresponding to the minimum values in contact angle. For low current locations, the relative contact angles have high values which indicate lower degradation. The extreme case occurs near the mid-span where contact angle peaks while the current stays lowest.

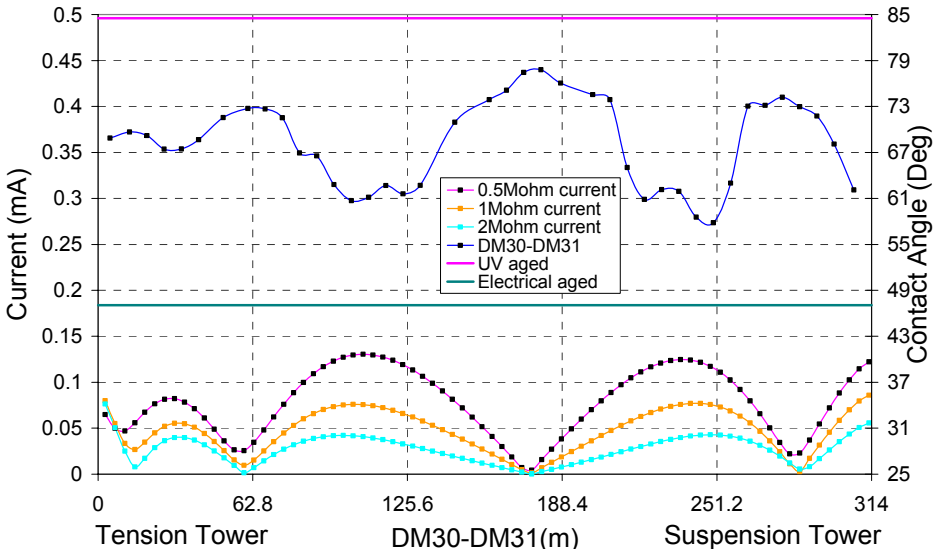

Figure 3-5: Correlation of contact angle and current in DM30-DM31 [65]

Figure 3-6 shows the trend line between the predicted leakage currents and measured contact angles. The contact angle decreases following the rise of leakage current as expected. The currents used for correlation are those for the surface conductivity of 0.5 MΩ/m as an example. In fact the surface conductivity is not uniform and constant throughout the cables service life, due to the complex environmental conditions. This correlation reveals that the loss in hydrophobicity on cable surface over the 15 years is approximately dependant on the magnitude of the local low leakage current.

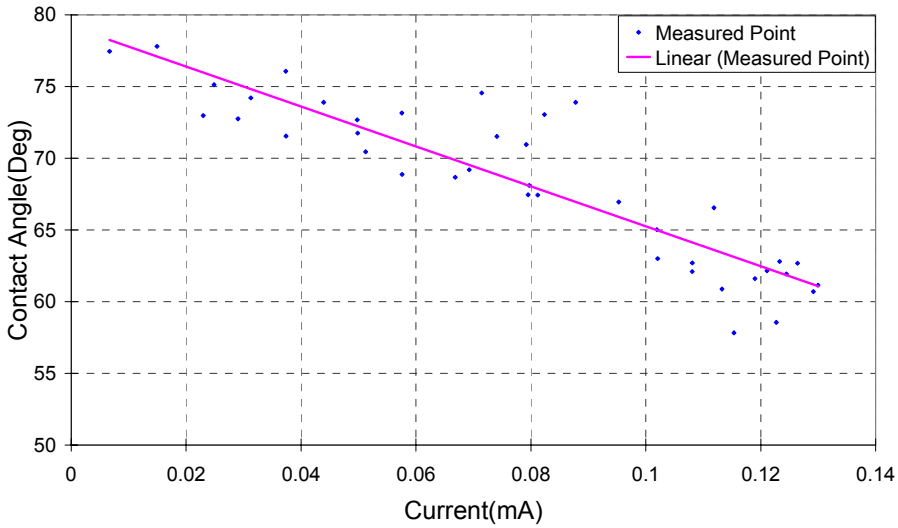

Figure 3-6: The trend line of contact angle against leakage current

3.6 SUMMARY

A series of investigations have been conducted on an ADSS cable after 15 years service in a benign environment looking for the evidence of long-term low current ageing.

Electrical field calculations show that these ADSS cables have been installed in suitable locations on the towers. Induced voltages on the cable surface are 1% of the line voltage. Calculations show that currents expected in this rural location are lower than those associated with damaging arcing (a few mA is required) with no more than 0.15 mA predicted on the sheath surface. Therefore, only low current ageing effects could be present through its service history.

Visual inspection shows the cable surface remains in a good condition as expected, with no major damage by the electrical discharge activities. Water droplet contact angle measurements reveal that the cable sheath has lost hydrophobicity due to natural UV radiation and long-term low surface current. UV irradiation from sunlight leads to ageing of the cable sheath. In addition the electrical current ageing contributes to ageing within a span. Some points along the cable near towers and midway in the two half spans perform a relatively lower hydrophobicity. This is the first time this has been recorded, and is an important result for cables and insulators in more aggressive installation conditions.

The correlation of contact angle and current with a span verifies that long-term low surface currents below 0.15 mA are a factor contributing to the ageing of cable surface properties, even if the conditions are such that dry-band arcing does not occur. This is the first such observation. However, ageing is not severe enough to be seen by any means other than hydrophobicity measurement.

CHAPTER 4

LOW CURRENT ARC COMPRESSION

4.1 THE ARC COMPRESSION PHENOMENON

Although a dry-band arc can extend to produce flashover under certain conditions, it is usually self-limiting when several milliamperes of low current are drawn [2]. Dry-band arcing is therefore generally considered as a long term ageing mechanism on insulation surfaces, illustrated in Figure 4-1 a). However, of particular concern is that in cases where the dry-band arc is compressed in length as demonstrated in Figure 4-1 b), the arc energy and correlated energy density will increase dramatically, which may accelerate the long-term ageing effect into a short-term hazard. This compression is a complicated phenomenon which may be caused by a variety of reasons in a real power system, and may be a rare event. However, a hypothesis of this thesis is that: even though these compressions only occur a limited number of times over the whole insulator service history, they may lead to the composite insulator failing much quicker than an insulator aged under normal dry-band arcing conditions.

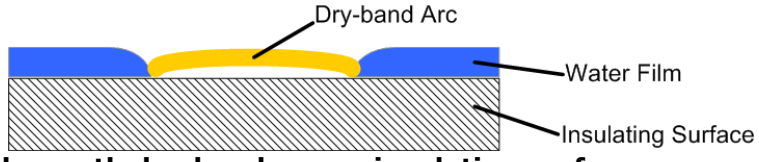

a) Normal growth dry-band arc on insulation surface

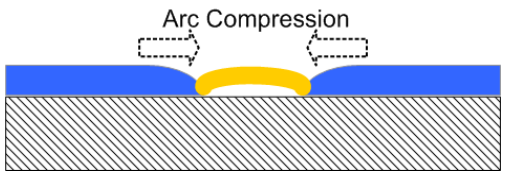

b) Dry-band arc compression in length

Figure 4-1: Typical dry-band arc on insulating surface with moisture

4.2 ARC COMPRESSION SITUATIONS

On outdoor transmission line systems, low current arcing on the insulation material surfaces is subject to complex environmental and electrical factors. Some situations may cause the arc to compress in length. The specified situations are respectively studied as follows:

4.2.1 ARC COMPRESSION ON INCLINED SURFACE WITH WATER FILM

The first situation describes arcing activity occurring on an inclined or even vertical insulation surface, shown in Figure 4-2.

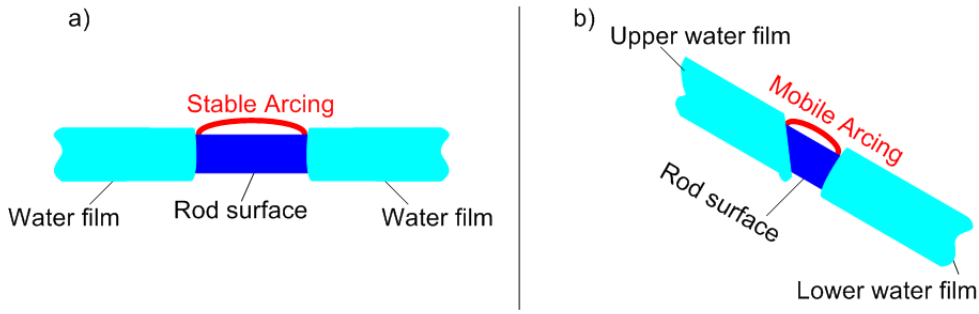

Figure 4-2: Dry-band arc compression on inclined surface between water films

In Figure 4-2 a), thermal and moisture balances have been reached allowing formation of a stable dry-band arc with relative constant maximum arc length and repeatable electrical behaviour. When the sample is inclined as in Figure 4-2 b), the upper water film and lower water film, whose edges are at the dry-band boundaries, will tend to move down the insulator core due to gravity. The upper film tends to move faster because of moisture feeding from the rod above it and because of the breakdown of surface tension due to the arc. The dry-band gradually moves down the rod by this means until the lower water film is replaced by the immobile metallic fitting. The metallic fitting then becomes an immovable lower edge of the dry-band. In the meantime, the upper water film can still move downwards. Following this, a single

stable dry-band arc remains but the arc length is physically reduced in length. The length of the arc is reduced to extinction unless a new balance is achieved.

For the transmission line elements, the possible situations for realizing dry-band arc compression in this situation are either arcing on the tensioned ADSS cable attaching to tower shown in Figure 4-3 a), or arcing on the suspension insulators with inclined surface shown in Figure 4-3 b).

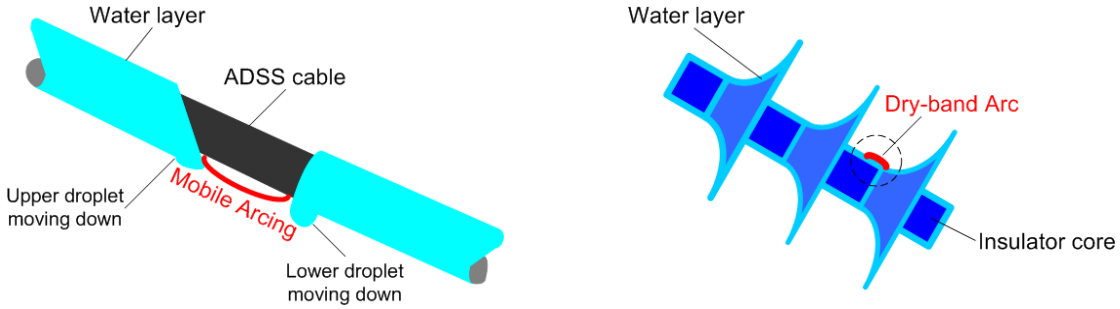

a) Arcing compression on inclined ADSS cable surface

b) Arcing compression on inclined insulator surface

Figure 4-3: Inclined surface for arc compression on power transmission lines

4.2.2 Arc Compression under Wind and Rain Environment

Figure 4-4 shows another possible situation for arc compression on insulation surface with wind and rain. As shown in Figure 4-4 a), with the wet deposition and induced leakage current flowing on the insulation surface, the dry-band arc could ignite and grow to the maximum length achieving the dynamic balance between the dry-band expansion by Joule heating effect and dry-band extinction by continuous water deposition. The effect of wind in the horizontal position, shown in Figure 4-4 b), is that the right-hand water film which is close to the wind source could be blown into the dry-band. In the meantime, the left-hand water film receives weaker wind but also starts moving towards the left. During this stage, the arcing could possibly continue striking so that the

whole dry-band area would move till the left part of water film firstly reaches the metallic fitting or cable joint and becomes stationary. In the meantime, the right-hand water film still moves leftwards. As the result, the dry-band arc is physically compressed in this situation.

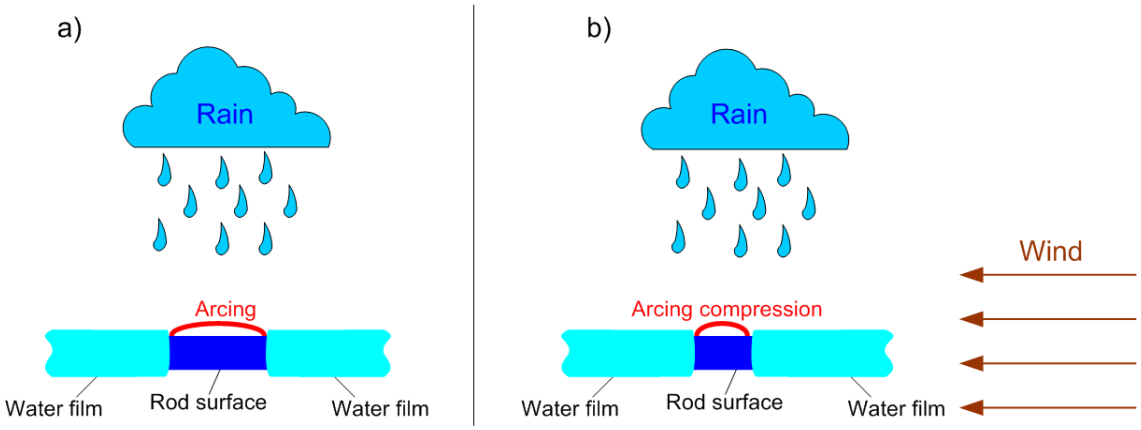

Figure 4-4: Dry band arc compression under wet rain and wind conditions

The following Chapter 5 of the *Thesis Experimental Part* will conduct the relevant tests base on the two proposed arcing compression situations above.

CHAPTER 5

EXPERIMENTAL

5.1 TESTING IN A FOG ENVIRONMENT

5.1.1 INTRODUCTION

The wet outdoor conditions around the insulator surface are of importance for electrical discharge growth, and one of the most common environmental factors affecting overhead line elements is fog. The inland areas may expose insulators to clean-fog, while the offshore or contaminated environments may involve the salt-fog. The experimental study in this chapter will be conducted to investigate the fog environment for the electrical discharge formation and growth, following the testing standards in accordance with IEC 61109. Here the dry-band arcing phenomenon in both clean-fog environments and salt-fog environments are compared. The discussion will focus on the electrical properties of arcs under the different fog conditions. The most severe environment will be identified as the basis for the further experimental studies in this thesis.

5.1.2 TEST ARRANGEMENT

Figure 5-1 demonstrates the arrangement of testing in a fog environment. The transformer provides single-phase AC voltage up to 42 kV at its secondary side. A current limiting resistor is used to limit the leakage current to less than 10 mA. A fibre-glass reinforced rod which is sheathed in silicone rubber insulation compound is used as the test sample. This structure represents a typical composite insulator core without sheds to simplify the test. The sample is suspended into the fog

environmental chamber with the high voltage end connected to the transformer secondary via the current limiting resistor, and the low voltage end is attached to the earthed frame via a 1 kΩ current measuring resistor. The connection points between the test circuit and sample are on electrodes, which are formed by wrapping copper strip tightly around the two ends of rod.

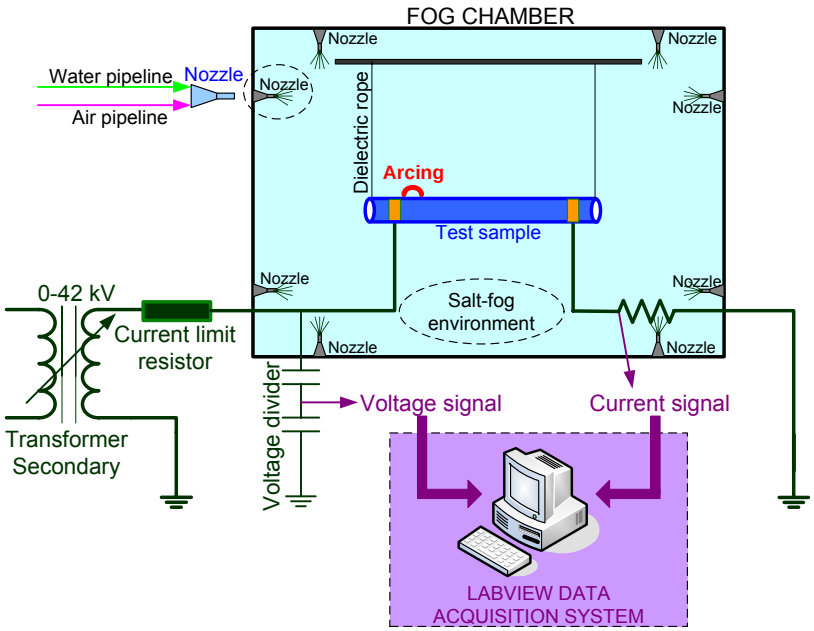

Figure 5-1: Test arrangement of Testing in a Fog Environment

The fog environmental chamber is a sealed and waterproof chamber with a total volume of 16.8 m^3. A 125 cm X 90 cm glass window allows visual observation of the experiment by the chamber operator although a full fog is in operation. Six nozzles are placed around the internal wall of chamber. An air pipeline and a water pipeline are introduced into the chamber and mixed together in the nozzles. Air is supplied from an air compressor with the maximum output of 100 psi. Water is pumped from a 220 litre tank filled with the solution which is either tap-water, de-ionized water or salt water depending on the test specification. The water is sprayed to a fog by the compressed air in the nozzles. The salt fog tests are in accordance with IEC 61109 (1992).

The control of the fog environmental chamber includes the fog precipitation rate control and voltage control. The air pressure regulator and pump valve are used to control the fog injection. As the required precipitation rate is 6.7 ± 1.7 l/hr, the air pressure regulator is set to 1 bar. Prior to running a test, the chamber precipitation rate can be verified using a 15 cm diameter petri dish on the chamber floor collecting 17.5±4.4 g of water per hour. Voltage control is achieved by the Labview system outside the chamber to control a motor running clockwise or anticlockwise to step up or down the rheostat feeding the transformer. A series of interlocks and trip switches such as door interlock, over current trip switch, timer relay switch and key interlock switch are attached to the chamber for the safety and security purposes.

The data measurement and acquisition system consists of a 10,000:1 voltage divider which is used to pick up the voltage across the sample. The 1 kΩ current measurement resistor is used to acquire the leakage current flowing on sample surface. Both voltage and current signals are recorded by a National Instrument Labview system. A video camera is used to capture the electrical discharges videos and images for the test record and arc length measurement purposes.

5.1.3 TEST PROCEDURE

Three groups of tests are conducted in the fog environment as follows,

5.1.3.1 ARC FORMATION TEST

This test aims to study the dry-band arc formation process from dry surface to wet surface until the arc ionization. The electrical properties in terms of voltage, current and their phase relationship are investigated during the test. Clean-fog produced by tap water (with conductivity of 600 μs/cm) is used in this test as the arcing phenomenon in the clean-

fog environment is gentle and gradual, which is relatively easy to capture.

I. Transformer voltage is fixed to 30 kV (RMS). The current limit resistor is chosen as 2 MΩ throughout the test.

II. The sample surface is uniformly roughened with abrasive paper to reduce its surface hydrophobicity for the ease of fog adhesion on the sample.

III. Initially before the fog injection, the sample surface needs to be dried throughout. After applying the source voltage, the fog is immediately switched on to produce the clean-fog with precipitation rate of 6.7 l/hr.

IV. By the continuous fog deposition together with the high voltage gradient across the sample, the dry-band arcing will eventually form on the surface. The arc voltage, current and arcing image are recorded for the whole process from surface getting wet to the arc formation.

5.1.3.2 ARC GROWTH TEST

The arc growth test is to investigate the process of free growth of arcs in the salt-fog environment. Arcs for different voltage and current levels with variable arc lengths are produced by the test with the following procedure:

I. The salt-fog is prepared and generated from salt mixed with water to a conductivity of 16,000 μs/cm.

II. The transformer voltage is fixed to approximately 10 kV (RMS) with a current limiting resistor to 8 MΩ, in order to get a long sustained, stable arc with 1.5 mA (peak) arcing current. In this way a balance is achieved

between arc expansion by Joule heating and arc extinction by fog deposition.

III. After 30 minutes, gradually increase the transformer voltage to obtain a 2.0 mA (peak) arc. The arc expands in length due to enhanced Joule heating. Wait for another 30 minutes until a new equilibrium is achieved.

IV. Keep increasing the transformer voltage to get 2.5 mA, 3.0 mA, 3.5 mA and 4.0 mA arcs, with 30 minute intervals between each level for the stable arc formation with respectively new balance.

V. Arcing voltage, current and arc lengths are recorded by the Labview for the further analysis.

5.1.3.3 FOG COMPARISON TEST

The arcing behaviour in both clean-fog and salt-fog surroundings are compared, in order to investigate the different discharge properties in variable environments, and to identify the most severe conditions for dry-band arcing growth. The test procedures are as follows:

I. Fill the water tank with tap water to create clean-fog environment around the sample.

II. Switch on the transformer, vary the voltage output (from 10 kV to 30 kV) to get stable arcs for different levels.

III. Clean the sample surface, refill the water tank with salt mixed water to reach a conductivity of 16,000 μs/cm. Generate salt-fog environment.

IV. Vary the voltage output (from 10 kV to 30 kV) to obtain the dry-band arcs for different levels corresponding to procedure II.

V. The voltage, current and arcing images are stored in the Labview data acquisition system. Further analysis is conducted based on the comparison of arcing phenomenon between clean-fog and salt-fog environment.

5.1.4 TEST RESULTS

5.1.4.1 ARC FORMATION TEST

For the dry-band arc initial formation, there are 5 stages identified as:

STAGE 1

At the beginning when the sample surface is still dry, the leakage current presents a peak value of 14 μA, which is low due to the excellent dielectric properties of silicone rubber. In the meantime, the current leads the voltage to approximately 90°, showing a capacitive characteristic and minimal resistive current on the sample. Figure 5-2 a) shows the measured voltage and current traces during this stage.

STAGE 2

After the sample surface has become wet due to the fog deposition, the surface impedance reduces and the leakage current begins to grow. In the meantime, the trace of leakage current gradually becomes inphase with the voltage, shifting from a capacitive to resistive nature. Figure 5-2 b) and c) show the phase and magnitude change of leakage current within 3 minutes after the fog injection.

STAGE 3

The current and voltage traces are ultimately in phase after 220 seconds from the test start in Figure 5-2 d), and the magnitude of leakage current significantly increases to 156 μA, which is 11 times higher than

the current at stage 1. Figure 5-3 summarizes the trend of current increasing and phase shifting from stage 1 to stage 3. The current increase is due to the continuous moisture formation which significantly reduces the surface resistance of sample and allows higher leakage current. The phase shift results from the transformation of sample surface property from capacitive (dry silicone rubber) to resistive (wet moisture).

STAGE 4

As the sample surface continues to become wetter forming a thicker layer of clean-fog deposition, the leakage current begins to distort after 470 seconds of test as shown in Figure 5-2 e). Low current discharges are present along with the current distortion, which increases with the rise of leakage current from 0.4 mA to 1.2 mA (peak) shown in Figure 5-2 f) and g).

STAGE 5

As the leakage current increases to above 1 mA, dry-band arcs occur. Initially there are several unstable arcs striking on the sample surface, but finally becomes one single arc shown in Figure 5-4. After approximate 48 minutes of the test running, the dry-band arc becomes stable with relatively constant length and repeatable voltage and current profiles for every power cycle shown in Figure 5-2 h).

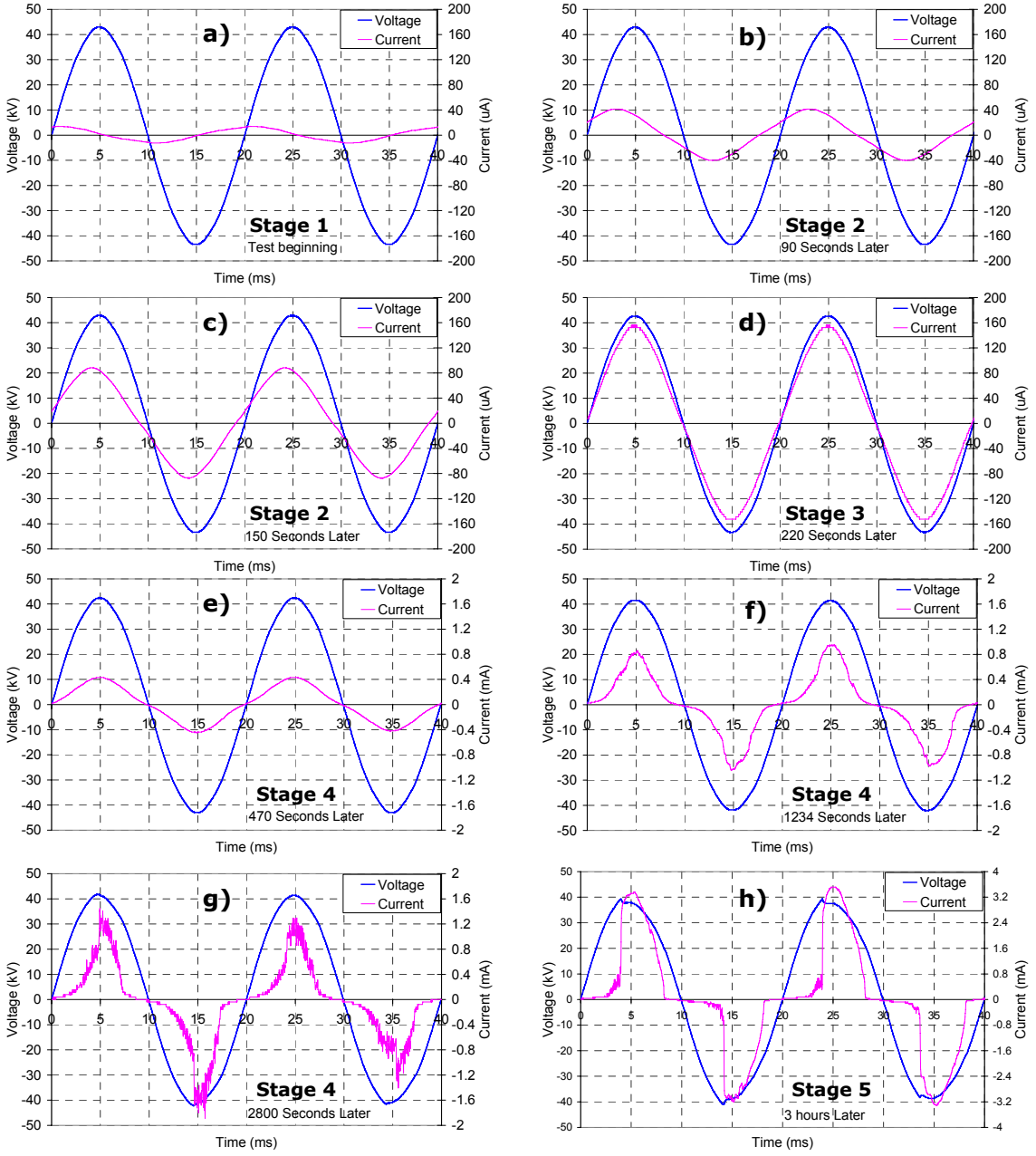

The current scale in a), b), c) and d) is ±200 μA; the current scale in e), f) and g) is 2 mA; the current scale in h) is 4 mA

Figure 5-2: Voltage and current curves from stage 1 to stage 5 in the clean-fog environment

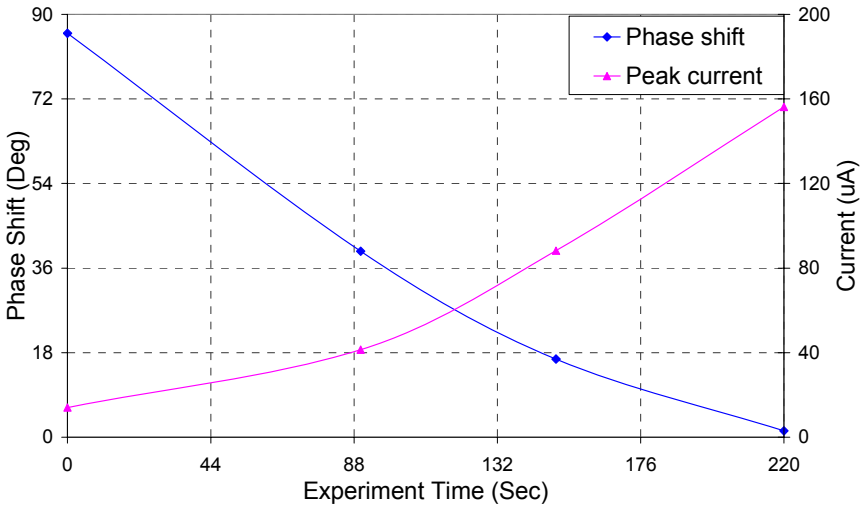

Figure 5-3: Summary of phase shift and current increase from stage 1 to stage 3 in the clean-fog environment

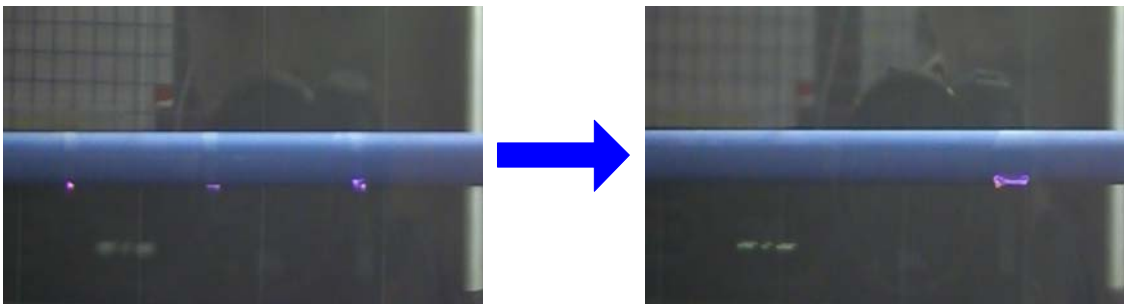

Figure 5-4: The transformation from several arcs to one single arc

5.1.4.2 ARC GROWTH TEST

Figure 5-5 shows the current and voltage profiles and corresponding arc lengths for different current levels of 1.5 mA, 2.0 mA, 2.5 mA, 3.0 mA, 3.5 mA and 4.0 mA in the salt-fog conditions specified in Part 5.1.3.2. Each test was conducted for at least 30 minutes to allow equilibrium to be achieved between arc expansion by joule heating and arc reduction by fog deposition. Although the instantaneous arcing current is changing with dynamic arcs in each angle, the dry-band length becomes constant following the establishment of equilibrium. Therefore, fairly constant arc lengths were measured in each case. The results show the dry-band arc grows in physical length when the arc current increases. The visible arc also becomes thicker and brighter for higher current levels. Detailed

discussion based on these results will be presented in the following part 5.1.5.2 (Results Analysis).

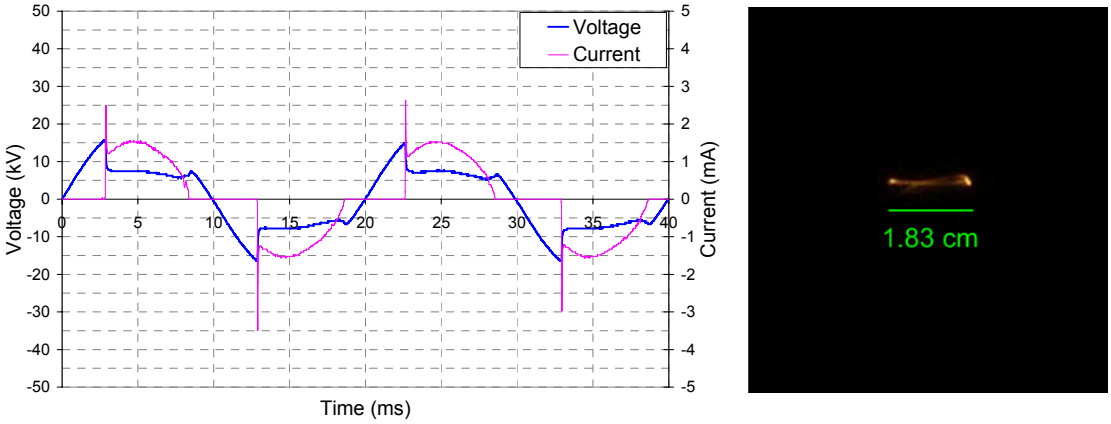

a) Dry-band arcing with 1.5 mA current (peak)

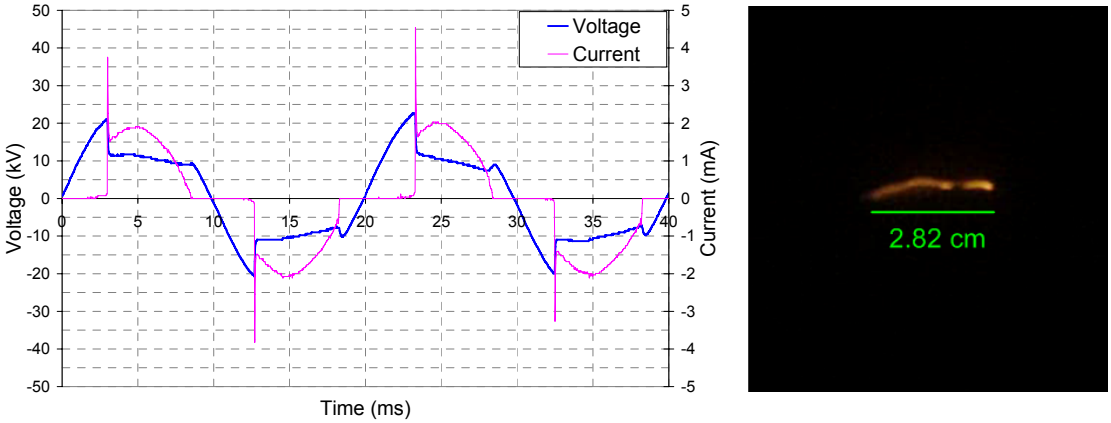

b) Dry-band arcing with 2.0 mA current (peak)

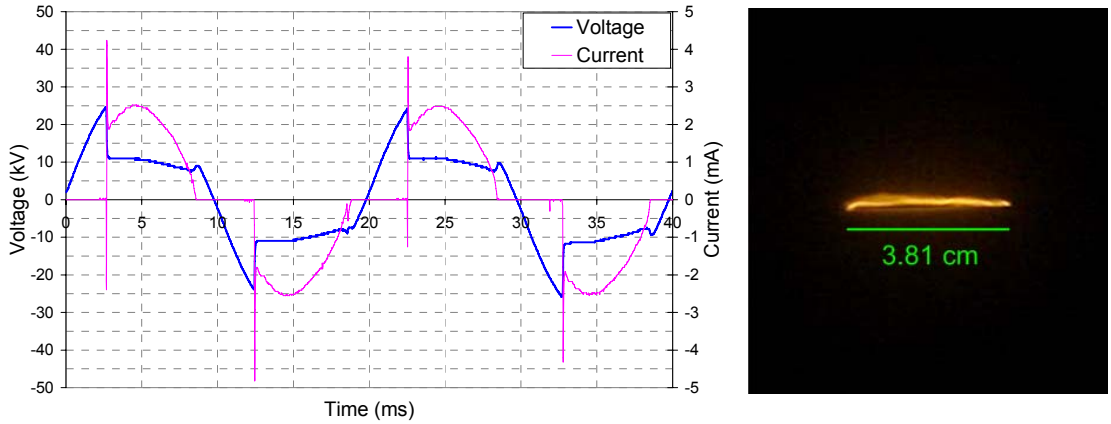

c) Dry-band arcing with 2.5 mA current (peak)

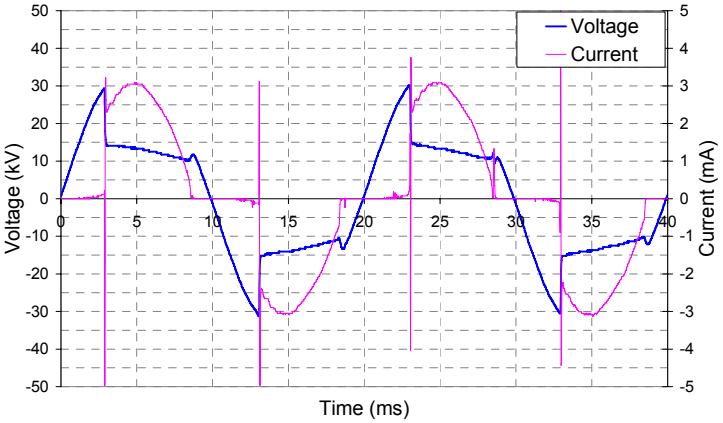

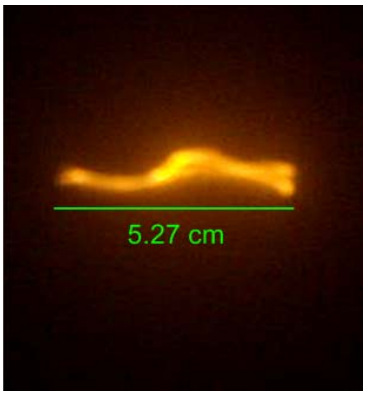

d) Dry-band arcing with 3.0 mA current (peak)

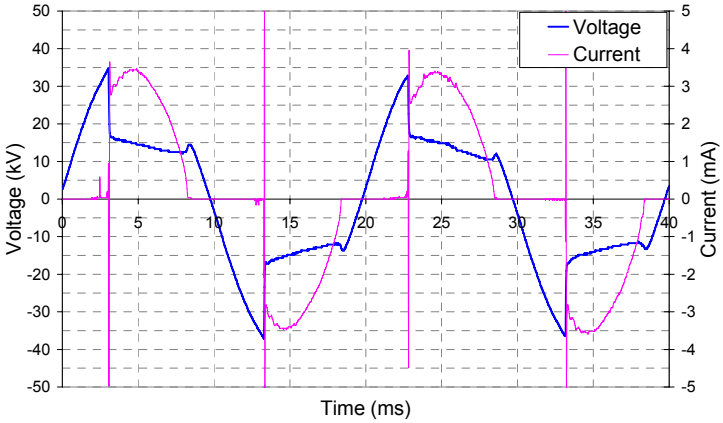

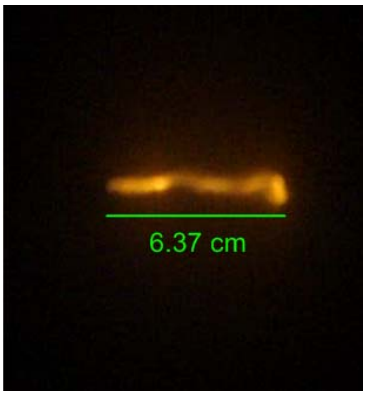

e) Dry-band arcing with 3.5 mA current (peak)

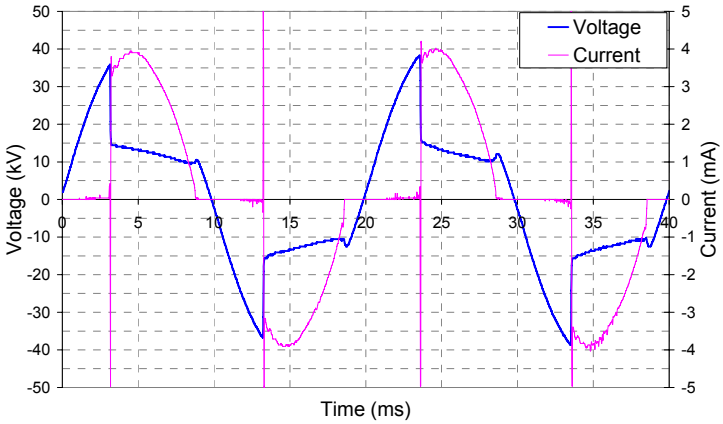

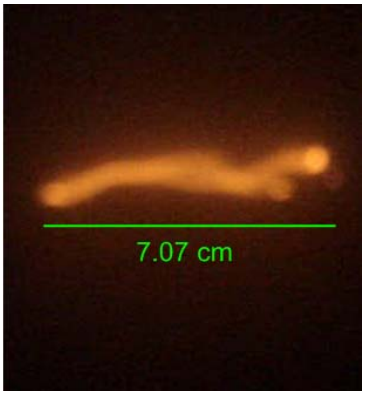

f) Dry-band arcing with 4.0 mA current (peak)

Figure 5-5: Dry-band arcs for different current levels from 1.5 mA to 4.0 mA in salt-fog environment
(Left figure shows electrical properties of discharge)
(Right image shows the discharge physical length)

5.1.4.3 FOG COMPARISON TEST

Figure 5-6 shows an example of arc images in both clean-fog and salt-Testing in a Fog Environments. Under the clean-fog condition, the arc burns with a blue colour. But in case of the salt-fog environment Figure 5-6 b), the arc flame appears yellow. This is due to the presence of sodium ion (Na^+) from salt-fog surroundings during the arcing period. Sodium makes the flame yellow and its spectrum tends to dominate over others.

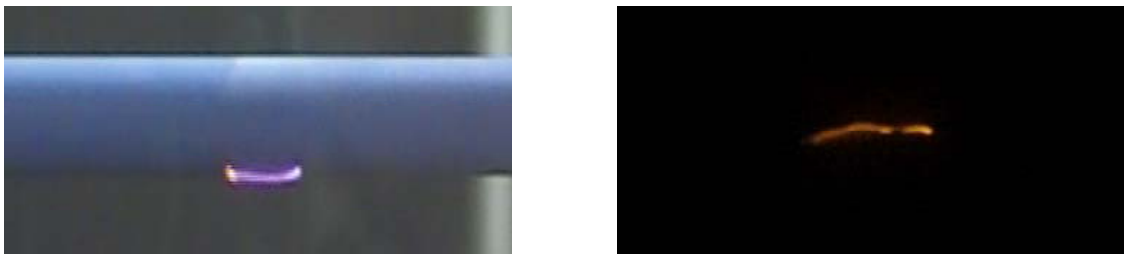

a) Dry-band arc in clean-fog **b) Dry-band arc in salt-fog**

Figure 5-6: Arc images in both clean-fog and salt-fog environment

Figure 5-7 shows an example of dry-band arc behaviours in respective clean-fog and salt-fog environment. The further discussion will be conducted in part 5.1.5.3.

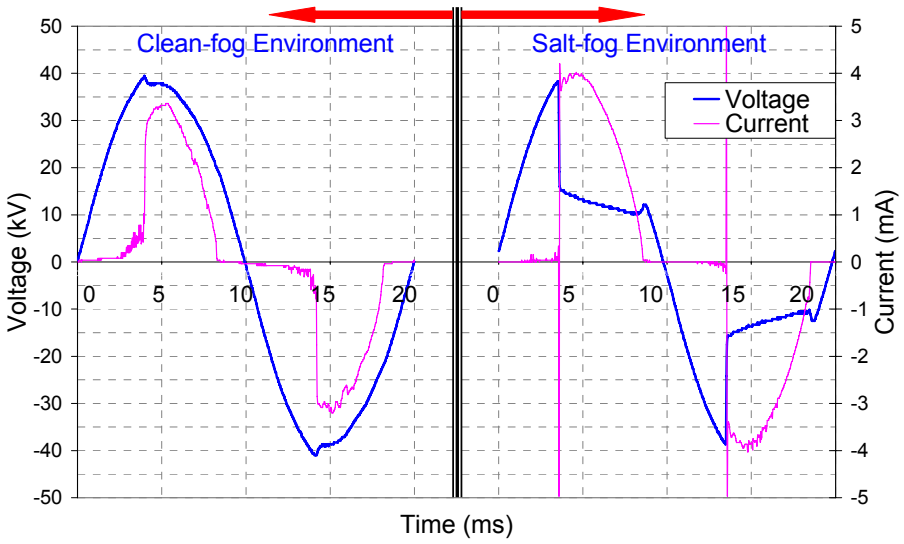

Figure 5-7: Voltage and current behaviours for arcs in different fog environments

5.1.5 RESULTS ANALYSIS

5.1.5.1 CHANGE OF MATERIAL SURFACE PROPERTY IN FOG ENVIRONMENT

From stage one to stage three in the results of the initial formation test (Figure 5-3, part 5.1.4.1), the voltage and current traces were 90 degrees out of phase, and gradually became in phase after 220 seconds of clean-fog injection. A simplified electrical model is used to analyze the change of surface property in Figure 5-8. The sample surface is represented by a capacitor parallel with a variable resistor. At the test beginning when the sample surface is still dry without fog injection, the variable resistor taps at point 'a' with an extremely high value. The majority of leakage current is flowing in the capacitor path given an initial dry current of 14 μA corresponding to the capacitance calculated around 1 pF, so that the capacitive property dominates the whole electrical characteristics of sample surface. From experimental observation, the current leads the voltage at this stage.

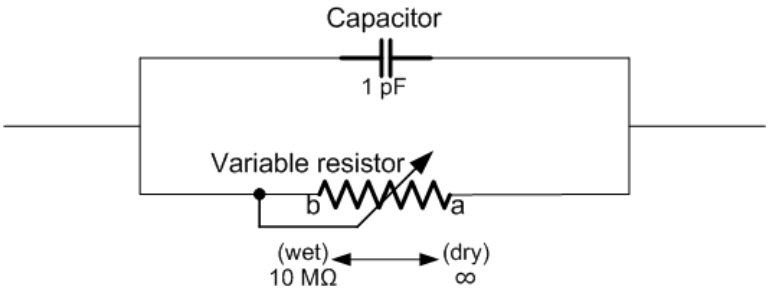

Figure 5-8: Electrical model of silicone rubber sample surface

When the sample becomes wet due to the fog deposition, the value of resistor drops dramatically, to the lowest value which is equivalent to the surface fog deposition resistance (around 6 MΩ for the clean fog case), but the capacitive part of circuit does not change. So the leakage current increases in the resistive branch, which changes the electrical characteristic of sample surface to be resistive of 10 MΩ (6 MΩ wet surface resistance and 4 MΩ arcing resistance). This is the reason why

the leakage current is finally in phase with test voltage after the sample surface being fully wetted.

5.1.5.2 COMPARISON BETWEEN ARCS WITH DIFFERENT CURRENT LEVELS

BREAKDOWN VOLTAGE AND ARC VOLTAGE

Figure 5-9 shows one cycle of typical voltage and current traces for 1.5 mA (peak) dry-band arcing. From A to B, the arc current stays at zero because of the high impedance of dry-band area. When the supply voltage reaches a certain value, the arc starts striking across the dry-band with the significant increase of arcing current. The breakdown voltage is defined as the threshold voltage for dry-band arc ignition. During the arcing period from B to C, the arc voltage is determined by:

$$u_a(t) = v_s - i_a(t) \times R_{resistor} - i_a(t) \times R_{moisture} \qquad 5\text{-}1$$

Where: $u_a(t)$ is the arc voltage, $i_a(t)$ is the arc current, v_s is the instantaneous open-circuit transformer voltage, $R_{resistor}$ is the current limiting resistor and $R_{moisture}$ is the total resistance of water layer.

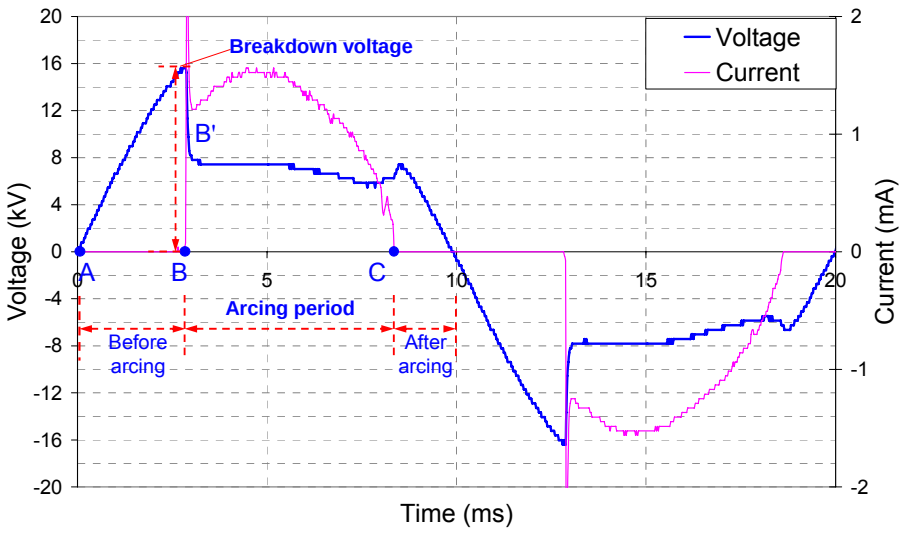

Figure 5-9: Identification of arcing period and breakdown voltage of 1.5 mA arc

In the salt-fog conditions, experimental work shows that the resistance of water layer ($R_{moisture}$) is approximately 0.85 kΩ (at room temperature) for the sample length of 30 cm. For all cases of arc current below 4 mA, the voltage drop across the water layer ($i_a(t)$ x $R_{moisture}$) is less than 0.02% of the arc voltage ($u_a(t)$) and in this analysis is neglected. So the measured voltage signal at the point of voltage divider in Figure 5-1 is approximately the arc voltage ($u_a(t)$), and the relationship between arc voltage and arc current can be simplified as:

$$u_a(t) = v_s - i_a(t) \times R_{resistor} \qquad 5\text{-}2$$

Figure 5-10 shows the relationship between the breakdown voltage, source voltage (peak) and arc length. Labels of 1.5 mA, 2.0 mA … 4.0 mA represent the arcs with the peak current from 1.5 mA to 4.0 mA respectively. The shorter dry-band length is corresponding to the lower breakdown voltage. If the arc current increases, the enhanced joule heating effect will expand the dry-band area, and therefore, requires higher voltage to breakdown the air gap. The result shows a linear relationship in the range of 1.8 cm to 7.1 cm length of arcs with 15.8 kV to 37.4 kV breakdown voltages.

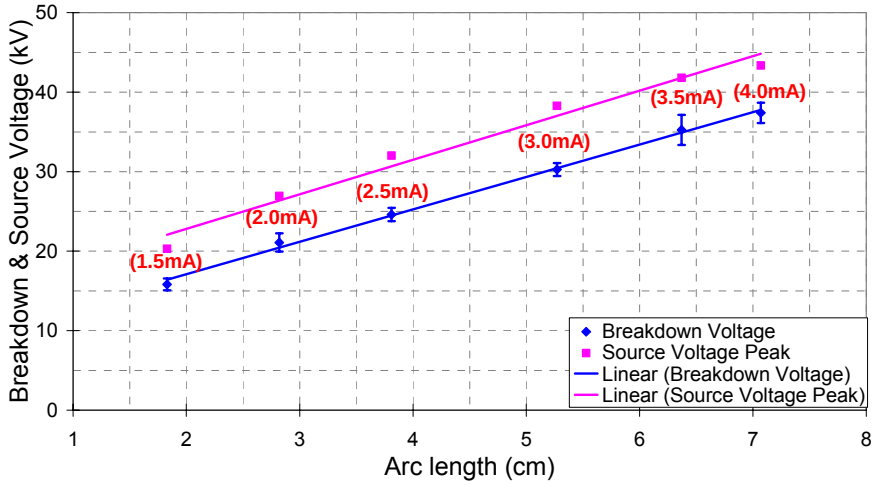

Figure 5-10: The relationship between breakdown voltage, source voltage peak and arc length

ARCING PERIOD

Figure 5-11 summaries the arcing period against arc length for the dry-band arcs from 1.5 mA to 4.0 mA (peak) in the salt-fog environment. As arc current increases, the arcing period shows slight reduction but no significant change. The arcing period is determined by the arc ignition time at point B and arc extinction time at point C as marked in Figure 5-9. As discussed in the previous section of '*breakdown voltage and arc voltage*', the arcing breakdown voltage increases linearly corresponding to the arc length expansion. The arc ignition time is fairly constant for different arcs shown in Figure 5-5. Further, the arc extinction time does not dramatically change for each case. Therefore, the arcing period reduces only 11.5% for an increase of arc length from 1.83 to 7.07 cm at different current levels.

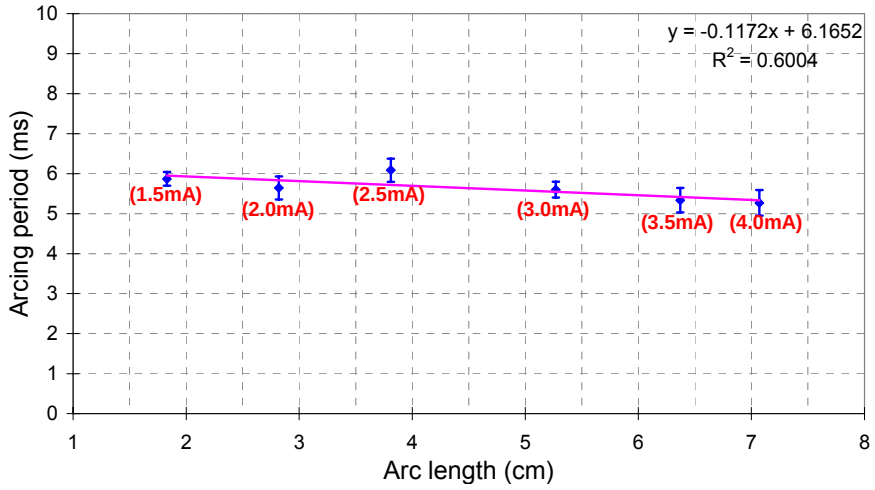

Figure 5-11: The relationship between arcing period and arc length

V-I CHARACTERISTICS

V-I (voltage against current) characteristics for dry-band arcs with different current levels show non-linear relationship between arcing voltage and current in Figure 5-12. For each individual current level, V-I curve with symmetrical two parts are observed in both positive and negative coordinates domain. The rough geometry of V-I curve appears a triangle shape, with point B (B' in negative half cycle) representing an arc ignition, point C (C' in negative half cycle) representing a peak

current arc and point A (A' in negative half cycle) representing an arc extinction, as demonstrated in an example of 4.0 mA arc. The line AB shows the V-I characteristic in the pre-arcing period, while line BC shows the change of V-I when the arc starts striking. The line CA represents the V-I curve during the arcing period, while line A to point (0,0) shows the V-I behaviour in the post-arcing period. Following the rise of transformer source voltage, both arcing voltage and current will be increased, corresponding to the larger triangle area from 1.5 mA to 4.0 mA dry-band arcs.

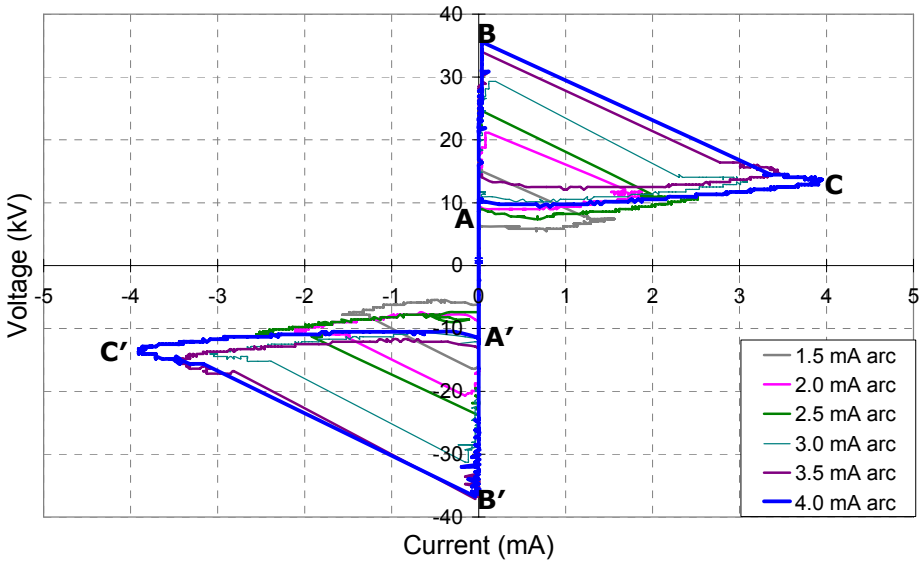

Figure 5-12: V-I (voltage against current) characteristics of dry-band arcs for different current levels from 1.5 mA to 4.0 mA

ARC RESISTANCE

The instantaneous arc resistance is calculated by the ratio of arc voltage and arc current traces measured from test:

$$r_{a(t)} = \frac{u_{a(t)}}{i_{a(t)}} \qquad 5\text{-}3$$

where $r_{a(t)}$ is the arc resistance, $u_{a(t)}$ is the measured arc voltage, $i_{a(t)}$ is the measured arc current.

Figure 5-13 shows an example of arc resistance for four half cycles of arcing activity with 2.5 mA peak current. Arc resistance varies from 4 MΩ to 6 MΩ during the arcing period, reaching the lowest value when the arc is fully developed with maximum arcing current. The highest arc resistance is taken from the point when the arc starts to strike.

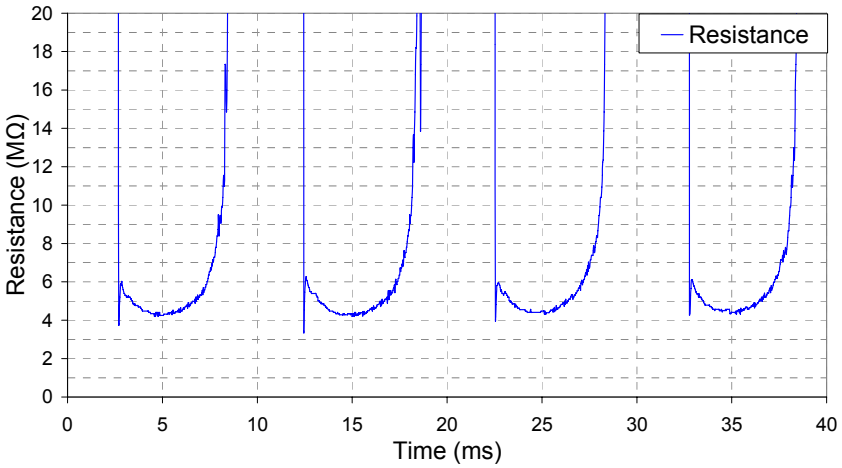

Figure 5-13: Instantaneous arc resistances of 2.5 mA peak current arcing for four consecutive half power cycles

Figure 5-14 summarizes the arc resistance for different arcs from arc growth tests in a salt-fog environment. The range of arc resistance variation gradually decreases from 5-7 MΩ to 3.5-5 MΩ. This is due to the faster growth rate of arcing current comparing to the arcing voltage when the supply voltage rises from a) to f) in Figure Figure 5-5.

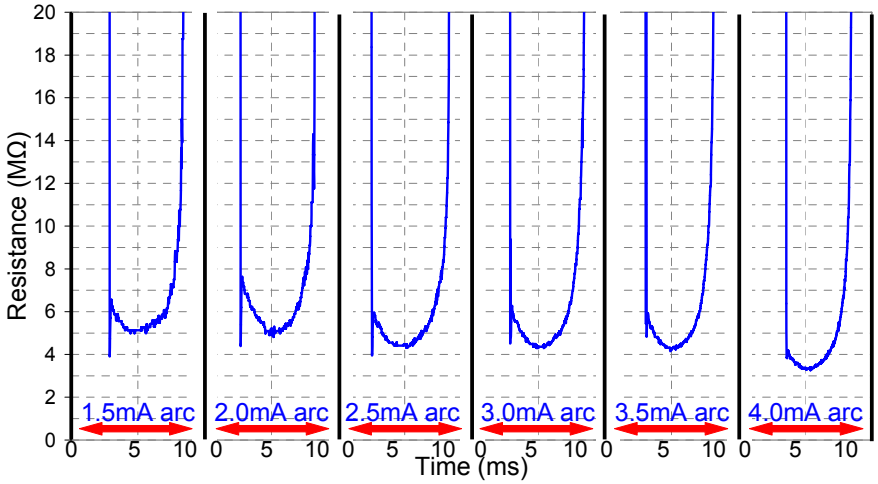

Figure 5-14: Instantaneous arc resistances of arcs in different current levels

ARCING RESISTIVITY

Figure 5-15 shows the instantaneous resistivity of arcs in different current levels in the salt-testing in a Fog Environment. The arc resistivity decreases faster than resistance from 1.0 mA to 4.0 mA because of the arc length expansion:

$$r_{resistivity}(t) = \frac{r_a(t)}{L_a} \qquad 5\text{-}4$$

Where $R_{resistivity}(t)$ is the instantaneous arc resistivity. $r_a(t)$ is the arc resistance, L_a is the measured arc length.

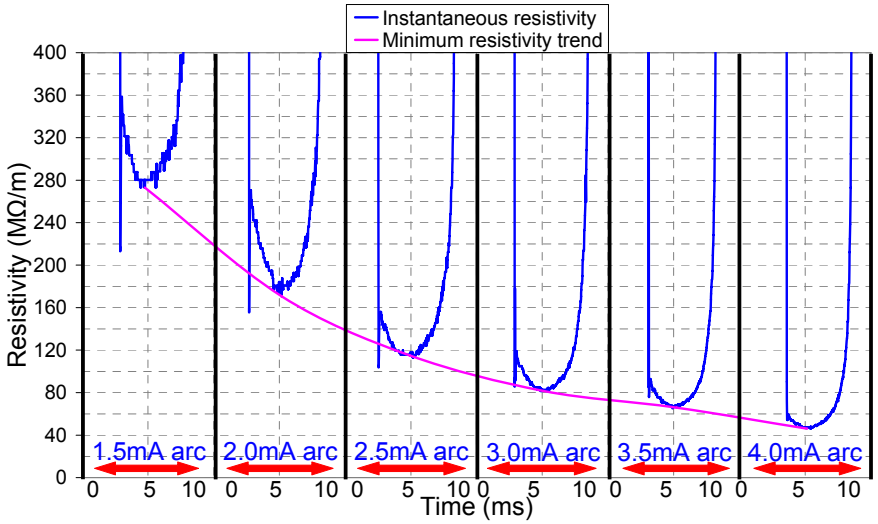

Figure 5-15: Instantaneous arc resistivity of arcs in different current levels

5.1.5.3 COMPARISON BETWEEN CLEAN-FOG AND SALT-FOG ENVIRONMENT

The fog comparison test described in part 5.1.3.3 yields the voltage and current traces of dry-band arcs in both clean-fog and salt-fog environments in Figure 5-7. For the salt-fog environment, the experimental measured voltage during the arcing period drops significantly from 38 kV to 15 kV, but for the clean-fog environment, the arcing voltage does not fall dramatically when the arc is burning. The reason for the difference is that the voltage signal measured at the high voltage sample end (in Figure 5-1) contains two parts which are arc

voltage and water layer voltage. As discussed from Equation 5-1 in section 5.1.5.2 '*Breakdown Voltage and Arc Voltage*', the water layer on the sample surface under the salt-fog environment is highly conductive to approximate 0.85 kΩ. Comparing to the minimum instantaneous arc resistance of 4 MΩ previously shown in Figure 5-14, the salt-water layer only holds less than 0.02% of arc voltage, so that can be neglected. In contrast, the resistance of water layer in the clean-fog environment, with the minimum possible value of 6 MΩ as discussed in section 5.1.5.1, is much higher than in the salt-fog condition, which could take up to 60% of arc voltage. Therefore, the measured voltage in the clean-fog consists largely of water layer voltage. From this point of view, the voltage signal from salt-fog environment can more precisely reflect the real arcing voltage by effectively reducing the water layer influence.

The arcing current is higher in the salt-fog environment compared to the clean-fog under the sample supply voltage in the Figure 5-7. This is due to the conductivity of moisture which allows more leakage current to flow. Therefore, the salt-fog environment represents the most severe conditions for test samples as the arcs can be fully developed on the material surface.

5.2 TESTING WITH INCLINED SAMPLES

5.2.1 INTRODUCTION

As discussed previously, the salt-fog environment can be considered as providing severe conditions for the dry-band arc growth on an insulation material surface. On overhead transmission lines, insulators are suspended in vertical or inclined positions which may enhance surface moisture's mobility because of gravity. This phenomenon, in turn, may affect arcing properties such as physical length due to arc compression (more detailed information is given in Chapter 4). In this section, Testing with Inclined Samples will be conducted to further analyze the electrical properties of compressed arcs on the insulation surface for different slope angles in the salt-fog environment. Arc length, breakdown voltage, arc current, arc power and arc energy will be analyzed and conclusions are drawn that the compressed arc may have a higher energy dissipation which could damage the material surface more rapidly and severely than normal arcing conditions.

5.2.2 TEST ARRANGEMENT

Figure 5-16 illustrates the design of the Testing with Inclined Samples. The test sample is a 22 mm diameter rod, consisting of 4 mm radial thickness commercial silicone rubber which is a typical composite insulator material on a glass-fibre reinforced core. The transformer secondary is fixed to 17.4 kV (RMS) with a 7 MΩ current limiting resistor to obtain 2.0 mA (peak value) arc current when the sample is in the horizontal position. The data acquisition system and salt-fog environmental chamber are the same as in part 5.1 of *Testing in a Fog Environment.*

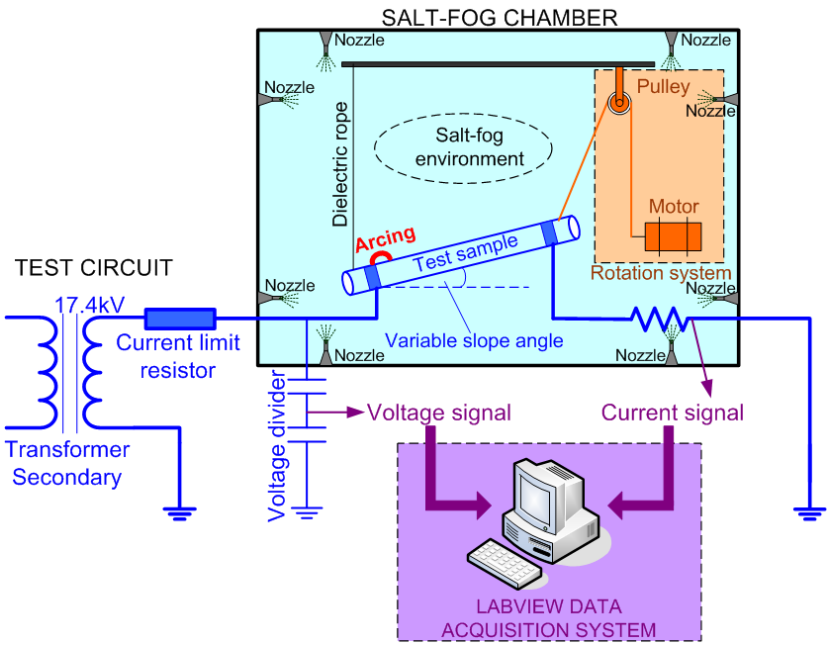

Figure 5-16: Test arrangement of Testing with Inclined Samples

A motor is introduced to control the inclination of sample. This rotation system connects to one sample end by a dielectric string via a pulley which is fitted on the chamber ceiling, while the other end of string is attached to a motor. This string is made from silicone rubber which can provide excellent dielectric properties to avoid leakage current flowing in this path. The motor is remotely controlled by a double-way switch outside the chamber to be rotated either clockwise or anticlockwise. The motor speed is chosen at 1.5 rpm giving a linear string speed of 1.2 mm/s in order to make sure the lifting or falling of the sample is smooth and gradual (approximately 20° of slope angle per minute).

The salt-fog environment is made by salt mixed with water to provide a conductivity of 16,000 μs/cm. The air pressure of fog injection is 1.0 bar, and the resulting precipitation rate in the chamber is approximate 0.2 l/m^3.

5.2.3 TEST PROCEDURE

I. The transformer voltage was fixed at 17.4 kV (RMS) throughout the tests. The sample was initially placed in the horizontal position. Then the salt-fog was immediately injected into chamber with the calibrated precipitation rate specified in part 5.2.2. It took approximately an hour to obtain a single stable arc on the material surface with equilibrium arc length.

II. The sample was lifted to 5°. The length of arc was reduced because of the movement of water layer by gravity. After 30 minutes, a new balance was achieved with a new arc length recorded. From experimental observation, normally the arc gradually moved down the rod until it reached the lower electrode.

III. The sample was lifted to 10°. 30 minutes were allowed for a new equilibrium to be reached. Then the sample was inclined to 15°, 20°, 25°, 30°, 35° with 30 minutes intervals between each slope angle. The relevant arcing data corresponding to each stage were recorded.

IV. When the slope angle reached 40°, the arcing was extinguished. At this stage the leakage current waveform became sinusoidal, and in phase with the supply voltage.

5.2.4 TEST RESULTS

Voltage and current signals were recorded for 5° slope increments between the horizontal and 40°, with associated arc lengths. Figure 5-17 shows an example of test results for each case.

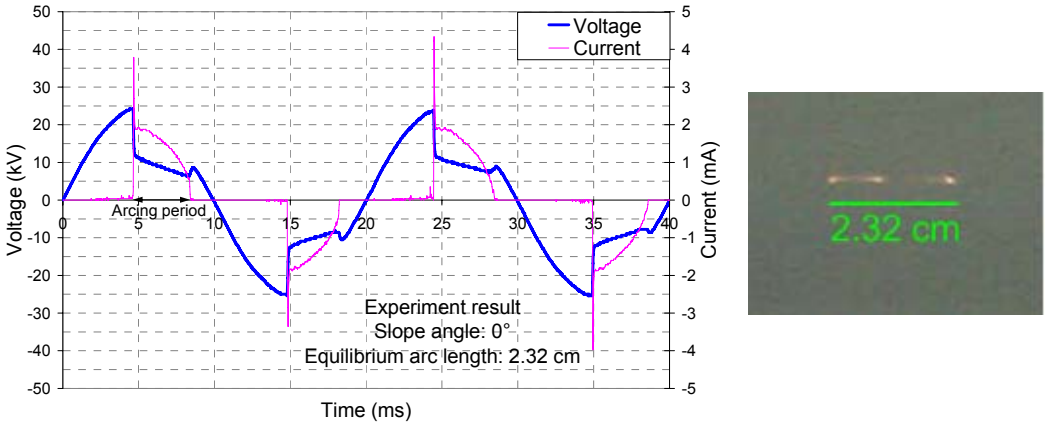

a) Dry-band arcing in horizontal position

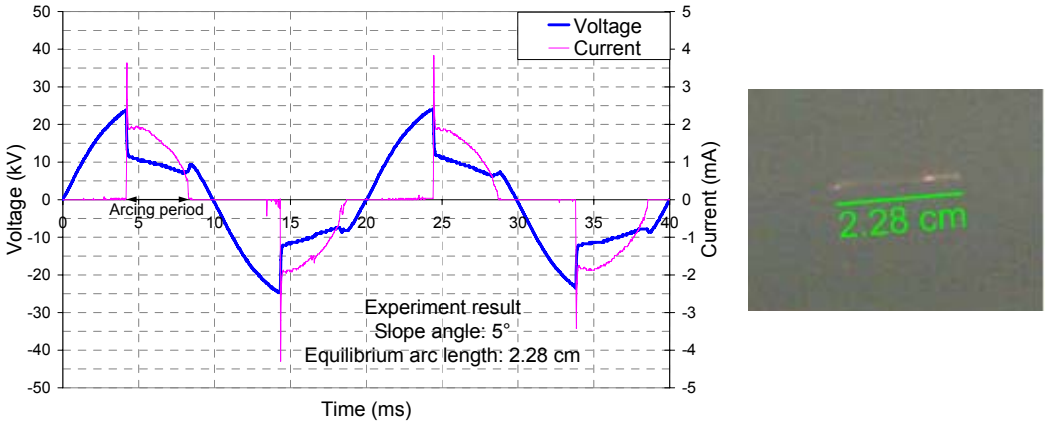

b) Dry-band arcing at 5° slope angle

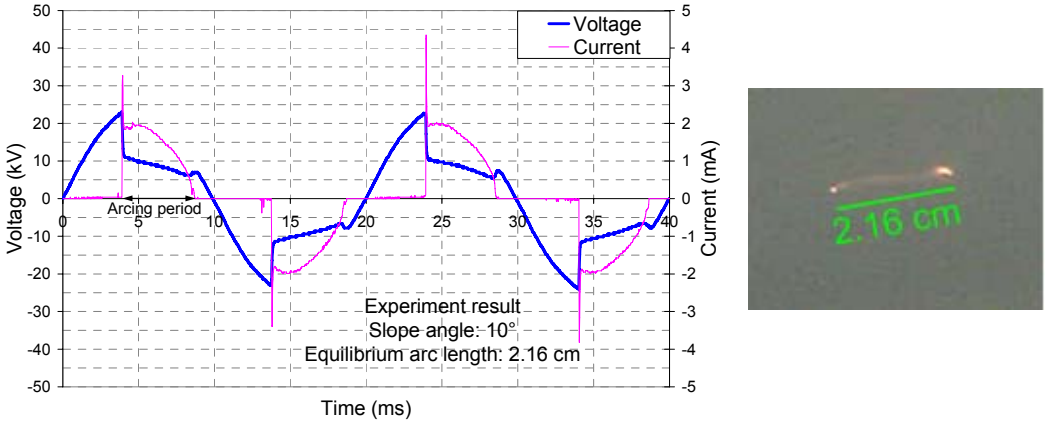

c) Dry-band arcing at 10° slope angle

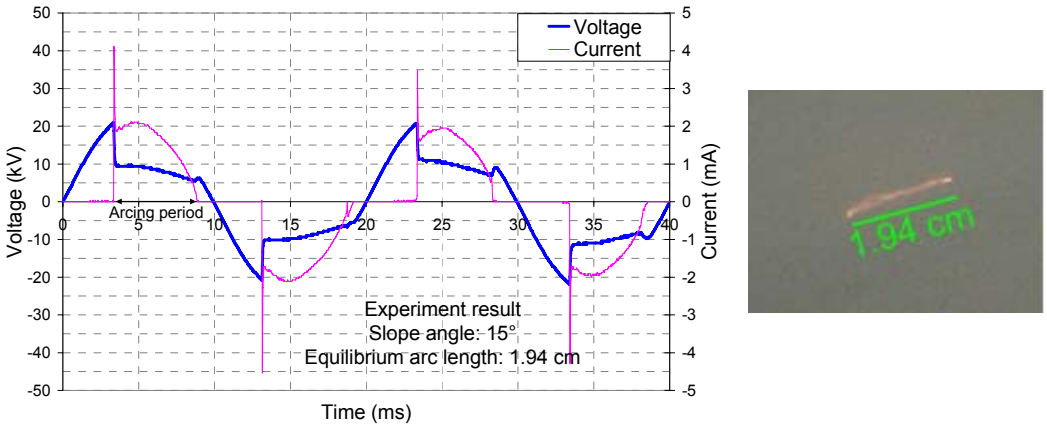

d) Dry-band arcing at 15° slope angle

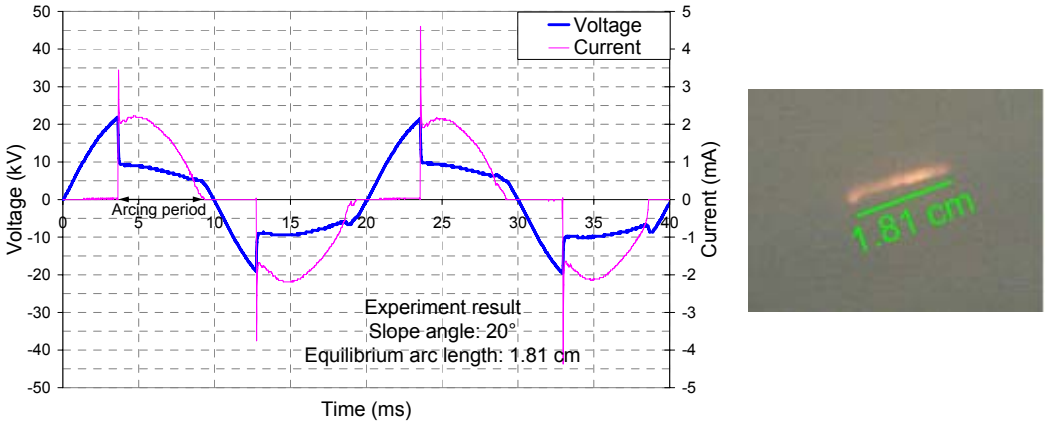

e) Dry-band arcing at 20° slope angle

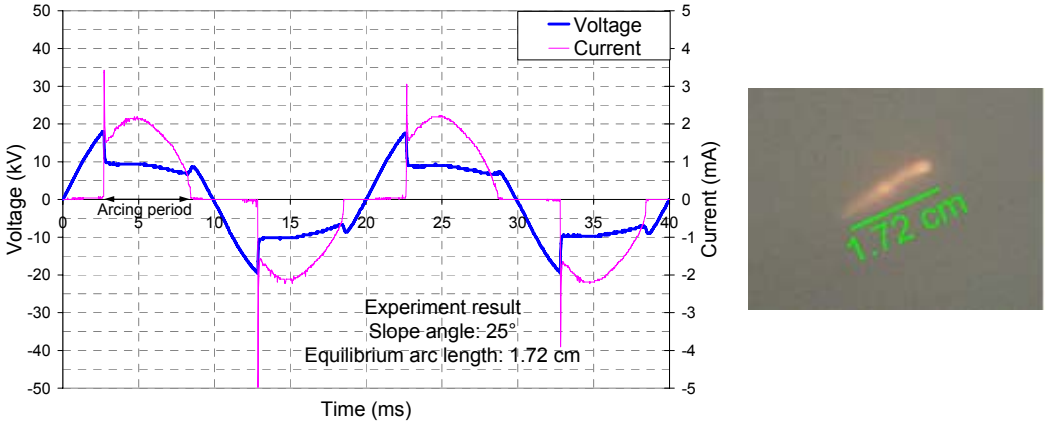

f) Dry-band arcing at 25° slope angle

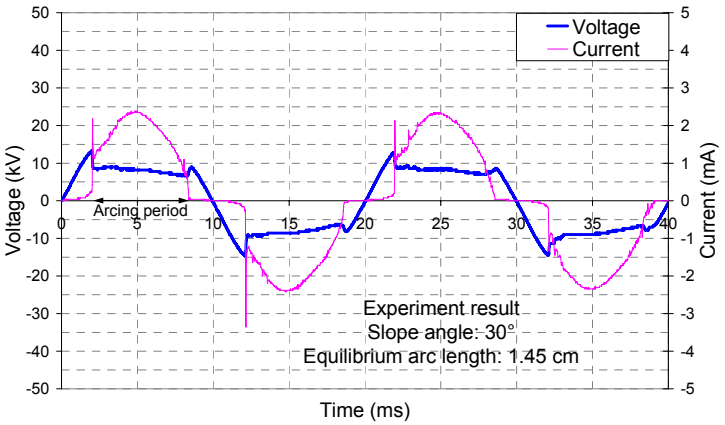

g) Dry-band arcing at 30° slope angle

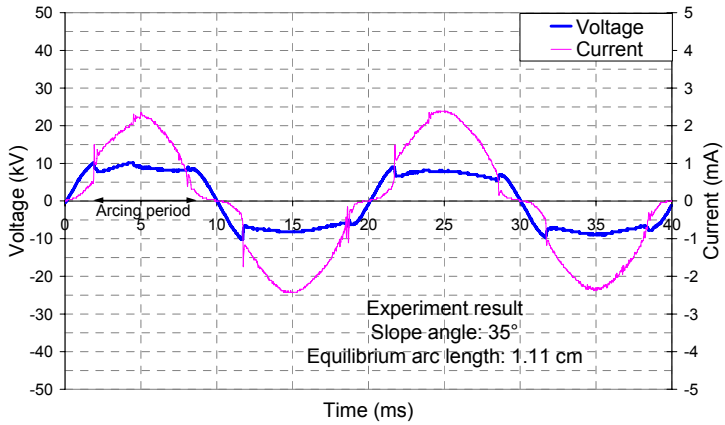

h) Dry-band arcing at 35° slope angle

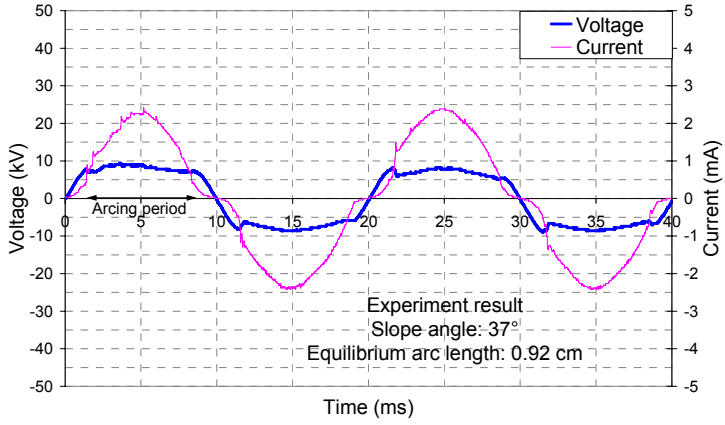

i) Dry-band arcing at 37° slope angle

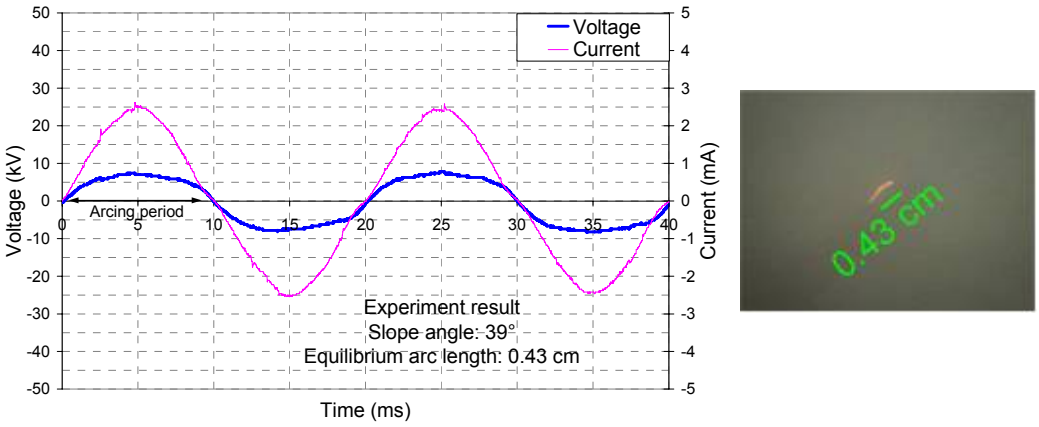

j) Dry-band arcing at 39° slope angle

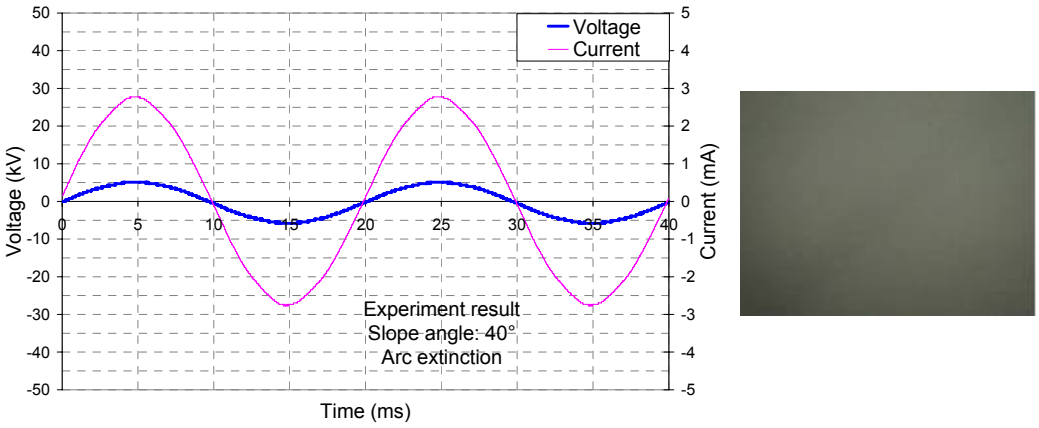

k) Dry-band arcing at 40° slope angle

Figure 5-17: Experimental results of current and voltage traces for inclined arc compression along with images showing arc physical lengths

5.2.5 Results Analysis

5.2.5.1 Arc Length

For the arc length analysis, images are extracted frame by frame from the test video, and the software named Vistametrix is used to measure the arc length from the image. For every half power cycle, the maximum arc length in the video is used for analysis. Figure 5-18 shows the relationship between arc length and slope angle. The dry-band arc has a maximum length of 2.32 cm when the sample is in horizontal position (0° slope angle); this is because the arc can freely grow without external forces moving the two water films at the dry-band edge.

Following the inclination of sample (from 5° to 35°), the dry-band length is continuously being compressed to 1.11 cm. When the slope angle reaches around 40°, the dry-band area is entirely submerged by the upper water film, in which case the arcing activity is extinguished.

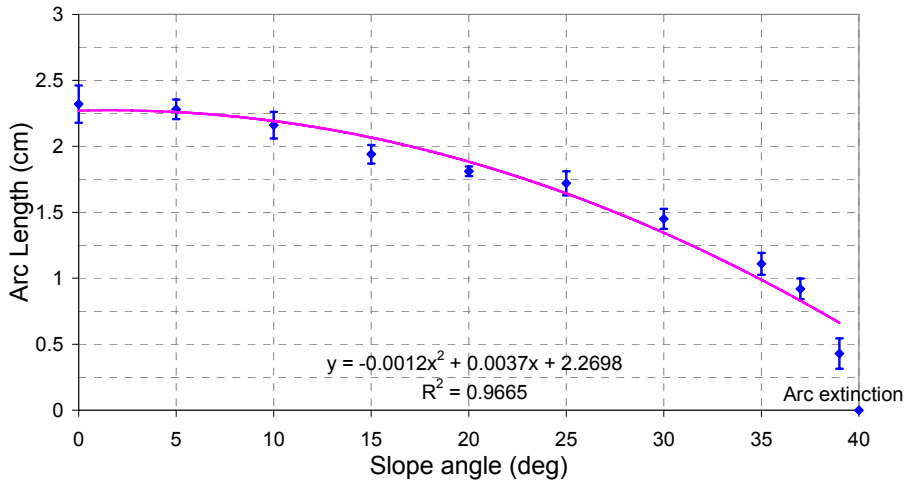

Figure 5-18: The relationship between arc length and slope angle

5.2.5.2 BREAKDOWN VOLTAGE

Figure 5-19 shows the relationship between the breakdown voltage (as defined in Figure 5-9) and arc length. Following the sample inclination from 0° to 35°, the breakdown voltage reduces linearly with dry-band length. This results from the dry-band arc compression which creates a shorter distance of air gap between two water layers, requiring a lower threshold voltage to breakdown the gap for arc ignition.

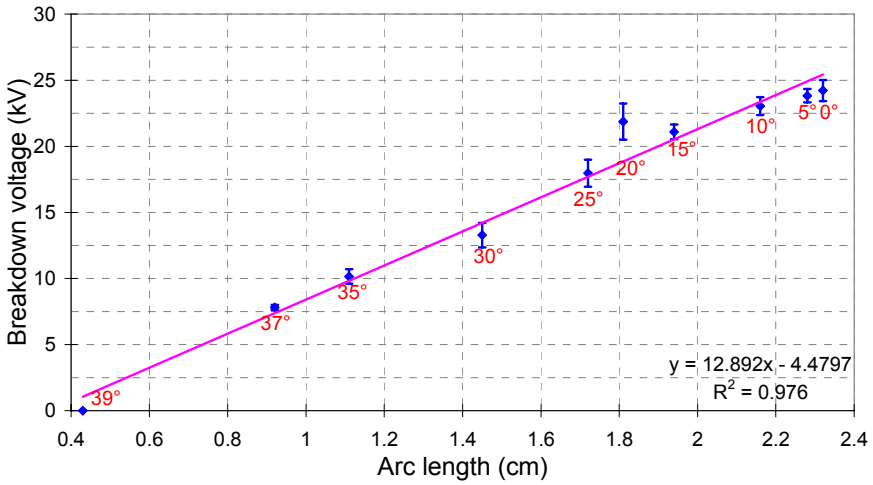

Figure 5-19: The relationship between breakdown voltage and arc length

5.2.5.3 ARCING PERIOD

As marked in Figure 5-17 from a) to k), the arcing period is defined as the period from arc ignition to arc extinction. Figure 5-20 summarizes the test results of arcing period changing with arc length. As the arc is compressed in length, the arcing period becomes longer. This is due to the change of arc ignition time when the arc length varies as discussed in part 5.2.5.2: a shorter dry-band requires a lower breakdown voltage, resultantly bringing forward the time for arc ignition. However, the arc extinction time remains unchanged due to the arc extinction voltage which is about the same for each case of slope angle.

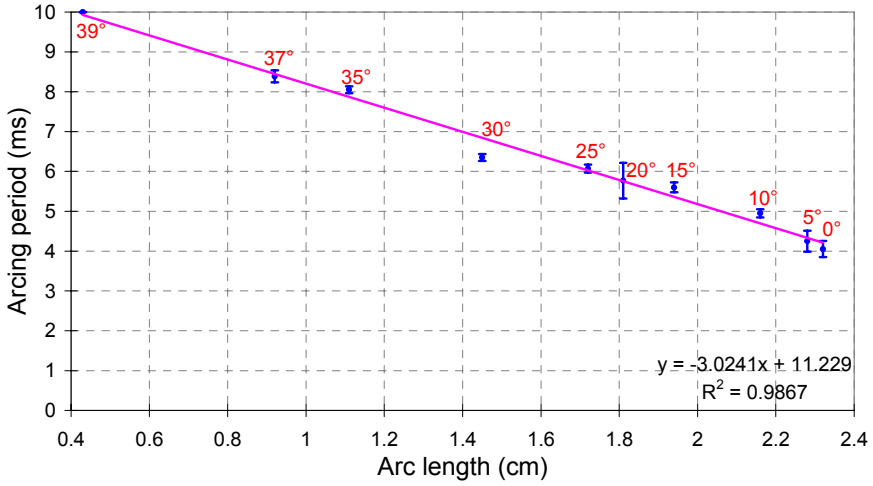

Figure 5-20: The relationship between arcing period and arc length

5.2.5.4 ARC CURRENT PEAK

The peak arcing current for each different dry-band length during the arcing compression process are analyzed in Figure 5-21. The result shows that the arc current peak rises linearly as arc length decreases. The reason for this trend is that the reduced length of dry-band also drops the resistance across the arcing area, which finally makes the arc current higher when the sample becomes more inclined. The extreme condition occurs at the slope angle of 40°, with dramatically increased leakage current to 2.8 mA. This is due to the extinction of dry-band which is replaced by the highly conductive water film.

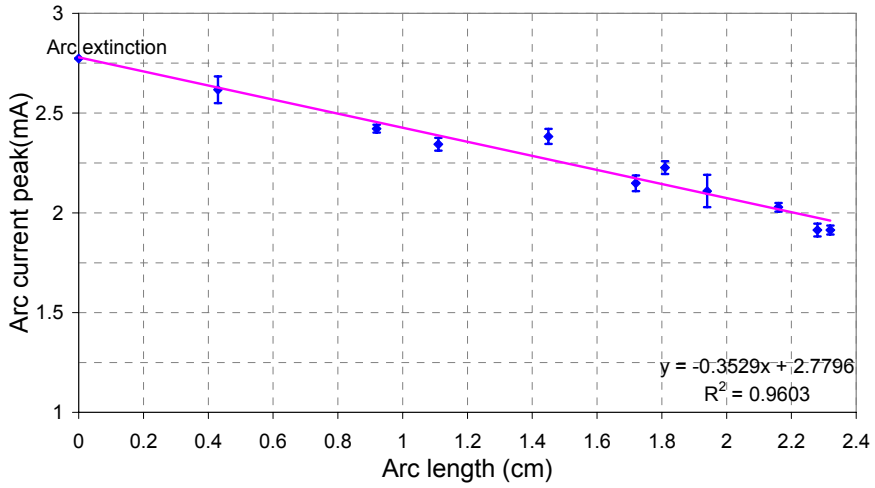

Figure 5-21: The relationship between arc current peak and arc length

5.2.5.5 V-I CHARACTERISTICS FOR ARC COMPRESSION

Figure 5-22 shows the V-I characteristics for arc compression from 2.32 cm to 1.11 cm on the inclined surface. The result shows the non-linear relationship between voltage and current during the arc compression process. When the arc reduces in length, the 'triangle area' of V-I characteristics becomes narrower and further reduces to a single line shape in extreme short arc situation with 35° slope angle. This is due to the less voltage and current distortion when the dry-band arc is about to be extinguished by the replacement of upper water film.

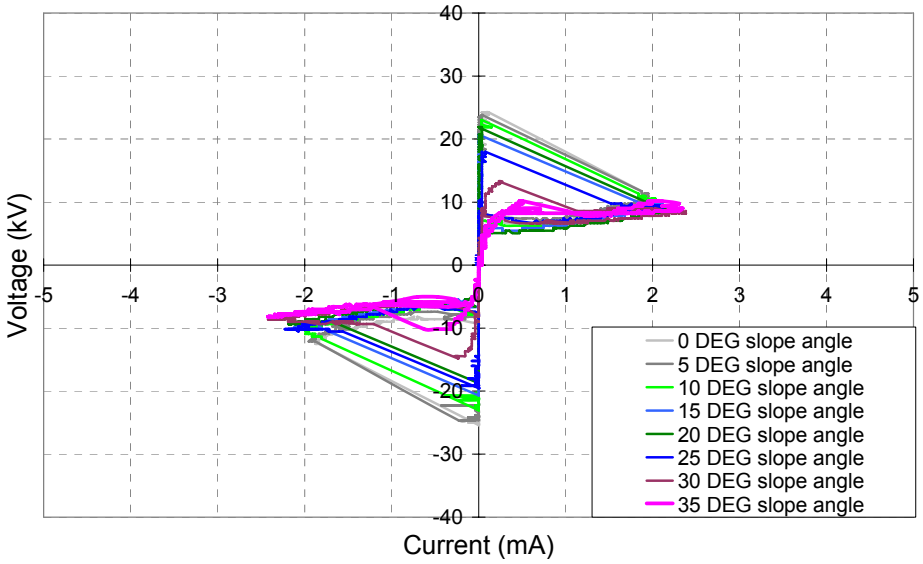

Figure 5-22: V-I characteristics of dry-band arcs for inclined arc compression

5.2.5.6 ARC RESISTANCE AND RESISTIVITY

Figure 5-23 shows the instantaneous arc resistances in different arc compression situations with the relevant change of arc length and slope angle. As discussed previously, one characteristic of instantaneous arc resistance is its minimum value, and this minimum resistance is located on the bottom of the 'U' where the arcing current is greatest. The trend line for minimum resistance indicates that the more inclined the sample with shorter arc length, the lower the arc resistance becomes. This is due to the reduction of dry-band length: when the arc has become more compressed, the arcing current peak increases (shown in Figure 5-21) but the arcing voltage does not change significantly with current.

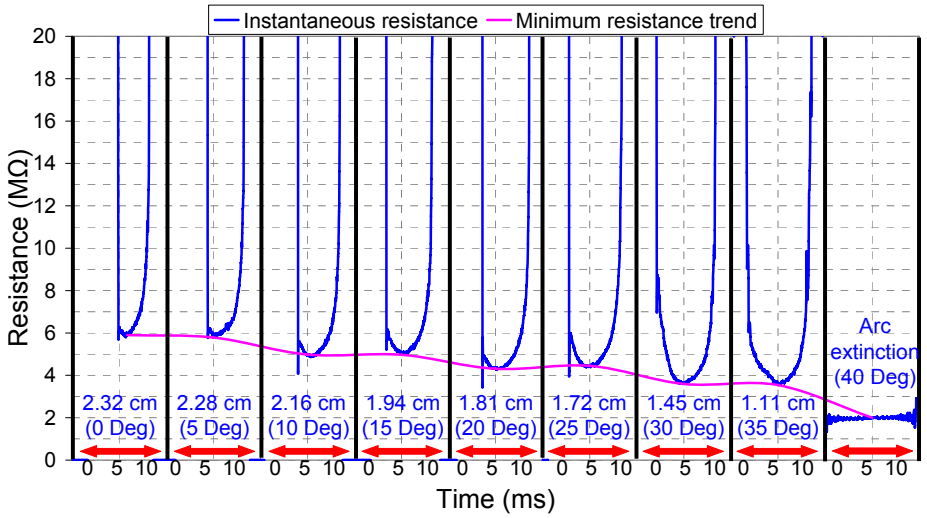

Figure 5-23: Instantaneous arc resistances of inclined compressed arcs with different arc lengths

Figure 5-24 shows the measured instantaneous arc resistivity, which also varies during the arcing period as a U shape curve. The trend line of minimum arc resistivity per half cycle as a function of arc length / slope angle is summarized in this figure. It is found that unlike the trend of resistance, the minimum arc resistivity does not significantly change with the arc compression, although the trend slightly varies but generally keeps constant throughout the arc compression process.

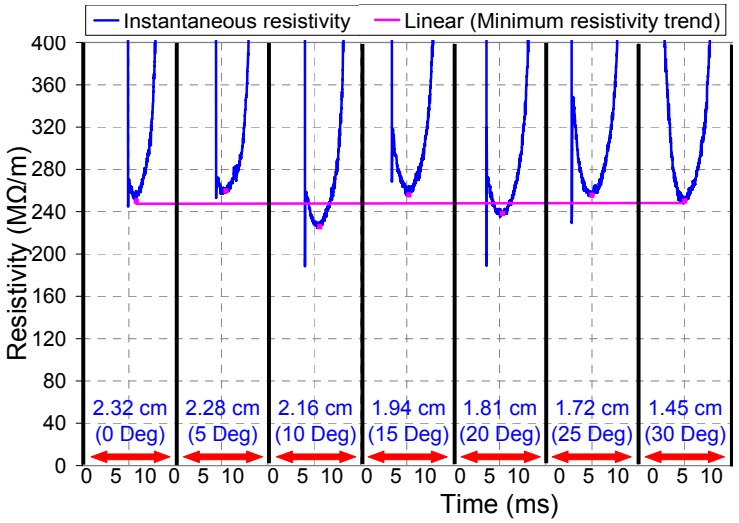

Figure 5-24: Instantaneous arc resistivity of inclined compressed arcs with different arc lengths

5.2.5.7 ARC POWER

Arc power is a significant factor leading to the damage or failure of insulator surface. When the insulator becomes inclined, the dry-band arcing has previously been reported as more detrimental to dielectric materials because the arc is being compressed [17]. In order to analyze the electrical properties of arc power under compression conditions, the current and voltage traces are acquired and the instantaneous arc power is calculated by

$$p_a(t) = u_a(t) \times i_a(t) \qquad 5\text{-}5$$

Where: $p_a(t)$ is the instantaneous power of arc, $u_a(t)$ is the arc voltage, $i_a(t)$ is the arc current.

Figure 5-25 c) shows an example result of instantaneous power calculation for dry-band arc with 5° slope angle, based on the measured voltage and current traces in a) and b).

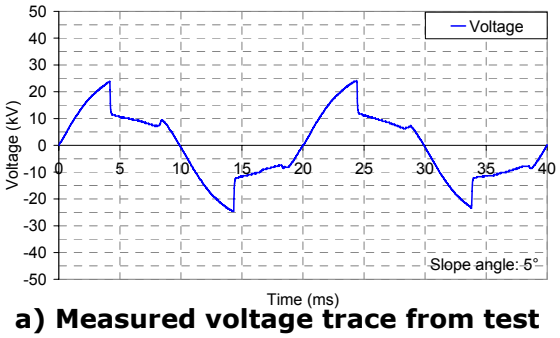

a) Measured voltage trace from test

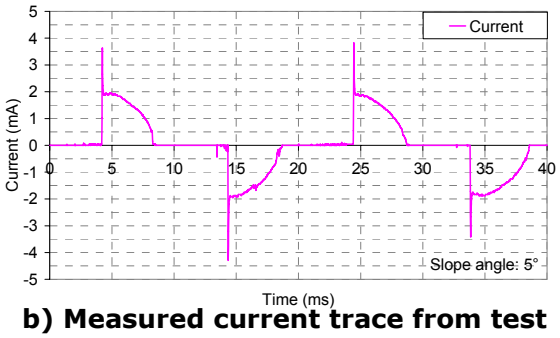

b) Measured current trace from test

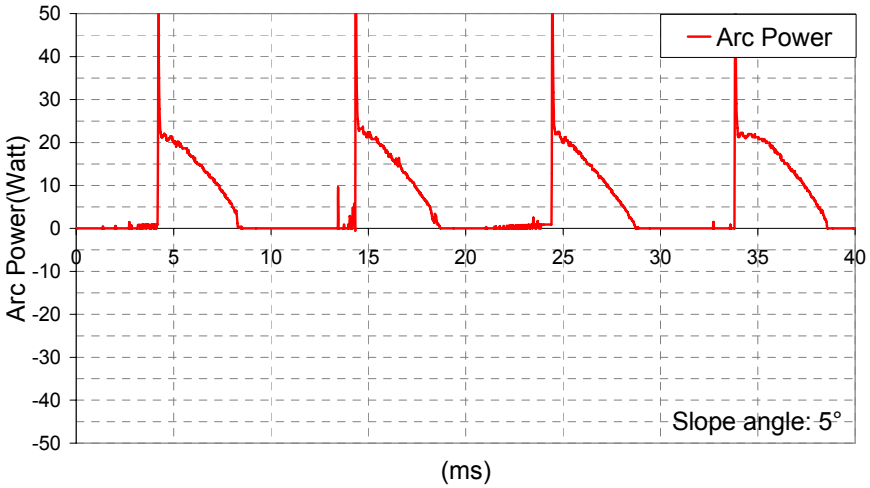

c) Calculated instantaneous arc power

Figure 5-25: Instantaneous arc power calculation based on 5° slope angle

Figure 5-26 summarizes the typical half cycle arc power for different slope angles. The result shows that the peak power for different arc lengths stays around 20 W without changing too much. However, the arcing period significantly increases with sample inclination.

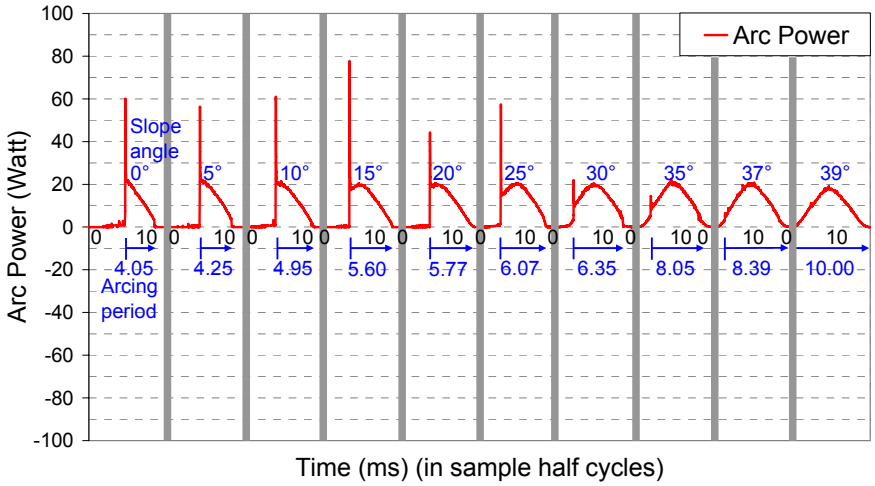

Figure 5-26: Instantaneous arc power calculation with a range of slope angles

5.2.5.8 ARC ENERGY

Accumulated arc energy for every cycle of a dry-band arc is calculated based on the instantaneous arc power in section 5.2.5.7. The calculation method is demonstrated in Figure 5-27 together with Equation 5-6. For

the experimental results, each cycle of dry-band arcing has 1600 measurement points. Based on these discrete data of arc power, the arc energy is analyzed as:

$$E_a = \sum_{n=1}^{1600} \left(p_a(t_n) + p_a(t_{n+1}) \right) \times t_n / 2 \qquad 5\text{-}6$$

Where: E_a is the arc energy per cycle. $p_a(t_n)$ is the arc power (W) at the n^{th} sample point, and t_n is the interval sample time (0.025 ms).

Appendix 1.1 shows the Matlab program for the arc energy calculation.

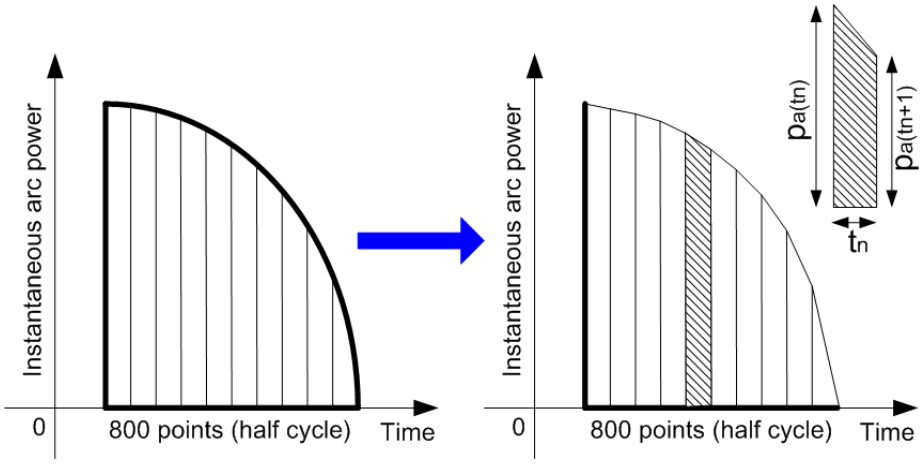

Figure 5-27: Arc energy calculation based on the instantaneous arc power

Figure 5-28 shows plots of arc energy against arc length for variable dry-band arcs with different voltage and current levels on the inclined sample surface. Additional tests were carried out following the same test procedures specified in part 5.2.3, but the transformer secondary voltage was fixed to different levels matched with different current limiting resistors to create arcing compression for various dry-band arcs. All the results generally show increased trends of arc energy with the reduction of arc length. The reason is that arcing activity will sustain longer following the arc compression process as shown in Figure 5-20, and there is an increase of peak arc current shown in Figure 5-21. In the

relatively higher energy arcs such as 15kV 7mA, 25kV 2 mA and 20 kV 10 mA (peak voltage and current), energies show flat or even positive trends in the highly compressed arcs which are shorter than 80% of their original maximum free-growth length. This is due to the reduction of arcing voltage during the arc compression process, which is able to further reduce the arcing energy in the deep compression situation.

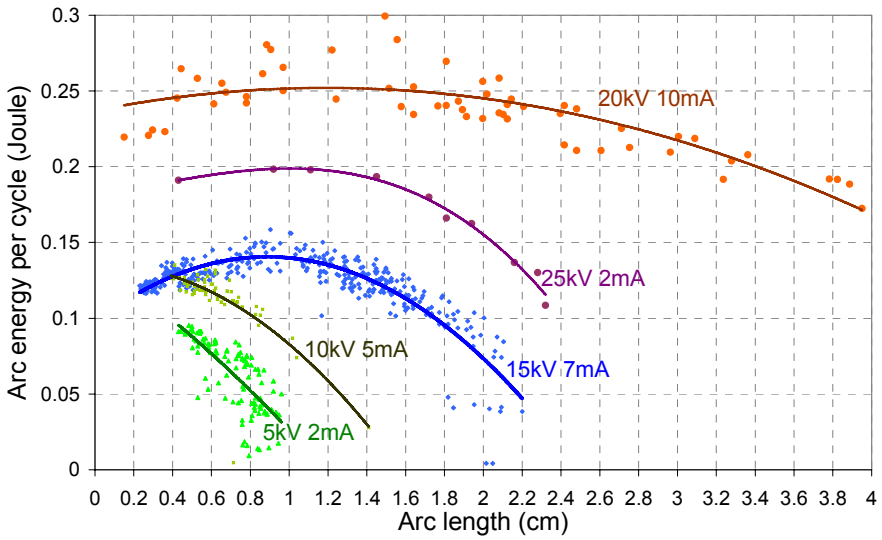

Figure 5-28: Experimental results of arc energy against arc length for different arcs in Testing with Inclined Samples

Figure 5-28 also gives a comparison between dry-band arcs in different current and voltage levels. Those results were achieved by using different source voltage and current limiting resistor to create different arcs. For example, The '15 kV 7 mA' represents the dry-band arc was made by 15 kV peak source voltage and owned 7 mA peak current at the initial non-compression situation with 2.2 cm's length. Low voltage and current arcs have shorter lengths and steeper energy trends compared to the high voltage and high current arcs.

5.2.5.9 ENERGY DENSITY

The energy density of arcs on material surface is calculated as energy divided by the dry-band area over which arcing occurs:

$$D=\frac{E}{2\pi RL_a}\ (\text{Joule/m}^2) \qquad 5\text{-}7$$

Where: R is the radius of sample rod, L_a is the arc length, and $2\pi RL_a$ is the dry-band area.

Figure 5-29 summarizes the change of energy density with arc length in different voltage and current levels of dry-band arcs from Testing with Inclined Samples. All the results show the energy density for different arcs increase by at least a factor of 6 after the reduction of arc length. This is due to the rise of arc energy together with reduction of dry-band area during the arc compression.

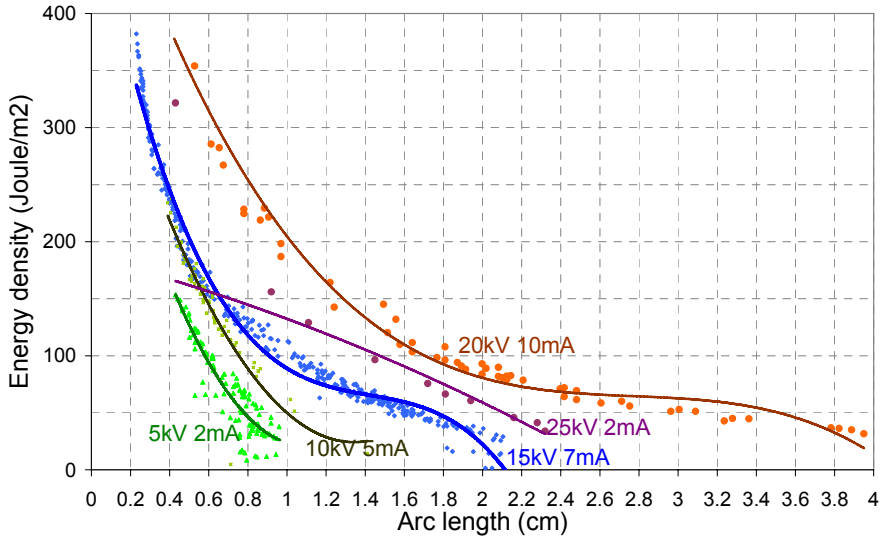

Figure 5-29: Experimental results of energy density against arc length for different arcs in Testing with Inclined Samples

In summary, the arc energy and energy density trends predict that there will be more potential damage to the material surface when the situation of arcing compression occurs as a result of the rise of corresponding arc energy and energy density.

5.3 TESTS BETWEEN WATER DROPS

5.3.1 INTRODUCTION

The arcing compression phenomenon can be present in another form on the composite insulator surface, such as discharges between water drops on an insulator core or sheds. Such activity can develop into arcs in high pollution and strong electrical field conditions. A theory is proposed that the water drops may be deformed under the electrical field and even be moved due to the electric field and the arc, and so become mobile. These mobile drops can change the physical length of arcs, and in turn, affect the arc power and energy on the insulation surface (more detailed information is given in Chapter 4). The experimental work in this part aims to establish two water electrodes with controllable separation, and a low current arc (similar to the dry-band arcs) between them. Instantaneous arcing voltage and current against time are recorded, and based on these data, the trends of breakdown voltage, peak current, arcing duration and arc energy as functions of arc length are analyzed. The arc length is assumed as a straight-line between drops and therefore equivalent to the drops' separation. This study allows an investigation into arc behavior independent of any dielectric surface. The results show that the arc energy and energy density will be increased following the compression of arc length between water drops, independent of a dielectric surface. The analysis agrees with the previous tests on the inclined sample in that the compression of arc length on an insulator is an important factor reflecting its ability to damage the material surface in service conditions.

5.3.2 TEST ARRANGEMENT

In order to create a low current arc between two water drops at various separations under the different voltage levels, the test circuit was designed and implemented as illustrated in Figure 5-30. A pair of syringes filled with water (tap water of conductivity 600 μs/cm) is placed horizontally with orifices facing each other. A copper wire is submerged into each syringe with wire tip installed in the middle of the orifice nozzle. One copper wire is connected high voltage end to transformer secondary via a current limiting resistor (8 MΩ), while the other wire is earthed. The purpose of this design is to create a voltage gradient between the copper wires, and strike an arc which makes contact directly to the water drop surface. The distance between the drops is adjustable for the simulation of various arc lengths, by the relative movement of syringes.

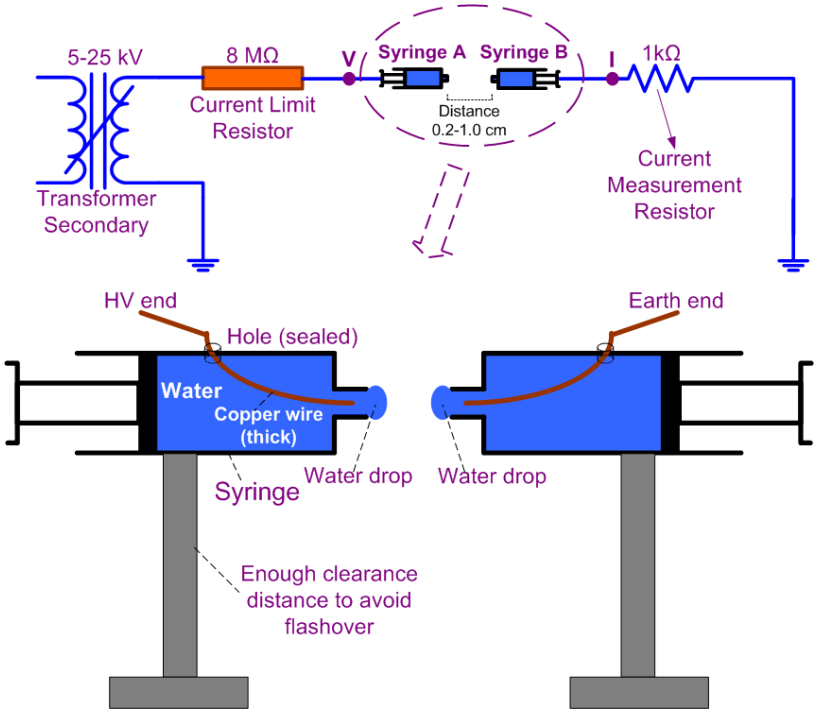

Figure 5-30: Test arrangement of water drops test.

The 10,000:1 voltage divider at point 'V' is used to measure the arcing voltage signal between the two water drops. The 1 kV current

measurement resistor is used to pick up arcing current from point 'I' in the test circuit. The data acquisition is based on the National Instrument Labview system as used in the previous tests. This arrangement has the additional advantage over the rod surface test, that the voltage measured, is virtually identical to the arc voltage. It may also be noted that the resulting change in geometry means for the same voltage and droplet separation the situation with a surface gives rise to higher field at the air, water and insulation triple point. However the absence of a surface allows greater droplet deformation.

5.3.3 TEST PROCEDURE

I. Initially the supply voltage was fixed to 5 kV (peak value). The distance between water drops was set at 0.2 cm, the voltage and current profiles were recorded.

II. The drops' separation was increased to 0.4 cm with supply voltage still fixed to 5 kV (peak value) throughout. After 10 minutes, the separation was set to 0.6 cm, then 0.8 cm and 1.0 cm with 10 minutes interval between each case. The voltage and current traces were recorded respectively.

III. The supply voltage was increased and fixed to 10 kV; the distance between water drops was changed at 0.2 cm steps from 0.2 cm to 1.0 cm.

IV. The supply voltage was continuously increased and fixed to 15 kV, 20 kV and 25 kV, with drops' separation changed from 0.2 cm to 1.0 cm for each voltage level. The corresponding arcing voltage and current curves were recorded.

5.3.4 TEST RESULTS

5.3.4.1 ARC STABILITY

Under different voltage levels and drops' separations during the test, discharges between water drops can be identified as three forms: no arc, unstable discharge and stable arc. Figure 5-31 gives examples of voltage and current traces for these respective cases:

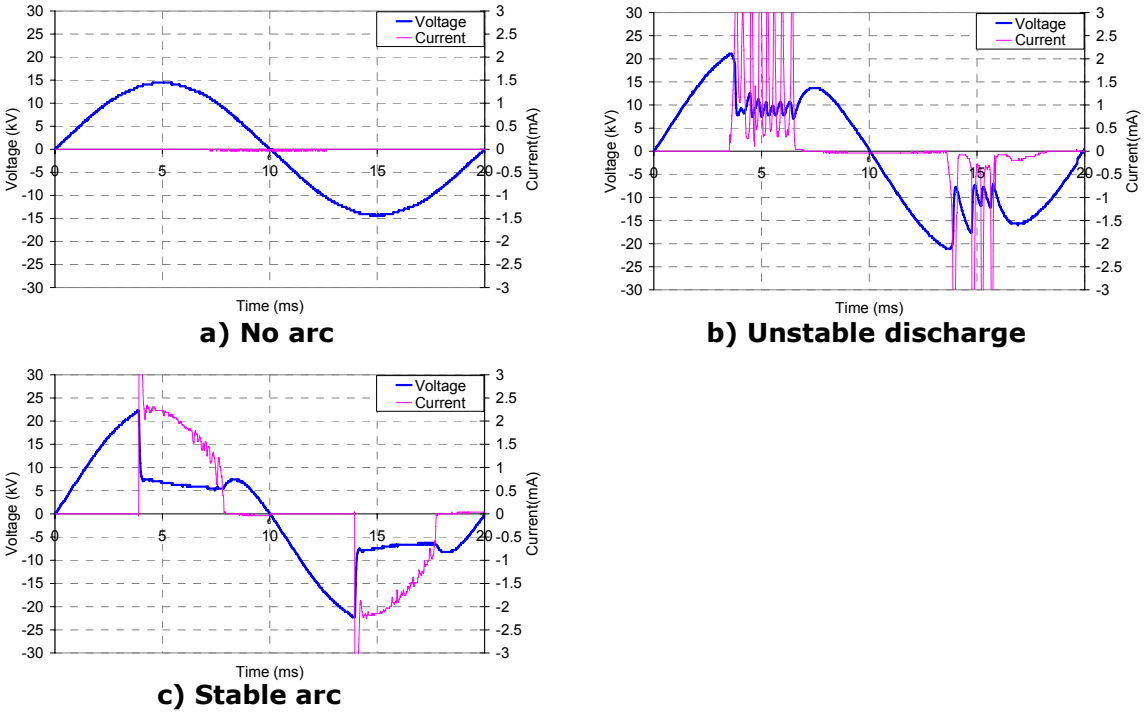

Figure 5-31: Three different cases of discharges between water drops.

Figure 5-31 a) describes the no arc situation with the measured voltage which is the same as supply voltage and no leakage current throughout. This results from insufficient supply voltage to breakdown the air gap between water drops. The unstable discharge specified in Figure 5-31 b) occurs when sufficient voltage is available to breakdown the air gap, but there is insufficient current to sustain an arc. Therefore the current signals have a saw-toothed shape when the air gap is discharging, together with an unstable discharge voltage. Stable arcs occur as in Figure 5-31 c) if there is both sufficient voltage to beak down the gap

and sufficient current to sustain the arc. In this case, the voltage signal drops to a fairly constant value during the arcing period, accompanied with arcing current sharply increasing to peak value, then continuously reducing to zero.

Table 5-1 summarizes the arc stability for every test conducted. 5 kV peak supply voltage was insufficient to generate any discharges. The first arc appears when supply voltage increased to 10 kV with 0.2 cm drop separation. Following the further increase of voltage level, the longer air gap can be broken down, with continuous voltage and current traces during the arc. The unstable discharge occurs when the 25 kV peak supply voltage attempting to break the 1.0 cm drops separation. If a higher value of current limiting resistor were used to reduce the arc energy further, unstable discharges would have been found for all experimental gaps and voltage in this test.

Table 5-1: Summary of arc stability in different voltage level and drop gap

Max current level / Gap (cm)	Voltage level	1.0	0.8	0.6	0.4	0.2
0.625 mA	5 kV	N	N	N	N	N
1.25 mA	10 kV	N	N	N	N	S
1.875 mA	15 kV	N	N	N	S	S
2.5 mA	20 kV	N	S	S	S	S
3.125 mA	25 kV	U	S	S	S	S

*N means no arcing, U means unstable arc, and S means stable arc

5.3.4.2 ARC LENGTH

The reduction of drop separation (from 0.8 cm to 0.2 cm) makes the arc shorter in physical length, which changes the situations with respective voltage and current traces under the voltage levels of 25kV, 20kV and 15 kV as shown in Figure 5-32.

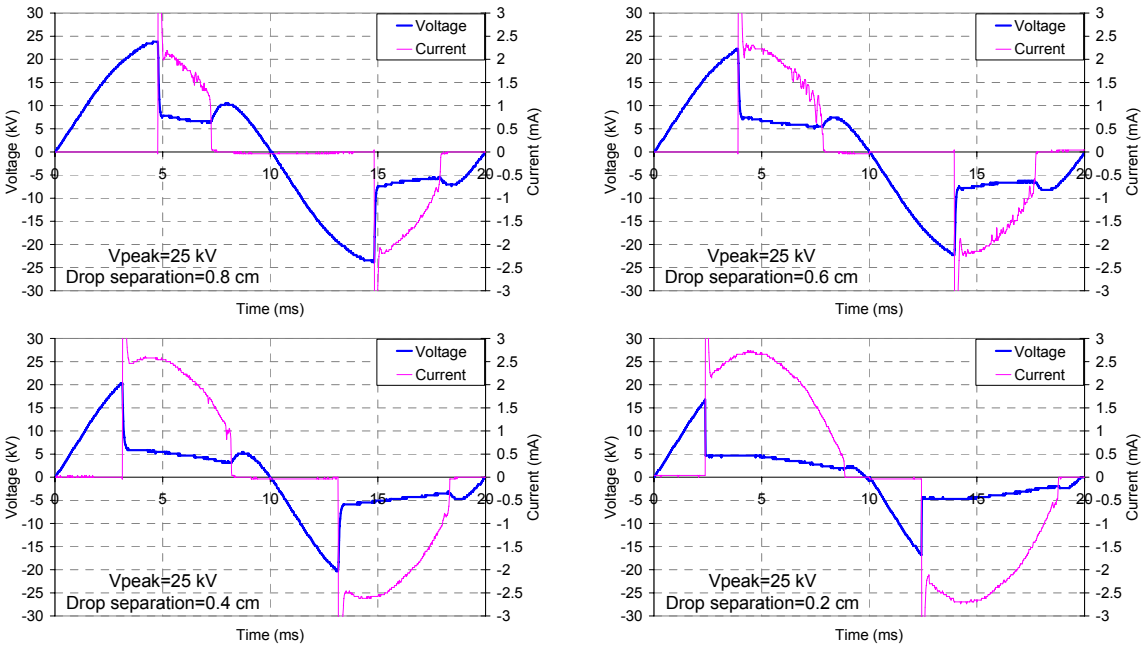

a) Reduction in droplet separation from 0.8 cm to 0.2 cm for a 25 kV peak supply voltage

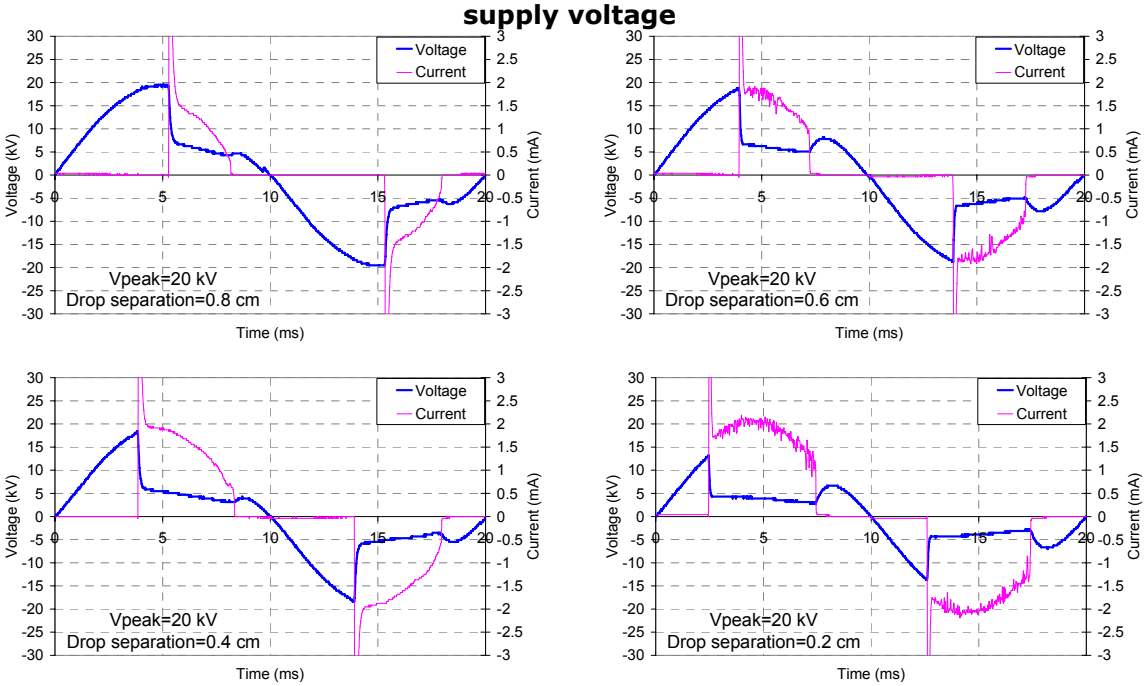

b) Reduction in droplet separation from 0.8 cm to 0.2 cm for a 20 kV peak supply voltage

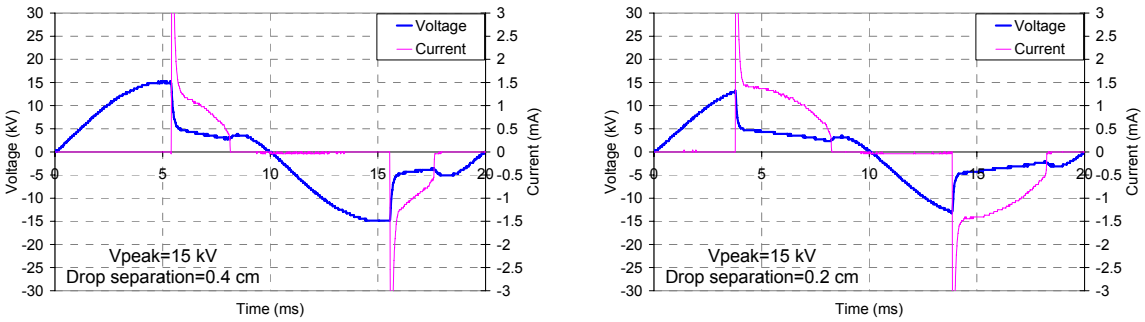

c) Reduction in droplet separation from 0.4 cm to 0.2 cm for a 15 kV peak supply voltage

Figure 5-32: Voltage and current traces with the reduction of initial distance between water drops under the different voltage levels

5.3.5 Results Analysis

5.3.5.1 Breakdown Voltage

Similar to the process for dry-band arcs from experimental part 5.1 and part 5.2, the breakdown voltage for stable arcs between water drops is identified as the minimum sufficient instantaneous voltage for the air gap penetration. Figure 5-33 shows the breakdown voltage changes with drop separation for the voltage levels from 10 kV to 25 kV. Results for all the voltage levels show that when the distance between water drops reduces, a lower breakdown voltage is required to ignite an arc. However, the breakdown voltage between water drops in this test also changes with the supply voltage magnitude: as the supply voltage level increases, the instantaneous breakdown voltage for the same gap distance rises as well. With metallic electrodes we would expect that breakdown voltage is only dependent on the electrode separation. This observation is due to water droplet distortion under the high electrical field when a voltage with the level of several kV is applied. The droplet distortion reduces the true inter-droplet gap distance for every power cycle during the testing. Higher source voltages have the more rapid rate of change of applied voltage, therefore allows higher instantaneous pre-breakdown values before the droplet gap reduces enough through

distortion to allow breakdown. This situation is different from the dry-band arc on a surface where water droplet distortion is much less likely to change the gap length (although this may happen in some circumstances).

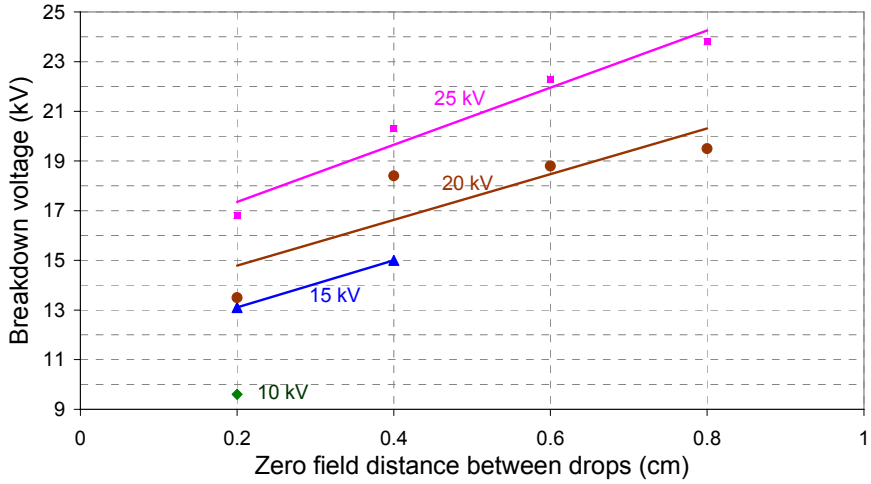

Figure 5-33: Breakdown voltage for stable arcs with supply voltage levels of 10 kV, 15 kV, 20 kV and 25 kV

5.3.5.2 ARC CURRENT PEAK

Figure 5-34 shows the peak arc current with different drop separation at the respective four voltage levels. The results demonstrate that the arc current increases corresponding to the reduction of physical distance between two water droplets. This is because the shorter air gap presents a shorter arc with lower impedance. This, in turn, allows higher arcing current to pass through.

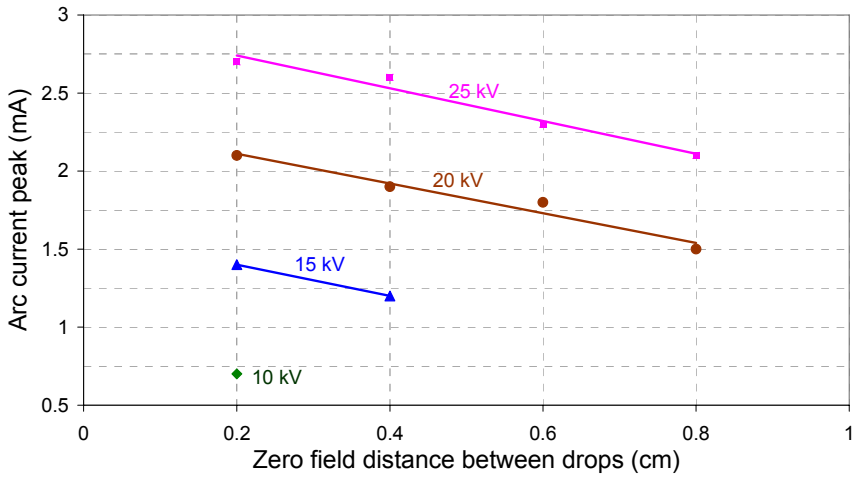

Figure 5-34: The change of arc current peak corresponding to variable distances under the different voltage levels of 10 kV, 15 kV, 20 kV and 25 kV

5.3.5.3 ARCING PERIOD

For dry-band arcs from part 5.1 and part 5.2, the arcing period is defined as the period from arc ignition to extinction in each half-cycle, with longer arc periods seen for lower drop separation as shown in Figure 5-35. The main parameter dominating the arcing period is arc ignition time, since the time for arc extinction is relatively constant as observed in Figure 5-32. The reduction of air gap between droplets decreases the breakdown voltage, which resultantly brings forward the arc ignition time, and ultimately extends the arcing period.

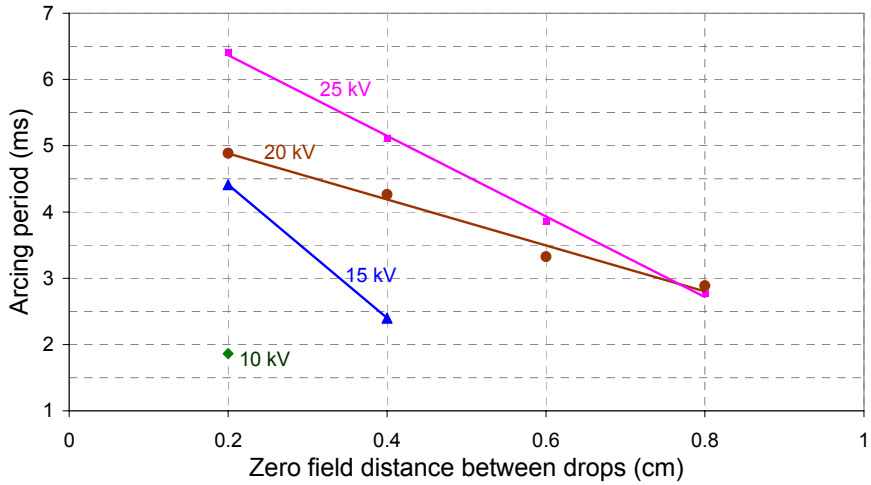

Figure 5-35: The change of arcing period corresponding to variable distances under the different voltage levels of 10 kV, 15 kV, 20 kV and 25 kV

5.3.5.4 ARCING ENERGY

The arcing energy calculation method is the same as in Figure 5-27 and Equation 5-6. The energy per cycle based on the measurement data is summarized in Figure 5-36. Under each voltage level, the arcing energy shows an increase trend with the reduction in drop separation. The results indicate that when the arc is reduced in length, the arcing energy could rise leading to more heat generation and transfer to the surrounding area.

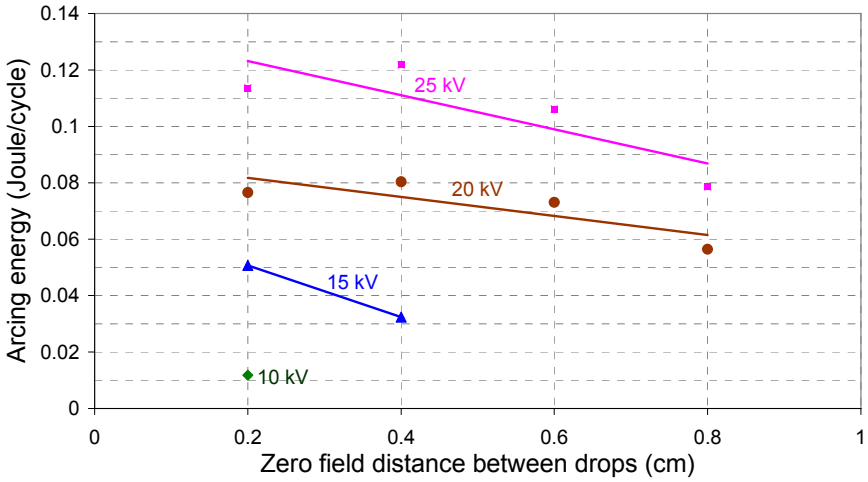

Figure 5-36: The change of arcing period corresponding to variable distances under the different voltage levels of 10 kV, 15 kV, 20 kV and 25 kV

5.3.5.5 ENERGY DENSITY

In order to calculate the energy density for arcs between water drops, an assumption is made to consider an arc as a cylinder with a concentrated source of energy at its geometrical centre as shown in Figure 5-37. The energy flowing through cylinder's curved surface is of most concern when considering energy transfer to an insulator surface. As a result, the energy density (energy distribution per unit surface area) is given by Equation 5-8,

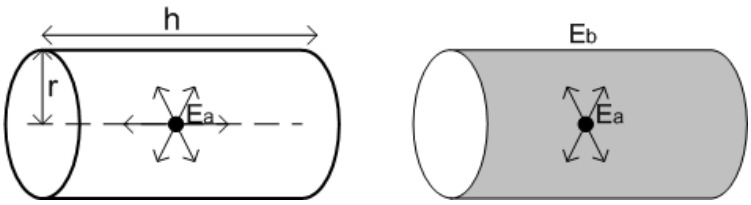

Figure 5-37: Cylinder model for calculation of arc energy density

$$D_b = \frac{E_b}{A_b} = \frac{E_a \dfrac{h/2}{\sqrt{r^2 + \left(\dfrac{h}{2}\right)^2}}}{2\pi r h} \qquad 5\text{-}8$$

Where: D_b is the energy density impinging on the curved cylinder surface A_b, E_b is the energy flowing through A_b, and E_a is the total arc energy. The cylinder length h is approximately the same as the distance between water drops in their static state, and the cylinder radius r is somewhat arbitrarily assumed to be 0.1 cm. For the general case of h>>r, $D_b=E_a/(2\pi rh)$.

The result of the calculation in Figure 5-38 shows the energy density increases by more than a factor of 4 for all cases from 15 kV to 25 kV in the test. This is due to the rise of energy analyzed previously and the further shrinkage in arcing area due to the arc length compression.

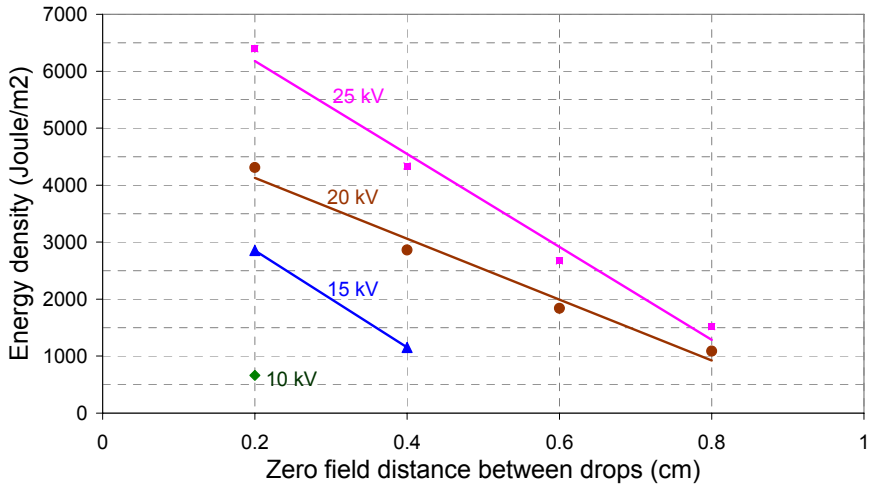

Figure 5-38: The change of arcing period corresponding to variable distances under the different voltage levels of 10 kV, 15 kV, 20 kV and 25 kV

This behaviour is very similar to that calculated and shown in Figure 5-29 for dry-band arcs. Although it should be noticed that Figure 5-29 shows energy per unit area of dry rod, whereas Figure 5-38 shows energy per unit area of arc surface. Essentially both are changed because of variation per unit length. The more linear behaviour seen in water-droplets may be due to effect of droplet distortion.

5.4 TESTS WITH ARTIFICIAL WIND AND RAIN

5.4.1 INTRODUCTION

In outdoor situations, insulators may be exposed to a number of environmental factors such as wind and rain. The electrical discharges on the insulator surface may be influenced by these factors. The interactions between electrical activities and environmental conditions may accelerate ageing of insulators, and therefore, need to be further investigated. In particular we aim to investigate whether wind can act to compress dry-band arcs in the way gravity has been shown to on inclined rod samples (section 5.2). This section describes experimental studies of the arcing phenomenon on insulation surfaces investigating the effect of rain and wind combinations. The experimental outcome contributes to a theory that the involvement of environmental factors could make the electrical discharges more aggressive to faster damage of the insulation surface.

5.4.2 WIND TEST ARRANGEMENT

Figure 5-39 shows the test arrangement for artificial Tests with Artificial Wind and Rain. The electrical test circuit comprises of a power transformer with variable output of 0 to 42 kV (peak) single phase a.c. voltage. The test sample is connected with the voltage source via a current limit resistor, while the other end is grounded. The resistor limits the leakage current flowing on the sample surface to 0.5-10 mA, in order to obtain a range of electrical activity types from unstable discharges to stable dry-band arcs.

The data acquisition system includes a voltage divider with the ratio of 1:10,000 to obtain the arcing voltage, and a 2000 Ω resistor to measure

the arc current. The voltage and current signals are recorded by Labview, and further analyzed using Matlab programming.

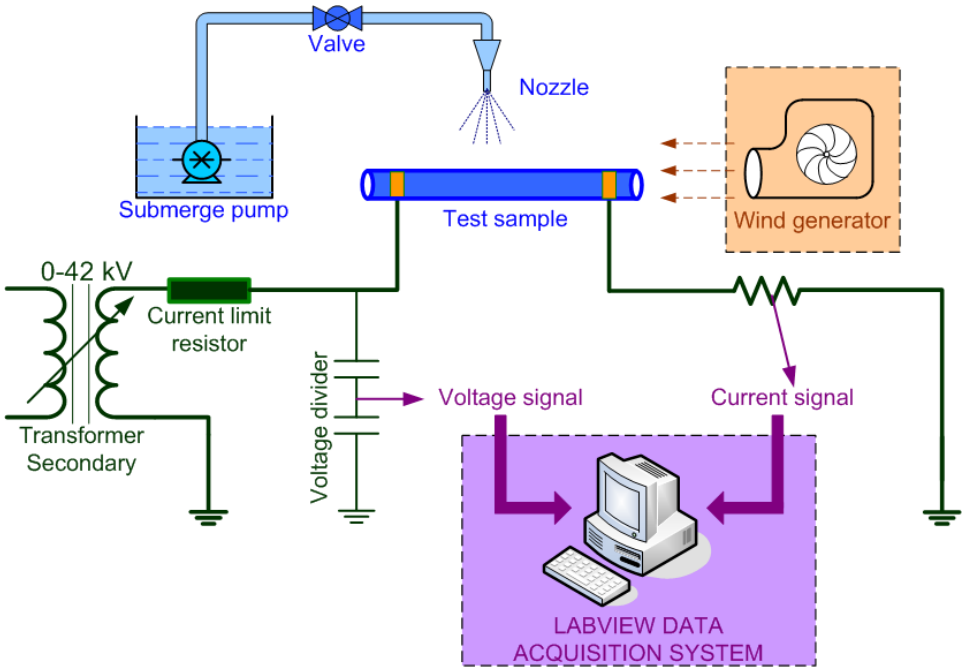

Figure 5-39: Test arrangement of Tests with Artificial Wind and Rain

The wind generator is able to produce the wind from different directions with variable output speed from 1 mph to 25 mph (miles per hour), which is equivalent to 0.45 to 11.18 m/s (meter per second). During the test, the wind speed is controlled by adjusting the wind generator input voltage, and the actual speed the sample sees is measured by a wind meter. As the sample is limited to 20 cm in length and close to the wind source, the wind speed has no significant change across the sample length, and can be considered as uniform. The spray system is introduced to create rain conditions on the sample surface. A water tank and submerged pump are used with controllable flow rate governed by valve. Two types of sprays are established from this system as strong and weak spray. The strong spray is quantified with the precipitation rate of 2.0 g/cm^2/hr (19.81 mm/hr) representing the moderate rain condition, and the weak spray is made with the precipitation rate of 0.12 g/cm^2/hr (1.14 mm/hr) representing the light rain condition. The spray uniformly falls into an area of approximate 1X1 m^2. Compared to the

size of sample rod with 22 mm diameter and 20 cm length, the spray is still capable to cover the full sample area even with the maximum wind injection.

5.4.3 TEST PROCEDURE

The test is designed to investigate two kinds of electrical discharge phenomenon which could be influenced by wind and rain conditions. The first scenario is based on the low current (less than 1 mA) unstable discharges (as shown in Figure 5-31 b); attempting to determine if the unstable discharges could become stable through the effects of wind and rain. The second scenario is based on the stable arcs with sufficient current (5-10 mA) as shown in Figure 5-31 c), to study whether the wind and rain could result in the arc compression situations. Therefore, two test procedures were established:

5.4.3.1 INVESTIGATION OF UNSTABLE DISCHARGES TO STABLE ARC TRANSITION

I. The transformer output voltage was fixed to 7.07 kV (rms) throughout the test. The current limiting resistor was chosen as 8 MΩ.

II. Both 'weak' and 'strong' sprays were used in tests for comparison. As quantified previously, weak spray with the precipitation rate of 0.12 $g/cm^2/hr$; while the strong spray with the precipitation rate of 2.0 $g/cm^2/hr$.

III. The test started with the sample having a dry surface when the voltage supply was energized. Immediately afterwards the spray system was switched on to wet the sample. At the same time, the wind generator was plugged into system with variable wind output specified for each test.

V. The current and voltage waveforms were recorded against time at a sample rate of 40 kHz/s. The test data were imported to Excel to further analyze the discharge shape profile. Programming in Matlab was used to calculate the discharge energy per cycle during the whole test period.

5.4.3.2 STABLE ARC TO ARC COMPRESSION TRANSITION

I. The transformer output voltage was respectively fixed to 20 kV, 15 kV, or 10 kV (peak) in each test, with current limiting resistor of 2 MΩ, corresponding to arcing currents of 10 mA, 7.5 mA and 5 mA (peak).

II. Both 'weak' and 'strong' spray were used in tests.

III. The test supply was switched on with the spray system. Typically after 30 minutes a stable dry-band arc developed with relatively constant arc length and repeatable arcing current and voltage traces for each power cycle.

IV. Once a stable dry-band arc was formed, the wind generator was switched on starting with low wind speed of 5 mph (2.24 m/s). The dry-band arc length was reduced in length by the wind blowing one water layer closer to the other. As a new balance was achieved, the arc length became constant again but shorter than previous case. Afterward, the wind speed is increased resulting in a further reduced arc length. The wind speed is continuously stepped up to a value which resulted in arc extinction. The maximum wind speed to extinguish an arc depended on the different environmental conditions and will be discussed later. During this compression process, the current and voltage signals were recorded against time by the Labview data acquisition system.

V. The test data are further analyzed in Excel and Matlab.

5.4.4 TEST RESULTS

5.4.4.1 UNSTABLE DISCHARGES BECOME STABLE AS A RESULT OF WIND

It is not simple to set up the unstable discharges under the spray conditions, and not every experiment could establish repeatable unstable discharges, as the falling water could occasionally and randomly interrupt the discharges within a dry-band area. Besides, the unstable discharges under the 1 mA peak discharge current are relatively weak comparing to the higher current stable dry-band arcs, so that can be destroyed by continuously water deposition from spray systems. Therefore, a fine and light spray should be chosen for this test situation, with the specified precipitation rate as described in test process 5.4.3.1, which is about 10 times stronger than a fog environment used in experimental sections 5.1 and 5.2.

The typical test results from test procedure 5.4.3.1 are shown in Figure 5-40. Four stages are identified as initial unstable discharges, unstable discharges reduction, stable arc appearance and stable arcs domination:

In the first stage, the voltage is sufficient to break the air gap between two water layers on the sample surface, but insufficient energy (represent by current) is available to sustain the discharges. Therefore, many current and voltage oscillations are observed throughout every power cycle.

In the second stage, as a result of wind injection (in the range of 5-20 mph), one water layer is moved towards the other, which reduced the separation between discharge water anode and water cathode, and in turn, decreased the arc length and reduced the breakdown voltage. Therefore, the oscillation reduces in frequency. This compression

process is normally against the high voltage electrode at the high voltage end as in Figure 5-40.

In the third stage, the air gap keeps reducing in length as a result of the wind. The current oscillation is being gradually taken over by the continuous current wave which significantly increases the discharge energy. At the moment when the discharge energy is sufficient to sustain an arc, the stable arc is seen. However, the initial stable arcs are still accompanied by some unstable current, till the arcs finally stabilized in stage four.

In the fourth stage, the stable arcs become dominant, achieving the transformation from unstable discharges to stable arcs as a result of wind.

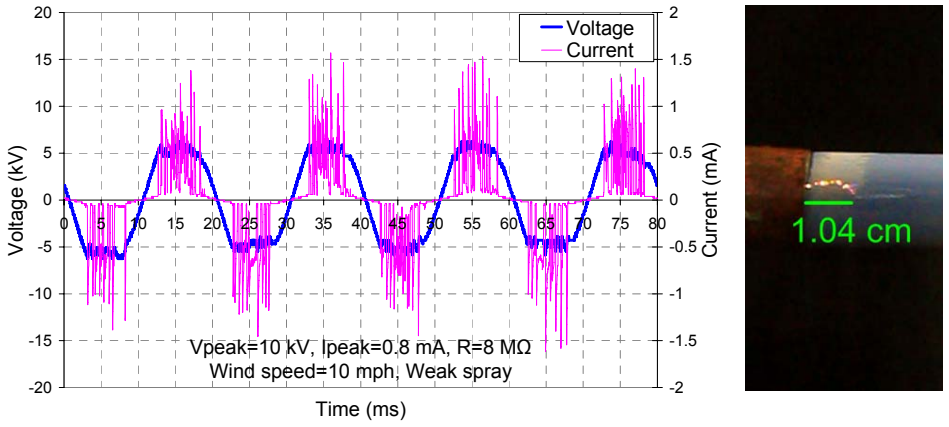

Stage 1: Initial unstable discharges

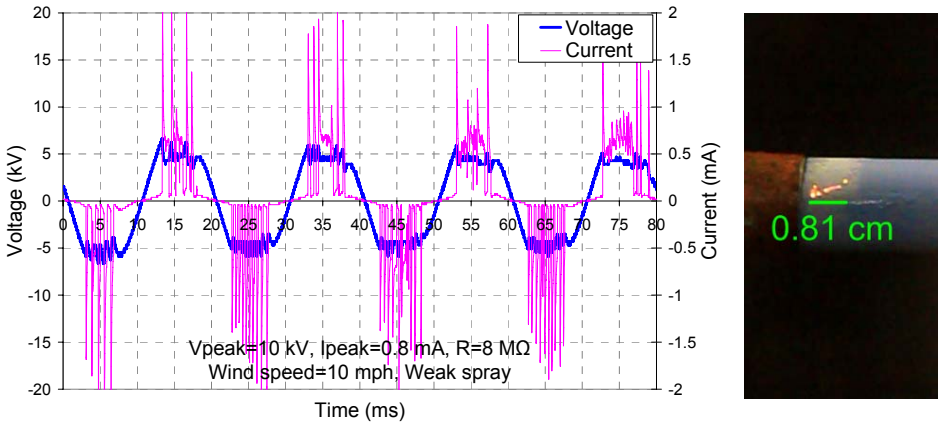

Stage 2: Reduced instability and oscillation frequency after 2.5 s

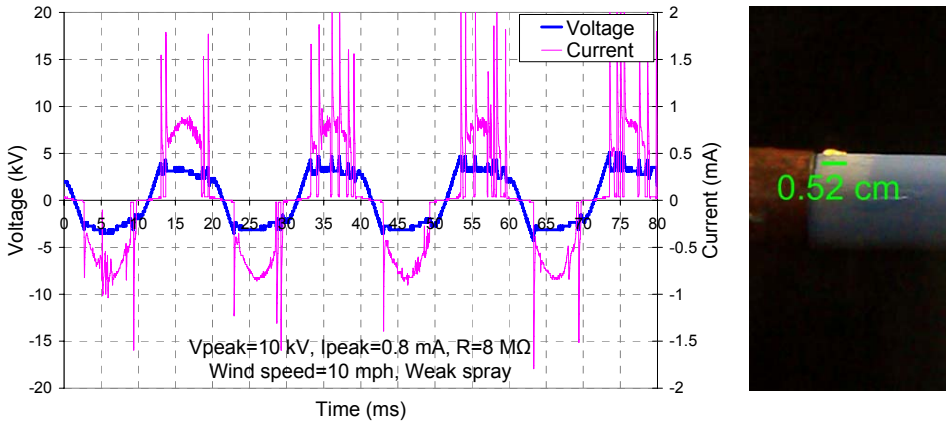

Stage 3: Stable arcs appear but accompany with some instability after 7 s

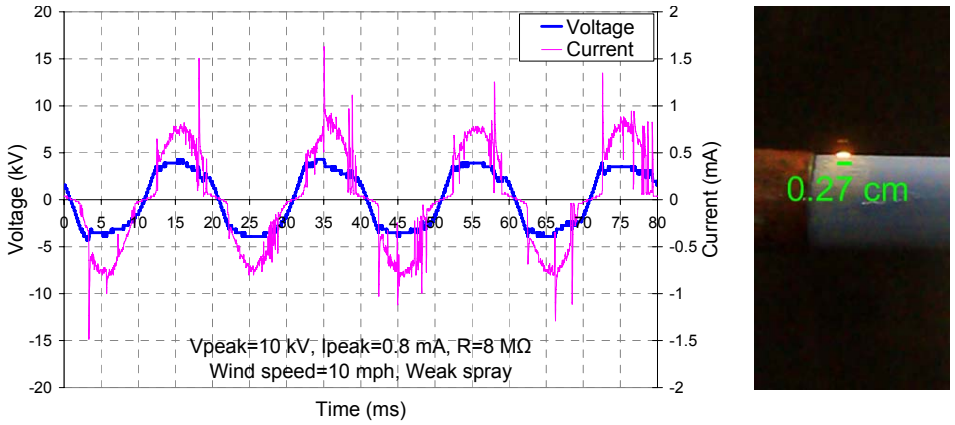

Stage 4: Stable arcs finally dominate after 8.5 s

Figure 5-40: Unstable discharges become stable after wind injection (Left figure shows electrical properties of discharge) (Right image shows the discharge physical length)

5.4.4.2 Stable Arc to Arc Compression by Wind Effect

Figure 5-41 shows an example result of arc compression by wind at 20 kV. The arc length freely grows to maximum of 3.72 cm, and remains stable under the weak rain conditions without wind. After the wind injection of 13 mph (5.85 m/s), the equilibrium arc length is reduced to 2.37 cm after 30 minutes, and keeps fairly constant as a new balance achieved between the arc expansion, rain deposition and wind injection. When the wind is further enhanced to 17 mph (7.65 m/s) and the equilibrium arc length is compressed and fixed to approximate 1.09 cm after another 30 minutes. The deepest compression occurs with wind speed of 23 mph (10.35 m/s) corresponding to extremely short arc

length of 0.32 cm, and the arc will be extinguished if any additional wind increase is applied. Tests with Artificial Wind and Rains at different voltage levels of 15 kV and 10 kV show the similar phenomenon of arc compression. During these tests the arc's physical compression in length is caused by wind effect rather than gravity as reported in the Testing with Inclined Samples (part 5.2). The result shows that both wind and gravity could equally lead to dry-band arcing compression.

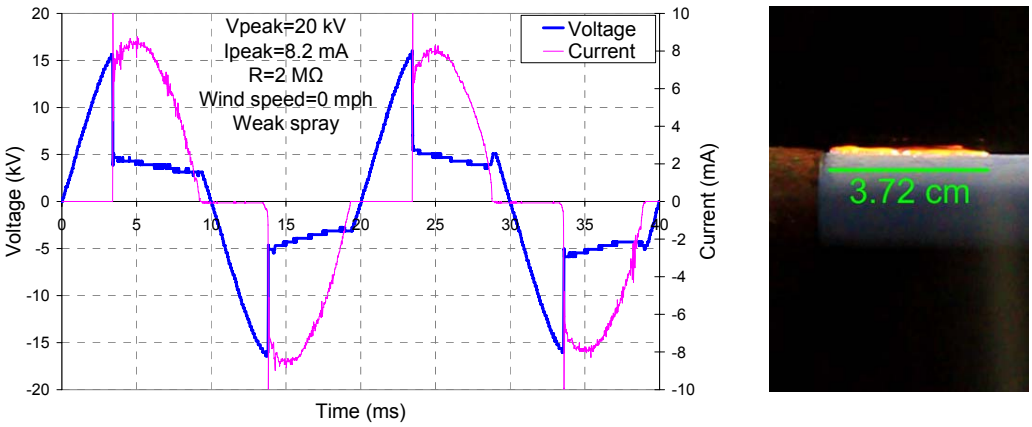

a) Free growth arc with 0 mph wind injection

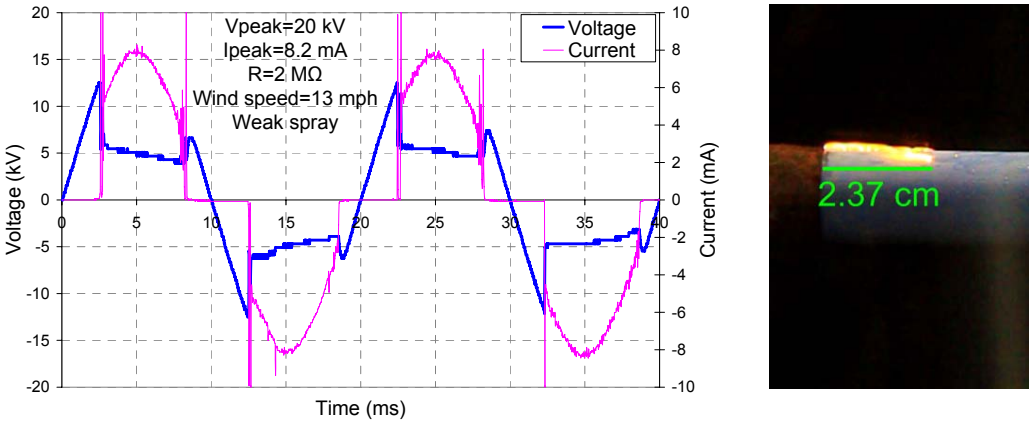

b) Arc is lightly compressed with 13 mph (5.85 m/s) wind injection

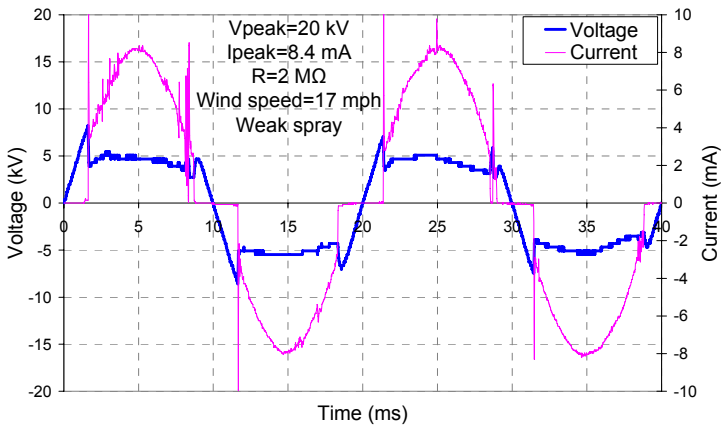

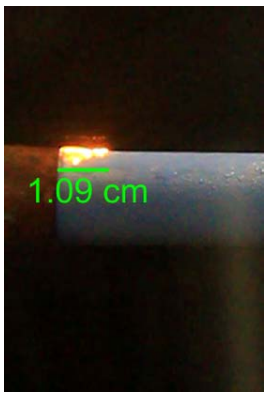

c) Arc is continuously compressed with 17 mph (7.65 m/s) wind injection

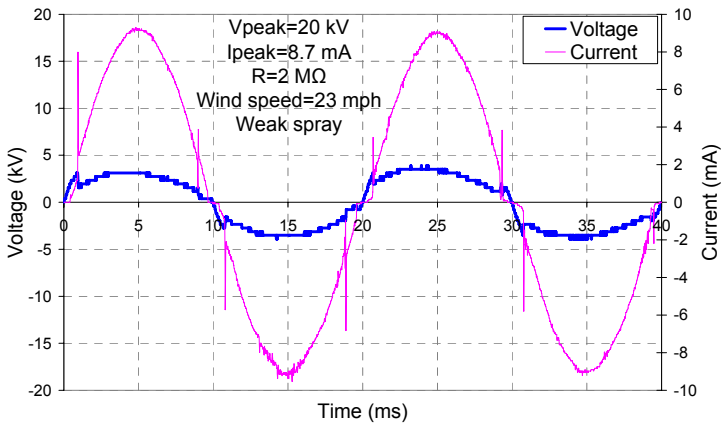

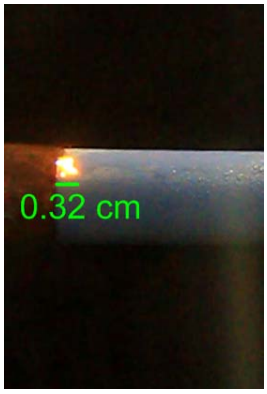

d) Arc is heavily compressed with 23 mph (10.35 m/s) wind injection (about to extinction)

Figure 5-41: Arc compression in 20 kV (peak) at different wind levels (Left figure shows electrical properties of arc) (Right image shows the arc physical length)

5.4.5 Results Analysis

5.4.5.1 Energy Trend from Unstable Discharge to Stable Arc

The change of arc energy as an unstable discharge becomes stable is analyzed based on the experimental data for every power cycle after the wind injection. Data are imported into Matlab and calculated by the program given in [Appendix 1.1]. An example of arc energy change against time from unstable to stable status is shown in Figure 5-42. Two zones are identified as the unstable discharge zone and the stable arc zone, where arc energy dramatically increases from one zone to the

other. The threshold energy between them is 0.01 Joule per cycle in this case. The result shows that the stable arcs develop higher energy than unstable discharges. Therefore, a significant conclusion has been discovered that by the wind and rain effect, the unstable discharges can be transformed to stable arcs with increase in energy, which may lead to more threat to insulation material surface.

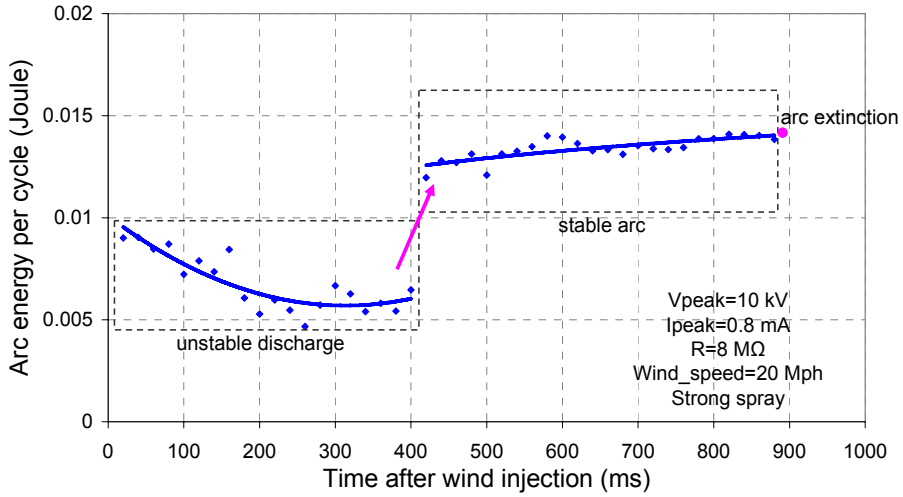

Figure 5-42: Energy change from unstable discharges to stable arcs under the 20 mph wind and strong spray conditions

Figure 5-43 shows another example of the arc energy transition from unstable discharges to stable arcs under different environmental conditions. In the situation of low wind and weak rain, it takes longer for discharges to transform from unstable to stable status, due to less water deposition and weaker wind moving the water layer in order to reduce the air gap. However, no major difference is observed on energy range of unstable discharge zone (from 0.005 to 0.01 Joule) and stable arc zone (from 0.01 to 0.015 Joule) between two cases. The detailed relationship of transformation time from unstable discharges to stable arcs under the variable environmental factors will be discussed later in this chapter.

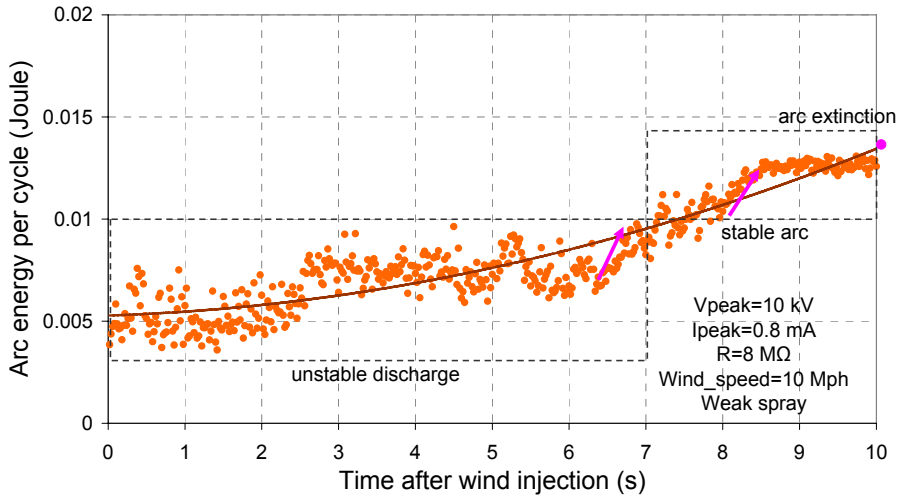

Figure 5-43: Energy trend from unstable discharges to stable arcs under the 10 mph wind and weak spray conditions

5.4.5.2 Energy Trend from Stable Arc to Arc Compression

Experiment results in 5.4.4.2 and Figure 5-41 a) to d) shows that a stable arc can be compressed in physical length by the wind. From the energy point of view, the compressed arc could have higher energy than stable arc as discussed in the previous chapter. The energy calculation based on the wind test data shows the similar increase of energy corresponding to the arc compression. Figure 5-44 gives an example of arc energy trend under the arc compression with wind injection for three times specified as 'wind 1', 'wind 2' and 'wind 3' under the same experimental conditions for a reproducibility study. Without the wind, the arc is free growth from minimum to full length of 3.7 cm, holding the fairly constant arc energy throughout. After the wind injection, all three tests showed that the arc energy tends to increase. This energy increase may bring extra heating to the material surface, which may bring more damage to material surface than normal arcing situations. A comparison test is conducted to apply the wind blowing perpendicular to the direction of water movement forming the arc compression. The result shows the energy trend which is fairly flat, as the wind does not contribute to the arc compression for this case.

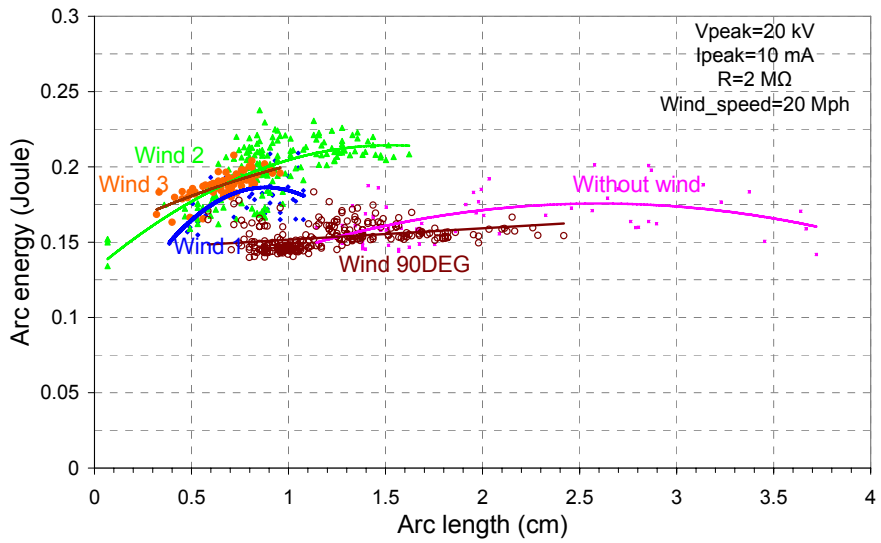

Figure 5-44: Energy trend from free-growth of an arc to arc compression with reduction in arc length

5.4.5.3 Effect on Arcing Activities of Different Wind and Rain Intensity

Figure 5-42 and Figure 5-43 suggest the different wind and spray injection conditions mainly affect the transformation period from the unstable discharges to stable arcs. The shorter period over which the transformation process takes, the more rapid increase of arc energy would be observed. Table 5-2 shows the transformation period under four kinds of spray and wind combinations: The strong spray with 20 mph (9 m/s) wind gives the shortest transformation time from unstable discharges to stable arc, while weak spray with 5 mph (2.25 m/s) wind produces the longest transformation time. From the transient energy analysis, this phenomenon indicates that the more severe environmental conditions, the quicker the discharge becomes stable, in turn with more accelerated rate of energy increase on material surface. However, the arc also extinguishes quicker as the impact of adverse conditions for arc survival. In practical outdoor conditions, the environmental will continually vary, the strong wind and heavy rain situation may have a higher possibility to transform the discharges from unstable to stable status, as a relatively shorter transformation period is required. However, from the energy accumulation point of view, the mild

conditions such as slow wind and weak spray might not be able to quickly and efficiently achieve the change from unstable to stable, but could sustain the stable arcs much longer than severe conditions (tens of seconds), which may accumulate more energy on the material surface.

Table 5-2: The transformation period from unstable discharges to stable arcs under different wind and rain situations

Spray / Wind / Period	Strong	Weak
20 mph (8.94 m/s)	0.88 s	3.1 s
15 mph (6.71 m/s)	1.5 s	12 s
10 mph (4.47 m/s)	1.6 s	20 s
5 mph (2.24 m/s)	1.8 s	100 s

(Source voltage=10 kV, current limit resistor=8MΩ)

The arc length during the compression process is also affected by the wind and spray levels. Figure 5-45 provides two examples of arc length changing as a result of wind under different spray levels. For each wind speed, the arc length reaches equilibrium (fixed to sustain for a period) and calculated from the average value of measured maximum arc length for 10 consecutive power cycles. The arc compression in the light rain condition starts from 10 mph (4.47 m/s) wind. Following the increase of wind strength, the arc keeps reducing in length until extinguished by the wind injection in excess of to 23 mph (10.35 m/s). Compared to the light rain situation, the heavy rain can achieve a new balance between the arc expansion by thermal heating and arc extinction by the rain effect at higher precipitation rate. Therefore, the initial no wind arc length is reduced to 2.2 cm from 3.7 cm due to the heavier water film deposition. The heavy rain also brings forward the arc compression starting wind speed to 6 mph (2.7 m/s). This may be due to the thicker water film and larger droplets which could be relatively easily moved by the wind on the sample surface. The same reason is likely to be behind the reduced threshold of wind speed (18 mph, 8.1 m/s) to extinguish the arc. The results show that the heavy rain situation would make the

arc compression by wind more likely, but more vulnerable to extinction if the wind is too strong.

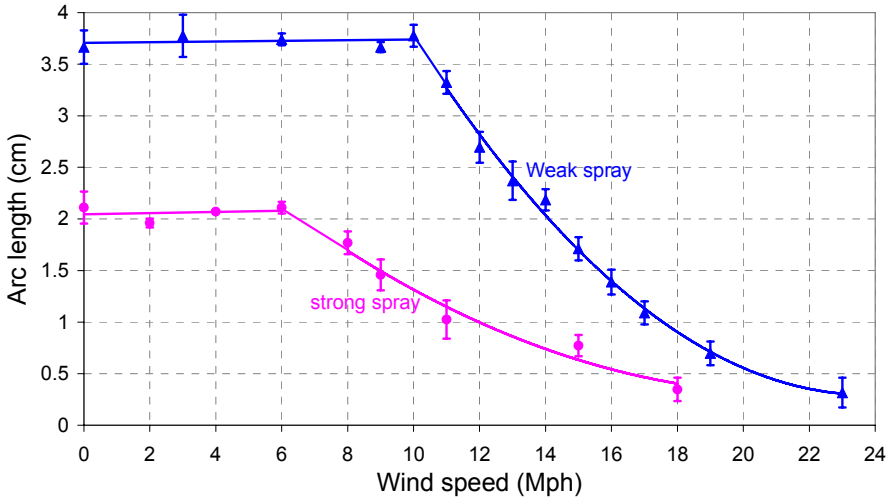

Figure 5-45: An example of arc compression under different wind and rain situations (20 kV, 10 mA arc)

5.4.5.4 Energy Density from Unstable Discharges to Stable Arcs

Energy density is calculated from the arc energy and discharge physical length. Figure 5-46 a) and b) give the energy density for two different wind and spray combinations. Both results show that when the unstable discharges transform to stable arcs, there is an increase in energy density. The ultimate peak energy density for stable arcs could be 8~9 times higher than the initial unstable situations. The analysis indicates that under the wind and rain conditions, the phenomenon of unstable discharges becoming stable arcs could sharply enhance the energy density on the material surface, which may lead to faster ageing than normal mild environmental situations. The more severe weather conditions, the quicker the energy density rises.

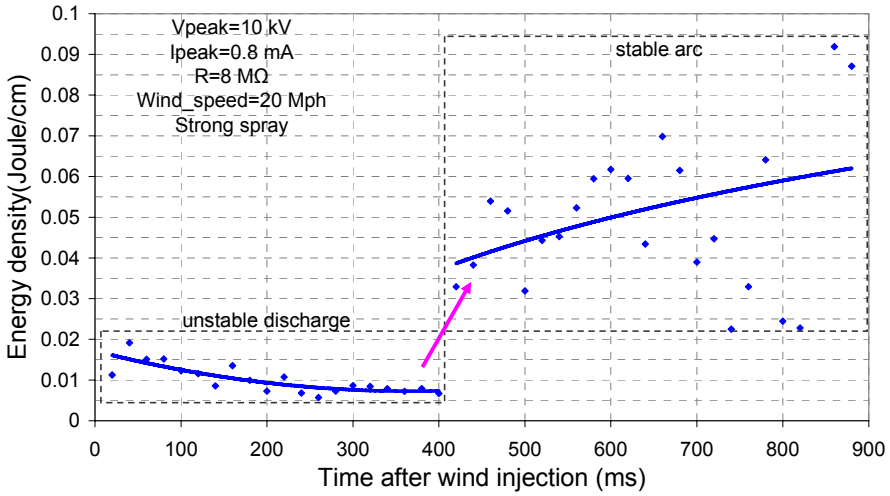

a) Under the 20 mph wind and strong spray conditions

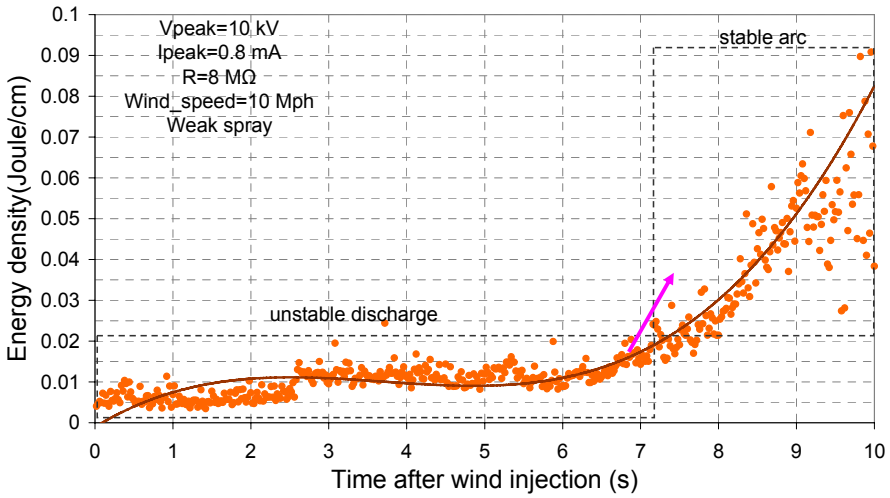

b) Under the 10 mph wind and weak spray conditions

Figure 5-46: The trend of energy density from unstable discharges to stable arcs

5.4.5.5 Energy Density against Arc Length During the Arc Compression

Figure 5-47 shows the change of energy density per cycle corresponding to the different arc lengths caused by arc compression. Wind 1, 2, and 3 represent the same speed of wind (20 mph) injection for three times to show the repeatability. Figure 5-47 a) demonstrates the trend of energy density during the 20 kV, 10 mA arc compression. The normal free-growth arc without wind injection shows a slightly increase in arc energy density against arc length from 3.7 cm to 2.0 cm. After the wind injection, the arc is physically compressed in length with significant

increase in energy density up to 10 times higher than normal free-growth arcs. The result b), which is at 15 kV, 7mA, arc compression from 1.8 cm to 0.2 cm, shows a sharper increase in energy density than result a) due to the low voltage weaker arcing activity which is more easily being compressed by rain and wind injection. In each experiment here, the arc extinction finally occurs in a few seconds after the 20 mph wind injection. However, both results indicate that the phenomenon of arc compression by wind could dramatically increase the energy density of arc in order of 10 times in wind and rain conditions, which could significantly threaten the insulation material surface due to a possibility of the surge increase in joule heating effects.

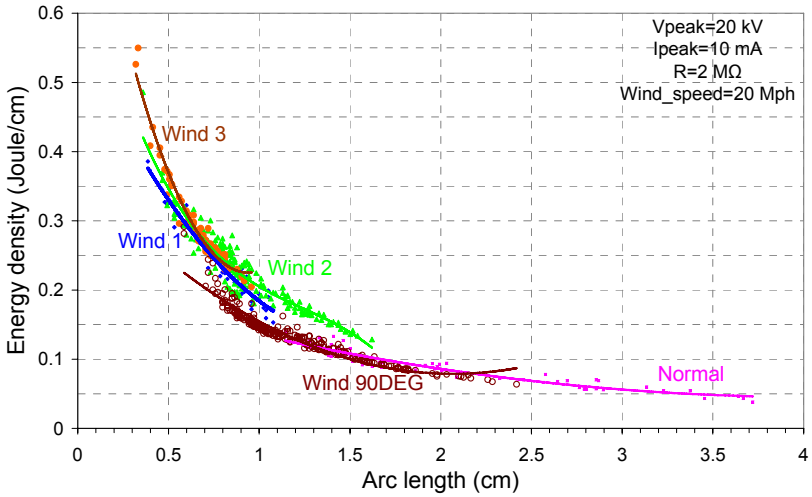

a) In the case of 20 kV 10 mA arc

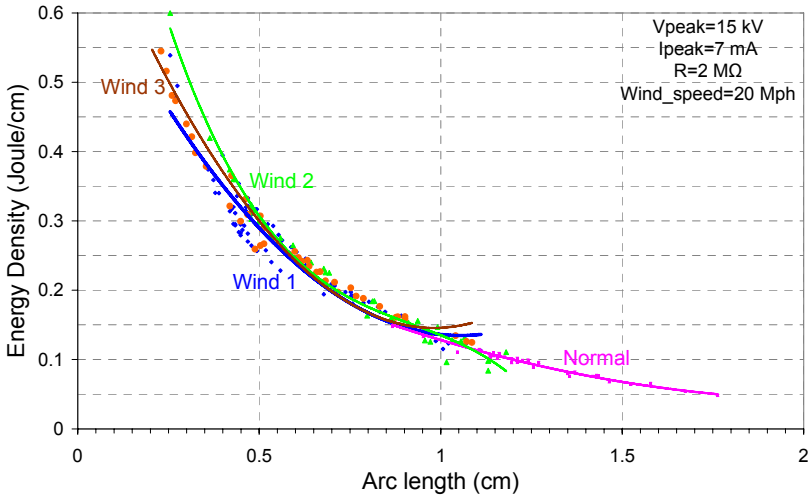

b) In the case of 15 kV 7 mA arc

Figure 5-47: The trend of energy density from free arc to arc compression with arc length

5.5 SUMMARY

The *Testing in a Fog Environment* has been conducted for the dry-band arc formation and growth. Clean fog has been used for arc growth test, and results show that during the wetting process, the property of sample surface changes from capacitive when the surface is completely dry to resistive when the surface becomes wet. The leakage current increases from zero to several mAs by the fog deposition, and a single stable arc has been finally observed after an equilibrium is achieved between dry-band arc expansion by leakage current heating and reduction by fog precipitation. An arc growth test has been conducted in a highly conductive fog environment. Test results show that with the increase of voltage and current levels of dry-band arcing, the corresponding arc physical length has been expanded, together with the increased breakdown voltage across the dry-band gap. The arcing period and minimum instantaneous arc resistance roughly remains unchanged during the arcing current increase, with the minimum instantaneous arc resistivity reducing following the arc length expansion. The dry-band arc in both clean-fog and salt-fog environments have been compared, and due to the conductivity of water layer, the salt-fog environment is able to create more severe arcing activities and allows more accurate measurement in arcing voltage, and therefore, was used as the testing environment for further *Testing with Inclined Samples*.

The Testing with Inclined Samples has been conducted in the salt-fog environment, to investigate the dry-band arcing on rod geometries, and has shown that stable arcs can be compressed in length by changing the angle of the rod to create an inclined surface. Such arcs remain stable and have been reduced in length by over 50%. As the dry-band and its associated arc are reduced in length the duration of the arcing period in each half cycle increases, as the breakdown voltage of the dry-band is reduced. The minimum resistance of the arc is also reduced with the arc

length leading to higher peak current as the arc length is diminished. However the arc minimum resistivity remains approximately unchanged. The prolonged arcing period and increased peak current lead to higher arc energy, and in particular higher energy density in per unit area of dry-band. The dry-band arc compression processes in different current and voltage levels have been repeated, and in all the cases studied here the arc energy density have increased by a factor of 10 as a result of arc compression in its length.

The *Tests between Water Drops* have been conducted to investigate low current arcing behaviours which were limited to a few mAs between water drops at varying separations. The tests have created the unstable discharges between water drops as the breakdown voltage reached the threshold for arc ignition but insufficient current (arc energy) to sustain such arc. For the test results of stable arcs, the dynamic behaviour of the drops in electric fields has a significant influence on the arc properties. For this reason the instantaneous breakdown voltage between droplets depends upon the applied source voltage. This factor will depend upon the droplet hydrostatics especially in this test, and may not occur for droplets on surfaces or other geometries with less mobility. Shorter arcs have increased arc current, duration, arcing energy and energy density. Reducing the drop gap from 0.8 mm to 0.2 mm increases the energy density in the arc by more than a factor of 4. This confirms the supposition that shorter arcs may age materials' surfaces faster than longer ones.

The *Tests with Artificial Wind and Rain* have been conducted to investigate the phenomenon of unstable discharges becoming stable arcs and further the process of stable arc compression as a result of external environmental sources. Rain was used to create moisture on the sample surface to allow low current discharges formation, while wind was used as the additional source to affect the discharge behaviour. The

results show that by keeping the source voltage unchanged, the low current (less than 1 mA) unstable discharges with high frequency oscillations could transform to stable arcs in certain wind speed from 5 mph (2.24 m/s) to 20 mph (8.94 m/s) and rain precipitation rate from 0.12 g/cm^2/h to 2.0 g/cm^2/h conditions. This transformation time could be accelerated by more severe environmental conditions such as strong winds and heavy rain. Energy analysis indicates that the unstable discharge energy per power cycle rises approximately 3 times in the stable state, with the correlated energy density increases up to 10 times during this process. The arc compression situations could be also achieved by wind driven moisture movement effect, with stronger wind speed corresponding to shorter equilibrium arc lengths. The heavy rain situation made the arc compression more likely. Both energy and energy density increases respectively by 2 times and 6 times during the arc compression process. This compression phenomenon is similar to that observed in the *Testing with Inclined Samples* by gravity. It is proven that both wind and the inclined gravity effect could make dry-band arc compression possible, and these compressions lead to arc energy and energy density increases on the insulation surface.

CHAPTER 6

SIMULATIONS OF LOW CURRENT ARCS

6.1 MODELLING OF STABLE DRY-BAND ARCS

6.1.1 DOUBLE SINUSOIDAL MODEL

6.1.1.1 DOUBLE SINUSOIDAL MODEL FROM EXPERIMENT RESULTS

A 'Double Sinusoidal Model' has been developed to simulate and analyze the electrical characteristics of a dry-band arc. In this model, two sinusoidal waves are introduced to simulate the experimental output of the I-t and V-t curves in the time domain, following the modelling process described in Figure 6-1.

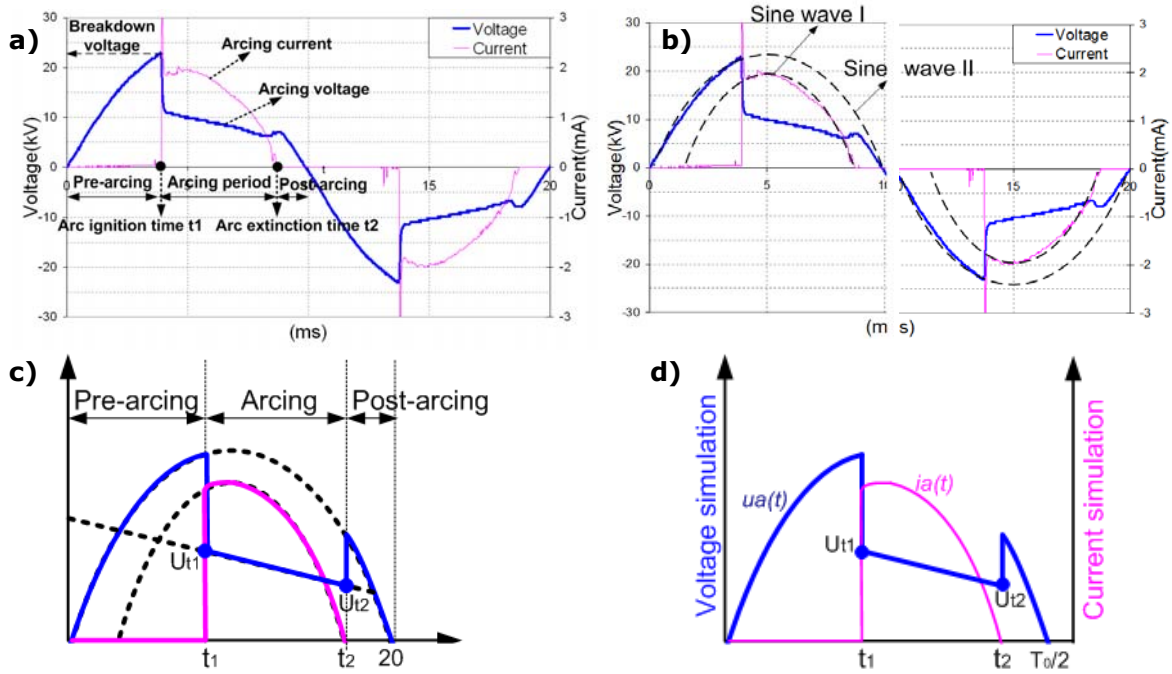

Figure 6-1: Double sinusoidal model based on the experimental I-t and V-t result

Figure 6-1 a) demonstrates the typical I-t (current) and V-t (voltage) curves of a dry-band arc from Testing with Inclined Samples with 10° slope angle as discussed in section 5.2 (and Figure 5-17). Based on this result, two sinusoidal waves with respective magnitude and angular frequency are chosen to fit the experimental results demonstrated in Figure 6-1 b). The following section 6.1.1.2 will explain how these two sinusoidal waves are fitted. The three different arcing periods which have been described as 'pre-arcing', 'arcing' and 'post-arcing' are used to distinguish the modelling approach in the time domain in Figure 6-1 c) as:

PRE-ARCING PERIOD ($0<t<t_1$)

The pre-arcing period starts from the beginning of a cycle (t=0) to the point where the arc ignites ($t=t_1$). In this period, the voltage trace increases from zero to a certain value (breakdown voltage) following the rise of source voltage, however, the current remains zero due to the high resistance of the dry-band dielectric surface. There is no arcing activity during this stage. The mathematic approach of modelling in pre-arcing period is described as:

$$\mathrm{i}_a(t) = 0 \qquad 6\text{-}1$$

$$\mathrm{u}_a(t) = \sqrt{2}U_a \sin \omega_u t \qquad 6\text{-}2$$

Where: $i_a(t)$ and $u_a(t)$ are simulated current (mA) and voltage (kV) traces in the pre-arcing period. U_a and ω_u are the rms value (kV) and angular frequency (rad/ms) of the voltage sinusoidal wave (Sine wave II).

ARCING PERIOD ($t_1<t<t_2$)

The arcing period sustains from arc ignition to arc extinction ($t_1<t<t_2$). The voltage initially reaches the breakdown voltage which allows arcing activity to start, then drops to a fairly constant value as 'arcing voltage'

throughout the whole arcing period. The current immediately increases from zero to peak which is a few miliamperes, then gradually reduces during the arcing period until it draws back to zero. The arcing voltage is determined by the arc resistance and the source impedance seen by the arc. The arc current is determined by the sum of these and the instantaneous applied voltage. The arcing period is described by:

$$\mathrm{i}_a(t) = \sqrt{2} I_a \sin \omega_i [t - (\frac{\pi}{\omega_u} - t_2)] \quad \text{6-3}$$

$$\mathrm{u}_a(t) = U_{t1} - \frac{U_{t1} - U_{t2}}{t_2 - t_1}(t - t_1) \quad \text{6-4}$$

Where: $i_a(t)$ and $u_a(t)$ are the simulated current (mA) and voltage (kV) traces in arcing period. I_a and ω_i are the rms value (mA) and angular frequency (rad/ms) of the current sinusoidal wave (Sine wave I). ω_u is angular frequency (rad/ms) of the voltage sinusoidal wave. t_1 is the arc ignition time (ms). t_2 is the arc extinction time (ms). U_{t1} is the arc ignition voltage (kV). U_{t2} is the arc extinction voltage (kV).

POST-ARCING PERIOD (t_2<t<T_0/2)

The post-arcing period is identified from arc extinction to the end of half cycle (t_1<t<10 ms). During this period, the voltage is always below the breakdown voltage, which is insufficient to strike an arc. Therefore, the current remains zero. In this stage, the dry-band area recovers its dielectric properties. The post-arcing period is described as:

$$\mathrm{i}_a(t) = 0 \quad \text{6-5}$$

$$\mathrm{u}_a(t) = \sqrt{2} U_a \sin \omega_u t \quad \text{6-6}$$

Where: $i_a(t)$ and $u_a(t)$ are the simulated current (mA) and voltage (kV) traces in post-arcing period. U_a and ω_u are the rms value (kV) and angular frequency (rad/ms) of the voltage sinusoidal wave (Sine wave

II). T_0 is the periodic time of the voltage sinusoidal wave. As to the UK power frequency of 50 Hz, T_0 is set to 20 ms.

The sign function (sgn) described in equation 6-7 is used to combine the equations from 6-1 to 6-6. After the combination, the modelling of I-t and V-t curves for the half cycle of dry-band arcing is obtained as:

$$\mathrm{sgn}(t)=\begin{cases}-1 & if\ t<0\\ 0 & if\ t=0\\ 1 & if\ t>0\end{cases} \qquad 6\text{-}7$$

$$\mathrm{i}_a(t)=\sqrt{2}I_a\sin\omega_i[t-(\frac{\pi}{\omega_u}-t_2)]\times\frac{1-sgn[(t-t_1)(t-t_2)]}{2} \qquad 6\text{-}8$$

$$\begin{aligned}\mathrm{u}_a(t)&=\sqrt{2}U_a\sin\omega_u t\times\frac{1+sgn[(t-t_1)(t-t_2)]}{2}\\ &+[U_{t1}-\frac{U_{t1}-U_{t2}}{t_2-t_1}(t-t_1)]\times\frac{1-sgn[(t-t_1)(t-t_2)]}{2}\end{aligned} \qquad 6\text{-}9$$

Where: $0<t<T_0/2$ (ms). Figure 6-1 d) illustrates the above I-t and V-t modelling approach for half power cycle.

In order to expand the simulated I-t and V-t traces into the whole time domain, the following equations are developed as:

$$\begin{cases}\left.\begin{aligned}\mathrm{i}_a(t)&=i_a(t-kT_0)\\ u_a(t)&=u_a(t-kT_0)\end{aligned}\right\}kT_0<t<(k+\frac{1}{2})T_0\\ \left.\begin{aligned}\mathrm{i}_a(t)&=-i_a(t-kT_0)\\ u_a(t)&=-u_a(t-kT_0)\end{aligned}\right\}(k+\frac{1}{2})T_0<t<(k+1)T_0\end{cases} \qquad 6\text{-}10$$

Where: k=0, 1, 2, 3…

6.1.1.2 MODELLING PARAMETERIZATION BASED ON TESTING IN A FOG ENVIRONMENTS

The double sinusoidal model presented in Equation 6-8 and 6-9 contains the unknown parameters of I_a, U_a, U_{t1}, U_{t2}, ω_i, ω_u, t_1 and t_2. These

parameters are changed corresponding to different current and voltage levels of the dry-band arcs. The stable dry-band arcs have been established in part 5.1 of *Testing in a Fog Environment*, with experimental current and voltage profiles of arcs (Figure 5-5) which can be used for the parameter estimation of a double sinusoidal model.

I_a – RMS VALUE OF CURRENT SINUSOIDAL WAVE (SINE WAVE I)

I_a is the rms value of the simulated current sinusoidal wave. $\sqrt{2}$Ia is equivalent to the maximum current available during the arcing period. For example, in order to simulate the dry-band arcing with 1.5 mA peak current, I_a is calculated as:

$$\sqrt{2}I_a^{1.5mA} = 1.5 \text{ mA} \quad 6\text{-}11$$

$$I_a^{1.5mA} = \frac{1}{\sqrt{2}} \times 1.5 = 1.06 \text{ mA} \quad 6\text{-}12$$

Where: $I_a^{1.5mA}$ is the rms value (mA) of simulated current sinusoidal wave for dry-band arcing with 1.5 mA current (peak).

The parameters of I_a for all the dry-band arcing cases from 1.5 mA to 4.0 mA peak current are listed in Table 3-1.

Table 6-1: Modelling parameter I_a for different levels of stable dry-band arcs

I_a	$I_a^{1.5mA}$	$I_a^{2.0mA}$	$I_a^{2.5mA}$	$I_a^{3.0mA}$	$I_a^{3.5mA}$	$I_a^{4.0mA}$
[mA]	1.06	1.41	1.77	2.12	2.47	2.83

U_a – RMS VALUE OF VOLTAGE SINUSOIDAL WAVE (SINE WAVE II)

U_a is the rms value of the simulated voltage sinusoidal wave. This is equivalent to the source voltage in the transformer secondary during the *Testing in a Fog Environment*. For example, the peak supply voltage to get 1.5 mA arcs was recorded as 20.31 kV during the test, therefore:

$$\sqrt{2}U_a^{1.5mA} = 20.31 \text{ kV} \quad 6\text{-}13$$

$$U_a^{1.5mA} = \frac{1}{\sqrt{2}} \times 20.31 = 14.36 \text{ kV} \quad 6\text{-}14$$

Where: $U_a^{1.5mA}$ is the rms value (mA) of simulated voltage sinusoidal wave for dry-band arcing with 1.5 mA current (peak).

The parameters of U_a for all the dry-band arcing cases from 1.5 mA to 4.0 mA peak current are listed in Table 6-2.

Table 6-2: Modelling parameter U_a for different levels of stable dry-band arcs

U_a	$U_a^{1.5mA}$	$U_a^{2.0mA}$	$U_a^{2.5mA}$	$U_a^{3.0mA}$	$U_a^{3.5mA}$	$U_a^{4.0mA}$
[kV]	14.36	19.06	22.65	27.07	29.56	30.66

U_{t1} – ARC VOLTAGE AT IGNITION

U_{t1} is the voltage across the arc at the point of arc ignition. It is also the upper limit of the inclined straight line of arcing voltage. Table 6-3 summarizes the U_{t1} for the arcing cases from 1.5 mA to 4.0 mA peak current based on the test results from *Testing in a Fog Environment*. For each case, four consecutive half cycles of test results were used, and U_{t1} (together with the following U_{t2}, t_1, and t_2, ω_i and ω_u) were calculated based on the average value extracted from these results.

Table 6-3: Modelling parameter U_{t1} for different levels of stable dry-band arcs

U_{t1}	$U_{t1}^{1.5mA}$	$U_{t1}^{2.0mA}$	$U_{t1}^{2.5mA}$	$U_{t1}^{3.0mA}$	$U_{t1}^{3.5mA}$	$U_{t1}^{4.0mA}$
[kV]	7.91	11.33	11.13	14.75	16.80	15.04

U_{t2} – ARC VOLTAGE AT EXTINCTION

U_{t2} is the voltage across the arc at the point of arc extinction. It is also the bottom limit of the inclined straight line of arcing voltage. Table 6-4 summarizes the U_{t2} for the arcing cases from 1.5 mA to 4.0 mA peak current based on the test results.

Table 6-4: Modelling parameter U_{t2} for different levels of stable dry-band arcs

U_{t2}	$U_{t2}^{1.5mA}$	$U_{t2}^{2.0mA}$	$U_{t2}^{2.5mA}$	$U_{t2}^{3.0mA}$	$U_{t2}^{3.5mA}$	$U_{t2}^{4.0mA}$
[kV]	6.54	8.30	8.01	10.64	11.91	10.64

t_1 – ARC IGNITION TIME

As discussed previously, t_1 is the arc ignition time between the pre-arcing period and the arcing period. Based on the test results, Table 6-5 summarizes the measured t_1 for the arcing cases from 1.5 mA to 4.0 mA peak current.

Table 6-5: Modelling parameter t_1 for different levels of stable dry-band arcs

t_1	$t_1^{1.5mA}$	$t_1^{2.0mA}$	$t_1^{2.5mA}$	$t_1^{3.0mA}$	$t_1^{3.5mA}$	$t_1^{4.0mA}$
[ms]	2.84	2.87	2.61	3.01	3.13	3.43

t_2 – ARC EXTINCTION TIME

t_2 is the arc extinction time between the arcing period and the post-arcing period. Based on the test results, Table 6-6 summarizes the measured t_2 for the arcing cases from 1.5 mA to 4.0 mA peak current.

Table 6-6: Modelling parameter t_2 for different levels of stable dry-band arcs

t_2	$t_2^{1.5mA}$	$t_2^{2.0mA}$	$t_2^{2.5mA}$	$t_2^{3.0mA}$	$t_2^{3.5mA}$	$t_2^{4.0mA}$
[ms]	8.73	8.42	8.76	8.68	8.66	8.84

ω_u – ANGULAR FREQUENCY OF VOLTAGE SINUSOIDAL WAVE (SINE WAVE II)

The simulated voltage sinusoidal wave is equivalent to a supply voltage which has the power frequency of 50 Hz, therefore, ω_u is determined by:

$$\omega_u = 2\pi f = 2 \times 3.14 \times 50 = 0.314 \text{ rad/ms} \qquad 6\text{-}15$$

Where: ω_u is the angular frequency of the simulated voltage sinusoidal wave.

The ω_u for all the experimental cases from 1.5 mA to 4.0 mA peak current arcs remain the same as demonstrated in Table 6-7.

Table 6-7: Modelling parameter ω_u for different levels of stable dry-band arcs

ω_u	$\omega_u^{1.5mA}$	$\omega_u^{2.0mA}$	$\omega_u^{2.5mA}$	$\omega_u^{3.0mA}$	$\omega_u^{3.5mA}$	$\omega_u^{4.0mA}$
[rad/ms]	0.314	0.314	0.314	0.314	0.314	0.314

ω_i – ANGULAR FREQUENCY OF CURRENT SINUSOIDAL WAVE (SINE WAVE I)

Based on the current measurement from the *Testing in a Fog Environment*, the following Equation 6-16 gives a determination example of the ω_i, and Table 6-8 lists all the calculated ω_i for the arcing cases from 1.5 mA to 4.0 mA current (peak).

$$\omega_i^{1.5mA} = \frac{\pi}{\frac{\pi}{\omega_u} - 2(\frac{\pi}{\omega_u} - t_2)} = \frac{3.14}{10 - 2\times(10 - 8.73)} = 0.421 \text{ rad/ms} \qquad 6\text{-}16$$

Where: $\omega_i^{1.5mA}$ is the angular frequency of simulated current sinusoidal wave for the 1.5 mA current (peak) dry-band arc, $t_1^{1.5mA}$ is the arc ignition time of the 1.5 mA current (peak) dry-band arc from Table 6-5, and $t_2^{1.5mA}$ is the arc extinction time of the 1.5 mA current (peak) dry-band arc from Table 6-6.

Table 6-8: Modelling parameter ω_i for different levels of stable dry-band arcs

ω_i	$\omega_i^{1.5mA}$	$\omega_i^{2.0mA}$	$\omega_i^{2.5mA}$	$\omega_i^{3.0mA}$	$\omega_i^{3.5mA}$	$\omega_i^{4.0mA}$
[rad/ms]	0.421	0.459	0.418	0.427	0.429	0.409

6.1.1.3 MODELLING RESULTS FOR STABLE ARCS

By substitution of the modelling parameters from Table 6-1 to Table 6-8, into the *Double Sinusoidal Model* presented in Equations 6-8 and 6-9, the I-t and V-t curves of stable dry-band arcs with different current levels can be simulated based on the *Testing in a Fog Environment*. Equations 6-17 and 6-18 show one of the simulation results with 1.5 mA peak current dry-band arc.

$$i_a^{1.5mA}(t) = 1.5\sin[0.421(t - 1.27)]\times\frac{1 - sgn[(t - 2.84)(t - 8.73)]}{2} \qquad 6\text{-}17$$

$$u_a^{1.5mA}(t) = 20.31\sin(0.314t) \times \frac{1+sgn[(t-2.84)(t-8.73)]}{2} + (-0.233t+8.57) \times \frac{1-sgn[(t-2.84)(t-8.73)]}{2} \quad 6\text{-}18$$

Where: $i_a^{1.5mA}(t)$ and $u_a^{1.5mA}(t)$ are simulated I-t and V-t curves for a 10 ms half cycle of the 1.5 mA peak current dry-band arc. $i_{a(t)}$ and $u_{a(t)}$ are multiplied by -1 when 10<t<20 (ms), and can be expanded to the whole time domain by using Equation 6-10.

The comparison between modelling results and experimental results of stable dry-band arcs for different current levels are demonstrated in Figure 6-2.

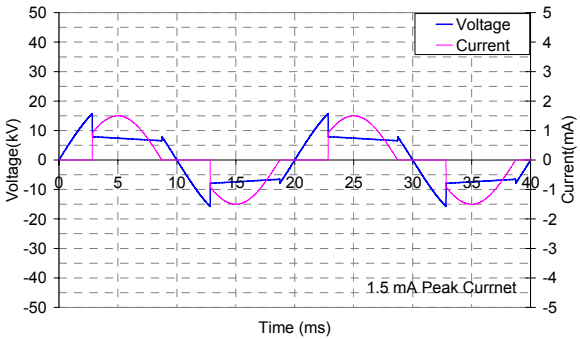

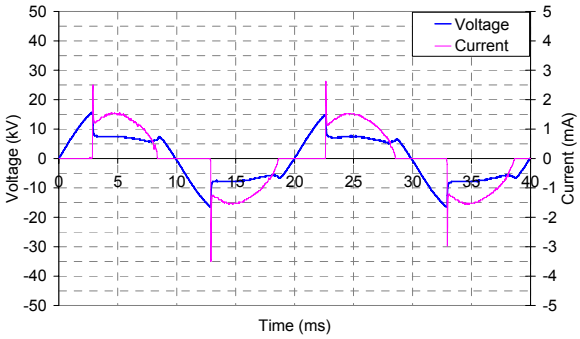

a) Modelling result **b) Experiment result**

For dry-band arcing with 1.5 mA current (peak)

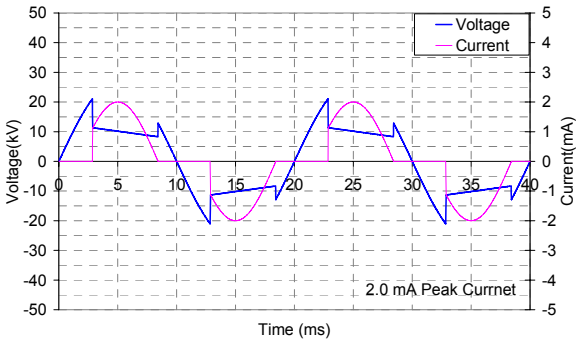

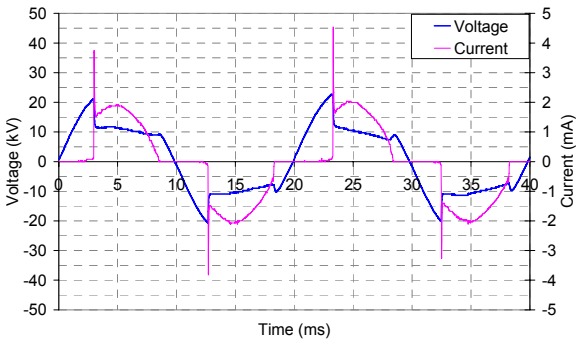

a) Modelling result **b) Experiment result**

For dry-band arcing with 2.0 mA current (peak)

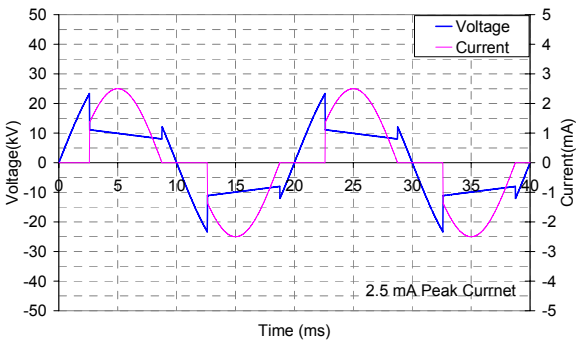

a) Modelling result

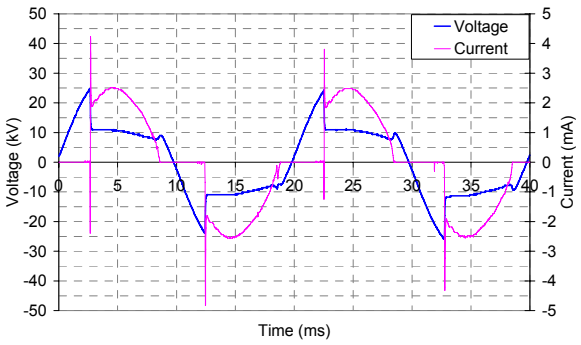

b) Experiment result

For dry-band arcing with 2.5 mA current (peak)

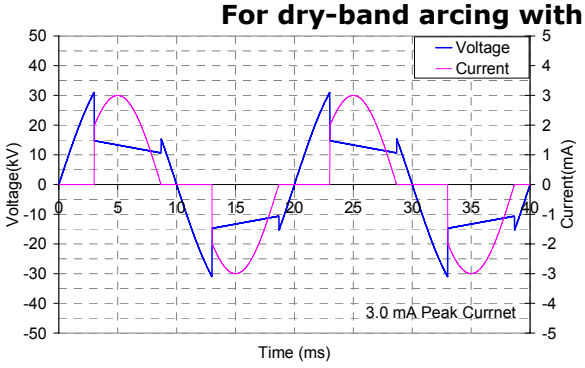

a) Modelling result

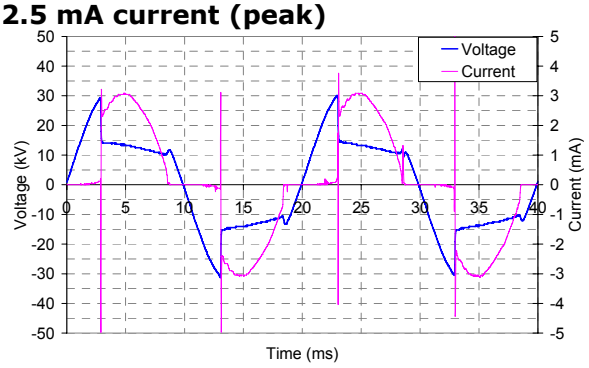

b) Experiment result

For dry-band arcing with 3.0 mA current (peak)

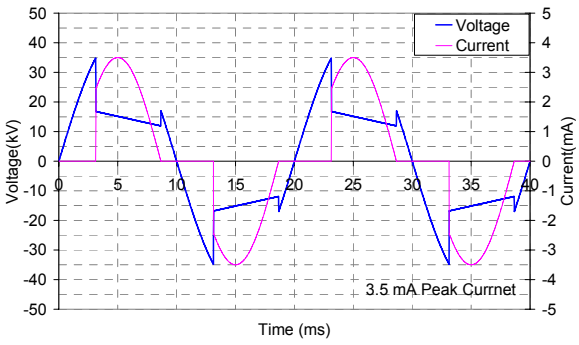

a) Modelling result

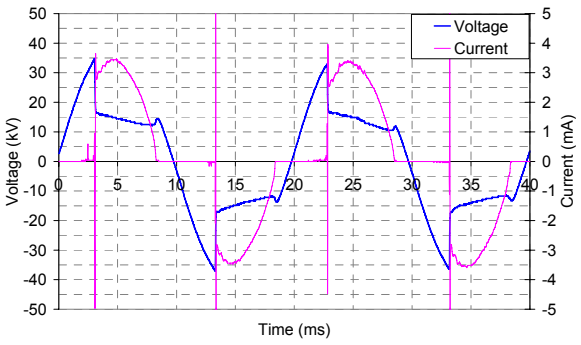

b) Experiment result

For dry-band arcing with 3.5 mA current (peak)

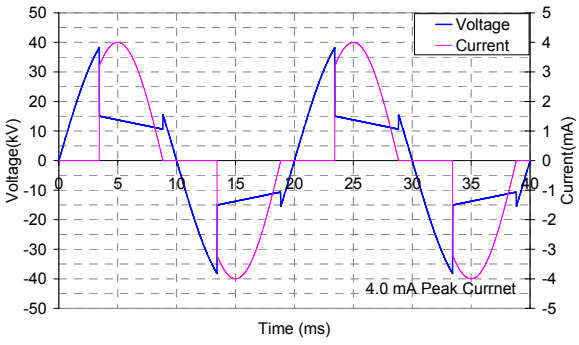

a) Modelling result

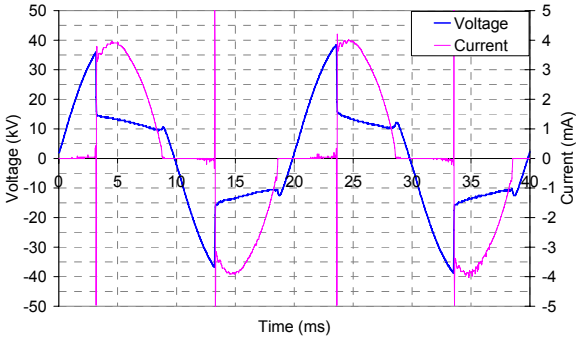

b) Experiment result

For dry-band arcing with 4.0 mA current (peak)

Figure 6-2: Simulated I-t and V-t traces from Double Sinusoidal Model comparing with experimental results in Testing in a Fog Environment

The correlation coefficient 'r' between modeling and experimental results in Figure 6-2 is calculated in each case, in order to verify the modelling validation of *Double Sinusoidal Model* for the simulation of stable dry-band arcs from section 5.1 of *Testing in a Fog Environment*. The equation for the correlation coefficient is:

$$Correl(X,Y) = \frac{\sum (x-\bar{x})(y-\bar{y})}{\sqrt{\sum (x-\bar{x})^2 (y-\bar{y})^2}} \qquad 6\text{-}19$$

Where: x is the data group 1, y is the data group 2. $\bar{x}$ and $\bar{y}$ are the mean values of data group 1 and 2.

The results show the r=0.993 for the voltage curve and r=0.984 for the current curve with 1.5 mA peak current arc; r=0.984 for the voltage curve and r=0.969 for the current curve with 2.0 mA peak current arc; r=0.985 for the voltage curve and r=0.981 for the current curve with 2.5 mA peak current arc; r=0.995 the for voltage curve and r=0.980 for the current curve with 3.0 mA peak current arc; r=0.984 for the voltage curve and r=0.973 for the current curve with 3.5 mA peak current arc; and r=0.981 for the voltage curve and r=0.965 for the current curve with 4.0 mA peak current arc. The above correlation coefficients show the good correlations between the experimental and modelling results, and further confirm the validity of Double Sinusoidal Model for simulating the I-t and V-t characteristics of stable dry-band arcs.

6.1.2 PSCAD SIMULATION

A PSCAD/EMTDC simulation was built based on the experimental circuit of the *Testing in a Fog Environment* with the test arrangement previously shown in Figure 5-1. This simulation aims to further study the I-t and V-t curves of stable dry-band arcs directly driven from a primary test circuit, together with the combination of modelling knowledge previously obtained from the *Double Sinusoidal Model* in Part 6.1.1.

6.1.2.1 SIMULATION CIRCUIT FOR STABLE ARCS FROM TESTING IN A FOG ENVIRONMENT

Figure 6-3 shows the detailed simulation circuit to create stable dry-band arcs in PSCAD software. Circuit parameters are directly abstracted from experimental test circuit in the *Testing in a Fog Environment*. The source voltage varies corresponding to arcs with different current levels. The guidelines for selecting source voltage have been previously listed in Table 6-2. For example, in order to simulate a dry-band arc with 1.5 mA peak current, the source voltage of 14.36 kV (RMS) was chosen as input to the PSCAD simulation circuit. The current limit resistor was set to 9 MΩ and the current measuring resistor was set to 1 kΩ following the experimental arrangement in Figure 5-1. The current signal $i_a(t)$ and voltage signal $u_a(t)$ are considered to be the arcing current and voltage and are the simulation output.

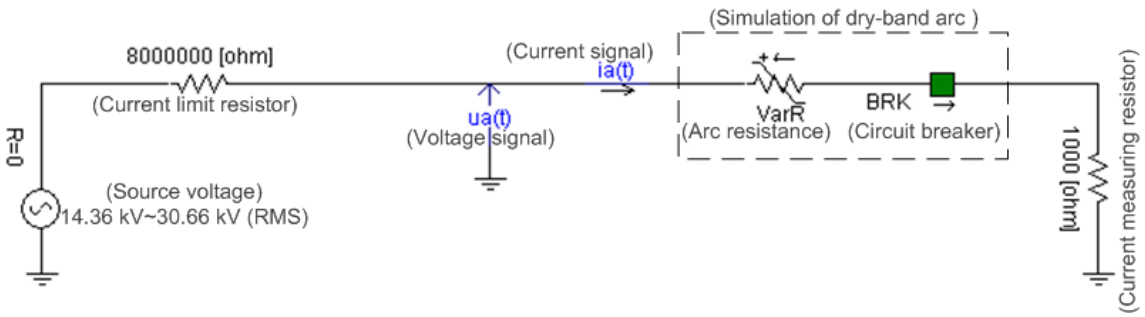

Figure 6-3: Simulation circuit for stable dry-band arcs in PSCAD

The simulation of the dry-band arc consists of a circuit breaker and a variable arc resistance in the PSCAD circuit. The circuit breaker 'BRK' is controlled by a control circuit to simulate the arc ignition and extinction. The arc resistance 'VarR' represents the instantaneous arc resistance during the arcing period. The detailed 'BRK' and 'VarR' will be respectively described in the following parts 6.1.2.2 and 6.1.2.3.

6.1.2.2 CIRCUIT BREAKER FOR ARC IGNITION AND EXTINCTION

Figure 6-4 a) shows the control circuit which is used to generate a signal as 'BRK' to control the open and close status of the circuit breaker. Impulse Generator 1 was set to a frequency of 100 Hz with time of first impulse at t_1 (arc ignition time). Together, Impulse Generator 2 was set to a frequency of 100 Hz with time of first impulse at t_2 (arc extinction time). These two impulse generators coordinate with two Sequential Units (both with settings of Starting point 0.0, increment 0.5) can generate the 'BRK' control signal demonstrated in Figure 6-4 b). In PSCAD, '0' logic signal controls circuit breaker to be at 'close' position, while '1' logic signal controls circuit breaker to be at 'open' position. Therefore, the output of control signal 'BRK' controls the circuit breaker to be closed during the arcing period from t_1 to t_2, bringing the arc resistance into the simulation circuit, but to be open other times when arc disappears, representing a high maximum resistance for the dry-band surface. The specified groups of t_1 and t_2 for PSCAD simulation in different arcing situations have been listed in Table 6-5 and Table 6-6.

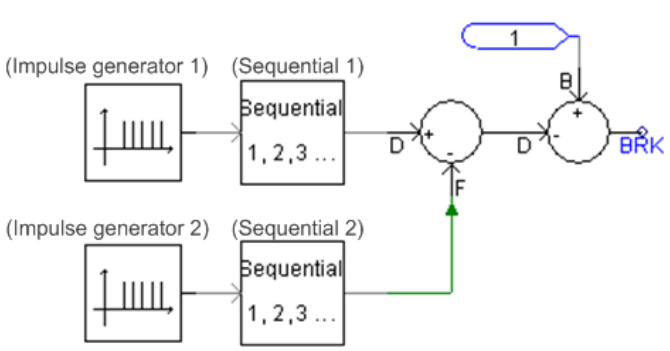

a) Control circuit to produce a control signal 'BRK'

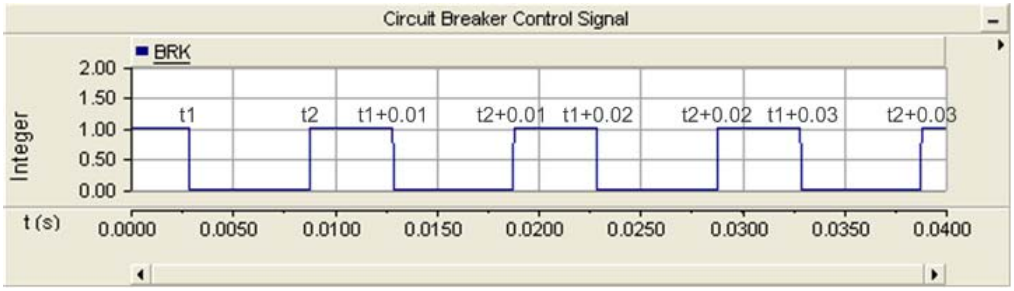

b) Output of control signal 'BRK'

Figure 6-4: Control Circuit of Circuit Breaker for arc ignition and extinction

6.1.2.3 SIMULATION OF INSTANTANEOUS ARC RESISTANCE

During the arcing period from t_1 to t_2, the instantaneous arc resistance from experimental result performs a 'U' shape shown in Figure 5-13 of the *Testing in a Fog Environment*. In the *Double Sinusoidal Model*, the instantaneous arc resistance can be represented by the ratio of simulated arc voltage to arc current. As the arc resistance only appears during the arcing period for times $t_1<t<t_2$, Equations 6-3 and 6-4 can be used for calculation:

$$r_a(t)=\frac{u_a(t)}{i_a(t)}=\frac{U_{t1}-\frac{U_{t1}-U_{t2}}{t_2-t_1}(t-t_1)}{\sqrt{2}I_a\sin\omega_i[t-(\frac{\pi}{\omega_u}-t_2)]}=\frac{dt+e}{a\sin(bt+c)} \qquad 6\text{-}20$$

Where: $i_a(t)$ and $u_a(t)$ are the simulated current (mA) and voltage (kV) in the arcing period from the *Double Sinusoidal Model*. $r_a(t)$ is the calculated instantaneous arc resistance (MΩ). I_a, U_{t1}, U_{t2}, t_1, t_2, ω_u and ω_i are constant parameters which have been previously determined and summarized in part 6.1.1.2 of *Modelling Parameterization Based on Testing in a Fog Environment*. a, b, c, d, e are simplified constant parameters for the arc resistance simulation in PSCAD. Based on modelling data from Table 3-1 to Table 6-8, calculated values of a, b, c, d and e for dry-band arcs with peak currents from 1.5 mA to 4.0 mA are shown in Table 6-9.

Table 6-9: Input parameters for instantaneous arc resistance in PSCAD simulation for different current levels of dry-band arc

Arcing Current Level	1.5 mA	2.0 mA	2.5 mA	3.0 mA	3.5 mA	4.0 mA
a	1.5	2.0	2.5	3.0	3.5	4.0
b	0.421	0.459	0.418	0.427	0.429	0.409
c	-0.535	-0.725	-0.518	-0.564	-0.575	-0.474
d	-0.233	-0.546	-0.507	-0.725	-0.884	-0.813
e	8.750	12.897	12.454	16.932	19.568	17.829

Figure 6-5 a) shows the simulation circuit of instantaneous arc resistance based on the Equation 6-20 drawn in PSCAD. The setting for Impulse Generator 3 was 100 Hz frequency with first impulse at 0.01 s, together with Sequential 3 (starting point 0, increment 0.5) to generate an output 'k' which is used to count the number of half cycles for continuous arc resistance simulation in the whole time domain. The input constants a=1.5, b=0.421, c=-0.535, d=-0.233 and e=8.750 are chosen for the dry-band arc with 1.5 mA peak current from Table 6-9 as an example. The simulation result of instantaneous arc resistance for this example is shown in Figure 6-5 b).

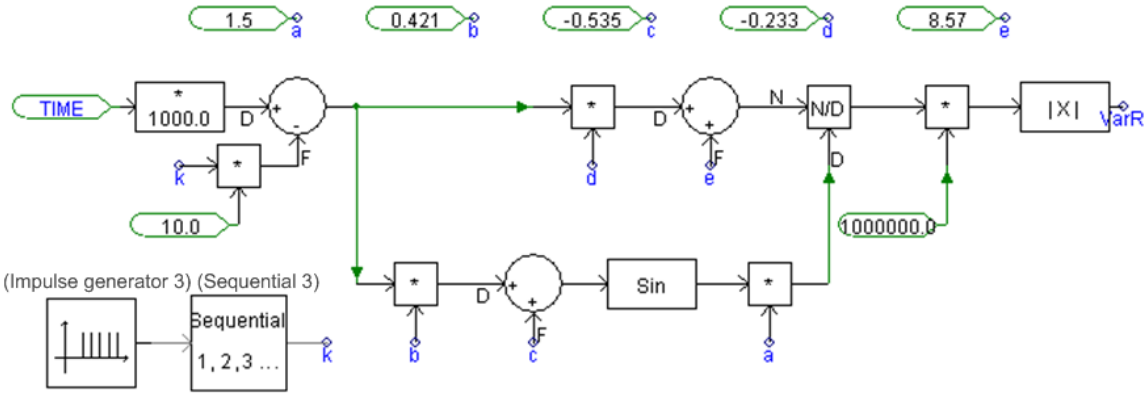

a) Simulation circuit to produce arc resistance 'VarR'

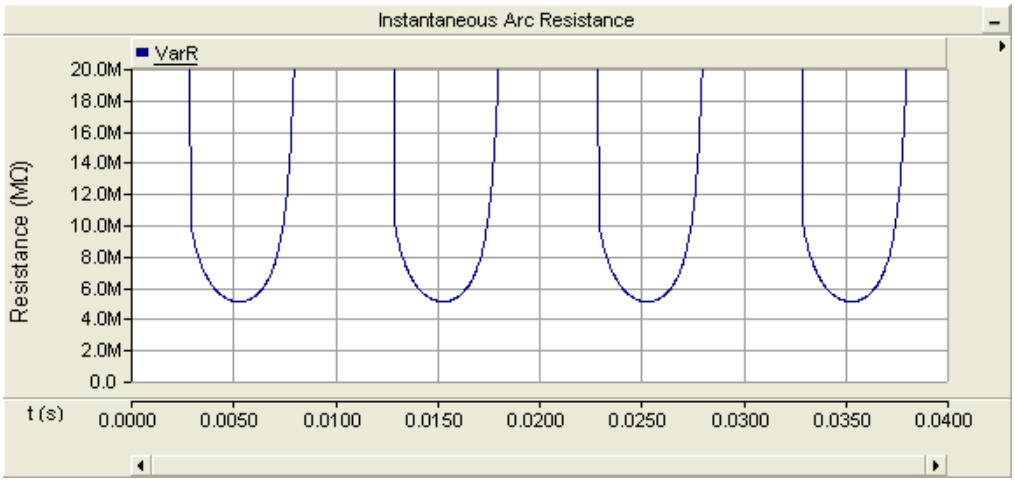

b) Output of arc resistance 'VarR'

Figure 6-5: Simulation circuit for instantaneous arc resistance in PSCAD

6.1.2.4 PSCAD SIMULATION RESULTS FOR STABLE ARC

By running the PSCAD simulation based on the simulation circuit in Figure 6-3, with the data of circuit breaker control signal in part 6.1.2.2 and calculated instantaneous arc resistance in part 6.1.2.3, the I-t and V-t curves for stable dry-band arcs with respective 1.5 mA, 2.0 mA, 2.5 mA, 3.0 mA, 3.5 mA and 4.0 mA peak current can be obtained in Figure 6-6.

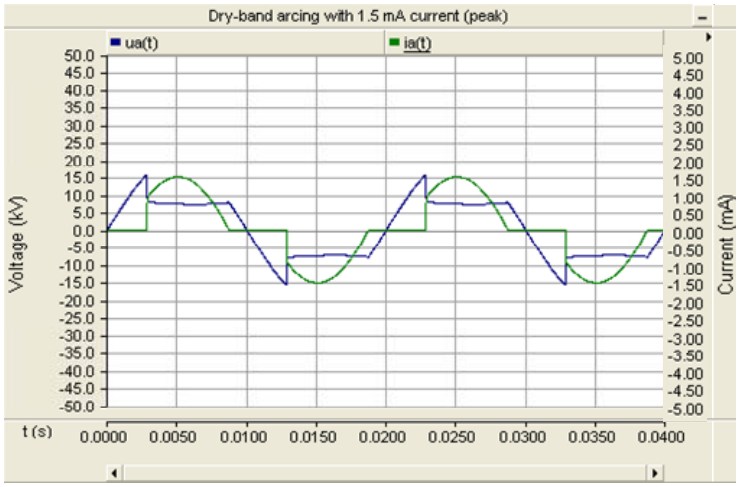

a) Simulated dry-band arcing with 1.5 mA current (peak)

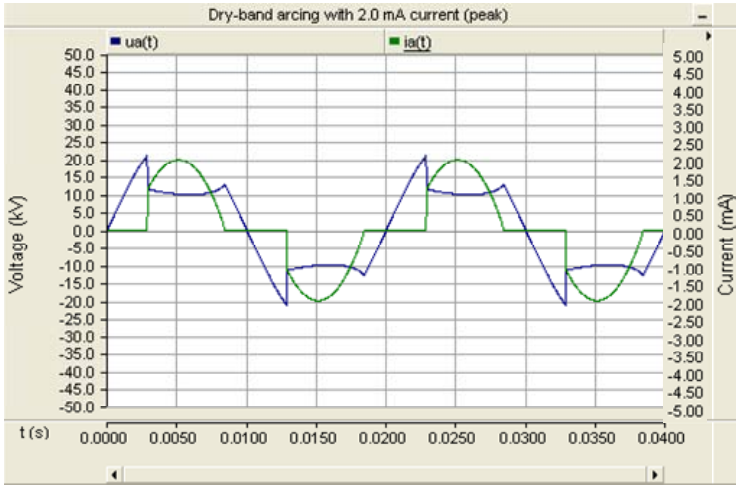

b) Simulated dry-band arcing with 2.0 mA current (peak)

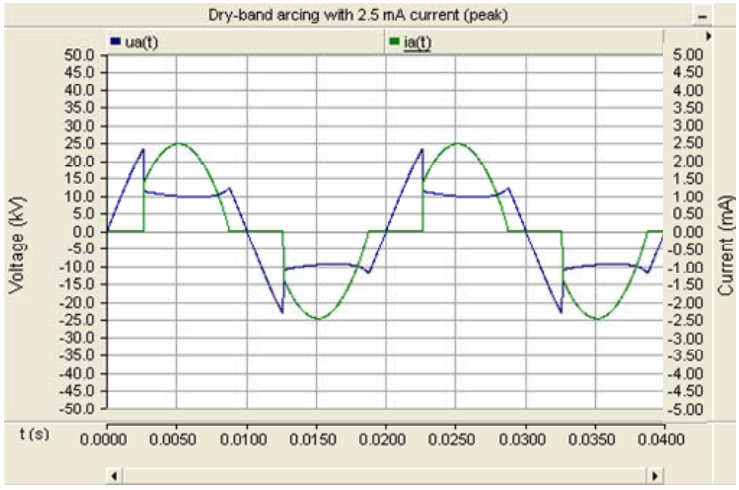

c) Simulated dry-band arcing with 2.5 mA current (peak)

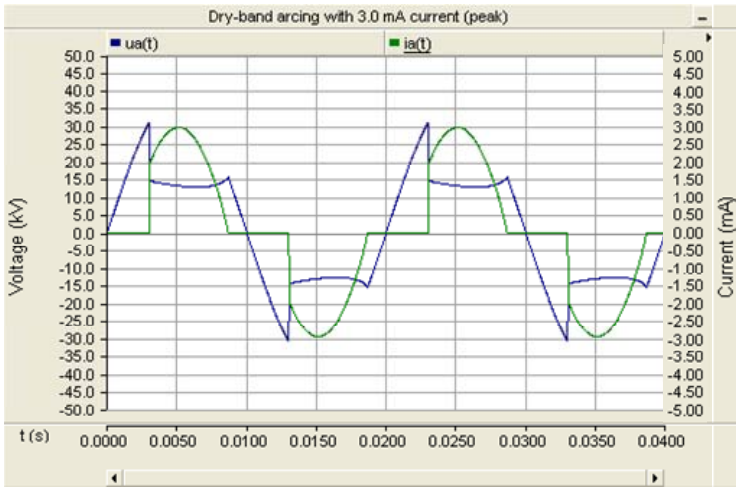

d) Simulated dry-band arcing with 3.0 mA current (peak)

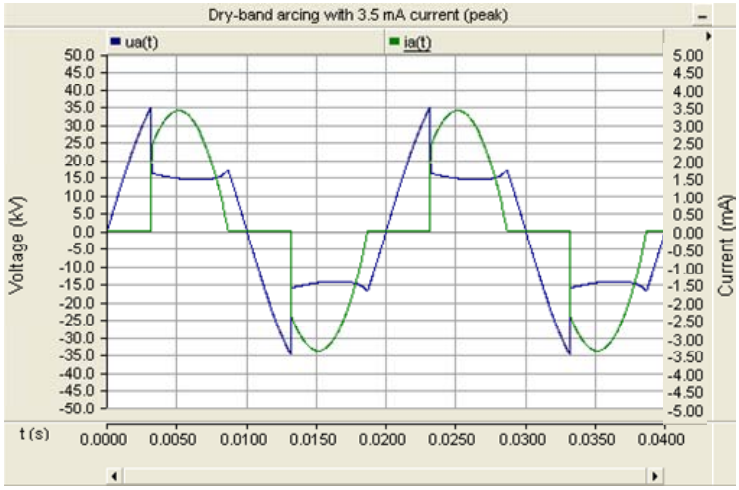

e) Simulated dry-band arcing with 3.5 mA current (peak)

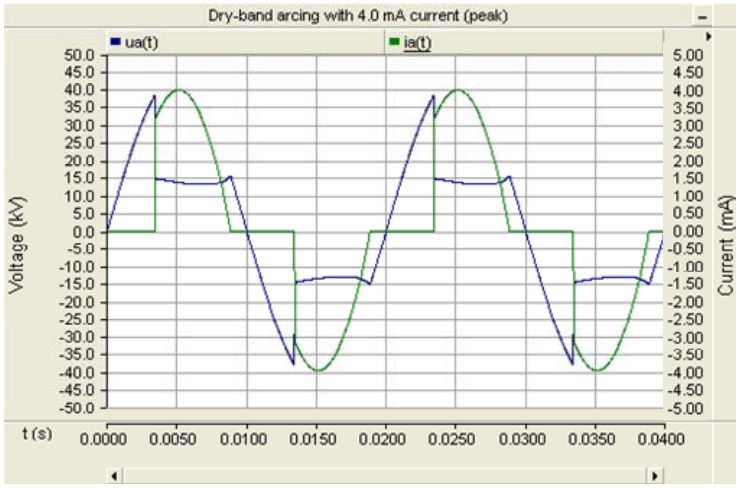

f) Simulated dry-band arcing with 4.0 mA current (peak)

Figure 6-6: PSCAD simulation result of I-t and V-t curves for stable dry-band arcs with different current levels

The correlation coefficient 'r' of the current (I-t) and voltage (V-t) curves for stable dry-band arcing between the experimental results from the *Testing in a Fog Environment*, modelling results from the *Double Sinusoidal Model* and simulation results from *PSCAD/EMTDC* are summarized in Table 6-10. The table shows 42% achieve correlation above 0.99, 75% above 0.98, 92% above 0.97 and all above 0.96. All results indicate good correlation between simulation, modelling results and experiment results. It also demonstrates the validation and accuracy of PSCAD simulation for stable dry-band arcing.

Table 6-10: Correlation coefficients 'r' for current and voltage curves of dry-band arcs between experimental results from Testing in a Fog Environment, modelling results from the Double Sinuoidal Model, and simulation results from PSCAD

I-t and V-t curves of Stable Dry-band Arcs	Arcing Levels	Experiment Result		Double Sinusoidal Model		PSCAD Simulation	
		V	I	V	I	V	I
Experiment Result	1.5 mA	1.000	1.000	0.993	0.984	0.991	0.984
	2.0 mA	1.000	1.000	0.984	0.969	0.978	0.970
	2.5 mA	1.000	1.000	0.985	0.981	0.980	0.979
	3.0 mA	1.000	1.000	0.995	0.980	0.992	0.980
	3.5 mA	1.000	1.000	0.984	0.973	0.980	0.971
	4.0 mA	1.000	1.000	0.981	0.965	0.979	0.965
Double Sinusoidal Model	1.5 mA	0.993	0.984	1.000	1.000	0.998	0.998
	2.0 mA	0.984	0.969	1.000	1.000	0.995	0.997
	2.5 mA	0.985	0.981	1.000	1.000	0.995	0.997
	3.0 mA	0.995	0.980	1.000	1.000	0.996	0.997
	3.5 mA	0.984	0.973	1.000	1.000	0.996	0.996
	4.0 mA	0.981	0.965	1.000	1.000	0.996	0.996
PSCAD Simulation	1.5 mA	0.991	0.984	0.998	0.998	1.000	1.000
	2.0 mA	0.978	0.970	0.995	0.997	1.000	1.000
	2.5 mA	0.980	0.979	0.995	0.997	1.000	1.000
	3.0 mA	0.992	0.980	0.996	0.997	1.000	1.000
	3.5 mA	0.980	0.971	0.996	0.996	1.000	1.000
	4.0 mA	0.979	0.965	0.996	0.996	1.000	1.000

6.2 MODELLING OF ARC COMPRESSION

6.2.1 DOUBLE SINUSOIDAL MODEL FOR ARC COMPRESSION

The situation of dry-band arc compression can be simulated by the *Double Sinusoidal Model* previously presented in Equations 6-8 and 6-9. The input parameters for modelling of arc compression are based on the experimental result from the *Testing with Inclined Samples* as follows:

6.2.1.1 MODELLING PARAMETERIZATION BASED ON TESTING WITH INCLINED SAMPLES

L_a – ARC LENGTH DURING THE COMPRESSION PROCESS

L_a is the physical length of the dry-band arc. During the arcing compression, L_a changes according to different compression situations. This variable parameter L_a is used as an input to the *Double Sinusoidal Model* to simulate the arcing compression process.

I_a – RMS VALUE OF CURRENT SINUSOIDAL WAVE (SINE WAVE I)

Figure 5-21 in the *Testing with Inclined Samples* shows the relationship between arc current peak and arc length. For the modelling parameterization, this relationship can be quantified as:

$$\sqrt{2}I_a = -0.3529L_a + 2.7796 \text{ mA} \qquad 6\text{-}21$$

$$I_a = \frac{1}{\sqrt{2}} \times (-0.3529L_a + 2.7796) = -0.25L_a + 1.97 \text{ mA} \qquad 6\text{-}22$$

Where: I_a is the rms value (mA) of the simulated current sinusoidal wave, and L_a is the arc length (cm).

U_a – RMS VALUE OF VOLTAGE SINUSOIDAL WAVE (SINE WAVE II)

During the arc compression in the *Testing with Inclined Samples*, the supply voltage was fixed throughout the whole compression process. U_a is equivalent to the instantaneous source voltage in transformer secondary, therefore, U_a is chosen as 17.4 kV (RMS value).

U_{t1}, U_{t2} – ARC IGNITION VOLTAGE, AND ARC EXTINCTION VOLTAGE

By observing the results of voltage measurement from the *Testing with Inclined Samples*, it is found that the arcing voltage reduces linearly in time from the maximum U_{t1} (arc ignition voltage) to the minimum U_{t2} (arc extinction voltage). For the modelling of different arc compression (inclined angle) situations, U_{t1} and U_{t2} are assumed to be fixed throughout the arcing period for simplification. U_{t1} is determined by:

$$U_{t1} = \frac{U_{t1}^{0^\circ} + U_{t1}^{5^\circ} + U_{t1}^{10^\circ} + U_{t1}^{15^\circ} + U_{t1}^{20^\circ} + U_{t1}^{25^\circ} + U_{t1}^{30^\circ} + U_{t1}^{35^\circ}}{8} = 10.19 \text{ kV} \qquad 6\text{-}23$$

Where: $U_{t1}^{0^\circ}$=11.91 kV, $U_{t1}^{5^\circ}$=12.01 kV, $U_{t1}^{10^\circ}$=11.23 kV, $U_{t1}^{15^\circ}$=10.84 kV, $U_{t1}^{20^\circ}$=9.57 kV, $U_{t1}^{25^\circ}$=9.67 kV, $U_{t1}^{30^\circ}$=8.98 kV, $U_{t1}^{35^\circ}$=7.32 kV, which are respectively the measured arc ignition voltage for dry-band arcs from 0° to 35° during the *Testing with Inclined Samples*.

U_{t2} is determined by:

$$U_{t1} = \frac{U_{t2}^{0^\circ} + U_{t2}^{5^\circ} + U_{t2}^{10^\circ} + U_{t2}^{15^\circ} + U_{t2}^{20^\circ} + U_{t2}^{25^\circ} + U_{t2}^{30^\circ} + U_{t2}^{35^\circ}}{8} = 6.98 \text{ kV} \qquad 6\text{-}24$$

Where: $U_{t2}^{0^\circ}$=8.11 kV, $U_{t2}^{5^\circ}$=7.32 kV, $U_{t2}^{10^\circ}$=6.45 kV, $U_{t2}^{15^\circ}$=7.13 kV, $U_{t2}^{20^\circ}$=6.15 kV, $U_{t2}^{25^\circ}$=7.13 kV, $U_{t2}^{30^\circ}$=6.93 kV, $U_{t2}^{35^\circ}$=6.64 kV, which are respectively the measured arc extinction voltage for dry-band arcs from 0° to 35° during the *Testing with Inclined Samples*.

t_1 – ARC IGNITION TIME

For the modelling of arc compression, t_1 varies according to different compression situations with different arc lengths. By analyzing experimental results in Figure 5-20 of the *Testing with Inclined Samples*, the relationship between arc length (L_a), arcing period (T_{arc}), arc ignition time (t_1) and arc extinction time (t_2) is established as:

$$T_{arc} = t_2 - t_1 = -3.02L_a + 11.23 \text{ ms} \quad 6\text{-}25$$

$$t_1 = f(L_a, t_2) = t_2 + 3.02L_a - 11.23 \text{ ms} \quad 6\text{-}26$$

Where: T_{arc} is the arcing period, t_1 is the arc ignition time, t_2 is the arc extinction time (all in ms) and L_a is the arc length (cm).

t_2 – ARC EXTINCTION TIME

According to the observation of current and voltage traces in Figure 5-17 from the *Testing with Inclined Samples*, t_2 slightly varies following the different arc compression situations. However, for the modelling input parameter t_2 is assumed as a constant value for simplification. The following equation is applied to obtain the t_2 as:

$$t_2 = \frac{t_2^{0^\circ} + t_2^{5^\circ} + t_2^{10^\circ} + t_2^{15^\circ} + t_2^{20^\circ} + t_2^{25^\circ} + t_2^{30^\circ} + t_2^{35^\circ}}{8} = 8.88 \text{ ms} \quad 6\text{-}27$$

Where: $t_2^{0^\circ}$=8.43 ms, $t_2^{5^\circ}$=8.61 ms, $t_2^{10^\circ}$=8.66 ms, $t_2^{15^\circ}$=8.74 ms, $t_2^{20^\circ}$=9.11 ms, $t_2^{25^\circ}$=8.59 ms, $t_2^{30^\circ}$=9.13 ms, $t_2^{35^\circ}$=9.74 ms, which are respectively the arc extinction time measured from *Testing with Inclined Samples* from 0° to 35°.

ω_u – ANGULAR FREQUENCY OF VOLTAGE SINUSOIDAL WAVE (SINE WAVE II)

For the arc compression, the simulated voltage sinusoidal wave is always equivalent to the supply voltage which has the power frequency of 50 Hz, therefore, ω_u is determined by:

$$\omega_u = 2\pi f = 2\times 3.14\times 50 = 0.314 \text{ rad/ms} \quad (6\text{-}28)$$

Where: ω_u is the angular frequency of simulated voltage sinusoidal wave.

ω_i – ANGULAR FREQUENCY OF CURRENT SINUSOIDAL WAVE (SINE WAVE I)

Based on the current measurements from the *Testing with Inclined Samples*, its angular frequency ω_i is slightly changed with different arc compression situations, but can be assumed as a fixed value in the modelling for the purpose of simplification.

$$\omega_i = \frac{2\pi}{\frac{T_i^{0°}+T_i^{5°}+T_i^{10°}+T_i^{15°}+T_i^{20°}+T_i^{25°}+T_i^{30°}+T_i^{35°}}{8}} = 0.408 \text{ rad/ms} \quad (6\text{-}29)$$

Where: $T_i^{0°}$=13.60 ms, $T_i^{5°}$=14.33 ms, $T_i^{10°}$=14.55 ms, $T_i^{15°}$=14.85 ms, $T_i^{20°}$=16.33 ms, $T_i^{25°}$=14.28 ms, $T_i^{30°}$=16.40 ms, $T_i^{35°}$=18.88 ms, which are respectively the measured current periodical time during the *Testing with Inclined Samples* of 0° to 35°.

6.2.1.2 MODELLING RESULTS FOR ARC COMPRESSION

By introducing the specified parameters from Part 6.2.1.1 to the *Double Sinusoidal Model* previously proposed in Equations 6-8 and 6-9, the modelling for dry-band arc compression is established as follows:

$$\mathrm{i}_a(t) = (-0.35L_a + 2.78)\sin[0.408(t-1.12)]\times\frac{1-sgn[(t-3.02L_a+2.35)(t-8.88)]}{2} \quad (6\text{-}30)$$

$$\begin{aligned}\mathrm{u}_a(t) &= 24.61\sin 0.314t\times\frac{1+sgn[(t-3.02L_a+2.35)(t-8.88)]}{2}\\ &+[10.19-\frac{3.21}{-3.02L_a+11.23}(t-3.02L_a+2.35)]\times\frac{1-sgn[(t-3.02L_a+2.35)(t-8.88)]}{2}\end{aligned} \quad (6\text{-}31)$$

Where: $i_a(t)$ and $u_a(t)$ are simulated I-t and V-t curves. 0<t<10 (ms). $i_a(t)$ and $u_a(t)$ are respectively multiplied by -1 when 10<t<20 (ms), and

can be expanded to the whole time domain by using Equation 6-10. L_a is the variable arc length during the compression.

Figure 6-7 shows the modelling results of I-t and V-t curves for arc lengths from 2.32 cm to 1.11 cm. These results show the *Double Sinusoidal Model* is capable of modelling dry-band arc compression with variable arc lengths. The main characteristics of measured current and voltage signals under arc compression in the *Testing with Inclined Samples* can be reflected in this simulation, with a prolonged arcing period corresponding to the length compressed arc.

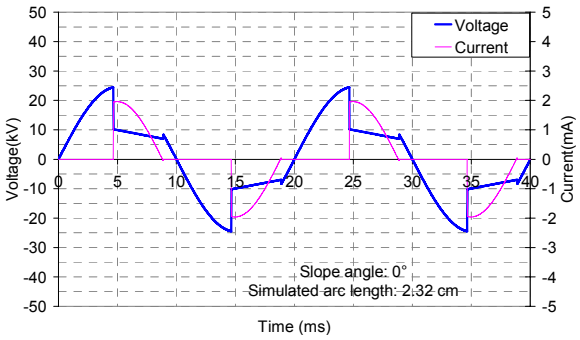

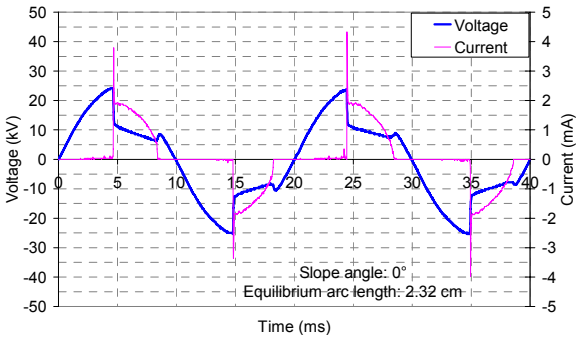

a) Modelling result **b) Experiment result**

For dry-band arcing with 2.32 cm arc length

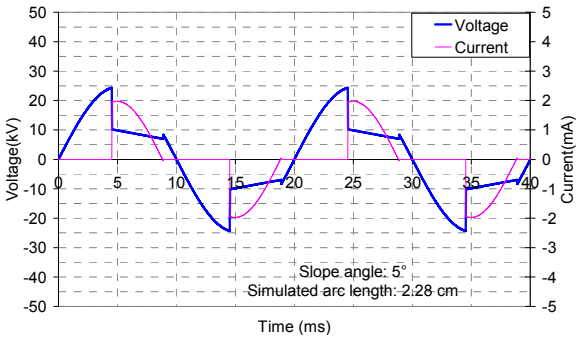

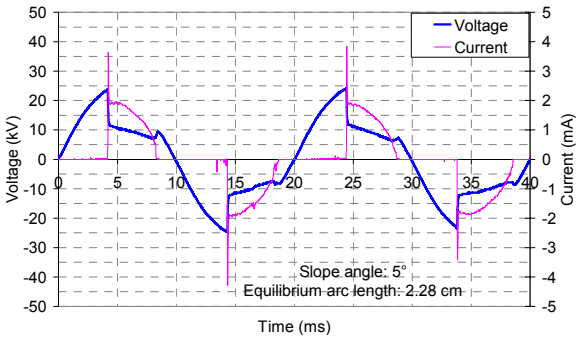

a) Modelling result **b) Experiment result**

For dry-band arcing with 2.28 cm arc length

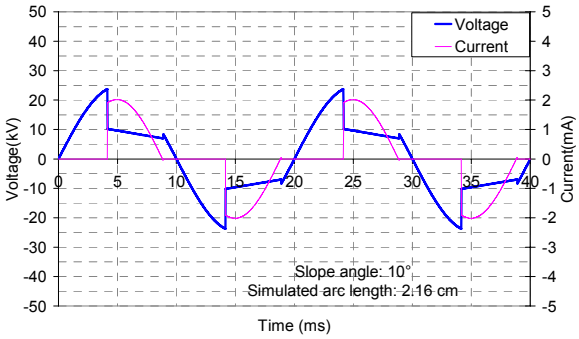

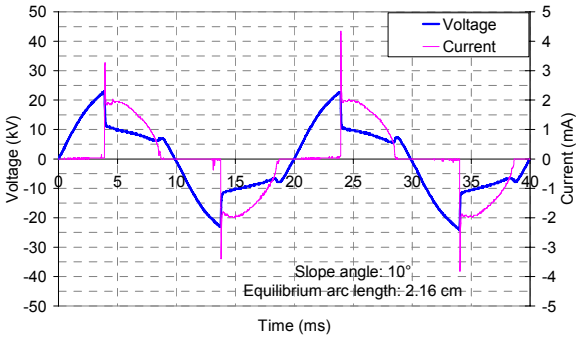

a) Modelling result **b) Experiment result**

For dry-band arcing with 2.16 cm arc length

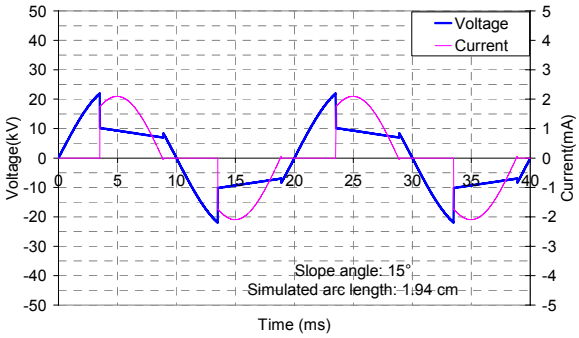

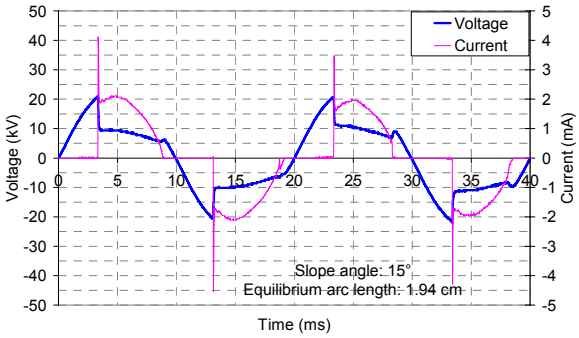

a) Modelling result **b) Experiment result**

For dry-band arcing with 1.94 cm arc length

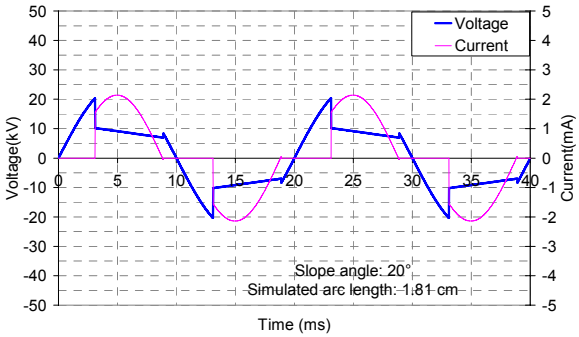

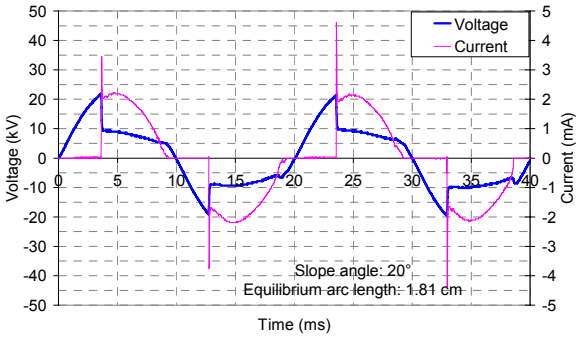

a) Modelling result **b) Experiment result**

For dry-band arcing with 1.81 cm arc length

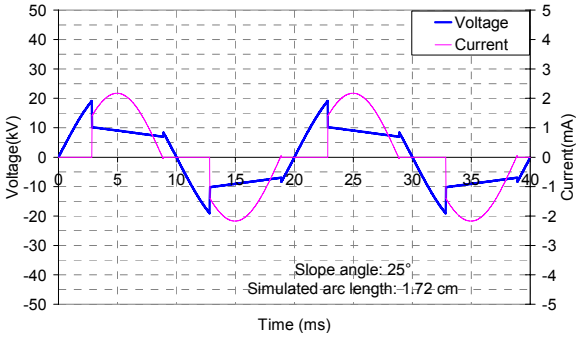

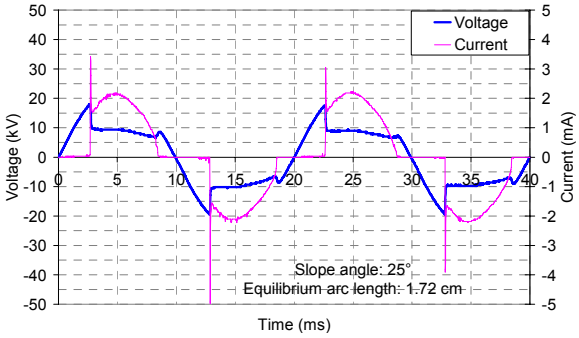

a) Modelling result **b) Experiment result**

For dry-band arcing with 1.72 cm arc length

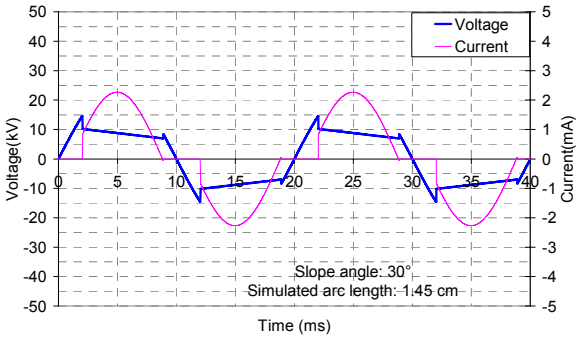

a) Modelling result

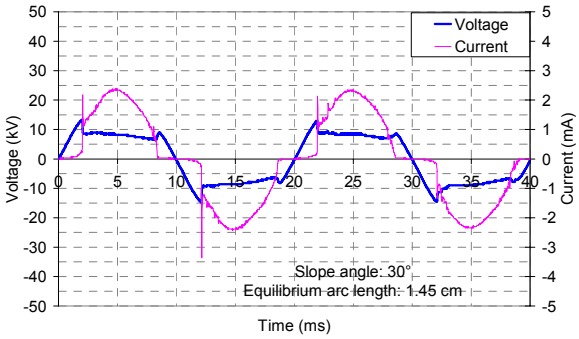

b) Experiment result

For dry-band arcing with 1.45 cm arc length

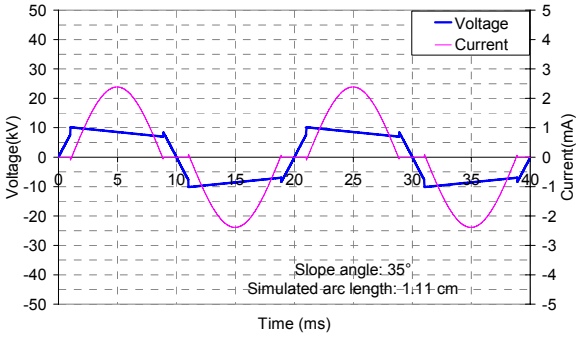

a) Modelling result

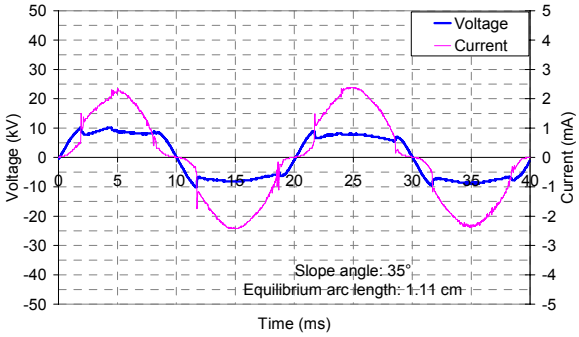

b) Experiment result

For dry-band arcing with 1.11 cm arc length

Figure 6-7: The Double Sinusoidal Model Simulated I-t and V-t traces for variable arc lengths under different arc compression situations comparing with experimental results from Testing with Inclined Samples

The correlation coefficient 'r' between modeling and experimental results in Figure 6-7 is calculated in each case, showing r=0.990 for voltage and r=0.951 for current with the 2.32 cm arc length; r=0.984 for voltage and r=0.915 for current with the 2.28 cm arc length; r=0.988 for voltage and r=0.941 for current with the 2.16 cm arc length; r=0.989 for voltage and r=0.957 for current with the 1.94 cm arc length; r=0.977 for voltage and r=0.956 for current with the 1.81 cm arc length; r=0.995 for voltage and r=0.983 for current with the 1.72 cm arc length; r=0.997 for voltage and r=0.995 for current with the 1.45 cm arc length; and r=0.992 for voltage and r=0.994 for current with the 1.11 cm arc length. The correlation coefficients confirm the validity of the Double Sinusoidal Model for simulating the I-t and V-t characteristics of dry-band arc compression events, and the assumptions of equations 6-23, 6-24 and 6-27 are satisfactory.

6.2.2 PSCAD SIMULATION FOR ARC COMPRESSION

6.2.2.1 SIMULATION CIRCUIT AND 'BRK' CONTROL CIRCUIT

The simulation circuit for dry-band arc compression is shown in Figure 6-8. The current limit resistor was chosen as 7.5 MΩ to better fit the experimental results. The reason for this is a possible error in the measurement of the original current limiting resistor used in experiment. The source voltage was fixed to 17.4 kV (RMS value) according to experimental conditions. The arrangement of circuit breaker control circuit was the same as in Figure 6-4. The settings of t_1 and t_2 for Impulse Generators 1 and 2 are based on the Equations 6-26 and 6-27 in part 6.2.1.1 of *Modelling Parameterization Based on Testing with Inclined Samples*. Therefore, the input of 'BRK' control circuit t_1 and t_2 are determined as: $t_1=3.02L_a-2.35$ (ms); $t_2=8.88$ (ms). The output of 'BRK' control signal for arc ignition and extinction in different compression situations is shown in Figure 6-9.

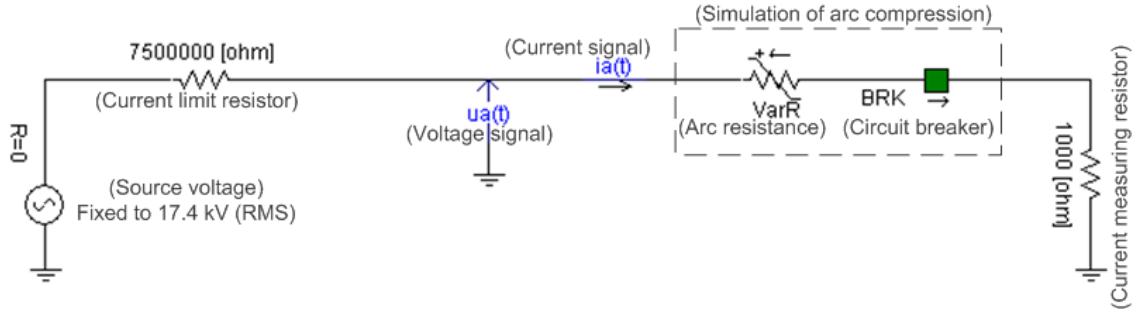

Figure 6-8: Simulation circuit for arc compression in PSCAD

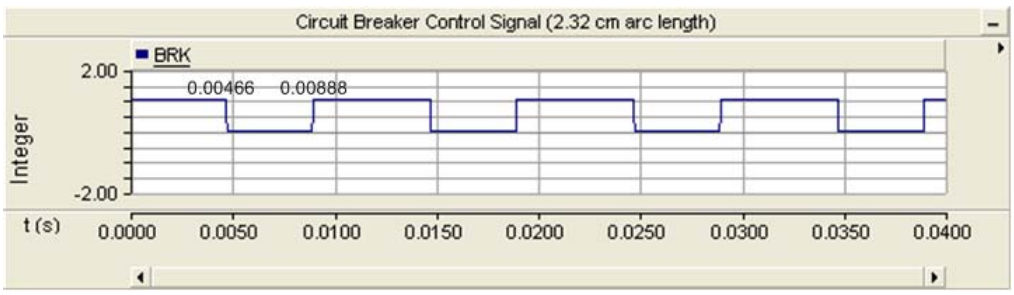

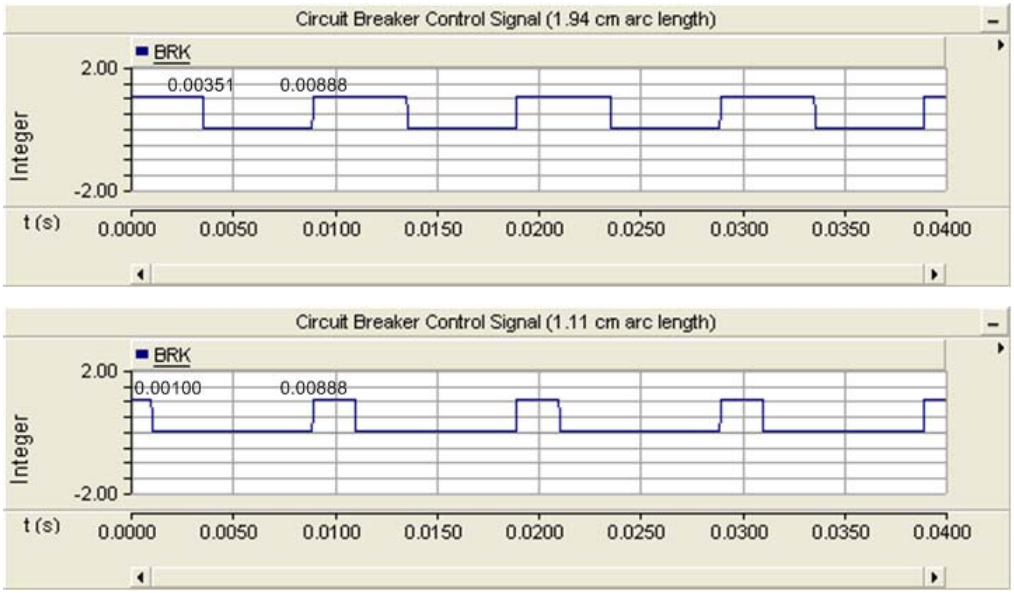

Figure 6-9: Example of control signal 'BRK' for different arc compression situations

6.2.2.2 SIMULATION OF INSTANTANEOUS ARC RESISTANCE FOR ARC COMPRESSION

For arc compression, the shape of instantaneous arc resistance changes with different arc length. Based on the *Double Sinusoidal Model*, Equations 6-30 and 6-31 within the period $t_1<t<t_2$ are used to calculate the arc resistance for compression situations as:

$$r_a(t)=\frac{u_a(t)}{i_a(t)}=\frac{10.19-\dfrac{3.21}{-3.02L_a+11.23}(t-3.02L_a+2.35)}{(-0.35L_a+2.78)\sin[0.408(t-1.12)]} \qquad 6\text{-}32$$

Where: $i_a(t)$ and $u_a(t)$ are the simulated current (mA) and voltage (kV) traces in the arcing period from the *Double Sinusoidal Model* for arc compression in Equations 6-30 and 6-31. $r_a(t)$ is the simulated instantaneous arc resistance (MΩ). L_a is the arc length which varies with different arc compression situations.

The simulation circuit for instantaneous arc resistance based on the calculation from equation 6-32 is demonstrated in Figure 6-10.

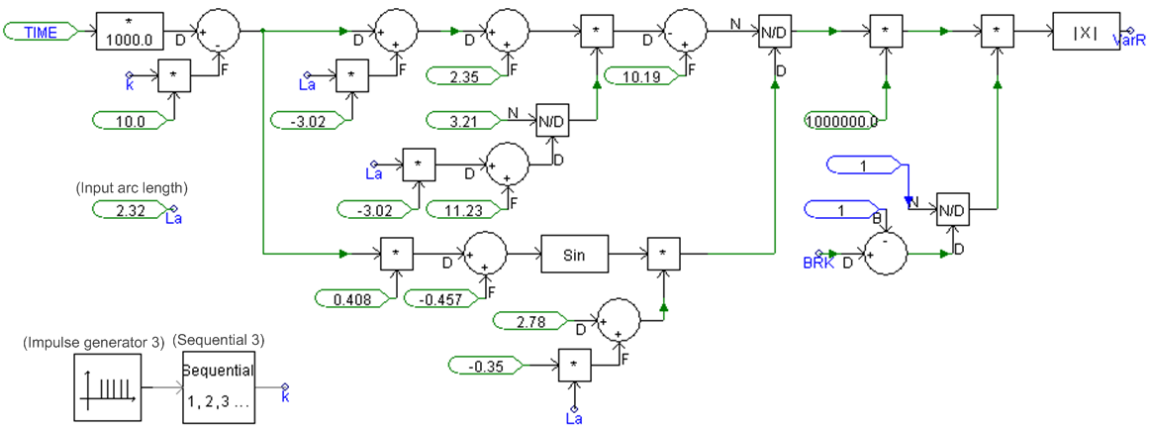

Figure 6-10: Example of control signal 'BRK' for different arc compression situations

The setting for Impulse Generator 3 remains at 100 Hz with the first impulse at 0.01 s, coordinating with Sequential 3 (starting point 0, increment 0.5) to generate an output 'k'. 'k' records the number of half cycles passed following the time elapses to achieve continuous arc resistance simulation in the time domain. The parameter of arc length L_a, which is used as the input of arc resistance simulation, is demonstrated in the circuit. Figure 6-11 gives an example of the simulation with a 2.32 cm arc length, and the output of arc resistance 'VarR' is shown in Figure 6-11, with examples included for different arc lengths.

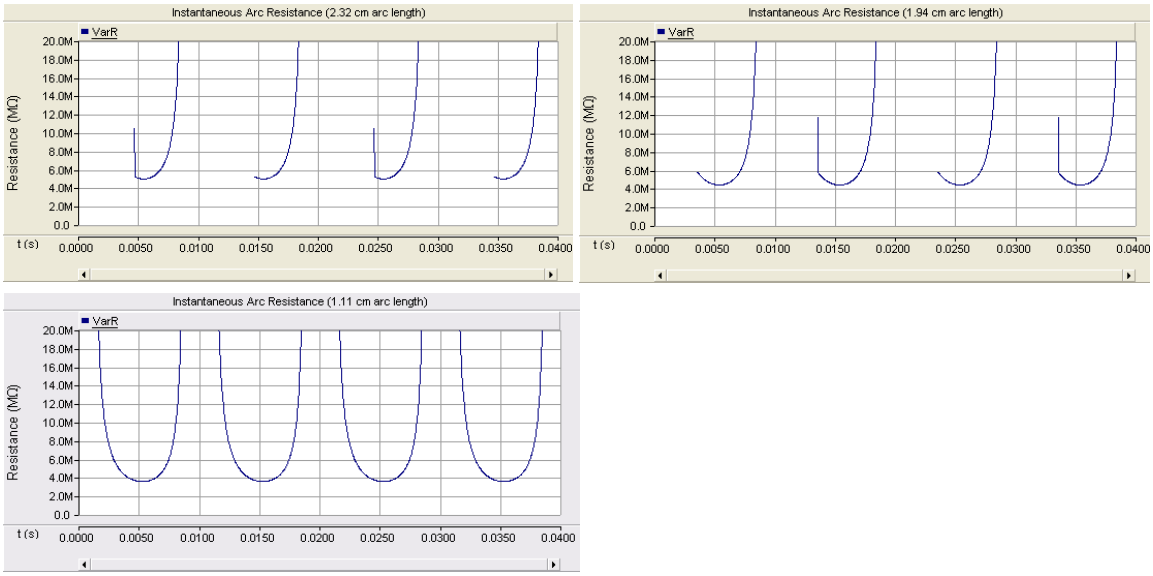

Figure 6-11: Examples of simulated arc resistance for arc lengths of 2.32, 1.94 and 1.11 cm during the arc compression

6.2.2.3 PSCAD SIMULATION RESULT FOR ARC COMPRESSION

By running the PSCAD simulation for arc compression, the I-t and V-t curves of dry-band arc with different arc compressed lengths from 2.32 cm to 1.11 cm current are simulated in Figure 6-12.

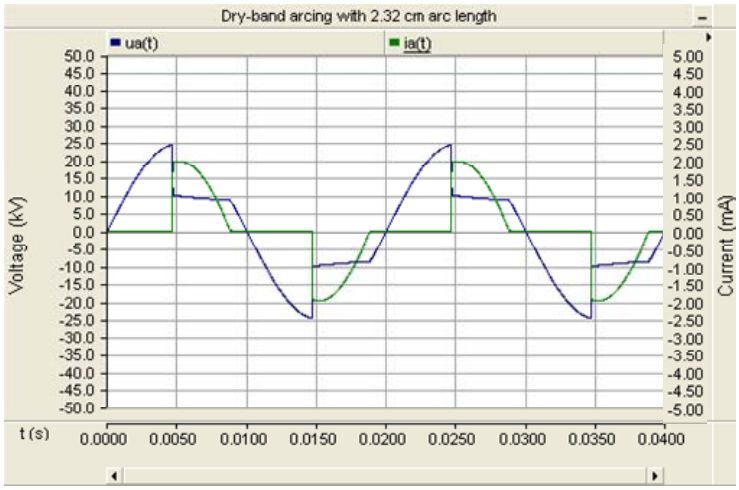

a) Simulated dry-band arcing with 2.32 cm arc length

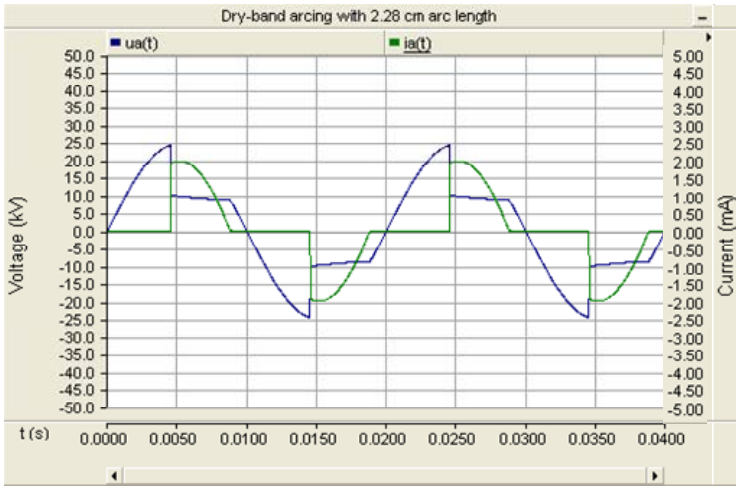

b) Simulated dry-band arcing with 2.28 cm arc length

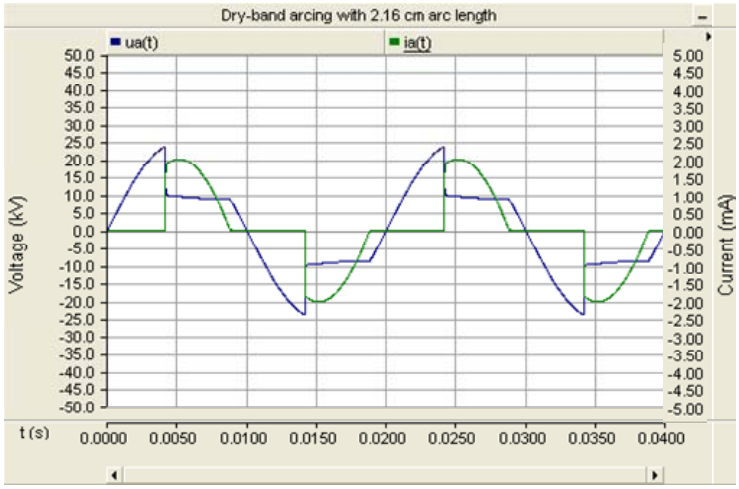

c) Simulated dry-band arcing with 2.16 cm arc length

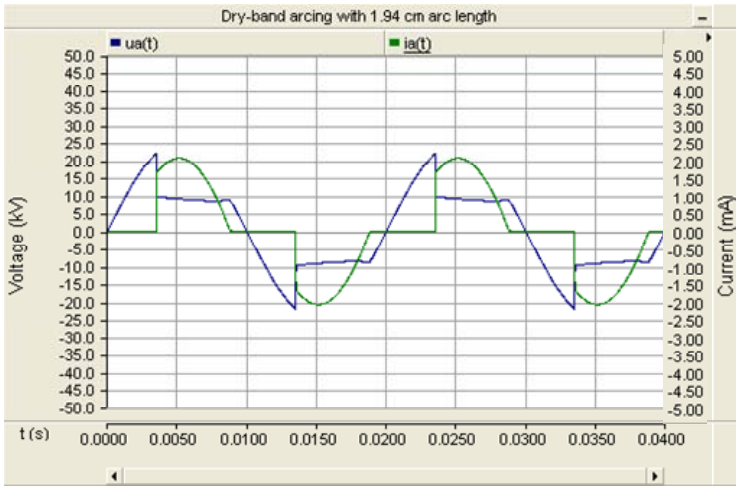

d) Simulated dry-band arcing with 1.94 cm arc length

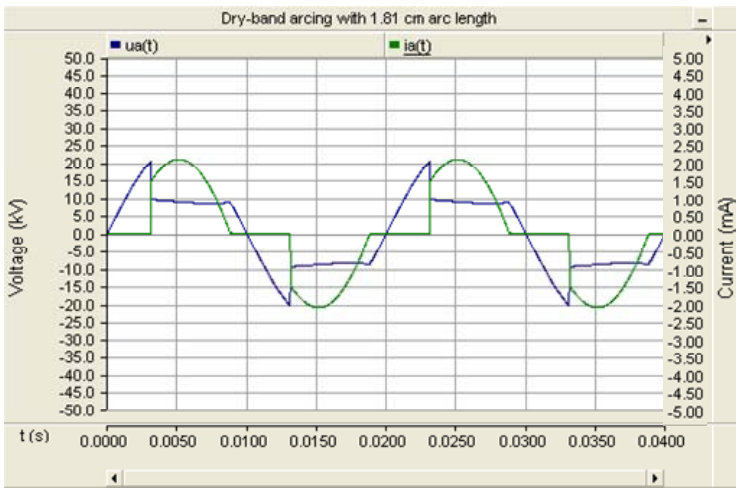

e) Simulated dry-band arcing with 1.81 cm arc length

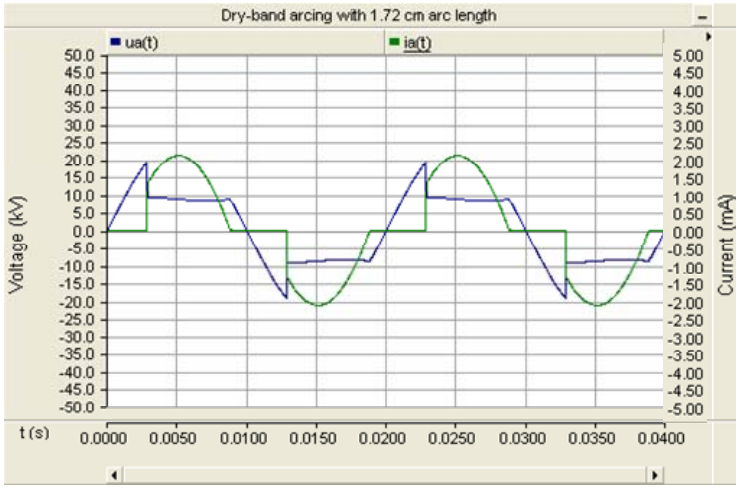

f) Simulated dry-band arcing with 1.72 cm arc length

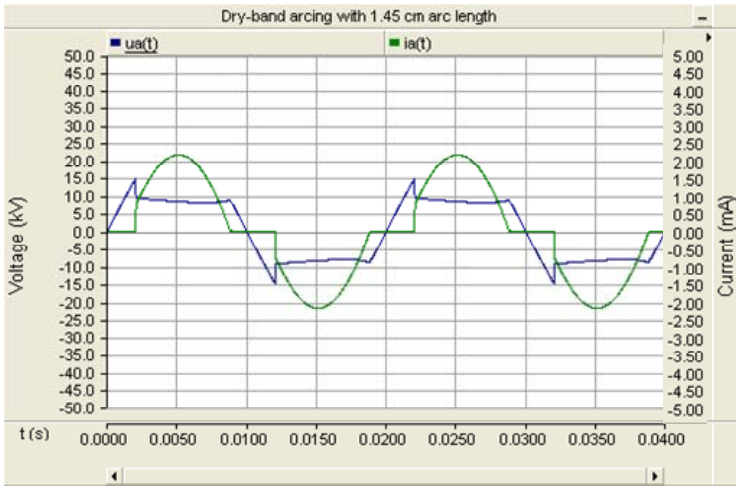

g) Simulated dry-band arcing with 1.45 cm arc length

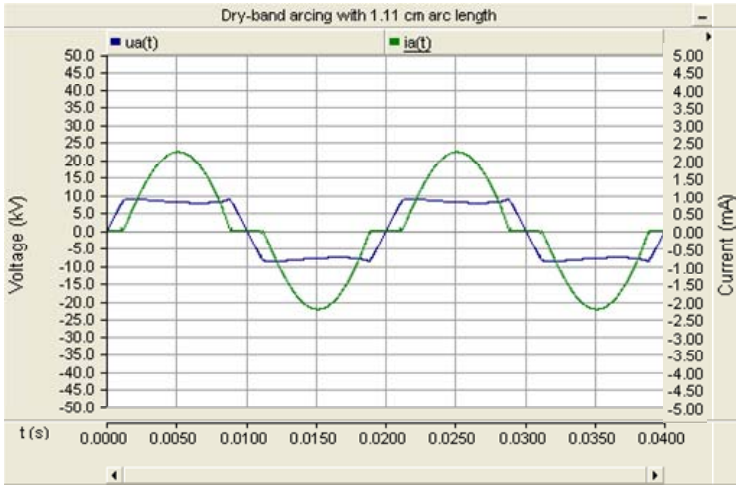

g) Simulated dry-band arcing with 1.11 cm arc length

Figure 6-12: PSCAD simulation result of I-t and V-t curves for arc compression with different arc lengths

The correlation coefficient 'r' of current (I-t) and voltage (V-t) curves for the situation of dry-band arc compression between experimental results from the *Testing with Inclined Samples*, modelling results from *Double Sinusoidal Model for arc compression*, and simulation results from *PSCAD/EMTDC* are summarized in Table 6-11.

Table 6-11: Correlation coefficients 'r' for current and voltage curves of arc compression between experimental results from Testing with Inclined Samples, modelling results from Double Sinuoidal Model, and simulation results from PSCAD

I-t and V-t curves of Stable Dry-band Arcs	Arcing Levels	Experiment Result		Double Sinusoidal Model		PSCAD Simulation	
		V	I	V	I	V	I
Experiment Result	2.32 cm	1.000	1.000	0.990	0.951	0.991	0.950
	2.28 cm	1.000	1.000	0.984	0.915	0.983	0.910
	2.16 cm	1.000	1.000	0.988	0.941	0.985	0.938
	1.94 cm	1.000	1.000	0.989	0.957	0.986	0.954
	1.81 cm	1.000	1.000	0.977	0.956	0.973	0.960
	1.72 cm	1.000	1.000	0.995	0.983	0.994	0.980
	1.45 cm	1.000	1.000	0.997	0.995	0.996	0.994
	1.11 cm	1.000	1.000	0.992	0.994	0.992	0.994
Double Sinusoidal Model	2.32 cm	0.990	0.951	1.000	1.000	0.997	0.993
	2.28 cm	0.984	0.915	1.000	1.000	0.997	0.993
	2.16 cm	0.988	0.941	1.000	1.000	0.997	0.994
	1.94 cm	0.989	0.957	1.000	1.000	0.997	0.996
	1.81 cm	0.977	0.956	1.000	1.000	0.997	0.997
	1.72 cm	0.995	0.983	1.000	1.000	0.997	0.997
	1.45 cm	0.997	0.995	1.000	1.000	0.997	0.998
	1.11 cm	0.992	0.994	1.000	1.000	0.996	0.999
PSCAD Simulation	2.32 cm	0.991	0.950	0.997	0.993	1.000	1.000
	2.28 cm	0.983	0.910	0.997	0.993	1.000	1.000
	2.16 cm	0.985	0.938	0.997	0.994	1.000	1.000
	1.94 cm	0.986	0.954	0.997	0.996	1.000	1.000
	1.81 cm	0.973	0.960	0.997	0.997	1.000	1.000
	1.72 cm	0.994	0.980	0.997	0.997	1.000	1.000
	1.45 cm	0.996	0.994	0.997	0.998	1.000	1.000
	1.11 cm	0.992	0.994	0.996	0.999	1.000	1.000

The results show 58% of 'r' reaches the correlations above 0.99, 75% of 'r' above 0.98, 79% of 'r' above 0.97, 81% of 'r' above 0.96, 92% of 'r' above 0.95 and all 'r' above 0.91. The correlation coefficient analysis indicates the good correlations between two kinds of simulation / modelling results and experiment results. It also proves the validation and accuracy of PSCAD simulation for dry-band arc compression.

6.2.3 Arc Energy and Energy Density during Arc Compression

Based on the simulation results of dry-band arc compression from the *Double Sinusoidal Model* and *PSCAD Simulation*, the respective energy trends during the arc compression process were calculated and compared with experimental results shown in Figure 6-13. The results show that in the situation of a dry-band being compressed in length, the reduction of arc length results in a rise in arc energy per half cycle.

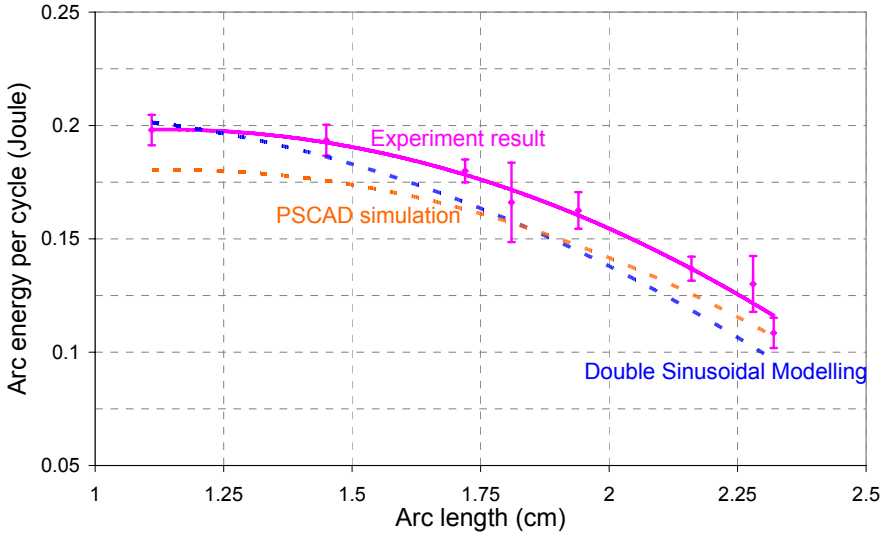

Figure 6-13: Experimental and simulation arc energy against arc length as a result of arc compression

Figure 6-14 demonstrates the change of arc energy density with arc length from experimental and simulation results. All the results agree that the energy density increases by a factor of 6 with the reduction of arc length from 2.32 cm to 1.11 cm. This is due to the simultaneous rise

of arc energy and the reduction of dry-band area during the arc compression.

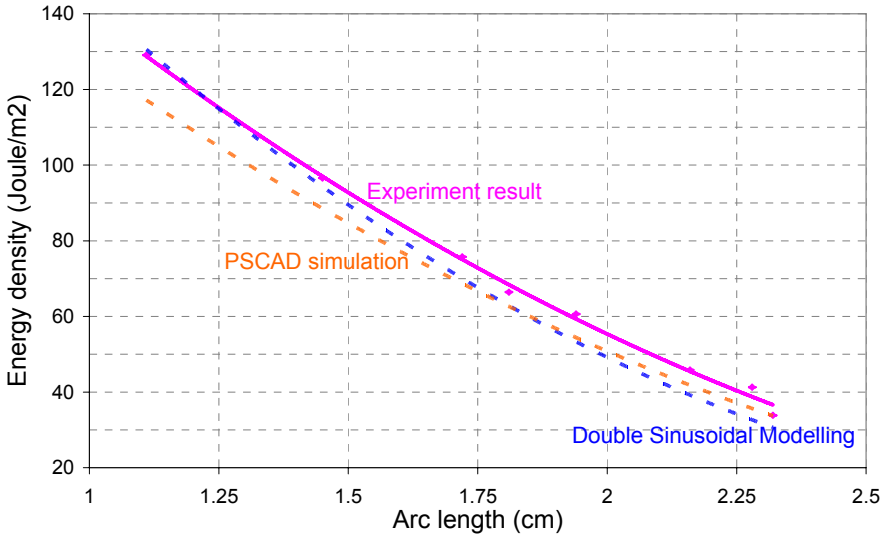

Figure 6-14: Experimental and simulation results of relationship between arc length and energy density charge during arc compression

6.3 MODELLING OF UNSTABLE DISCHARGES

6.3.1 PSCAD SIMULATION CIRCUIT FOR UNSTABLE DISCHARGES

As discussed previously in section 5.4 from the *Tests with Artificial Wind and Rain*, the unstable discharges with less than 1 mA peak current appears, with instabilities in both current and voltage signals, and can be transformed to a more stable status in certain conditions. In order to better understanding the electrical behaviour of unstable discharges, the PSCAD simulation was conducted based on the existing experimental arrangement. The detailed simulation circuit is shown in Figure 6-15.

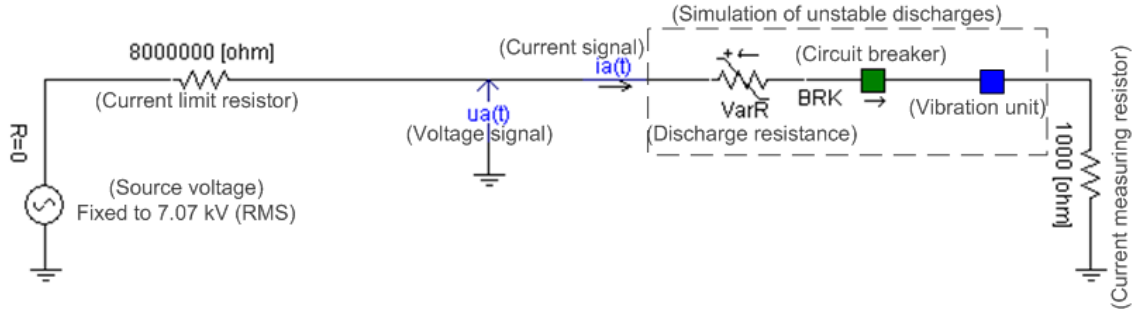

Figure 6-15: Simulation circuit for unstable discharges in PSCAD

The source voltage in the simulation was chosen as 7.07 kV (RMS) with a current limit resistor of 8 MΩ in order to create the similar experimental situations to the *Tests with Artificial Wind and Rain*. The simulation of unstable discharges contains the three separate units as: VarR, BRK and vibration unit. The VarR is used to simulate the instantaneous unstable discharge resistance during the discharge period. The BRK is to operate the circuit breaker to simulate discharge ignition and extinction at time of t_1 and t_2. By observing the experimental results, t_1 was fixed to 1.7 ms and t_2 was equal to 8.5 ms throughout the whole simulation. The BRK control circuit was arranged the same as in Figure 6-4 a). The output of BRK control signal to operate circuit breaker is shown in Figure 6-16.

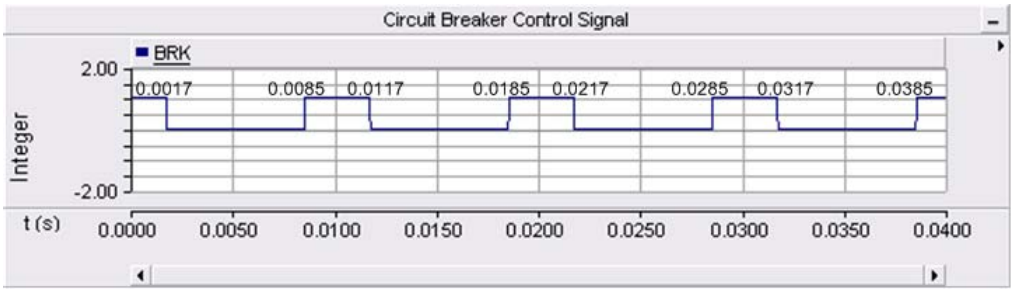

Figure 6-16: Control signal 'BRK' for simulation of unstable discharges

The vibration unit was designed for the simulation of unstable discharges. The detailed circuit for vibration unit will be demonstrated in the following part.

6.3.2 Simulation of Unstable Discharge Resistance with Vibration Unit

The simulation of instantaneous unstable discharge resistance consists of two parts: the smooth discharge resistance which is described in Figure 6-17 a); and the vibration discharge resistance with an example of 1000 Hz vibration frequency shown in Figure 6-17 b). The combination of two parts of resistance contributes to the entire unstable discharge resistance 'VarR' shown in Figure 6-17 c).

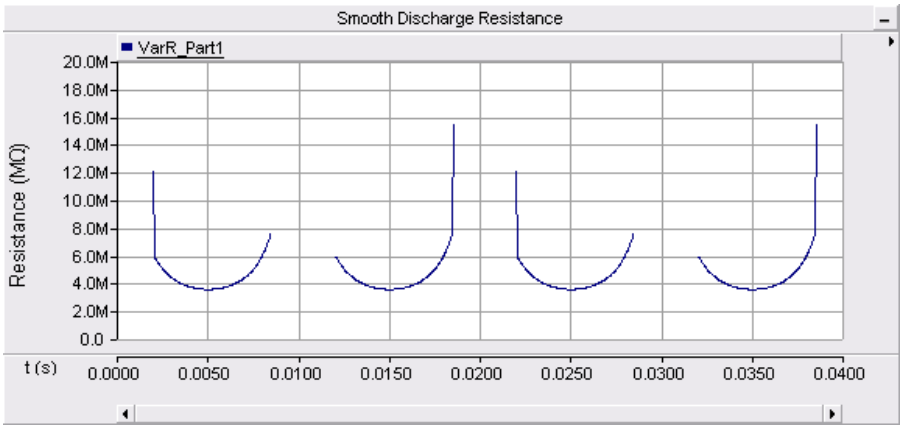

a) Resistance simulation part_1: The smooth discharge resistance

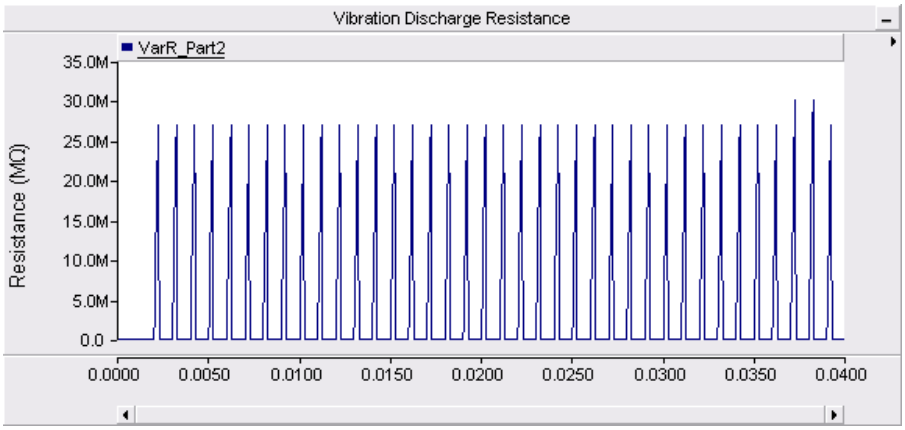

b) Resistance simulation part_2: The vibration discharge resistance

c) Combination of both parts as the output of entire unstable discharge resistance 'VarR'

Figure 6-17: Simulation result of entire unstable discharge resistance 'BRK'

Figure 6-18 shows the simulation circuit for generating these two parts of resistance. For the smooth discharge resistance, the simulation circuit is based on the Equation 6-33 observing directly from the experimental result of stable arcs. For the vibration discharge resistance, the simulation circuit contains the three vibration generation units which are impulse generator 1 (frequency of impulse train varies at 50~2000 Hz, initial impulse at 0.0017 s), impulse generator 2 (frequency of impulse train varies at 50~2000 Hz, initial impulse at 0.00225 s) and triangle signal generator (signal frequency fixes at 2000 Hz, maximum output level 60, minimum output level 0), coordinating with sequential 1 and sequential 2 (both with setting of starting point 0.0, increment 0.5), to generate vibration discharge resistance from the range of 50 Hz to 2000 Hz dependant on different development stage of the unstable discharges.

The combination circuit is used to combine the two parts of resistance together in order to obtain the entire unstable discharge resistance 'VarR' shown in Figure 6-17 c).

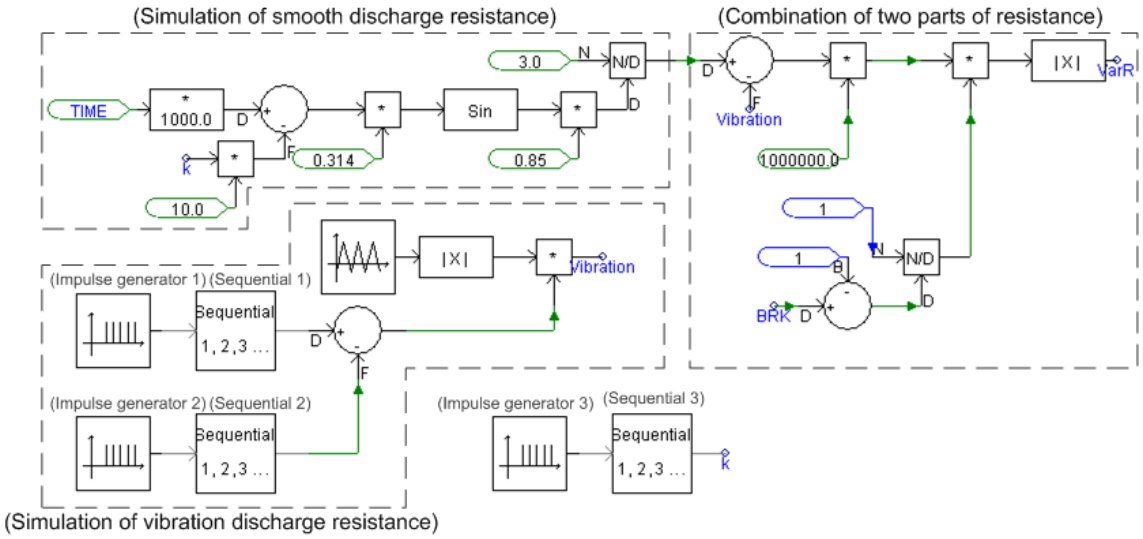

Figure 6-18: Simulation circuit for entire unstable discharge resistance

$$r_a(t) = \frac{u_a(t)}{i_a(t)} = \frac{3.0}{0.85\sin(0.314t)} \ \text{MΩ} \qquad \text{6-33}$$

6.3.3 PSCAD Simulation Results for Unstable Discharges

Based on the simulation circuit and control circuit stated from part 6.3.1 and 6.3.2, the simulation results for unstable discharges and the transforming process from unstable status to stable arc are shown in Figure 6-19, together with the relative experimental results from the *Tests with Artificial Wind and Rain*.

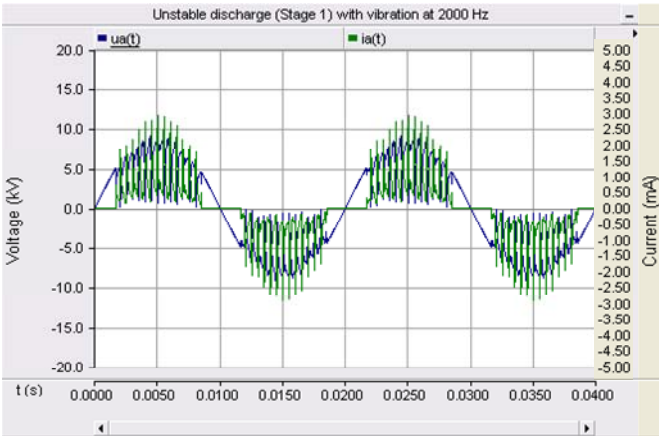

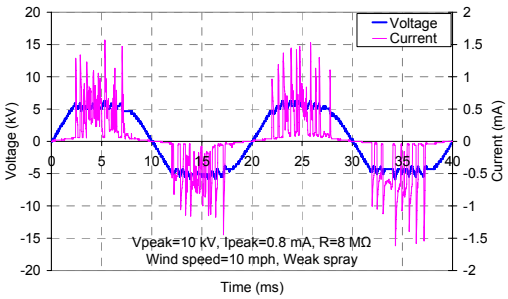

b) Experimental result at stage 1

Stage 1: a) Initial unstable discharges with vibration frequency at 2000 Hz

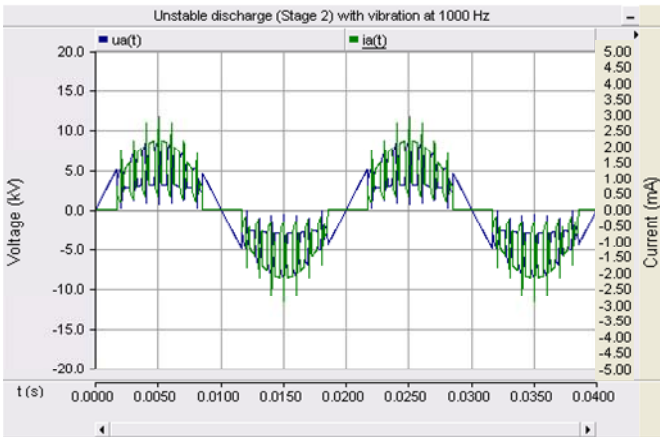

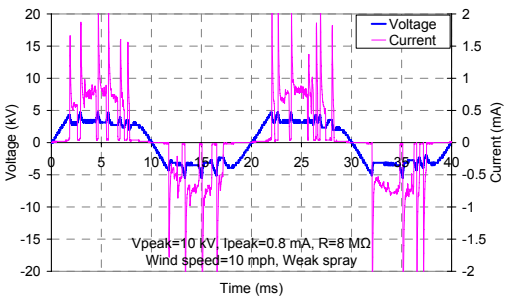

b) Experimental result at stage 2

Stage 2: a) Unstable discharges with reduced vibration frequency to 1000 Hz

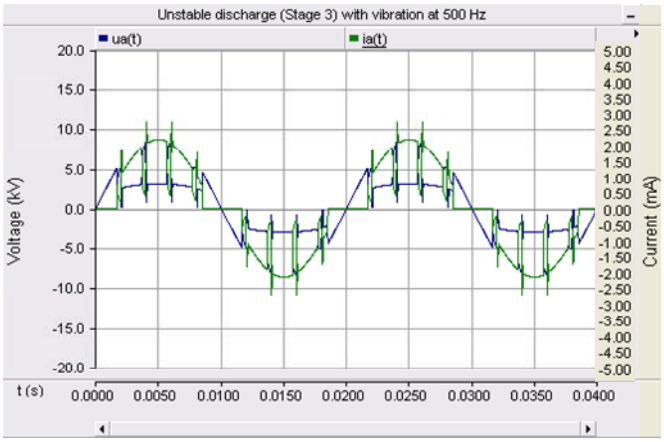

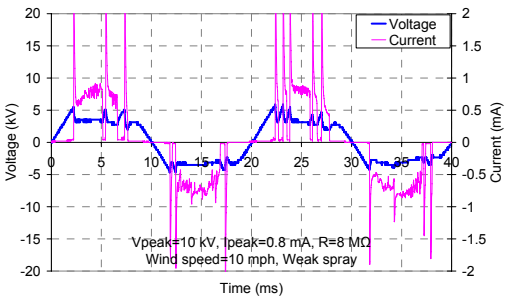

b) Experimental result at stage 3

Stage 3: a) Stable arcs appear accompany with vibration frequency at 500 Hz

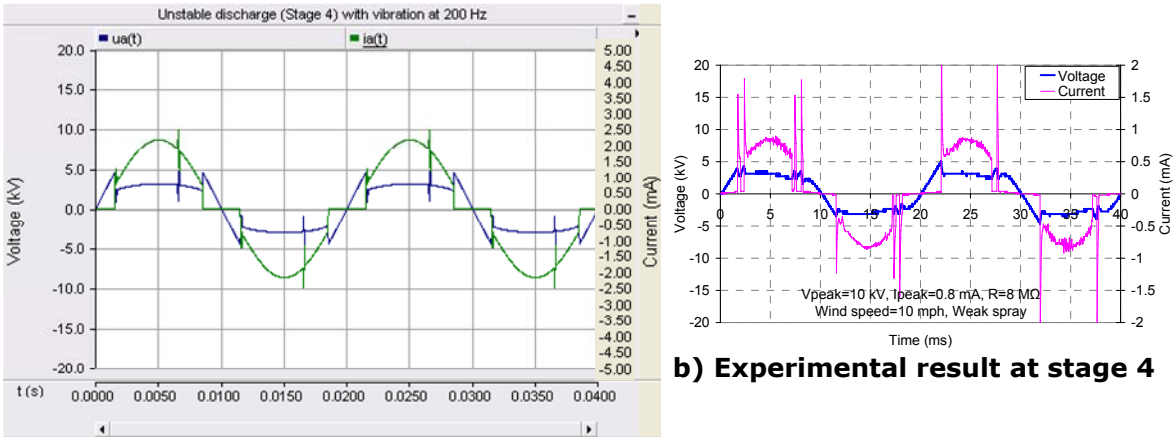

b) Experimental result at stage 4

Stage 4: a) Stable arcs dominate with reduced vibration frequency to 200 Hz

Figure 6-19: Simulation result of unstable discharges

The correlation coefficients 'r' between the simulation and experiment results of unstable discharges show r=0.69 for the voltage and r=0.76 for the current in stage 1; r=0.69 for the voltage and r=0.75 for the current in stage 2; r=0.67 for the voltage and r=0.83 for the current in stage 3; r=0.76 for the voltage and r=0.89 for the current in stage 4. In the real situation, the vibrations in the experimental results are random in each power cycles from stage 1 to 4, and difficult to be predicted in the simulation conditions. However, the PSCAD simulation here can reflect the main feature of unstable discharge phenomenon based on the experimental test circuit.

6.3.4 Arc Energy and Energy Density from Unstable Discharges to Stable Arcs

Based on the PSCAD simulation of unstable discharges become stable arcs, the energy trend during this process for respective four stages was calculated and shown in Figure 6-20, together with the previous experimental result from Figure 5-43 of the *Tests with Artificial Wind and Rain* in section 5.4. Result shows the agreed increase trends of energy for both experiment and simulation results, from unstable discharges to stable status. The simulation stage 1 (2000 Hz vibration discharges), stage 2 (reduced 1000 Hz vibration discharges) and part of

stage 3 (stable arc appears with 500 Hz vibration) could be classified as unstable discharge period according to experiment results. The rest simulation stage 4 (stable arc with lower than 500 Hz vibration) falls into the experiment indicated stable arc period with energy higher than 0.01 Joule per cycle.

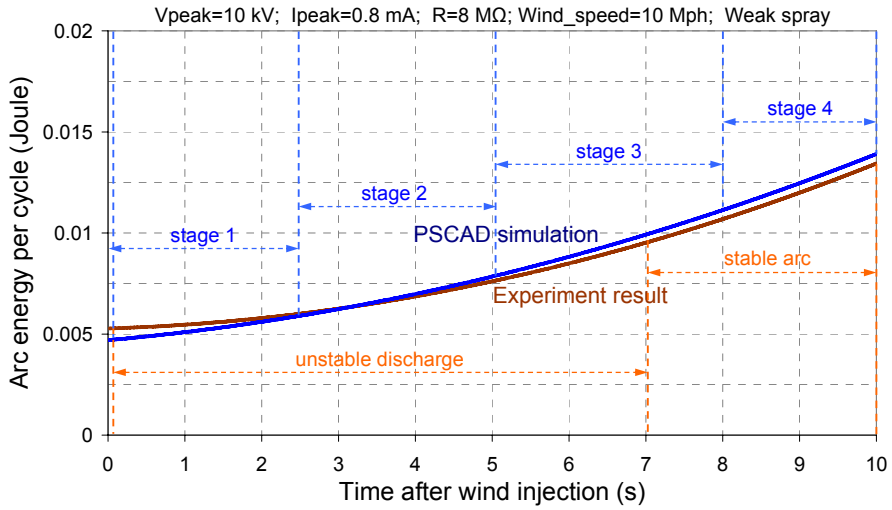

Figure 6-20: Arc energy trends from unstable discharges to stable arcs for both PSCAD simulation and experiment results

Figure 6-21 shows the energy density trends of unstable discharges becoming stable for the PSCAD simulation and experiment results. Both results show the similar trends that during the discharge status changing from unstable to stable, the energy density increases by an order of 10 times from initial unstable discharges to final stable arcs, which may give harmful effects on the insulation material surface due to this transformation process.

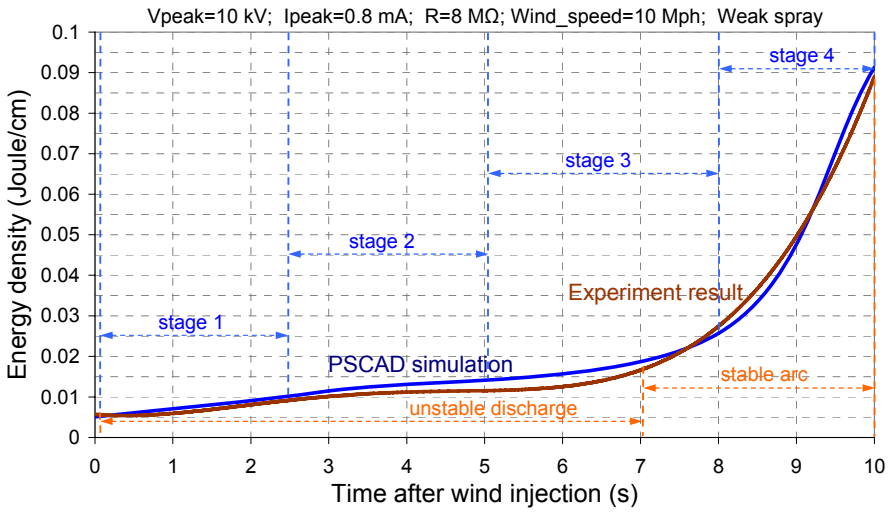

Figure 6-21: Energy density trends from unstable discharges to stable arcs for both PSCAD simulation and experiment results

6.4 MODELLING OF THERMAL DYNAMICS OF ARCS

6.4.1 TRIPLE CYLINDER MODEL

In order to further investigate the heat flow inside the low current arc (dry-band arc) and from the arc to its surroundings, the triple cylinder model is introduced. The ideal of the original model was developed for the investigation of high current (approximate 500A), low voltage (approximate 20V), and short (up to 6 mm) arcs between metal contacts in switchgear [63]. In this thesis, this model is applied to dry-band arcs with low current (1-5mA), high voltage (10-25kV) and between water electrodes. The reason why the thesis author used this model is that there are limited thermal dynamic models available for low current dry-band arcs. This is the best fitted model for the work here according to author's view. Figure 6-22 shows the proposed triple cylinder model.

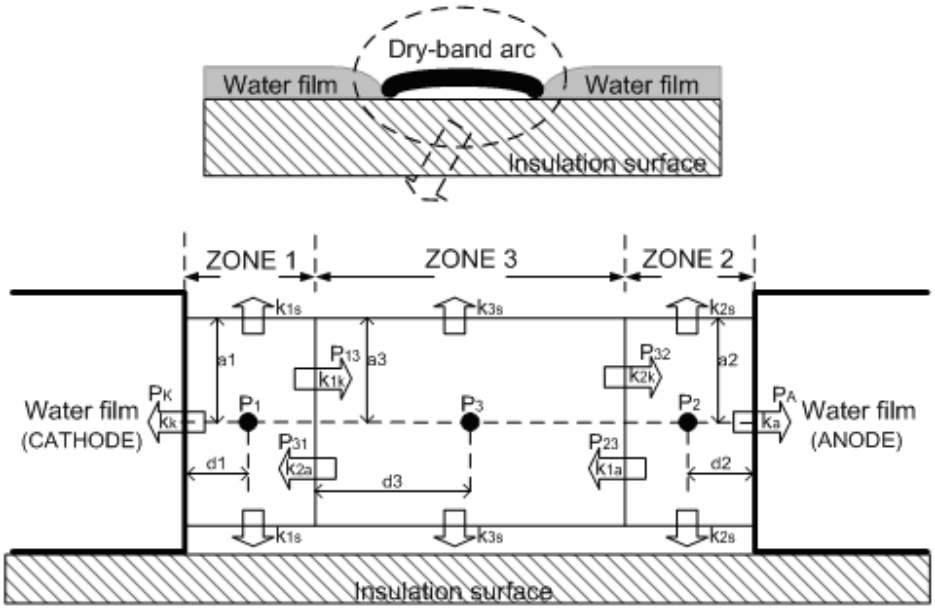

Figure 6-22: Triple cylinder thermal model with three distinguish zones and corresponding power flow in every direction

When the dry-band arcing occurs, the water film has been divided into two parts by the dry-band on the material surface. The edge of those two water film can be considered as cathode and anode electrodes respectively, while the dry-band area is assumed to be an air gap between these two electrodes at atmosphere pressure. In this model, three zones are identified as follows:

ZONE 1: CATHODE SPOT REGION (NEAR CATHODE ARC ZONE)

Zone 1 is defined as the 'cathode spot region' which is cylinder shaped with radius a_1 and length $2xd_1$. A concentrated source of heat P_1 is located in the geometrical centre of the cylinder. P_K is the power delivered to the cathode. P_{13} and P_{31} are the power transported to or from zone 3. k_k is the coefficient of heat penetration to the cathode. k_{1k} is the coefficient of the power flow from zone 1 to zone 3. k_{2a} is the coefficient of power flow from zone 3 to zone 1. k_{1s} is coefficient of power flow from zone 1 to the insulation surface.

ZONE 2: ANODE SPOT REGION (NEAR ANODE ARC ZONE)

Zone 2 is named as the 'anode spot region' which is cylinder shaped with radius a_2 and length $2xd_2$. A concentrated source of heat P_2 is located in the geometrical centre of the cylinder. P_a is the power delivered to the anode. P_{23} and P_{32} are the power transported to or from zone 2. k_a is the coefficient of heat penetration to the anode. k_{1a} is the coefficient of power flow from zone 2 to zone 3. k_{2k} is the coefficient of power flow from zone 3 to zone 2. k_{2s} is the coefficient of power flow from zone 2 to the insulation surface.

ZONE 3: ARC COLUMN (CENTRAL ARC ZONE)

Zone 3 is named as the 'arc column' which is cylinder shaped with radius a_3 and length $2xd_3$. A concentrated source of heat P_3 is located in the geometrical centre of the cylinder. K_{3s} is the coefficient of power flow from zone 3 to the insulation surface.

6.4.2 THERMAL FLOW CALCULATION

The modelling calculation is based on the arcing zones 1, 2 and 3 specified in the previous section. In each cylinder zone, a concentrated source of heat (P_1, P_2 or P_3) dissipates heat energy to both the cylinder lateral surfaces and cylinder faces as demonstrated in Figure 6-23.

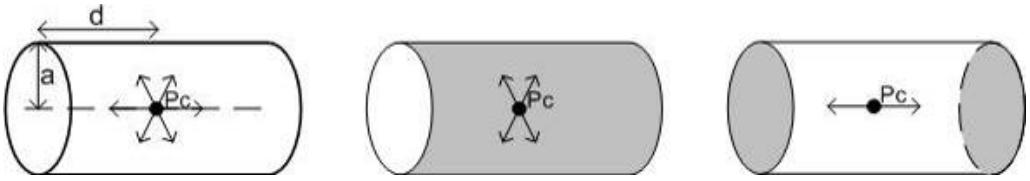

a) Cylinder model with Pc | **b) Power flowing through cylinder lateral surface** | **c) Power flowing through cylinder face**

Figure 6-23: Energy flow calculation for one cylinder model (each arcing zone) [63]

According to Figure 6-23 b), the total power flowing through the cylinder lateral surface is [63]

$$P_b = P_c \frac{d}{\sqrt{a^2 + d^2}} \qquad 6\text{-}34$$

Where: P_b is the power flowing through the cylinder lateral surface, P_c is the source power, a is the cylinder radius and d is half of the cylinder length.

According to Figure 6-23 c), the power flowing through one of the cylinder faces is [63]

$$P_p = \frac{1}{2} P_c \left(1 - \frac{d}{\sqrt{a^2 + d^2}}\right) \qquad 6\text{-}35$$

Where: P_p is the power flowing through the cylinder face.

Based on the Equations 6-34, 6-35 and power flowing diagram in Figure 6-22, the energy flows for triple cylinder model are summarized as follows:

The total instantaneous power delivered to the cathode is given by [63]

$$P_K(t)=\frac{1}{2}k_k\left\{P_1(t)\left(1-\frac{d_1(t)}{\sqrt{a_1(t)^2+d_1(t)^2}}\right)+k_{2a}\left\{\begin{array}{l}\frac{1}{2}P_3(t)\left(1-\frac{d_3(t)}{\sqrt{a_3(t)^2+d_3(t)^2}}\right)+\\ k_{1a}\frac{1}{2}P_2(t)\left(1-\frac{d_2(t)}{\sqrt{a_2(t)^2+d_2(t)^2}}\right)\end{array}\right\}\right\} \quad 6\text{-}36$$

Where: $P_K(t)$ is power delivered to the cathode, k_k is the coefficient of heat penetration to cathode, k_{2a} is the coefficient of power flow from the arc column to the cathode spot, k_{1a} is the coefficient of power flow from the anode spot to the arc column.

The total instantaneous power delivered to the anode is given by [63]

$$P_A(t)=\frac{1}{2}k_a\left\{P_2(t)\left(1-\frac{d_2(t)}{\sqrt{a_2(t)^2+d_2(t)^2}}\right)+k_{2k}\left\{\begin{array}{l}\frac{1}{2}P_3(t)\left(1-\frac{d_3(t)}{\sqrt{a_3(t)^2+d_3(t)^2}}\right)+\\ k_{1k}\frac{1}{2}P_1(t)\left(1-\frac{d_1(t)}{\sqrt{a_1(t)^2+d_1(t)^2}}\right)\end{array}\right\}\right\} \quad 6\text{-}37$$

Where: $P_A(t)$ is power delivered to the anode, k_a is the coefficient of heat penetration to the anode, k_{2k} is the coefficient of power flow from the arc column to the anode spot, k_{1k} is the coefficient of power flow from the cathode spot to the arc column.

Instantaneous powers from zone 1, zone 2 and zone 3 delivered to the material surface are given by

$$P_{1S}(t)=k_{1s}\left\{P_1(t)+k_{2a}\left\{\begin{array}{l}\frac{1}{2}P_3(t)\left(1-\frac{d_3(t)}{\sqrt{a_3(t)^2+d_3(t)^2}}\right)+\\ k_{1a}\frac{1}{2}P_2(t)\left(1-\frac{d_2(t)}{\sqrt{a_2(t)^2+d_2(t)^2}}\right)\end{array}\right\}\right\}\left(\frac{d_1(t)}{\sqrt{a_1(t)^2+d_1(t)^2}}\right) \quad 6\text{-}38$$

$$P_{2S}(t)=k_{2s}\left\{P_2(t)+k_{2k}\left\{\begin{array}{l}\frac{1}{2}P_3(t)\left(1-\frac{d_3(t)}{\sqrt{a_3(t)^2+d_3(t)^2}}\right)+\\ k_{1k}\frac{1}{2}P_1(t)\left(1-\frac{d_1(t)}{\sqrt{a_1(t)^2+d_1(t)^2}}\right)\end{array}\right\}\right\}\left(\frac{d_2(t)}{\sqrt{a_2(t)^2+d_2(t)^2}}\right) \quad 6\text{-}39$$

$$P_{3S}(t)=k_{3s}\left\{\begin{array}{l}P_3(t)+\frac{1}{2}k_{1k}P_1(t)\left(1-\frac{d_1(t)}{\sqrt{a_1(t)^2+d_1(t)^2}}\right)+\\ \frac{1}{2}k_{1a}P_2(t)\left(1-\frac{d_2(t)}{\sqrt{a_2(t)^2+d_2(t)^2}}\right)\end{array}\right\}\left(\frac{d_3(t)}{\sqrt{a_3(t)^2+d_3(t)^2}}\right) \quad 6\text{-}40$$

Where: $P_{1S}(t)$, $P_{2S}(t)$ and $P_{3S}(t)$ are the power delivered to material surface from zone 1, zone 2 and zone 3 respectively. k_{1S}, k_{2S} and k_{3S} are coefficients of heat penetration to material surface from zone 1, zone 2 and zone 3 respectively.

6.4.3 Thermal Flow for Dry-band Arc Compression

When the dry-band arc is compressed, three stages will be involved as described in Figure 6-24. The model used changes in different stages of compression as follows:

Stage 1:

In the first stage, the length of arc column (zone 3) is reducing, while the lengths of zone1 and zone2 are assumed unchanged. The thermal calculation is based on the *Three Cylinder model* at this stage.

Stage 2:

The arc length continues reducing until equal to the zone 1 and zone 2 lengths, when the arc column (zone 3) disappears. The *Three Cylinder model* without zone 3 will then be used for heat flow calculation.

STAGE 3:

In the final stage, zone1 and zone 2 are compressed equally until the arc length reduces to zero.

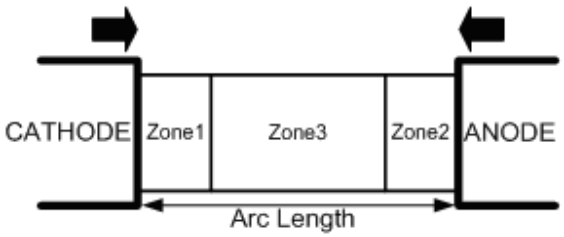

a) Dry-band arc compression stage 1

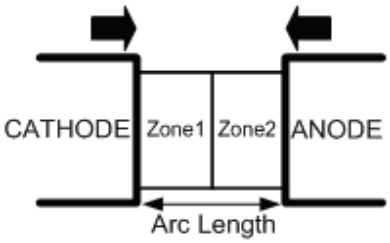

b) Dry-band arc compression stage 2

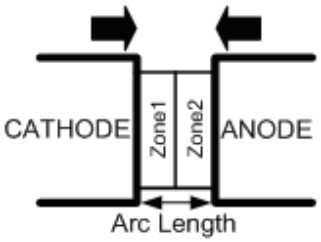

c) Dry-band arc compression stage 3

Figure 6-24: Thermal modelling of dry-band arc compression

6.4.4 MODELLING PARAMETERIZATION FOR THE TRIPLE CYLINDER MODEL

a_1, a_2, a_3 – THE CYLINDER RADIUS FOR ZONE 1, ZONE 2 AND ZONE 3

An assumption is made that $a_1(t)=a_2(t)=a_3(t)$ at all times during the dry-band arcing and arcing compression process. This assumption is supported by the literature [63] and made for simplification purposes. $a_i(t)$ is calculated from

$$a_1(t) = a_2(t) = a_3(t) = K_L i_a(t) \text{ mA} \quad \text{6-41}$$

Where: $i_a(t)$ is the instantaneous arc current, K_L is the constant coefficient so that the cylinder radius changes in time with the instantaneous arc current. Proportionality is assumed so that a higher current corresponds to a thicker arcing zone. K_L can be determined from the maximum value of $a_1(t)$ and the maximum available current of $i_a(t)_{max}$. From the measurement of the water layer thickness based on the specified salt-fog precipitation rate in the *Testing with Inclined Samples*, $a_1(t)_{max} \approx 1$ mm. $i_a(t)_{max}=1.89$ mA according to the previous test result with 0° slope angle, and so $K_L=(1 \text{ mm})/(1.89 \text{ mA}) =0.0005278$ m/mA.

d_1, d_2, d_3 – THE CYLINDER LENGTH FOR ZONE 1, ZONE 2 AND ZONE 3

An assumption is made that $d_1(t)=d_3(t)$ at all times during the dry-band arc and arcing compression process. $d_2(t)$ is changed with physical arc length following the arc compression process. The following assumptions are made: $d_1(t)=d_3(t)=a_1(t)=a_3(t)$ when $d_2(t) \neq 0$ (representing stage 1 during the arcing compression in part 6.4.3); $2d_1(t)=2d_3(t)=L_a/2$ when $d_2(t)=0$ (representing the stage 2 and 3 during the arcing compression in part 6.4.3). These assumptions are from [63] and for simplification.

$u_1(t)$, $u_2(t)$, $u_3(t)$ – THE VOTALGE DISTRIBUTIONS IN ZONE 1, ZONE 2 AND ZONE 3

Voltage drops in zone 1, zone 2 and zone 3 are assumed to be identical [63]. Therefore, $u_1(t)=u_2(t)=u_3(t)=u_a(t)/3$, where $u_a(t)$ is the instantaneous arc voltage. This assumption is from [63] and for simplification.

$i_1(t)$, $i_2(t)$, $i_3(t)$ – THE CURRENT THROUGH ZONE 1, ZONE 2 AND ZONE 3

Current flowing through zone 1, zone 2 and zone 3 are assumed to be identical. Therefore, $i_1(t)=i_2(t)=i_3(t)=i_a(t)$, where $i_a(t)$ is the instantaneous arc current.

$p_1(t)$, $p_2(t)$, $p_3(t)$ – THE POWER IN ZONE 1, ZONE 2 AND ZONE 3

$p_1(t)$, $p_2(t)$ and $p_3(t)$ are instantaneous concentrated power located in the geometry centre of zone 1, zone 2 and zone 3 respectively. The following equations $p_1(t)=u_1(t)xi_1(t)$, $p_2(t)=u_2(t)xi_2(t)$, $p_3(t)=u_3(t)xi_3(t)$ are used to calculate $p_1(t)$, $p_2(t)$ and $p_3(t)$ in the modelling calculation.

k_k, k_{1a}, k_{2a}, k_a, k_{1k}, k_{2k}, k_{1s}, k_{2s}, k_{3s} – Coefficients from Equations 6-36 to 6-40 in Triple Cylinder Model

According to the thermal measurement, the average arcing temperature is around 300 °C. The edge of water film is up to 100 °C, for the reason that the water evaporation and deposition rate are in the dynamic balance, maintaining the water temperature to be approximately 100 °C. Therefore, the heat transfer coefficients are ambitiously calculated as 100 °C/300 °C≈30%, which makes the values of k_k, k_a, k_{1s}, k_{2s}, k_{3s} to be 0.3. The coefficients of heat transfer between different arc regions are set to $K_{1a}=k_{2a}=k_{1k}=20\%$, $k_{2k}=50\%$ according to literature [63].

Table 6-12 summarizes all the coefficients used in the *Triple Cylinder Model* described from Equations 6-36 to 6-40.

Table 6-12: Calculated coefficients for Triple Cylinder Model [63] based on *Testing with Inclined Samples*

Slope Angle (DEG)	Arc Length (cm)	Kk	K1a	K2a	Ka	K1k	K2k	K1s	K2s	K3s
0°	2.32	0.3	0.2	0.2	0.3	0.2	0.5	0.3	0.3	0.3
5°	2.28	0.3	0.2	0.2	0.3	0.2	0.5	0.3	0.3	0.3
10°	2.16	0.3	0.2	0.2	0.3	0.2	0.5	0.3	0.3	0.3
15°	1.94	0.3	0.2	0.2	0.3	0.2	0.5	0.3	0.3	0.3
20°	1.81	0.3	0.2	0.2	0.3	0.2	0.5	0.3	0.3	0.3
25°	1.72	0.3	0.2	0.2	0.3	0.2	0.5	0.3	0.3	0.3
30°	1.45	0.3	0.2	0.2	0.3	0.2	0.5	0.3	0.3	0.3
35°	1.11	0.3	0.2	0.2	0.3	0.2	0.5	0.3	0.3	0.3
40°	0.00	0.3	-----	-----	0.3	-----	-----	0.3	0.3	-----

6.4.5 Calculation Results from Triple Cylinder Model

The power distribution inside the arcing region and radiation from the arcing plasma to its surrounding were calculated in Matlab and the designed program shown in [Appendix 1.2]. These calculations were based on the *Triple Cylinder Model* proposed from Equations 6-36 to 6-40, the parameters estimation from part 6.4.4, and test results of current $i_a(t)$ and voltage $u_a(t)$ curves from *Testing with Inclined Samples* as modelling input. Figure 6-25 gives examples of calculation results of arc power radiation to different directions including to the insulation material surface.

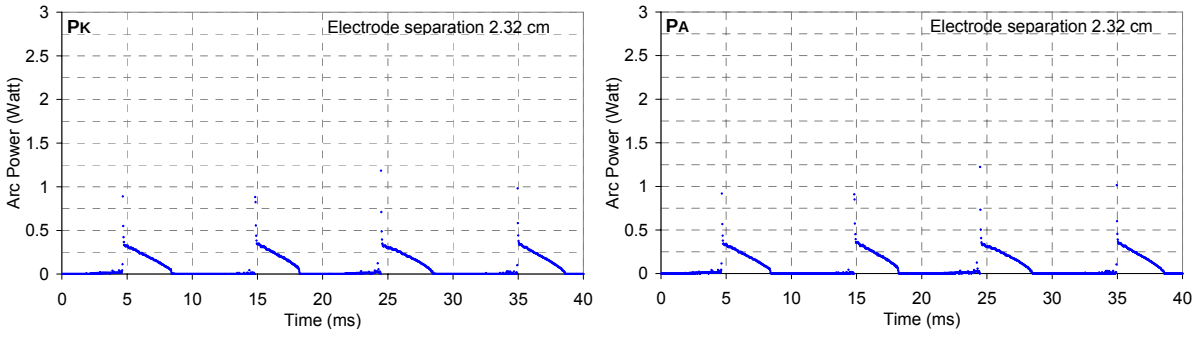

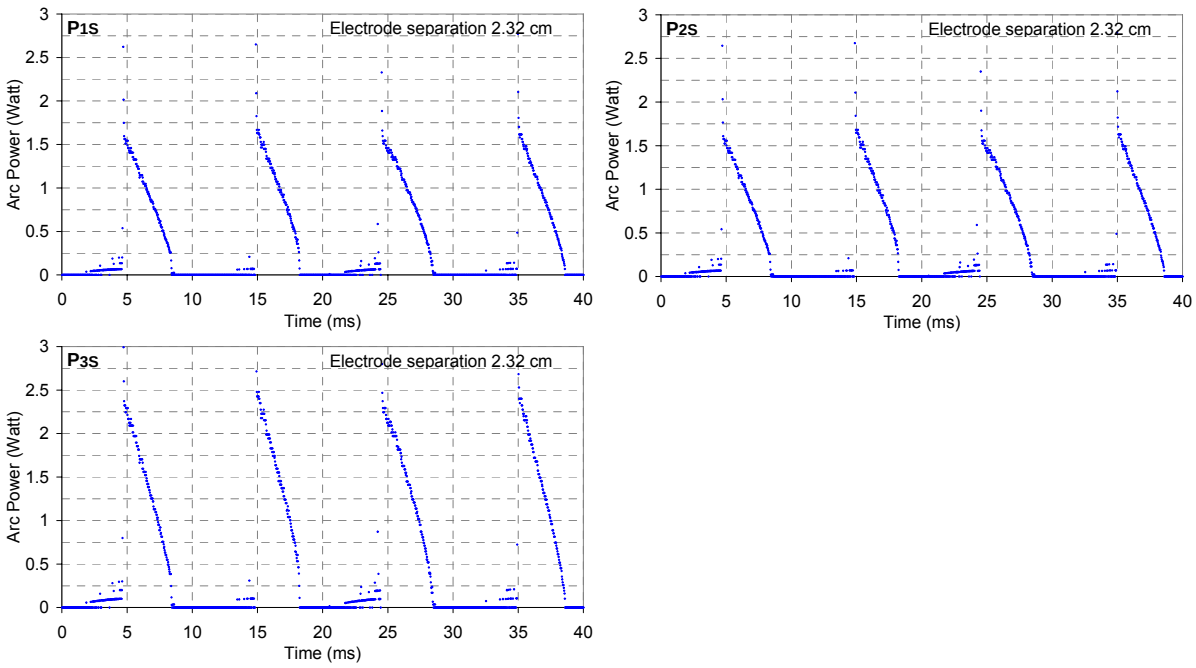

a) Instantaneous power radiations for 2.32 cm arc length

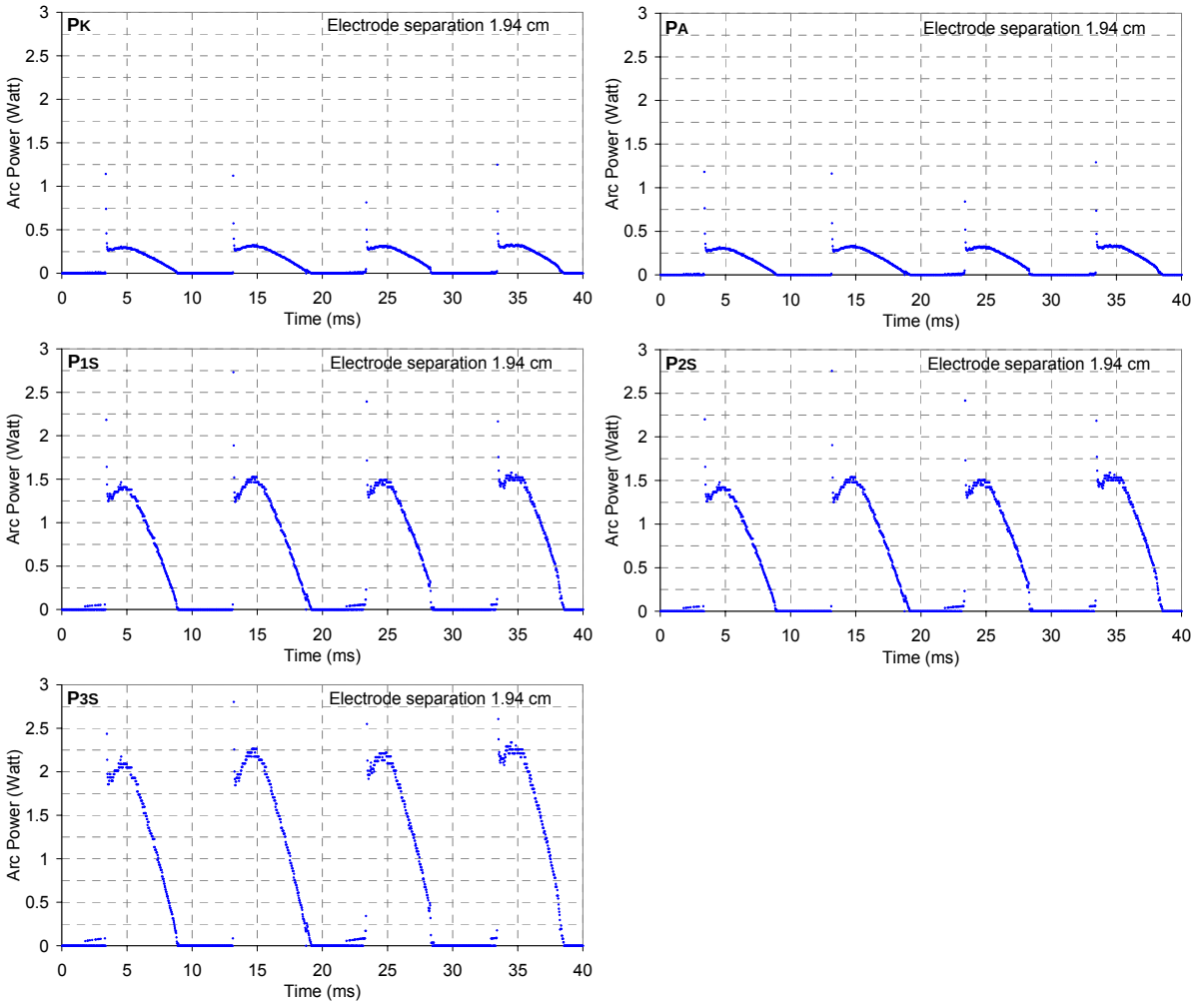

b) Instantaneous power radiations for 1.94 cm arc length

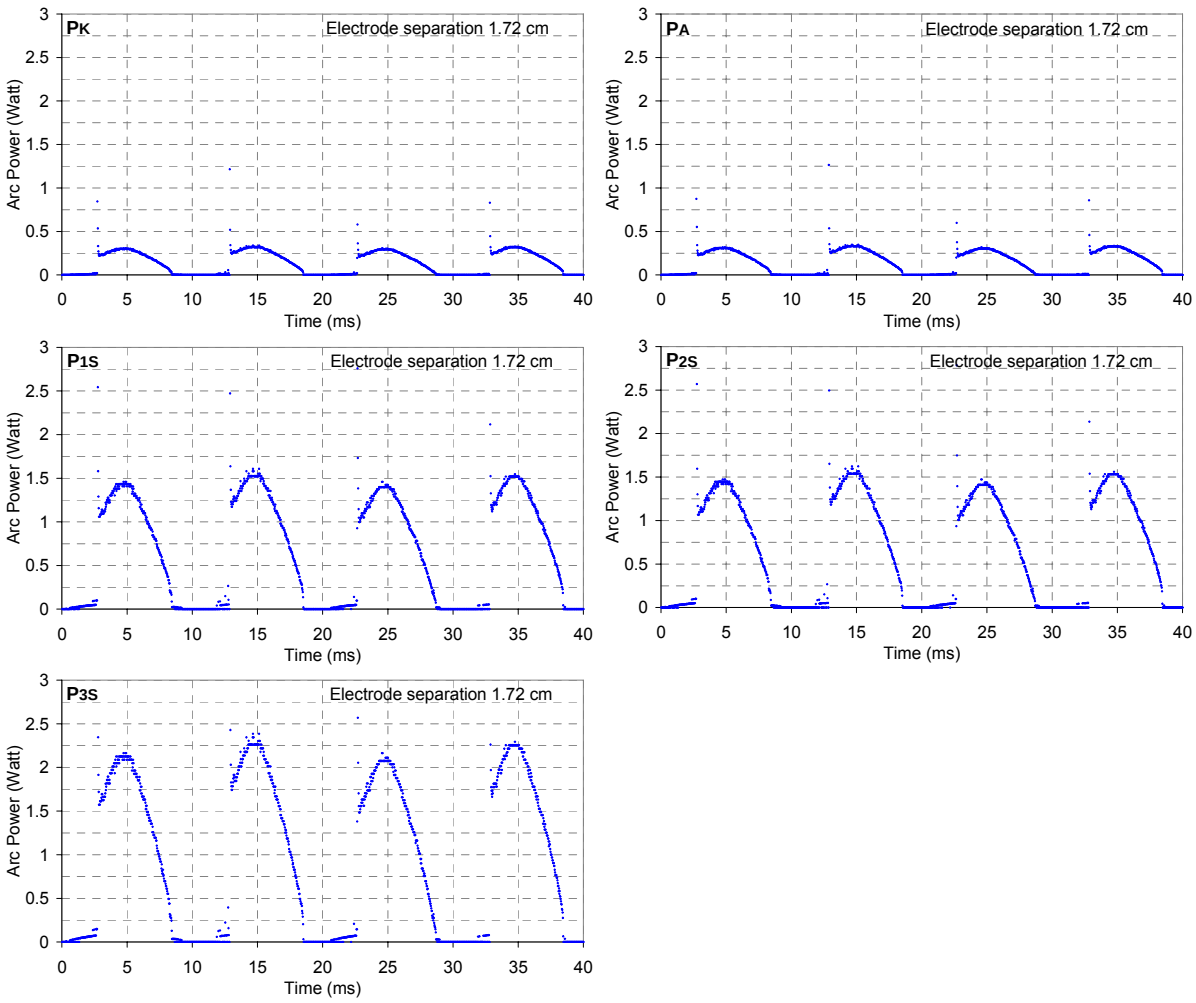

c) Instantaneous power radiations for 1.72 cm arc length

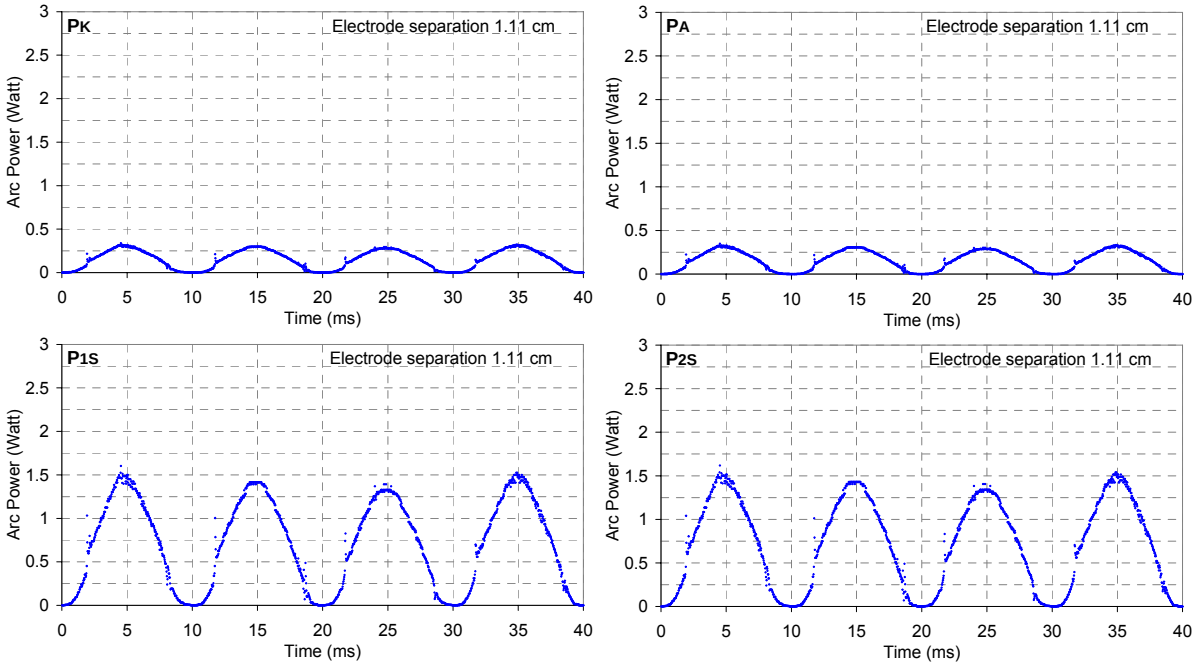

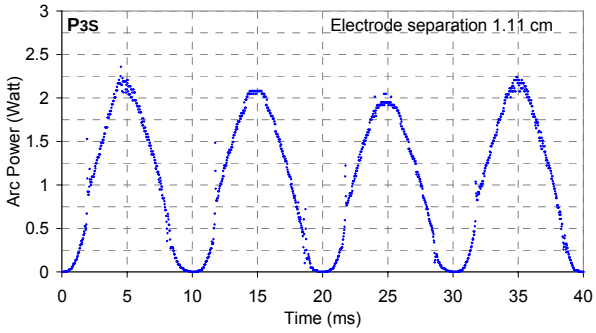

d) Instantaneous power radiations for 1.11 cm arc length

Figure 6-25: Result of calculated power radiation from zone 1, zone 2 and zone 3 to cathode (P_K), anode (P_A), and insulation material surfaces (P_{1S}, P_{2S}, P_{3S})

Based on the calculation results of instantaneous power radiations; the total energy dissipation in all directions from the arc can be calculated by using Equation 6-42 in Matlab [program in Appendix 1.3], and the results are shown in Table 6-13.

$$E = \int_0^T P(t)tdt \qquad 6\text{-}42$$

Where: E is the accumulated energy for one power cycle of dry-band arcing. T is 20 ms. P(t) is the instantaneous arc power radiation for each direction calculated shown in Figure 6-25.

Table 6-13: Energy radiation from dry-band arcing to surroundings in a power cycle

Arc Length	Energy to Cathode	Energy to Anode	Cathode to Insulation Surface	Anode to Insulation Surface	Column to Insulation Surface
L_a [cm]	E_K [Joule]	E_A [Joule]	E_{1S} [Joule]	E_{2S} [Joule]	E_{3S} [Joule]
2.32	0.001622	0.00167	0.00772	0.007789	0.011478
2.28	0.001944	0.002002	0.009254	0.009337	0.013758
2.16	0.002045	0.002106	0.009733	0.00982	0.014466
1.94	0.002429	0.002503	0.011561	0.011665	0.017175
1.81	0.002483	0.002559	0.011818	0.011925	0.017547
1.72	0.00269	0.002772	0.012802	0.012919	0.019005
1.45	0.002893	0.002984	0.013766	0.013893	0.020408
1.11	0.002964	0.003061	0.014091	0.014228	0.020821

Figure 6-26 shows the examples of energy dissipation extracted from Table 6-13. The energy calculation results show that following the dry-band arc compression process, the energy dissipations in all directions from the arc (E_K, E_A, E_{1S}, E_{2S} and E_{3S}) are increased. E_{1S}, E_{2S} and E_{3S}, which are respective energy radiations from cathode, anode and arc column to insulation material surfaces, give the largest contribution.

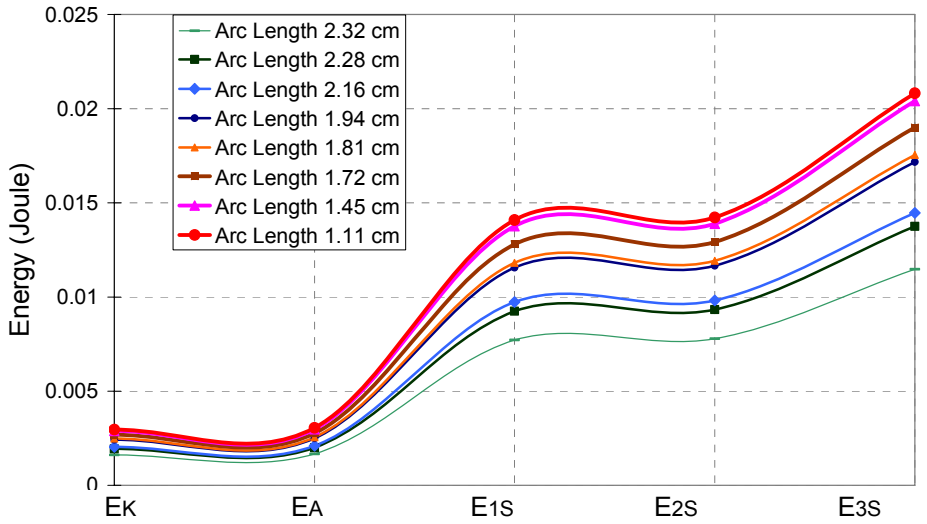

*(E_K=Energy to Cathode, E_A=Energy to Anode, E_{1S}=Cathode to Insulation Surface, E_{2S}=Anode to Insulation Surface, E_{3S}=Column to Insulation Surface)

Figure 6-26: Modelling results of dry-band arcing energy for different radiation directions

6.5 SUMMARY

The two simulation approaches, which are the respective *Double Sinusoidal Model* and *PSCAD simulation*, have been proposed to simulate low current dry-band arcing events. The *Double Sinusoidal Model* was based on test results from Chapter 5 of the *Thesis Experimental Part*, while the *PSCAD simulation* was based on the test circuit arrangement for variable testing conditions. The outcome of simulated current and voltage curves from both simulation approaches show good correlation with experimental data, for the different situations of stable arcs, arc compression and process of unstable discharges becoming stable. The simulation work agrees with experimental work showing that a dry-band arc will become more detrimental if it is transformed from unstable discharges to stable arcs, or physically compressed in length, for any reason.

The *Triple Cylinder Model [63]*, which integrates the *Double Sinusoidal Model* as the input data, is able to calculate the energy flow inside the arc region and from arc to its environment. This thermal modelling work indicates that when the arc is compressed in length due to external movement of adjacent moisture for the reason either by gravity or wind, the arc energy radiation is enhanced in all the directions from the arc plasma to its surrounding. The worst case may happen when the arc length is extremely short, which could increase the possibility of damage to the substrate. The instantaneous arc power and accumulated arc energy in the middle of arcing area facing the material surface are highest. Therefore, the material may suffer more damage across that region. The energy dissipation to both water electrodes (edge of two water films) is lower than other directions. The compression of naturally occurring dry-band arcs may therefore consequently accelerate the material ageing process.

CHAPTER 7

DISCUSSION

7.1 LONG-TERM LOW CURRENT AGEING WITHOUT DISCHARGES

The research on a retired ADSS cable after 15 years' service found evidence of surface degradation under long-term low current ageing. The visual observation verified no major ageing signs were contributed from electrical discharges. However, the contact angle measurement revealed the cable sheath had lost its hydrophobicity, and this surface change was non-uniform and variable along the entire cable span. Further electric field calculation successfully correlated with cable surface degradation indicating that long term low leakage current could possibly reduce the surface quality of outdoor insulation materials. This is the first of such observation. The main reason for this form of degradation may come from the long time Joule heating effect. The surface sections which are subject to relatively higher leakage currents may lose their hydrophobicity first, and in turn, allows moisture to be more easily deposited. The moisture may further bring larger leakage current passing through and again reduce the hydrophobicity on such surface sections. Those two physical mechanisms may be further affected and accelerated by each other, and eventually cause surface degradation on outdoor insulations.

7.2 THE PROPERTIES OF LOW CURRENT ARCS

7.2.1 ARC STABILITY AND CURRENT

Research in [30] suggests that the arc voltage is only responsible for arc ignition, and the arc energy (reflected by arc current) is the key factor

to sustain an arc. In the Chapter 5 of *Thesis Experimental Part*, for the cases of peak arcing currents higher than 1 mA, stable arcs are observed with sustained arcing current and voltage profiles throughout the whole arcing period, shown in Figure 5-5, Figure 5-17, Figure 5-32 and Figure 5-41. A special case appears in Figure 5-31 b) from the *Tests between Water Drops*, with an unstable discharge observed under a 25 kV source voltage and between 1.0 cm electrode separation. In this case the voltage is high enough to generate a discharge, but the electrode separation is too large to sustain an arc. By reducing the water electrode separation to 0.8 cm, a stable arc is observed.

The unstable discharges are observed for the discharge current below 1 mA in Figure 5-40 of the *Tests with Artificial Wind and Rain*. In this case the current (energy) is insufficient to sustain an arc, so that the discharge appears as 'unstable'. These unstable discharges (with energy less than 0.01 Joule per cycle) could be transformed into stable arcs (with energy higher than 0.01 Joule per cycle) by external wind effect to reduce the dry-band length, and therefore creating a shorter discharge length. This transformation process has been successfully achieved in experimental conditions even when the arcing current was less than 1 mA.

From the research in this thesis, it is clear that both factors of insufficient arcing current (energy) and the long discharge length could contribute to the instability of low current arcs. This unstable status could be possibly transferred into a stable one by increasing the arc current level or reducing the discharge route. The threshold current (energy) between unstable and stable discharges is 1 mA (0.01 Joule per cycle) according to the experimental work in this thesis.

7.2.2 ARC LENGTH

Generally, arc length changes instantaneously with variable instantaneous arc current available. However, in this research the maximum available arc length for each power cycle were recorded and used as 'arc length' for data acquisition and analysis. Therefore, each half cycle of an arc corresponds to only one arc length and this assumption is used throughout the whole thesis.

A balance can be achieved between arc heating to expand the dry-band area and moisture deposition to reduce this area. In the experimental situations, the arc heating effect can be adjusted by changing the values of source voltage, and the available maximum arcing current which is restricted by the current limiting resistor; while the moisture deposition can be controlled by fog precipitation rate or spray flow rate. Therefore, an 'equilibrium arc length' can be obtained after the balance is achieved, with a fairly constant arc length observed in every consecutive power cycles.

Arc length can be changed due to experimental conditions. For the of *Testing in a Fog Environment*, the arc length extended following the increase of source voltage, as a more powerful arc with higher voltage and current level could produce more Joule heating to expand the dry-band area, therefore increasing the arc length. In contrast, in the *Testing with Inclined Samples*, the dry-band area was compressed in length due to the gravity of upper water film on an inclined sample, confining an arc length. The *Tests between Water Drops* manually adjusted the water electrode separation to obtain the arcs with 'expected' lengths. In the *Tests with Artificial Wind and Rain*, by changing moisture deposition such as increasing or decreasing rain precipitation levels, or by modifying external forces such as enhancing or weakening the wind injection, the arc length could also be changed.

7.2.3 BREAKDOWN VOLTAGE

In the *Thesis Experimental Part* of Chapter 5, the relationships between breakdown voltage and arc length were respectively shown in Figure 5-10 of *Testing in a Fog Environment*, Figure 5-19 of *Testing with Inclined Samples*, Figure 5-33 of *Tests between Water Drops* and Figure 5-41 of *Tests with Artificial Wind and Rain*. All the results show the similar trends that the breakdown voltage reduces when the arc length (electrode separation) decreases: In the *Testing in a Fog Environment*, the breakdown voltage increased following the rise of source voltage leading to the expansion of dry-band length by more powerful arcs. In the *Testing with Inclined Samples*, the breakdown voltage of an arc dropped on more inclined samples as the dry-band arc was compressed in length. In the *Tests between Water Drops*, the breakdown voltage increased in case of the two droplets moving towards to each other, shortening the water electrodes' separation. In the *Tests with Artificial Wind and Rain*, the breakdown voltage reduced corresponding to the arc length reduction resulting from wind compression.

Breakdown voltage for a low current arc striking between water electrodes also depends on the dynamic change of water droplet shape under the electric fields. In the *Tests between Water Drops*, research found that the breakdown voltage also changed with source voltage levels for the same electrode separation, due to the 'real' arc length change between mobile water electrodes. This arrangement of an arc striking in the free air allowed more freedom for the water electrodes' movement and distortion than the arcing activities on the solid insulation surface. Therefore, no such phenomenon was observed in other tests with the surface presence.

7.2.4 ARCING PERIOD

The arcing period is the period from arc ignition to arc extinction. For 'the free-growth arcs' in the *Testing in a Fog Environment*, the arcing period kept approximately constant for the different current levels from 1.5 mA to 4.0 mA (Figure 5-11), due to the breakdown voltage increases with the source voltage to make the arc ignition time roughly constant. For the 'length-compressed arcs' in Figure 5-17 of the *Testing with Inclined Samples*, and in Figure 5-41 of the *Tests with Artificial Wind and Rain*, the arcing period was prolonged corresponding to the arc length reduction. This was due to the decrease in breakdown voltage bringing forward the arc ignition time under the same source voltage. But the arc extinction time did not change much according to the experimental observations.

Research in this thesis indicates that the arcing period is a key factor for the arc energy change as the arc striking for longer period may allow more energy accumulation. This is also the main reason for the energy increase during the arc compression process.

7.2.5 ARC RESISTANCE AND RESISTIVITY

The instantaneous arc resistance for stable arcs performed a 'U' shape in the experimental works from Chapter 5. For the 'free-growth arcs' in the *Testing in a Fog Environment*, the minimum value of instantaneous arc resistance (R_{min}) had similar values in the arcing levels of 1.5 mA to 4.0 mA in Figure 5-14, while the minimum instantaneous arc resistivity (R'_{min}) reduced significantly following the arcing level increases in Figure 5-15, due to the resultant expansion of dry-band arc length following the rise of arc current and voltage. In contrast, for the 'length-compressed arc' created in *Testing with Inclined Samples*, the trend of R_{min} reduced from an arc length of 2.32 cm to 1.11 cm during the arc

compression process, while the R'_{min} still kept fairly constant throughout. This was due to the fixed R'_{min} under the same source voltage and arc current level, even in the arc compression situations. But the dry-band area kept reducing during the process, leading to the drop of R_{min} from 6 MΩ cm to 3.5 MΩ.

7.2.6 Arc Energy and Energy Density

The changes of arc energy and energy density were analyzed in the two main situations: the unstable discharges becoming stable arcs and the stable arcs being compressed in physical length. The first situation was achieved by the *Tests with Artificial Wind and Rain*, with energy calculation examples shown in Figure 5-42 and Figure 5-43, demonstrating the arc energy could rise from less than 0.01 Joule per cycle (unstable discharges) to higher than 0.01 Joule per cycle (stable arcs) with up to 3 times increase during the process. The energy density changes for the first situation were shown in Figure 5-46, with the order of 10 times increase from unstable discharges to stable arcs. The second arc compression situation was created respectively in both the *Testing with Inclined Samples* and *Tests with Artificial Wind and Rain*. Both of which showed the increase trend in arc energy following the arc length compression for different arcing levels on inclined insulation surfaces in Figure 5-28, and for arcs under the wind impact in Figure 5-44. For the energy density analysis during the arc compression process, results showed significant rise in energy density for different arcing levels on inclined insulation surface up to 10 times from Figure 5-29, and up to 6 times' increase due to the wind effected arc compression in Figure 5-47.

The arc energy and energy density trends in this thesis indicate that the low current discharges could become more detrimental to insulation material surfaces in terms of enhanced heat radiation under certain

events, such as unstable discharges becoming stable and arc compression in physical lengths.

7.3 Modelling and Simulation of Low Current Arcs

7.3.1 Modelling Parameter Extraction from Experimental Results

The data extraction was based on observing the experimental results in terms of I-t and V-t curves stored in Excel files. Each power cycle contained 800 points of sample data and the modelling parameters of breakdown voltage, arc ignition time and voltage, arc extinction time and voltage, arc current peak were obtained based on the digital values of data group from Excel with Matlab programming to select the best fit data. This method ensures better accuracy for the modelling of low current discharges from the range of less than 1 mA to several mA.

7.3.2 Modelling Assumptions

The Double Sinusoidal Model for the modelling of dry-band arc compression in section 6.2.1 made a few assumptions that the arcing voltage was an inclined straight line during the arcing period and this line was unchanged for the different arc length from 2.32 cm to 1.11 cm. This assumption was for simplification and could reflect the main shape of arcing voltage during the tests. The arc extinction time was also assumed to be constant during the arc compression process, determined by calculating the mean value of all cases from the *Testing with Inclined Samples*. A similar assumption was made for angular frequency of current sinusoidal wave to be a constant value throughout the arc compression process, although the above parameters where slightly changed with different arc length from the measurement results. Those assumptions were all acceptable as the modelled I-t and V-t curves have

shown high correlation with the experimental results summarized in Table 6-10 and Table 6-11. However, the arc energy and energy calculations still demonstrated some errors (less than 10%) compared with experiment in Figure 6-13 and Figure 6-14.

The PSCAD simulations for low current stable arcs and arc compression were conducted based on the experimental test circuits. Assumptions were made that the current limiting resistor was unchanged for each of simulation. Refering to the real experimental conditions, the current limiting resistor did changed with temperature variation resulting from leakage current during the testing period. The current limiting resistor used for test may rise in temperature up to 20°C according to measurement (within 12.5% of resistance change). This assumption for the PSCAD simulation circuit was for simplification and proved to be acceptable, as the evidence of high correlation with experimental results were shown in Table 6-10 and Table 6-11. However, for the arc energy and energy density calculations, errors (less than 10%) still existed between PSCAD calculation results and experimental results, shown in Figure 6-13 and Figure 6-14.

The PSCAD simulation for unstable discharges made the assumption that the frequency of discharge voltage and current instability was initially at 2000 Hz, and reduced towards stable arcs to a final 200 Hz. This is an ambitious assumption that for the real testing cases in the *Tests with Artificial Wind and Rain*, the unstable discharges varied by every single power cycle and the exact shape of instability could be hardly predicted. However, the PSCAD simulation based on this assumption could reflect the main characteristics of unstable discharges with evidence shown in Figure 6-17. But the correlation coefficients between simulation and experiment results for unstable discharges (part 6.3.3) were not as accurate as for stable arcs.

The Triple Cylinder Model for the modelling of thermal dynamics of arcs made a few assumptions. First assumption was on three cylinder regions identified as 'Cathode spot region', 'Anode spot region' and 'Arc column'. In the real situations, experimental work in Chapter 5 showed the arcing region was changed by time with no constant appearance as either a 'cylinder shape' or 'three distinguish regions'. This assumption was the basic structure of this model and for reflecting the rough power flow inside the arc and from arc to its surroundings. The second assumption was made for the heat transfer coefficients inside the arc and from arcing region to surroundings. The coefficients k_k, k_a, k_{1s}, k_{2s}, k_{3s} were determined by the evaluation of temperature difference between arc and water films. This is an ambitious assumption and could reflect the basic heat transfer coefficients from arcing region to insulation material surfaces. The coefficients of heat transfer between different arc regions which were respectively K_{1a}, k_{2a}, k_{1k}, and k_{2k} were taken from literature [63]. This model was original designed for high current, low voltage arcs and has limitation on the low current dry-band arc application. Due to the difficulties in measuring the arc plasma temperature in every directions, this model has not been verified through experimental approaches.

CHAPTER 8

CONCLUSION

In this thesis, the ageing phenomenon of outdoor insulation under low leakage currents has been investigated. The research was focused on the two main elements: the low current ageing without obvious electrical discharges, and the low current arcs with extreme arcing compression situations. Two kinds of methodologies have been used in this research; these are classified as experimental study and simulation. Experimental work conducted was: the contact angle measurement for insulation surface examination, testing in a fog environment, testing on the inclined samples, testing between water droplets and tests under artificial wind and rain. The simulation work carried out was: electric field calculations, Double Sinusoidal Model, Triple Cylinder Model, and PSCAD simulation.

The *Contact Angle Measurement* and *Electric Field Calculations* provided evidence that the long-term low leakage current could degrade the ADSS cable sheath on a 132 kV transmission lines after 15 years of service.

The *Testing in a Fog Environment* has experimentally established stable dry-band arcs on insulation rod, identified the arcing development stages, observed material surface property changes during the arc formation, analyzed the arcing properties in terms of arc voltage and breakdown voltage, arc current, arcing period, arc resistance and resistivity. The salt-fog conditions have been identified as the most severe conditions for low current dry-band arc growth.

The *Testing on the Inclined Samples* has successfully created dry-band arc compression events. Following the reduction of arc length, the breakdown voltage reduced making the arcing period longer; the peak of arc current increased following the drop of arc resistance. As a result, both arc energy and energy density were dramatically increased which might potentially bring severe heating effects to the insulation materials.

The *Testing between Water Drops* created conditions to study low current arcing between water contacts with variable separation without the influence of insulation surfaces. Unstable discharges were observed in this test in situations which had enough voltage to ignite an arc but insufficient current to sustain it. The trends of energy and energy density showed significant increases following the reduction of arc length between two droplets. This research proved that the 'arc compression' retained its nature without the impact of insulation surfaces, with both increase in arc power and energy resulting more heating effect from arcing regions.

The *Testing with Artificial Wind and Rain* successfully provided other environmental situation for low current arc (several mAs) compression, and also the possible transformation from extreme low current unstable discharges (lower than 1 mA) to stable arcs by the impact of wind. Both the processes of arc compression and unstable discharges becoming stable showed the arc energy and energy density could increase significantly.

The simulation works developed a novel *Double Sinusoidal Model* to simulate the voltage and current profiles of dry-band arc and its compression process. The *PSCAD simulation* based on the experimental circuits successfully simulated the test results from the fog environmental tests, inclined sample tests, and artificial wind and rain tests with high degrees of correlation. The *Triple Cylinder Model* was

developed to calculate the heat radiation from arcs to their surroundings especially to material surfaces. The simulation work successfully replicates the experimental observation that during the arc compression process, the arc energy and its density were dramatically increased, and the heat radiation from arc to material surfaces were significantly enhanced.

The final conclusion of this thesis is to confirm that the low current arc compression phenomenon could have severe impact on surface insulation. Therefore, the lifetime of the insulation materials could not be only determined by the long-term ageing effect, but also rare events such as low current arc compressions. Such extreme events may dominate the insulation lifetime and cause unexpected failures to power systems.

CHAPTER 9

FUTURE WORK

Future experimental work should focus on the real geometry of insulators on overhead transmission lines, investigating low current discharges on the more complex insulator surfaces and the possibility of transformation from low energy arcs to certain extreme conditions such as dry-band arc compression, or from unstable discharges to stable arcs, both of which have been already discussed in this thesis. As discussed, the materials may fail quicker when exposed to 'normal' low current ageing conditions. Signs of degradation of transmission line elements under such events may be reported in the future based on the theory proposed in this thesis, and heightened awareness of the process.

Experimental work between water drops was found that the droplets under AC electric field without an insulation surface may be highly deformed, and this may affect the electrical behaviours of low current arcs such as breakdown voltage and arc length. This phenomenon needs to be further studied by applying high speed camera into experiment, and the links between electric field strength, water distortion images and arcing properties need to be further established.

Modelling work for low current discharges should be further developed. Double sinusoidal model should expand its applications for simulating arcs with higher current and voltage levels. The capability of such model for wider applications needs to be assessed. The investigation also needs to be conducted searching for the reason why currents during the arcing period appear as sinusoidal waveforms, together with the minimum arc resistance fairly constant with different current levels from 1 mA to 5 mA.

Thermal models should be further implemented by considering the real shape of arcs. The distances from the arcing plasma to material surfaces from cathode, anode and arc column are different, and that needs to be taken into consideration. Due to the experimental limitations, difficulties are existed to measure the thermal flow inside the arc and near surrounding regions. Therefore, a new route needs to be found to further verified the validly of thermal models and provide experimental support for modelling parameters.

A new model should be built based on the physics of discharges, which is able to help understanding the instability of discharges, and the reason for transformation to more stable situations. Ideas of using static arc resistance and investigating the relationship between this resistance and arc length need to be further carried out for arc compression cases.

REFERENCES

[1] J.S.T.Looms, *Insulators for High Voltages*. London: Peter Peregrinus Ltd, 1990.

[2] J. F. Hall, "History and bibliography of polymeric insulators for outdoor applications," *IEEE Transactions on Power Delivery*, vol. 8, pp. 376-385, 1993.

[3] R. S. Gorur, E. A. Cherney, and J. T. Burnham, *Outdoor Insulators*. Phoenix, Arizona, USA, 1999.

[4] G. F. Moore, "Part 7: Optical Fibres in Power Transmission Systems," in *Electric Cables Handbook*, 3rd Edition ed: Blackwell Science, 1997, pp. 685-752.

[5] A. Haddad and D. Warne, *Advanced in High Voltage Engineering*. London: The institution of Electrical Engineers, 2004.

[6] C. N. Carter, J. Deas, N. R. Haigh, and S. M. Rowland, "Applicability of all-dielectric self-supporting cable system to very high voltage overhead power lines," *46th Proc. International Wire and Cable Symposium*, 1997, pp. 624-631.

[7] made-in-china.com. vol. 2010: http://image.made-in-china.com/2f0j00ZBEacGrJgfgm/25KV-Polymer-Suspension-Insulator.jpg, 26 Oct 2010.

[8] K. Kamo, T. Nakanishi, Y. Hayashi, and R. Matsuoka, "Reproducing tests of brittle fractures of polymer insulators," *Proceedings of the 6th International Conference on Properties and Applications of Dielectric Materials*, 2000, pp. 395-398 vol.1.

[9] S. Wu, *Polymer interface and adhesion*. New York: Technology & Engineering, 1982.

[10] N. E. Frost and M. Krenceski, "Hydrophobicity recovery in silicone insulators: a closer look at testing," *IEEE International Symposium on Electrical Insulation*, 2002, pp. 220-223.

[11] Y. Li, "Application of composite insulators in seriously contaminated areas," in *Eleventh International Symposium on High Voltage Engineering(Conf. Publ. No. 467)*, 1999, pp. 180-183 vol.4.

[12] R. G. Houlgate and D. A. Swift, "Composite rod insulators for AC power lines: electrical performance of various designs at a coastal testing station," *IEEE Transactions on Power Delivery*, vol. 5, pp. 1944-1955, 1990.

[13] R. Hackam, "Outdoor HV composite polymeric insulators," *IEEE Transactions on Dielectrics and Electrical Insulation*, vol. 6, pp. 557-585, 1999.

[14] M. Kumosa, L. Kumosa, and D. Armentrout, "Failure analyses of nonceramic insulators Part 1: Brittle Fracture Characteristics," *IEEE Electrical Insulation Magazine*. vol. 21, May/June 2005, pp. 14-27.

[15] A. J. Davies, P. Radage, S. M. Rowland, and D. J. Walker, "The selection of materials for a long span, dielectric, aerial, self-supporting cable for optical communications," *Plastics in Telecomms*. vol. VI London, 1992, pp. 27/1-27/10.

[16] S. M. Rowland, K. Craddock, C. N. Carter, I. Houghton, and D. Delme-Jones, "The development of a metal-free, self-supporting, optical cable for use on long span, high voltage overhead power lines," in *Proc 36th Int Wire and Cable Symposium*, 1987, pp. 449-456.

[17] S. M. Rowland and F. Easthope, "Electrical ageing and testing of dielectric self-supporting cables for overhead power lines," *IEE Proceedings-Science, Measurement and Technology*, vol. 140, pp. 351-356, 1993.

[18] S. M. Rowland, "Sheathing materials for dielectric, aerial, self-supporting cables for application on high voltage power lines," *6th IEE Conference on Dielectric materials, Measurements and Applications*, 1992, pp. 53-56.

[19] H. Ye, J. Zhang, Y. M. Ji, W. Y. Sun, K. Kondo, and T. Imakoma, "Contamination accumulation and withstand voltage characteristics of various types of insulators," *Proceedings of the 7th International Conference on Properties and Applications of Dielectric Materials*, 2003, pp. 1019-1023 vol.3.

[20] G. G. Karady, "Flashover mechanism of non-ceramic insulators," *IEEE Transactions on Dielectrics and Electrical Insulation,* vol. 6, pp. 718-723, 1999.

[21] E. A. Cherney and D. J. Stonkus, "Non-ceramic insulators for contaminated environments," *IEEE Transactions on Power Apparatus and Systems,* vol. PAS-100, pp. 131-142, 1981.

[22] S. E. Kim, E. A. Chemey, and R. Hackam, "Effect of dry band arcing on the surface of RTV silicone rubber coatings," in *IEEE International Symposium on Electrical Insulation* Baltimore, MD USA, 1992.

[23] A. J. Phillips, D. J. Childs, and H. M. Schneider, "Aging of nonceramic insulators due to corona from water drops," *IEEE Transactions on Power Delivery,* vol. 14, pp. 1081-1089, 1999.

[24] D. Windmar, "Water Drop Initiated Discharges in Air," *Uppsala University*. vol. PHD Thesis, 1994.

[25] A. J. Phillips, D. J. Childs, and H. M. Schneider, "Water drop corona effects on full-scale 500 kV non-ceramic insulators," *IEEE Transactions on Power Delivery,* vol. 14, pp. 258-265, 1999.

[26] K. Katada, Y. Takada, M. Takano, T. Nakanishi, Y. Hayashi, and R. Matsuoka, "Corona discharge characteristics of water droplets on hydrophobic polymer insulator surface," *Proceedings of the 6th International Conference on Properties and Applications of Dielectric Materials*, 2000, pp. 781-784 vol.2.

[27] I. J. S. Lopes, S. H. Jayaram, and E. A. Cherney, "A method for detecting the transition from corona from water droplets to dry-band arcing on silicone rubber insulators," *IEEE Transactions on Dielectrics and Electrical Insulation,* vol. 9, pp. 964-971, 2002.

[28] V. M. Moreno and R. S. Gorur, "Effect of long-term corona on non-ceramic outdoor insulator housing materials," *IEEE Transactions on Dielectrics and Electrical Insulation,* vol. 8, pp. 117-128, 2001.

[29] Y. Koshino, I. Umeda, and M. Ishiwari, "Deterioration of silicone rubber for polymer insulators by corona discharge and effect of fillers," *Annual Report. Conference on Electrical Insulation and Dielectric Phenomena*, 1998, pp. 72-79 vol. 1.

[30] Q. Huang, G. G. Karady, B. Shi, and M. Tuorninen, "Calculation of the electric field distribution on ADSS fiber optic Ccable," *Conference on Electrical Insulation and Dielectric Phenomena*, 2003, pp. 379-382.

[31] S. M. Rowland and I. V. Nichols, "Effects of dry-band arc current on ageing of self-supporting dielectric cables in high fields," *IEE Proceedings -Science, Measurement and Technology,* vol. 143, pp. 10-14, 1996.

[32] B. F. Hampton, "Flashover mechanism of polluted insulation," *IEE Proceedings,* pp. 985-990, 1964.

[33] X. Zhang, S. Rowland, and V. Terzija, "Increased energy in stable dry-band arcs due to length compression," *IEEE Transactions on Dielectrics and Electrical Insulation,* vol. 17, pp. 473-480.

[34] A. E. Guile, "The protection of high-voltage insulators from power-arc damage," *Proceedings of the IEE - Part A: Power Engineering,* vol. 108, pp. 317-323, 1961.

[35] P. Ranon, M. Kristiansen, F. Lehr, and L. Hatfield, "Insulator damage in high current discharges," *IEEE Transactions on Magnetics,* vol. 22, pp. 1695-1698, 1986.

[36] R. Matsuoka, K. Tanaka, H. Shinokubo, and J. T. Burnham, "Damage of nonceramic insulator end fittings by power arc currents," in *IEEE 8th International Conference on Transmission & Distribution Construction, Operation & Live-Line Maintenance*, 1998, pp. 278-284.

[37] C. L. Phan and M. Hara, "Leakage current and flashover performance of iced insulators," *IEEE Transactions on Power Apparatus and Systems,* vol. PAS-98, pp. 849-859, 1979.

[38] R. S. Gorur, A. D. L. O, H. El-Kishky, M. Chowdhary, H. Mukherjee, R. Sundaram, and J. T. Burnham, "Sudden flashover of nonceramic insulators in artificial contamination tests," *IEEE Transactions on Dielectrics and Electrical Insulation,* vol. 4, pp. 79-87, 1997.

[39] A. d. L. O and R. S. Gorur, "Flashover of contaminated nonceramic outdoor insulators in a wet atmosphere," *Dielectrics and Electrical Insulation, IEEE Transactions on,* vol. 5, pp. 814-823, 1998.

[40] K. Seog-Hyeon, E. A. Cherney, R. Hackam, and K. G. Rutherford, "Chemical changes at the surface of RTV silicone rubber coatings on insulators during dry-band arcing," *IEEE Transactions on Dielectrics and Electrical Insulation,* vol. 1, pp. 106-123, 1994.

[41] C. N. Carter, "Dry band electrical activity on optical cables strung on overhead power lines," in *Proc. 37th International Wire and Cable Symposium*, 1988, pp. 117-121.

[42] S. M. Rowland, "Prevention of dry-band arc damage on ADSS cables," *IEEE Transactions on Dielectrics and Electrical Insulation,* vol. 13, pp. 765-772, 2006.

[43] S. M. Rowland, "Engineering a solution to the aging of HV self-supporting cables by dry-band arcing," *IEEE Electrical Insulation Magazine,* vol. 22, pp. 33-43, 2006.

[44] F. Kaidanov, R.Munteanu, and G.Sheinfain, "Damages and destruction of fiber optic cables on 161 kV overhead transmission lines," *IEEE Electrical Insulation Magazine,* vol. 16, pp. 16-23, 2000.

[45] G. G. Karady, G. Besztercey, and M. W. Tuominen, "Corona caused deterioration of ADSS fiber-optic cables on high voltage lines," *IEEE Transactions on Power Delivery,* vol. 14, pp. 1438-1447, 1999.

[46] D. A. Brewer, L. A. Dissado, and M. J. Parry, "Limitations on the damage mechanism in dry band arcing on all dielectric self supporting cables," in *Sixth International Conference on Dielectric Materials, Measurements and Applications*, 1992, pp. 49-52.

[47] G. G. Karady, S. Baozhuang, H. Qi, D. Srinivasan, and M. W. Tuominen, "Experimental investigation of the aging process on ADSS optical fiber cables," in *IEEE Power Engineering Society General Meeting*, 2003, p. 228 Vol. 1.

[48] S. Baozhuang, G. G. Karady, H. Qi, and M. W. Tuominen, "Experimental studies of the characteristics of dry band arcing on ADSS fiber optic cables," *IEEE Transactions on Power Delivery,* vol. 19, pp. 1936-1940, 2004.

[49] X. Zhang, S. M. Rowland, and V. Terzija, "Increased energy in stable dry-band arcs due to length compression," *IEEE Transactions on Dielectrics and Electrical Insulation,* vol. 17, pp. 473-480.

[50] X. Zhang, "Analysis of High Voltage Optical Cable Performance," in *The University of Manchester*. vol. MSc Dissertation Manchester, 2007.

[51] *ASTM D2303 Standard Test Methods for Liquid-Contaminant, Inclined-Plane Tracking and Erosion of Insulating Materials*, Sep 10, 1997.

[52] L. H. Meyer, S. H. Jayaram, and E. A. Cherney, "Correlation of damage, dry band arcing energy, and temperature in inclined plane testing of silicone rubber for outdoor insulation," *IEEE Transactions on Dielectrics and Electrical Insulation,* vol. 11, pp. 424-432, 2004.

[53] S. M. Rowland and F. C. Lin, "Stability of alternating current discharges between water drops on insulation surfaces," *J. Phys. D: Appl. Phys,* vol. 39, pp. 3067-3076, 2006

[54] "IEC 1109 Standard: Artificial Pollution Tests on High Voltage Insulators to be Used in A.C. Systems."

[55] A. H. El-Hag, S. H. Jayaram, and E. A. Cherney, "Fundamental and low frequency harmonic components of leakage current as a diagnostic tool to study aging of RTV and HTV silicone rubber in salt-fog," *IEEE Transactions on Dielectrics and Electrical Insulation,* vol. 10, pp. 128-136, 2003.

[56] Y. Zhu, M. Otsubo, N. Anami, C. Honda, O. Takenouchi, Y. Hashimoto, and A. Ohono, "Change of polymeric material exposed to dry band arc discharge [polymer insulator applications]," in *Annual Report Conference on Electrical Insulation and Dielectric Phenomena*, 2004, pp. 655-658.

[57] A. H. El-Hag, "Detection of dry-band arcing using time series modeling [silicone rubber insulator arcing]," in *Annual Report Conference on Electrical Insulation and Dielectric Phenomena*, 2004, pp. 615-618.

[58] N. Anami, Y. Zhu, S. Hashimoto, M. Otsubo, C. Honda, O. Takenouchi, and Y. Hashimoto, "Evaluation of dry band arc on the polymeric insulator using differential technique and distortion factor of leakage current," in *Annual Report. Conference on Electrical Insulation and Dielectric Phenomena*, 2003, pp. 414-417.

[59] S. Baozhuang, H. Qi, G. G. Karady, and M. W. Tuominen, "Studies on the length of dry band arcs on ADSS fiber optic cables," in *Annual Report. Conference on Electrical Insulation and Dielectric Phenomena*, 2003, pp. 353-356.

[60] H. Qi, G. G. Karady, B. Shi, and M. Tuominen, "Numerical simulation of dry-band arcing on the surface of ADSS fiber optic cable," *IEEE Transactions on Dielectrics and Electrical Insulation,* vol. 12, pp. 496-503, 2005.

[61] V. Terzija and H. J. Koglin, "On the modeling of long arc in still air and arc resistance calculation," *IEEE Transactions on Power Delivery,* vol. 19, pp. 1012-1017, 2004.

[62] V. Terzija, G. Preston, M. Popov, and N. Terzija, "New static 'AirArc' EMTP model of long arc in free air," *IEEE Transactions on Power Delivery*, accepted for publication on 04/10/2010.

[63] P. Borkowski and E. Walczuk, "Thermal models of short arc between high current contacts," *Proceedings of the Forty-Seventh IEEE Holm Conference on Electrical Contacts*, 2001, pp. 259-264.

[64] S. M. Rowland, K. Kopsidas, and X. Zhang, "Aging of polyethylene ADSS sheath by low currents," *IEEE Transactions on Power Delivery,* vol. 25, pp. 947-952.

[65] S. M. Rowland, X. Zhang, and K. Kopsidas, "Ageing of an ADSS cable sheath on a 132kV overhead transmission line," in *Annual Report Conference on Electrical Insulation and Dielectric Phenomena*, 2008, pp. 192-195.

APPENDIX 1: MATLAB PROGRAMS

APPENDIX 1.1

(Arc Energy calculation based on the measured I-t and V-t files)

```
clear; clc; column=0;

% read V-t and I-t data from measurement results field as '1.log',
'2.log', '3.log'…; each file contains 3200 rows, 2 columns, 4 power
cycles of data. 1st column is voltage data group, 2nd column is current
data group

for dataNo=(1:40) %This example contains 40 recorded files of data
    data_name_part=int2str(dataNo);
    data_name=[data_name_part '.log'];
    IVdata=dlmread(data_name);

    % energy calculation for every half power cycles
    Energyunit=0;
    for halfcycle=(1:8) % each files contains 8 half power cycles
      for row=((halfcycle-1)*400+1:halfcycle*400)
      energyunit=energyunit+(IVdata(row,1)*IVdata(row,2)+IVdata(row+1,1)*
      IVdata(row+1,2))*0.025*0.001/2;
        if row==halfcycle*400
            column=column+1;
            energy_result(1,column)=energyunit; % write energy results
            energyunit=0;
        end
      end
    end
end
```

APPENDIX 1.2

(Calculation of instantaneous power distribution based on the Triple Cylinder Model)

```
clear
datamax=xlsread('V I profile.xls') %load V I profile
%parameter setting
Kk=0.3
K1a=0.2
K2a=0.2
Ka=0.3
K1k=0.2
K2k=0.5
K1=0.2
K2=0.2
```

```
K1s=0.3
K2s=0.3
K3s=0.3
KL=0.000528
Larcmax=0.0111 %arc length change by case
%calculation start
for i=1:1600
    I(i)=abs(datamax(i,15)) %change by case
    V(i)=abs(datamax(i,16)) %change by case
    P1(i)=0.001*1/3*V(i)*I(i)
    P2(i)=0.001*1/3*V(i)*I(i)
    P3(i)=0.001*1/3*V(i)*I(i)
    a1(i)=KL*I(i)
    a2(i)=a1(i)
    a3(i)=a1(i)
    d1(i)=a1(i)
    d2(i)=a1(i)
    d3(i)=Larcmax-d1(i)-d2(i)
end
for t=1:1600
    if (I(t)==0)|(V(t)==0)
        Pk(t)=0
        Pa(t)=0
        P1s(t)=0
        P2s(t)=0
        P3s(t)=0
    else
Pk(t)=1/2*Kk*(P1(t)*(1-d1(t)/sqrt(a1(t)^2+d1(t)^2))+K2a*(1/2*P3(t)*(1-
d3(t)/sqrt(a3(t)^2+d3(t)^2))+K1a*1/2*P2(t)*(1-
d2(t)/sqrt(a2(t)^2+d2(t)^2))))

Pa(t)=1/2*Ka*(P2(t)*(1-d2(t)/sqrt(a2(t)^2+d2(t)^2))+K2k*(1/2*P3(t)*(1-
d3(t)/sqrt(a3(t)^2+d3(t)^2))+K1k*1/2*P1(t)*(1-
d1(t)/sqrt(a1(t)^2+d1(t)^2))))

P1s(t)=K1s*(P1(t)+K2a*(1/2*P3(t)*(1-
d3(t)/sqrt(a3(t)^2+d3(t)^2))+K1a*1/2*P2(t)*(1-
d2(t)/sqrt(a2(t)^2+d2(t)^2))))*d1(t)/sqrt(a1(t)^2+d1(t)^2)

P2s(t)=K2s*(P2(t)+K2k*(1/2*P3(t)*(1-
d3(t)/sqrt(a3(t)^2+d3(t)^2))+K1k*1/2*P1(t)*(1-
d1(t)/sqrt(a1(t)^2+d1(t)^2))))*d2(t)/sqrt(a2(t)^2+d2(t)^2)

P3s(t)=K3s*(P3(t)+1/2*K1k*P1(t)*(1-
d1(t)/sqrt(a1(t)^2+d1(t)^2))+1/2*K1a*P2(t)*(1-
d2(t)/sqrt(a2(t)^2+d2(t)^2)))*d3(t)/sqrt(a3(t)^2+d3(t)^2)
    end
end
%data collection
for n=1:1600
    Result(n,1)=Pk(n)
    Result(n,2)=Pa(n)
    Result(n,3)=P1s(n)
    Result(n,4)=P2s(n)
    Result(n,5)=P3s(n)
end
```

APPENDIX 1.3

(Calculation of arc energy distribution based on the Triple Cylinder Model)

```
clear
% inital result
Pk_result=0
Pa_result=0
P1s_result=0
P2s_result=0
P3s_result=0
datamax=xlsread('result_P.xls') % read Pk, Pa, P1s, P2s, P3s for 1600
% creat Pk, Pa, P1s, P2s, P3s data base
for i=1:1600
    Pk(i)=datamax(i,36) %change by case
    Pa(i)=datamax(i,37) %change by case
    P1s(i)=datamax(i,38) %change by case
    P2s(i)=datamax(i,39) %change by case
    P3s(i)=datamax(i,40) %change by case
end
% Calculate ENERGY
for t=1:1599
    Pk_result=Pk_result+1/2*(Pk(t)+Pk(t+1))*0.025
    Pa_result=Pa_result+1/2*(Pa(t)+Pa(t+1))*0.025
    P1s_result=P1s_result+1/2*(P1s(t)+P1s(t+1))*0.025
    P2s_result=P2s_result+1/2*(P2s(t)+P2s(t+1))*0.025
    P3s_result=P3s_result+1/2*(P3s(t)+P3s(t+1))*0.025
end
% reformat for final result
Final_result(1)=Pk_result
Final_result(2)=Pa_result
Final_result(3)=P1s_result
Final_result(4)=P2s_result
Final_result(5)=P3s_result
```

APPENDIX 2: LIST OF PUBLICATIONS

a) S. M. Rowland, X. Zhang, and K. Kopsidas, "The impact of system voltage on the ageing of All-Dielectric Self-Supporting cables on overhead lines", 2008 IEEE International Symposium on Electrical Insulation, Vancouver, Canada, pp. 641-644, 2008.

b) S. M. Rowland, X. Zhang, and K. Kopsidas, "Ageing of an ADSS cable sheath on a 132kV overhead transmission line", Conference on Electrical Insulation and Dielectric Phenomena, CEIDP Annual Report, Quebec, Canada, pp. 192-195, 2008.

c) S. M. Rowland, K. Kopsidas, and X. Zhang, "Aging of polyethylene ADSS sheath by low currents," IEEE Transactions on Power Delivery, vol. 25, pp. 947-952, 2010.

d) X. Zhang, S. M. Rowland, and V. Terzija, "Increased energy in stable dry-band arcs due to length compression," IEEE Transactions on Dielectrics and Electrical Insulation, vol. 17, pp. 473-480, 2010.

e) X. Zhang and S. M. Rowland, "Dry-band arc compression and resultant arc energy changes," 11th INSUCON International Electrical Insulation Conference, Birmingham, United Kingdom, pp. 308-313, 2009.

f) X. Zhang, S. M. Rowland and V. Terzija, "Modelling of dry-band arc compression", 16th International Symposium on High Voltage Engineering, Cape Town, South Africa, pp. 284, 2009.

g) X. Zhang and S. M. Rowland, "Behaviour of low current discharges between water drops," IEEE Conference on Electrical Insulation and Dielectric Phenomena, Virginia Beach, USA, pp. 437-440, 2009.

h) X. Zhang and S. M. Rowland, "Modelling of dry-band discharge events on insulation surfaces," 2010 IEEE International Symposium on Electrical Insulation (ISEI), San Diego, California, USA, pp. 1-5, 2010.